THEORETICAL STUDIES ON ROTATING-SPIN-ORBIT-COUPLED AND SPIN-ORBITAL-ANGULAR-MOMENTUM -COUPLED SPINOR CONDENSATES

DOCTORAL THESIS

by

PARAMJEET

(2018PHZ0003)

DEPARTMENT OF PHYSICS
INDIAN INSTITUTE OF TECHNOLOGY ROPAR

MARCH, 2024

Theoretical studies on rotating-spin-orbit-coupled and spin-orbital-angular-momentum-coupled spinor condensates

A thesis submitted
in partial fulfillment of the requirements
for the degree of

DOCTOR OF PHILOSOPHY
by

Paramjeet
(2018PHZ0003)

DEPARTMENT OF PHYSICS
INDIAN INSTITUTE OF TECHNOLOGY ROPAR

March, 2024

Paramjeet: *Theoretical studies on rotating-spin-orbit-coupled and spin-orbital-angular-momentum-coupled spinor condensates*

This thesis is dedicated to

My family
for their patience and support

Certificate

This is to certify that the thesis entitled **Theoretical studies on rotating-spin-orbit-coupled and spin-orbital-angular-momentum-coupled spinor condensates** submitted by **Paramjeet (2018PHZ0003)** for the award of the degree of **Doctor of Philosophy** to Indian Institute of Technology Ropar is a record of bonafide research work carried out under my guidance and supervision. To the best of my knowledge and belief, the work presented in this thesis is original and has not been submitted, either in part or full, for the award of any other degree, diploma, fellowship, associateship or similar title of any university or institution.

In my opinion, the thesis has reached the standard fulfilling the requirements of the regulations relating to the degree.

Name: Dr. Sandeep Gautam
Department: Physics
Indian Institute of Technology Ropar
Rupnagar, Punjab 140001
Date: 27-03-24

Declaration of Originality

I hereby declare that the work which is being presented in the thesis entitled **Theoretical studies on rotating-spin-orbit-coupled and spin-orbital-angular-momentum-coupled spinor condensates** has been solely authored by me. It presents the result of my own independent investigation/research conducted during the time period from July 2018 to March 2024 under the supervision of Dr. Sandeep Gautam, Assistant Professor, Department of Physics, Indian Institute of Technology Ropar. To the best of my knowledge, it is an original work, both in terms of research content and narrative, and has not been submitted or accepted elsewhere, in part or in full, for the award of any degree, diploma, fellowship, associateship, or similar title of any university or institution. Further, due credit has been attributed to the relevant state-of-the-art and collaborations with appropriate citations and acknowledgments, in line with established ethical norms and practices. I also declare that any idea/data/fact/source stated in my thesis has not been fabricated/falsified/misrepresented. All the principles of academic honesty and integrity have been followed. I fully understand that if the thesis is found to be unoriginal, fabricated, or plagiarized, the institute reserves the right to withdraw the thesis from its archive and revoke the associated degree conferred. Additionally, the institute also reserves the right to appraise all concerned sections of society of the matter for their information and necessary action. If accepted, I hereby consent for my thesis to be available online in the institute's open access repository, inter-library loan, and the title and abstract to be made available to outside organizations.

Name: Paramjeet
Entry Number: 2018PHZ0003
Program: Ph. D.
Department: Physics
Indian Institute of Technology Ropar
Rupnagar, Punjab 140001

Date: 27-03-24

Acknowledgement

First, I would express my sincere gratitude to my thesis supervisor Dr. Sandeep Gautam, for not only providing me this opportunity but also for his invaluable guidance throughout the process. His uncompromising approach to research has made a deep impression on me. His knowledge, experience, support, and motivation have allowed me to grow as a researcher. I am thankful to him for his constructive suggestions and encouragement, which played a significant role in this accomplishment.

I extend my gratitude to my collaborators Dr. Arko Roy and Dr. R. Kishor Kumar for providing valuable input in our collaborative projects and enhanced my knowledge with fruitful discussions.

I sincerely acknowledge the support of members of the doctoral committee at IIT Ropar: Dr. Shubhrangshu Dasgupta, Dr. Rakesh Kumar, and Dr. Mukesh Kumar from the Department of Physics and Dr. Arvind Kumar Gupta from the Department of Mathematics. I am immensely grateful to Dr. Deepika Chaudhary for her constant motivation and encouragement throughout the journey. I appreciate the cooperation provided by Mr. Anshu Vaid and the other department staff over the years. My sincere thanks go out to Parkash for his refreshing cups of tea, as without that this Ph.D. journey would have been exhausting.

I would like to express my heartfelt gratitude to the friends I was fortunate to have during this journey. I am immensely thankful to Manju for being such a caring and wonderful friend and like a sister to me. I extend my gratitude to the cherished friends Arzoo (@ only roommate), Monika, Shagun, and Bipasha for always being there for me and sharing laughter, party nights, and cultural festivals, all of which have made this journey truly memorable. I express my gratitude to the colleagues in my research group, Pardeep, Rajat, and Ritu, for their valuable discussions and selfless help. Special thanks to Rajat for engaging in numerous interesting scientific and non-scientific conversations. I must also mention that Rajat and Manju made this journey more enjoyable through insightful conversations, shared random party nights, engaging gossip, healthy teasing, and countless moments of shared laughter have been invaluable. I would like to thank Nancy for all the conversations, party nights, and memories. I also thank Chayan, Mukesh, Vasu Dev, Sahil, Kusum, Rakhi, Daman, Sanjay, Sahab, and Katyani for our invaluable discussions and for sharing with me the joy of hearty laughter. Special thanks to Dr. Kalyani Agarwal, Dr. Malika Kaushik, Dr. Riya Wadwa, Dr. Arzoo Sharma, and Dr. Piyush Pratap Singh for the sweet memories.

I am immensely grateful to my family, with a special heartfelt appreciation for my mother, father, mother-in-law, and father-in-law for making my dreams their own. I owe them for believing in me, being unconditionally supportive, and for their countless sacrifices throughout the process. Their patience, love, and blessings have helped me complete this journey. This acknowledgment would be incomplete without mentioning my husband, Gaurav Ruhal, who always be on my side in every situation and motivates me to achieve higher and higher. His understanding and patience kept me going when life seemed difficult. Thank you is a small word to express my gratitude to him.

Finally, I thank IIT Ropar for providing me with the fellowship (through MHRD), giving me all the necessary resources for my research, as well as the financial support I needed to present my work at various conferences during my doctoral study.

Last but not the least, I must say- *I thank God since everything happens due to the will and blessings of Almighty!*

Abstract

The spin-orbital-angular-momentum (SOAM) coupling has emerged as an important theme in the field of spinor Bose-Einstein condensates (BECs) since its experimental realization a few years ago [Chen *et al.*, Phys. Rev. Lett. **121**, 113204 (2018), Chen *et al.*, Phys. Rev. Lett. **121**, 250401 (2018)]. The coupling emulates the SOAM coupling in atomic physics as it couples the spin and the orbital angular momentum of the atom; in contrast to the spin-orbit (SO) coupling between spin and the linear momentum of the atom [Lin *et al.*, Nature, **471**, 7336 (2011)].

This thesis studies the interplay of SO coupling and rotation in spinor BECs, specifically at high rotation frequencies. We consider rotating SO-coupled spin-1 and spin-2 BECs trapped in quasi-two-dimensional harmonic potentials with two types of SO coupling, namely an equal-strength mixture of Rashba and Dresselhaus couplings and Rasbha SO coupling. The combined effect of interactions, SO coupling with moderate to high rotation frequencies are analyzed systematically by variational methods and exact numerical solutions of the single-particle Hamiltonian. Using single-particle Hamiltonian, which is exactly solvable for an equal-strength mixture of Rashba and Dresselhaus couplings, we illustrate that a boson in these rotating SO- and coherently-coupled condensates is subjected to effective toroidal, symmetric double-well, or asymmetric double-well potentials under specific coupling and rotation strengths. In the presence of mean-field interactions, using the coupled Gross–Pitaevskii equations at moderate to high rotation frequencies, the analytically obtained effective potential minima and the numerically obtained coarse-grained density maxima position are in excellent agreement. In the spin-1 system, we observe that at moderate to high rotation frequencies, the spin expectation per particle of even an antiferromagnetic spin-1 Bose-Einstein condensates (BEC) approaches unity, indicating a similarity in the response of ferromagnetic and antiferromagnetic SO-coupled BECs at moderate to fast rotations. Similarly, in spin-2 systems, the antiferromagnetic, cyclic, and ferromagnetic phases exhibit similar behaviour at higher rotations.

In the second part of this thesis, motivated by the recent experiments [Chen *et al.*, Phys. Rev. Lett. **121**, 113204 (2018), Chen *et al.*, Phys. Rev. Lett. **121**, 250401 (2018)], we investigate the low-lying excitation spectrum of the ground-state phases of spin-orbital-angular-momentum-coupled spin-1 condensates. At vanishing detuning, a ferromagnetic SOAM-coupled spin-1 BEC can have two ground-state phases, namely coreless and polar-core vortex states, whereas an antiferromagnetic BEC supports only polar-core vortex solution. The angular momentum per particle, longitudinal magnetization, and excitation frequencies display discontinuities across the phase boundary between the coreless vortex and polar-core vortex phases. The low-lying excitation spectrum evaluated by solving the Bogoliubov-de-Gennes equations is marked by avoided crossings and, hence, the hybridization of the spin and density channels. The spectrum is further confirmed by the dynamical evolution of the ground state subjected to a perturbation suitable to excite a density or a spin mode and a variational analysis for the density-breathing mode.

Furthermore, we investigate the collective excitation spectrum of the annular stripe phase, which breaks two continuous symmetries: rotational and U(1) gauge symmetry. Since the annular stripe phase becomes more probable in the SOAM-coupling models corresponding to larger orbital angular momentum transfer imparted by the pair of Laguerre-Gaussian beams, we consider the Hamiltonian corresponding to $4\hbar$ orbital angular momentum transfer. The different considerations of angular-momentum transfer to the atoms by the pair of Laguerre-Gaussian beams yield different single-particle Hamiltonians and, consequently, different phase diagrams. In the presence of antiferromagnetic interactions, for different values of coupling strength and detuning, we observe the annular stripe phase along with two circular symmetric phases identified by the charge singularities of $(+4, 0, -4)$ and $(+8, +4, 0)$ in the $j = +1, 0, -1$ spin components, respectively, and calculate their low-lying excitation spectrum.

Contents

List of Figures

List of Tables

List of Abbreviations

3D - three dimensional

BEC - Bose-Einstein condensate

BECs - Bose-Einstein condensates

CGPEs - coupled Gross-Pitaevskii equations

GP - Gross-Pitaevskii

KE - kinetic energy

q1D - quasi-one-dimensional

q2D - quasi-two-dimensional

SE - spin-exchange

SO - spin-orbit

SOAM- spin-orbital-angular-momentum

SP - spin-preserving

TSBE - time-splitting Backward–Euler

TSCN - time-splitting Crank–Nicolson

TSFS - time-splitting Fourier pseudospectral

Chapter 1

Introduction

In 1924, Satyendra Nath Bose [7] examined the characteristics of photons, successfully rederiving Planck's law for black-body radiation by considering the indistinguishability of light quanta. Later, Albert Einstein [8] expanded on Bose's findings in 1925, specifically addressing the statistical properties of an ideal gas of bosons and predicting a new state of matter known as Bose-Einstein condensate (BEC). The condensation occurs when weakly interacting bosons, confined within an external potential, are cooled to a temperature close to zero [9]. Under these conditions, quantum phenomena manifest themselves at a macroscopic level, as a significant portion of bosons will autonomously fill the lowest quantum state [10]. The collaborative work of Bose and Einstein led to the formulation of the statistical framework (Bose-Einstein statistics) describing the distribution of identical particles possessing integer spin, known as bosons. Later in 1938, Fritz London proposed the idea of BEC as a mechanism for explaining superconductivity and superfluidity in liquid helium [11]. Superfluid helium exhibits many remarkable properties, such as zero viscosity and quantized vortices [12–16]. Later, it was found that these same properties are observed in gaseous Bose-Einstein condensates (BECs) [17–19]. These experiments followed the first successful experimental realization of a BEC by Eric Cornell, Carl Wieman, and their colleagues at JILA on June 5, 1995, using vapours of ^{87}Rb [20]. A few months later, BEC of ^{23}Na atoms was observed by the group led by Wolfgang Ketterle at MIT [21]. Almost at the same time, the research group of Randall Hulet at Rice University reported the observation of condensates with ^{7}Li atoms [22]. These condensates of a few hundred atoms led to important experimental findings, such as the observation of quantum mechanical interference between two different condensates [23], realization of a pulsed atom laser [24], supernova-like expansion of the condensate [25], etc. Hence, Cornell, Wieman and Ketterle won the 2001 Nobel Prize in Physics for their achievements.

In 1999, a significant breakthrough was achieved at JILA when a vortex was experimentally observed using a BEC of ^{87}Rb atoms, incorporating two distinct hyperfine spin states [17]. Shortly thereafter, the ENS group successfully created vortices in a rotating, cigar-shaped BEC consisting of a single component, revealing small vortex arrays containing four vortices [18]. Later, the MIT group achieved a milestone by creating larger rotating condensates and observed highly ordered triangular lattices known as "Abrikosov" lattices of vortices [19]. During the same year, Leanhardt *et al.* introduced an innovative technique called "topological phase imprinting" to create a coreless vortex within a spinor $f = 1$ BEC [26]. A few years later, the JILA group also studied the equilibrium properties of a triangular lattice of vortices [27]. Understanding the quantized vortex state is very important to gain deeper insights into the aforementioned observations related to rotating condensates and the phenomenon of superfluidity [28–32]. These quantized vortex states can be routinely detected in various experimental setups, including rotating single-, multi-component, and spinor BECs [33].

Among the various species where Bose-Einstein condensation has been experimentally observed include ^{87}Rb [20,34], ^{23}Na [21,35], ^{7}Li [22], ^{85}Rb [25], ^{4}He [36,37], ^{41}K [38], ^{133}Cs [39], ^{52}Cr [40], etc. To facilitate the study of BECs, the mean-field theory is extensively employed, which involves substituting the two-particle interactions in the system with an average or effective interaction, often referred to as a molecular field [41]. This approach simplifies the multi-body problem into a one-body problem, enabling the calculation of atomic interactions using an effective interaction proportional to the s-wave scattering length(s). The mean-field model of the condensate is expressed by the Gross-Pitaevskii (GP) equation [42–45].

1.1 Spinor BEC

The very first BEC was formed utilizing an atom in a single spin state of ^{87}Rb [20], and later, it was successfully created by using a single state of ^{23}Na [21]. In these systems, only the atoms in a week-field-seeking state were magnetically trapped, hence the freezing of their spin degrees of freedom. In contrast, optical traps allow for the trapping all the magnetic sublevels of a hyperfine manifold by a state-independent potential, thereby preserving the spin degrees of freedom [46]. The spin f of the atom is the sum of the electron spin S and the nuclear spin I, e.g. ^{23}Na atom with $S = 1/2$ and $I = 3/2$ can have $f = 1$ or $f = 2$. The $2f + 1$ possible spin states belonging to a given f manifold can be labelled $|f, m\rangle$. In these optical traps, the $2f + 1$ hyperfine spin states (of a spin-f atom) associated with the spin projection quantum number $m = -f, -f+1, ..., f$ can interconvert by spin-exchange collisions subject to the selection rules, which is a striking consequence of the spin degrees of freedom. In experiments, it is possible to have spinor BEC of two spin states, namely $|f, m\rangle$ and $|f, m-1\rangle$, which is treated as a pseudospin-1/2 system [47,48]. The spinor BECs of ^{87}Rb and ^{23}Na can correspond to hyperfine manifolds with $f = 1$ or $f = 2$ [49], whereas those of ^{52}Cr [50] and ^{85}Rb correspond to $f = 3$ [1]. In spinor BECs, several phases are possible depending on the nature of the interactions [1,51–54].

The hyperfine spin states of atoms can change during two-body scattering events in spinor Bose gases. To incorporate this in the Hamiltonian, one must consider the total hyperfine spin of the two particles. When two identical spin-f bosonic particles collide, they can have a total spin $\mathcal{F} = 0, 2, \ldots, 2f$ as the odd $\mathcal{F}$ values are prohibited in the s-wave limit due to symmetry considerations [1]. The scattering length, which is dependent on the total spin $\mathcal{F}$, can take up to $f + 1$ distinct values, say $a_0, a_2, \ldots, a_{2f}$ [1]. The Hamiltonian of a Bose gas with two-body inter-boson interactions can be expressed as [44]

$$\hat{H} = \hat{H}_0 + \hat{H}_{\text{int}}, \tag{1.1}$$

where $\hat{H}_0$ includes the kinetic energy and trapping potential terms and $\hat{H}_{\text{int}}$ is the part for mutual interaction between particles. For a dilute Bose gas with interparticle separation much larger than the range of interaction, the mutual interaction between the particles can be replaced by contact interaction, then these two constituents of the Hamiltonian in Eq. (1.1) are defined as [1]

$$\hat{H}_0 = \int d\mathbf{r} \sum_{m=+f}^{-f} \hat{\psi}_m^\dagger(\mathbf{r},t) \left(-\frac{\hbar^2}{2M}\nabla^2 + V(\mathbf{r},t) \right) \hat{\psi}_m(\mathbf{r},t), \quad \hat{H}_{\text{int}} = \sum_{\mathcal{F}=0}^{2f} \hat{H}_{\text{int}}^{\mathcal{F}}, \tag{1.2}$$

where

$$\hat{H}_{\text{int}}^{\mathcal{F}} = \frac{g_{\mathcal{F}}}{2} \int d\mathbf{r} \sum_{\mathcal{M}=-\mathcal{F}}^{\mathcal{F}} \hat{A}_{\mathcal{F}\mathcal{M}}^\dagger(\mathbf{r})\, \hat{A}_{\mathcal{F}\mathcal{M}}(\mathbf{r}), \tag{1.3}$$

is the interaction part of the Hamiltonian corresponding to the two bosons mutually scattering with a total spin of $\mathcal{F}$. In Eq. (1.3), $g_{\mathcal{F}} = 4\pi\hbar^2 a_{\mathcal{F}}/M$, where $\hbar$ is the reduced Planck's constant and M is the mass of the atom, and $\hat{A}_{\mathcal{F}\mathcal{M}}$ (irreducible operator) is defined as [1]

$$\hat{A}_{\mathcal{F}\mathcal{M}}(\mathbf{r}) = \sum_{m,m'=-f}^{f} \langle \mathcal{F}, \mathcal{M} \mid f, m; f, m' \rangle\, \hat{\psi}_m(\mathbf{r}) \hat{\psi}_{m'}(\mathbf{r}), \tag{1.4}$$

which annihilates a pair of bosons at $\mathbf{r}$. Using Eqs. (1.3) and (1.4), $\hat{H}_{\text{int}}$ can be rewritten as

$$\hat{H}_{\text{int}} = \frac{1}{2} \int d\mathbf{r} \sum_{m_1 m_2 m_1' m_2'} C_{m_1' m_2'}^{m_1 m_2} \hat{\psi}_{m_1}^\dagger(\mathbf{r}) \hat{\psi}_{m_2}^\dagger(\mathbf{r}) \hat{\psi}_{m_2'}(\mathbf{r}) \hat{\psi}_{m_1'}(\mathbf{r}), \tag{1.5}$$

where m_1 and m_2 are magnetic quantum number and can take a value from $f, f-1, \ldots, -f$ and

$$C_{m_1' m_2'}^{m_1 m_2} \equiv \frac{4\pi\hbar^2}{M} \sum_{\mathcal{F}=0,2,\ldots,2f} a_{\mathcal{F}} \left\langle f, m_1; f, m_2 \left| \hat{\mathcal{P}}_{\mathcal{F}} \right| f, m_1'; f, m_2' \right\rangle, \tag{1.6}$$

with $\hat{\mathcal{P}}_{\mathcal{F}} = \sum_{\mathcal{M}=-\mathcal{F}}^{\mathcal{F}} |\mathcal{F}, \mathcal{M}\rangle\langle\mathcal{F}, \mathcal{M}|$ being the projection operator onto a two-body state with the total spin angular momentum $\mathcal{F}$. Using Eq. (1.2) along with Eqs. (1.5) and (1.6), the second-quantized Hamiltonian for an interacting spin $f = 1$ BEC can be written as [1,45,55,56]

$$\hat{H} = \int d\mathbf{r} \left[\frac{\hbar^2}{2M} \nabla\hat{\psi}_m^\dagger . \nabla\hat{\psi}_m + V \hat{\psi}_m^\dagger \hat{\psi}_m + \frac{c_0}{2} \hat{\psi}_m^\dagger \hat{\psi}_m^\dagger \hat{\psi}_{m'} \hat{\psi}_{m'} + \frac{c_1}{2} \hat{\psi}_m^\dagger \hat{\psi}_{m'}^\dagger \mathbf{S}_{ml} . \mathbf{S}_{m'l'} \hat{\psi}_l \hat{\psi}_{l'} \right], \tag{1.7}$$

where the summation over repeated indices is implied, $\hat{\psi}_m^\dagger$ ($\hat{\psi}_m$) is a creation (annihilation) operator, and c_0 and c_1 are interaction parameters defined as

$$c_0 = \frac{4\pi\hbar^2(a_0 + 2a_2)}{3M}, \quad c_1 = \frac{4\pi\hbar^2(a_2 - a_0)}{3M}, \tag{1.8}$$

and $\mathbf{S} = (S_x, S_y, S_z)$ with $S_{\nu=x,y,z}$ denoting the irreducible representation of the angular momentum operator for a spin-f particle. The (m,m')th element of these $(2f+1)\times(2f+1)$ matrices are

$$(S_x)_{m,m'} = \frac{1}{2}\left[\sqrt{(f-m+1)(f+m)}\delta_{m-1,m'} + \sqrt{(f+m+1)(f-m)}\delta_{m+1,m'}\right], \tag{1.9a}$$

$$(S_y)_{m,m'} = \frac{1}{2\iota}\left[\sqrt{(f-m+1)(f+m)}\delta_{m-1,m'} - \sqrt{(f+m+1)(f-m)}\delta_{m+1,m'}\right], \tag{1.9b}$$

$$(S_z)_{m,m'} = m\delta_{mm'}. \tag{1.9c}$$

Similarly, using Eqs. (1.2), (1.5) and (1.6), the second-quantized Hamiltonian for a spin-2 BEC is [1,51,57]

$$\begin{aligned}\hat{H} = & \int d\mathbf{r}\left[\frac{\hbar^2}{2M}\nabla\hat{\psi}_m^\dagger.\nabla\hat{\psi}_m + V\hat{\psi}_m^\dagger\hat{\psi}_m + \frac{c_0}{2}\hat{\psi}_m^\dagger\hat{\psi}_m^\dagger\hat{\psi}_{m'}\hat{\psi}_{m'} + \frac{c_1}{2}\hat{\psi}_m^\dagger\hat{\psi}_{m'}^\dagger\mathbf{S}_{ml}.\mathbf{S}_{m'l'}\hat{\psi}_l\hat{\psi}_{l'}\right.\\ & \left. + \frac{c_2}{2}\hat{\psi}_m^\dagger\hat{\psi}_{m'}^\dagger\langle 2,m;2,m' \mid 0,0\rangle\langle 0,0 \mid 2,l;2,l'\rangle\hat{\psi}_l\hat{\psi}_{l'}\right],\end{aligned} \tag{1.10}$$

where

$$c_0 = \frac{4\pi\hbar^2(4a_2+3a_4)}{7M}, \quad c_1 = \frac{4\pi\hbar^2(a_4-a_2)}{7M}, \quad c_2 = \frac{4\pi\hbar^2(7a_0-10a_2+3a_4)}{7M}, \tag{1.11}$$

and $\langle 0,0 \mid 2,l;2,l'\rangle$ can be expressed as [1]

$$\langle 0,0 \mid 2,m;2,m'\rangle = \delta_{m+m',0}\frac{(-1)^{2-m}}{\sqrt{2f+1}}. \tag{1.12}$$

1.1.1 Mean-field approximation

In a many-body system with BEC, the field operator can be decomposed as

$$\hat{\psi}_m(\mathbf{r},t) = \hat{\psi}_m^0(\mathbf{r},t) + \delta\hat{\psi}_m(\mathbf{r},t), \tag{1.13}$$

where $\hat{\psi}_m^0(\mathbf{r},t)$ is the field operator which annihilates an atom from condensate in the hyperfine sublevel m, and $\delta\hat{\psi}_m(\mathbf{r},t)$ is the fluctuation operator, which can be thermal, quantum, or any other fluctuation that promotes the atoms to higher energy states. The operators $\hat{\psi}_m^0(\mathbf{r},t)$ and $\delta\hat{\psi}_m(\mathbf{r},t)$ can be expressed using the orthonormalized set of single-particle wave functions $\varphi_{\alpha,m}(\mathbf{r},t)$ as

$$\hat{\psi}_m^0(\mathbf{r},t) = \hat{a}_{0,m}(t)\varphi_{0,m}(\mathbf{r},t), \tag{1.14a}$$

$$\delta\hat{\psi}_m(\mathbf{r},t) = \sum_{\alpha\neq 0}\hat{a}_{\alpha,m}(t)\varphi_{\alpha,m}(\mathbf{r},t), \tag{1.14b}$$

where α is the index of the single particle level, $\hat{a}_{\alpha,m}$ ($\hat{a}_{\alpha,m}^\dagger$) is the annihilation (creation) operator, which satisfies the commutation relations

$$[\hat{a}_{\alpha,m},\hat{a}_{\beta,k}^\dagger] = \delta_{\alpha,\beta}\delta_{m,k}, \quad [\hat{a}_{\alpha,m},\hat{a}_{\beta,k}] = [\hat{a}_{\alpha,m}^\dagger,\hat{a}_{\beta,k}^\dagger] = 0. \tag{1.15}$$

The BEC occurs when one of the single-particle states, say $\alpha = 0$, is macroscopically occupied. The number operator of the condensate can be defined as $\hat{N}_{0,m} = \hat{a}^{\dagger}_{0,m}\hat{a}_{0,m}$, and then, $\hat{N}_{0,m}|N_{0,m}\rangle = N_{0,m}|N_{0,m}\rangle$, where $(|N_{0,-f}\rangle, |N_{0,-f+1}\rangle, \ldots, |N_{0,f}\rangle)^{\mathrm{T}}$ is the condensate state with $N_0 = \sum_m N_{0,m}$ number of atoms. Using the commutation relations, we can write

$$\frac{(\hat{a}_{0,m}\hat{a}^{\dagger}_{0,m} - \hat{a}^{\dagger}_{0,m}\hat{a}_{0,m})}{N_{0,m}}|N_{0,m}\rangle = \left(\frac{1}{N_{0,m}}\right)|N_{0,m}\rangle, \tag{1.16}$$

which tends to approach zero in the limit of macroscopic occupation of the ground state. This allows these two operators to be approximated by numbers, i.e. $\hat{a}^{\dagger}_{0,m} \approx \hat{a}_{0,m} \approx \sqrt{N_{0,m}}$. This approximation is termed as Bogoliubov approximation [44,58], which can be used in Eq. (1.14a) and then to rewrite Eq. (1.13) as

$$\begin{aligned} \hat{\psi}_m(\mathbf{r},t) &\approx \sqrt{N_{0,m}}\;\varphi_{0,m}(\mathbf{r},t) + \delta\hat{\psi}_m(\mathbf{r},t), & (1.17a)\\ &= \psi_m(\mathbf{r},t) + \delta\hat{\psi}_m(\mathbf{r},t), & (1.17b)\end{aligned}$$

where $\psi_m(\mathbf{r},t) = \langle\hat{\psi}_m(\mathbf{r},t)\rangle$ with $\langle\ldots\rangle$ denoting the ensemble average is the wave function of m^{th} spin component [59]. Assuming the temperature of the gas is well below the critical temperature, a significant fraction of the atoms will occupy the same ground state; the fluctuation operator then can be neglected $\delta\hat{\psi}_m(\mathbf{r},t) = 0$, leading to $\hat{\psi}_m(\mathbf{r},t) = \psi_m(\mathbf{r},t)$, which is the mean-field approximation.

1.1.2 Mean-field model for a spin-1 condensate

As discussed in the previous subsection, under the mean-field approximation, the field operators are replaced by c-numbers, resulting in the transformation of Eq. (1.7) to the energy functional [1,55,56,60]

$$E[\psi_m] = \int d\mathbf{r}\left[\sum_{m=+1}^{-1}\psi_m^*\left(-\frac{\hbar^2}{2M}\nabla^2 + V\right)\psi_m + \frac{c_0}{2}\rho^2 + \frac{c_1}{2}|\mathbf{F}|^2\right], \tag{1.18}$$

where $\rho(\mathbf{r}) = \sum_m |\psi_m(\mathbf{r})|^2$ is the total density of the system, and $\mathbf{F} = (F_x, F_y, F_z)$ is the spin-density vector with three components defined as

$$\begin{aligned} F_x &= \frac{1}{\sqrt{2}}[(\psi_1^* + \psi_{-1}^*)\psi_0 + \psi_0^*(\psi_1 + \psi_{-1})],\\ F_y &= \frac{\iota}{\sqrt{2}}[(\psi_{-1}^* - \psi_1^*)\psi_0 + \psi_0^*(\psi_1 - \psi_{-1})],\\ F_z &= \sum_m m|\psi_m|^2. \end{aligned}$$

The time evolution of the mean-field is given by [1]

$$\iota\hbar\frac{\partial\psi_m}{\partial t} = \frac{\delta E}{\delta\psi_m^*}, \tag{1.20}$$

which results in the following three coupled Gross-Pitaevskii equations (CGPEs):

$$\iota\hbar\frac{\partial\psi_{\pm1}}{\partial t} = \left(-\frac{\hbar^2\nabla^2}{2M} + V + c_0\rho \pm c_1F_z\right)\psi_{\pm1} + \frac{c_1}{\sqrt{2}}F_{\mp}\psi_0, \tag{1.21a}$$

$$\iota\hbar\frac{\partial\psi_0}{\partial t} = \left(-\frac{\hbar^2\nabla^2}{2M} + V + c_0\rho\right)\psi_0 + \frac{c_1}{\sqrt{2}}F_{-}\psi_{-1}, \tag{1.21b}$$

where $F_{\pm} = F_x \pm \iota F_y$.

When the parameter c_1 is positive, the energy functional (1.18) achieves its minimum value, with a zero magnetization spinor configuration, resulting in the antiferromagnetic or polar phase as the ground-state phase, and attributed, respectively, to equal populations in spin states with magnetic quantum numbers $m = \pm1$ or all the atoms residing in the spin state with $m = 0$ [1,55,56]. In contrast, when c_1 is negative, the ground-state phase is ferromagnetic, where the system can be considered polarized or magnetic, demonstrating a net magnetization [1,60].

1.1.3 Mean-field model for a spin-2 condensate

Similarly, using the mean-field approximation in Eq. (1.10), the energy functional of a spin-2 BEC is [1,51,57,61–63]

$$E[\psi_m] = \int d\mathbf{r}\left[\sum_{m=+2}^{-2}\psi_m^*\left(-\frac{\hbar^2}{2M}\nabla^2 + V\right)\psi_m + \frac{c_0}{2}\rho^2 + \frac{c_1}{2}|\mathbf{F}|^2 + \frac{c_2}{2}|\Theta|^2\right], \tag{1.22}$$

where

$$\begin{aligned}
F_x &= \psi_1^*\psi_2 + \psi_1\left(\sqrt{\frac{3}{2}}\psi_0^* + \psi_2^*\right) + \sqrt{\frac{3}{2}}\psi_0\left(\psi_1^* + \psi_{-1}^*\right) + \psi_{-1}\left(\sqrt{\frac{3}{2}}\psi_0^* + \psi_{-2}^*\right) + \psi_{-1}^*\psi_{-2},\\
F_y &= \iota\left[\psi_1^*\psi_2 + \psi_1\left(\sqrt{\frac{3}{2}}\psi_0^* - \psi_2^*\right) + \sqrt{\frac{3}{2}}\psi_0\left(-\psi_1^* + \psi_{-1}^*\right) + \psi_{-1}\left(-\sqrt{\frac{3}{2}}\psi_0^* + \psi_{-2}^*\right) - \psi_{-1}^*\psi_{-2}\right],\\
F_z &= \sum_{m=+2}^{-2} m|\psi_m|^2, \quad \Theta = \frac{1}{\sqrt{5}}(2\psi_{+2}\psi_{-2} - 2\psi_1\psi_{-1} + \psi_0^2),
\end{aligned}$$

is the spin-singlet pair amplitude. For a spin-1 BEC, the spin-singlet pair amplitude $\Theta = (2\psi_1\psi_{-1} - \psi_0^2)/\sqrt{3}$ and magnetization $|\mathbf{F}|$ are related, and either the former or the latter can be independently varied in the energy functional [1]. In contrast, in a spin-2 BEC, both can be varied independently in a specific region of the $(|\mathbf{F}|, |\Theta|)$ parameter space [1]. The $|\Theta|$ for a spin-2 BEC attains its maximum value for a time-reversal invariant order parameter of the antiferromagnetic phase, whereas it is zero for the ferromagnetic phase. From Eq. (1.20) and Eq. (1.22), we get a set of five CGPEs

$$\iota\hbar\frac{\partial\psi_{\pm2}}{\partial t} = \mathcal{H}\psi_{\pm2} + c_1(F_{\mp}\psi_{\pm1} \pm 2F_z\psi_{\pm2}) + \frac{c_2}{\sqrt{5}}\Theta\psi_{\mp2}^*, \tag{1.24a}$$

$$\iota\hbar\frac{\partial\psi_{\pm1}}{\partial t} = \mathcal{H}\psi_{\pm1} + c_1\left[\sqrt{\frac{3}{2}}F_{\mp}\psi_0 + F_{\pm}\psi_{\pm2} \pm F_z\psi_{\pm1}\right] - \frac{c_2}{\sqrt{5}}\Theta\psi_{\mp1}^*, \tag{1.24b}$$

$$\iota\hbar\frac{\partial\psi_0}{\partial t} = \mathcal{H}\psi_0 + c_1\sqrt{\frac{3}{2}}(F_-\psi_{-1} + F_+\psi_{+1}) + \frac{c_2}{\sqrt{5}}\Theta\psi_0^*, \tag{1.24c}$$

where

$$\mathcal{H} = \left(-\frac{\hbar^2\nabla^2}{2M} + V + c_0\rho\right) \text{ and } F_\pm = F_x \pm \iota F_y. \tag{1.25a}$$

Depending on the values of c_1 and c_2, three magnetic phases can emerge, namely ferromagnetic, antiferromagnetic, and cyclic phase [1,63] as illustrated in Fig. 1.1. In the case $c_1 < 0$ and $c_2 > 0$, the system's energy decreases with increasing magnetization, indicating a ferromagnetic ground state. Conversely, when $c_1 > 0$ and $c_2 < 0$, the system's lowest energy state occurs when magnetization is absent, characterizing these states as polar or antiferromagnetic. If both c_1 and c_2 are positive, cyclic phase emerges as the ground state phase [51,61,62]. The strength of interactions, as determined by scattering lengths, can potentially be controlled through the use of optical or magnetic Feshbach resonances, providing a means to manipulate the system's behavior [64].

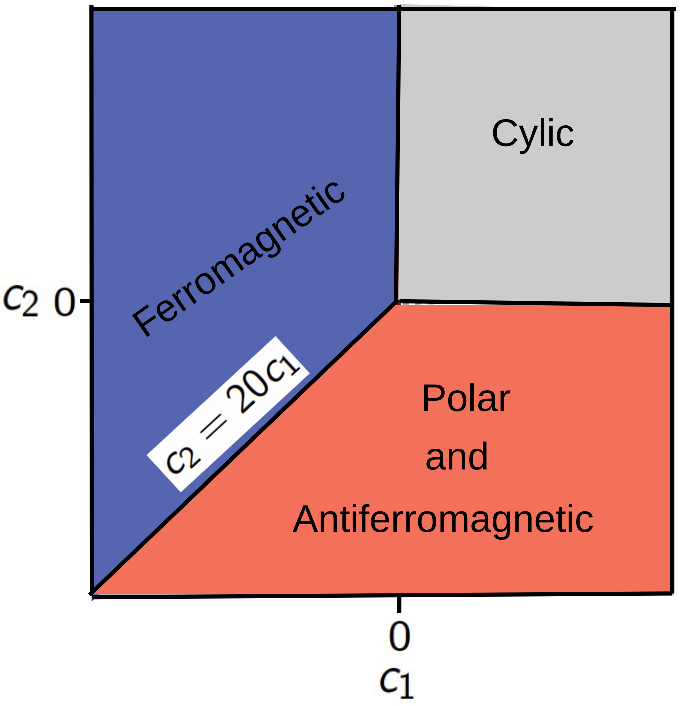

Figure 1.1: The phase diagram in c_2-c_1 plane illustrating ferromagnetic, antiferromagnetic, polar, and cyclic phases. The order parameter for the ferromagnetic, antiferromagnetic, polar, and cyclic phases are, respectively, $\sqrt{n(\mathbf{r})}(1,0,0,0,0)^T$, $\sqrt{n(\mathbf{r})}(1,0,0,0,1)^T/\sqrt{2}$, $\sqrt{n(\mathbf{r})}(0,0,1,0,0)^T$, and $\sqrt{n(\mathbf{r})}(1,0,\iota\sqrt{2},0,1)^T/2$. The polar and the antiferromagnetic phases exhibit different symmetries but are degenerate at the mean-field level [1].

1.2 Spin-orbit coupling

Spin-orbit (SO) interaction is an interesting phenomenon that arises due to the coupling of an elementary particle's intrinsic angular momentum (spin) with its orbital motion.

Here, spin is an intrinsic property of an elementary particle, such as an electron, which does not have a classical counterpart. However, the particle's momentum or velocity is directly related to its classical counterpart.

The SO coupling has implications in various systems such as quantum spin Hall states [65], topological insulators [66], spintronics [67], etc. To understand the SO coupling, consider an electron moving with velocity $\mathbf{v}$ under the effect of the electric field $\mathbf{E} = E_0\hat{\boldsymbol{z}}$. The moving electron experiences a magnetic field $\mathbf{B}$ given as

$$\mathbf{B} = -\frac{\mathbf{v}\times\mathbf{E}}{c^2}. \tag{1.26}$$

This magnetic field $\mathbf{B}$ facilitates the coupling between the electron's spin and its orbital angular momentum, leading to the SO coupling. The effective SO Hamiltonian can be defined as

$$\begin{aligned}
H_{\mathrm{SO}} &= -\boldsymbol{\mu}_e.\mathbf{B}, && \text{(1.27a)}\\
&= -\left(-\frac{g_e\mu_B\mathbf{S}}{\hbar}\right).\left(-\frac{\mathbf{v}\times\mathbf{E}}{c^2}\right), && \text{(1.27b)}\\
&= -\frac{\hbar g_e\mu_B E_0}{2Mc^2}(\mathbf{k}\times\hat{z}).\boldsymbol{\sigma}, && \text{(1.27c)}\\
&= \frac{\hbar g_e\mu_B E_0}{2Mc^2}(-k_y, k_x, 0).\boldsymbol{\sigma}, && \text{(1.27d)}\\
&= \Omega(\mathbf{k}).\boldsymbol{\sigma}, && \text{(1.27e)}
\end{aligned}$$

where $\Omega(\mathbf{k}).\boldsymbol{\sigma}$ illustrates the coupling between spin $\mathbf{S} = \hbar\boldsymbol{\sigma}/2$ and the momentum $\hbar\boldsymbol{k}/M$, $\boldsymbol{\mu}_e$ is magnetic moment, g_e is Landé's factor, and μ_{B} is the Bohr magneton. The coefficient $\hbar g_e\mu_{\mathrm{B}}E_0/2Mc^2$ in Eq. (1.27b) is the strength of Rashba SO coupling. These SO coupling interactions typically arise from the absence of mirror symmetry in two-dimensional systems [68], giving rise to the Rashba SO coupling. However, in bulk crystals, the lack of inversion symmetry results in a different form of SO coupling, known as linear Dresselhaus SO coupling [69], where $\Omega(\mathbf{k})$ in Eq. (1.27c) can be written as $\gamma_D(k_y, k_x, 0)$. These

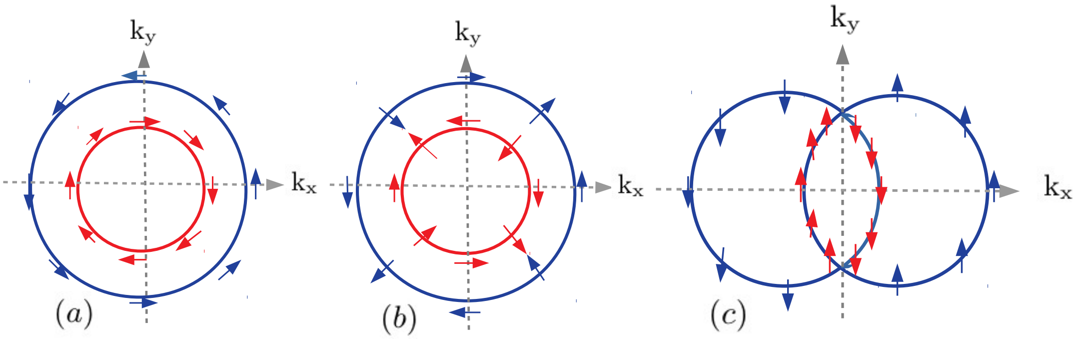

Figure 1.2: (a)-(c) represents the spin structure arising from SO coupling in a system without an inversion center: (a) Rashba, (b) Dresselhaus, and (c) persistent spin texture configurations. The blue and red arrows signify the spin orientation for the two electronic subbands resulting from SO coupling corresponding to the SO coupling field $\Omega(\mathbf{k})$. Reproduced from *Nature Communications* vol. 9, 2763, 2018 [2].

Rashba and Dresselhaus SO couplings lead to a chiral spin-texture of electronic bands in momentum space as shown in Figs. 1.2(a) and 1.2(b), respectively. The combination of symmetric Rashbha and Dresselhaus couplings gives rise to a new SO coupling interaction [2,70]. This can be attained when the magnitudes of γ_{R} and γ_{D} are equal, resulting in a unidirectional SO field with $\Omega(\mathbf{k}) = \gamma_D(k_y, 0, 0)$ or $\Omega(\mathbf{k}) = \gamma_D(0, k_x, 0)$. This coupling couples the atoms in one direction only and is known as a persistent spin texture whose schematic representation is shown in Fig. 1.2(c).

1.2.1 Synthetic SO-coupled BECs

Both the Rashba and Dresselhaus couplings play pivotal roles in numerous physical phenomena such as spin Hall effects [65], spintronics [67], topological insulators [66], quantum simulations [71,72]. Exploring these fundamental phenomena in ultracold atoms presents a fascinating avenue for research in quantum degenerate gases. However, it is crucial to emphasize that in atomic gases, the constituent atoms are electrically neutral. Consequently, the possibility of particles experiencing a Lorentz force in the presence of external magnetic fields is precluded. In this context, the artificial gauge fields provide a route for exploring the physics emanating from the Lorentz force using neutral atoms [73]. The experimental realization of artificial gauge fields [73,74] and SO coupling between the spin and the linear momentum of electrically neutral bosons [75] has paved the way to hitherto inaccessible research direction to the researchers. The first experimental realization of synthetic SO coupling in cold gases was done by employing a method based on Raman coupling [4,75].

To understand the experimentally implemented method for generating SOC through Raman coupling, we consider a scenario where two lower-energy states are connected by lasers to a higher-energy state as shown in Fig. 1.3. For that, we consider two laser beams of frequencies ω_1 and ω_2 which are close to resonance and couple internal states through a dipolar coupling denoted as $H_{\text{dip}} = -\hat{\boldsymbol{d}}.\boldsymbol{E}$, where $\hat{\boldsymbol{d}}$ is the dipole operator, and

$$\boldsymbol{E} = \boldsymbol{E}_1 \cos\left(\boldsymbol{k}_1 \cdot \boldsymbol{r} - \omega_1 t\right) + \boldsymbol{E}_2 \cos\left(\boldsymbol{k}_2 \cdot \boldsymbol{r} - \omega_2 t\right) \tag{1.28}$$

is the electric field. For these two Raman lasers, the electric-dipole interaction Hamiltonian is expressed as

$$H(t) = \begin{pmatrix} 0 & 0 & \hat{\boldsymbol{d}}_{13} \cdot \mathbf{E}(\mathbf{r}, \mathbf{t}) \\ 0 & \epsilon_2 & \hat{\boldsymbol{d}}_{23} \cdot \mathbf{E}(\mathbf{r}, \mathbf{t}) \\ [\hat{\boldsymbol{d}}_{13} \cdot \mathbf{E}(\mathbf{r}, \mathbf{t})]^* & [\hat{\boldsymbol{d}}_{23} \cdot \mathbf{E}(\mathbf{r}, \mathbf{t})]^* & \epsilon_3 \end{pmatrix}, \tag{1.29}$$

where $\hat{\boldsymbol{d}}_{ij} = \langle i|\hat{\boldsymbol{d}}|j\rangle$; $|1\rangle$, $|2\rangle$, $|3\rangle$, are basis states with energies $(0, \epsilon_2, \epsilon_3)$, respectively; and

$$\hat{\boldsymbol{d}}_{ij} \cdot \boldsymbol{E}(\boldsymbol{r}, t) = \Omega_1 \cos\left(\boldsymbol{k}_1 \cdot \boldsymbol{r} - \omega_1 t\right) + \Omega_2 \cos\left(\boldsymbol{k}_2 \cdot \boldsymbol{r} - \omega_2 t\right), \tag{1.30}$$

here $\Omega_1 = \hat{\boldsymbol{d}}_{ij}.\boldsymbol{E_1}$ and $\Omega_2 = \hat{\boldsymbol{d}}_{ij}.\boldsymbol{E_2}$. To remove the time dependence of the Hamiltonian,

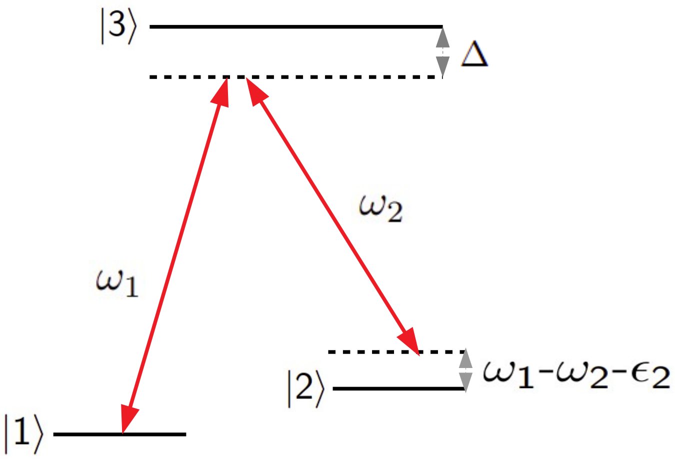

Figure 1.3: The Figure shows the process of generating SO coupling using two Raman lasers with frequencies ω_1 and ω_2. ($\omega_1 - \omega_2 \approx \epsilon_2 - \epsilon_1 \ll \epsilon_3$) which couple low-energy states $|1\rangle$, $|2\rangle$ and $|3\rangle$. This introduces coupling between $|1\rangle$ and $|2\rangle$ states as a second-order process [3,4].

we consider a time-dependent unitary operator to move the system to a rotating frame of reference, where $\psi' = U\psi$, and $H' = UHU^\dagger - \iota U \partial_t U^\dagger$. The appropriate unitary operator is

$$U = \begin{pmatrix} 1 & 0 & 0 \\ 0 & e^{-\iota(\omega_2 - \omega_1)t} & 0 \\ 0 & 0 & e^{\iota\omega_1 t} \end{pmatrix}, \tag{1.31}$$

which results in [4]

$$H' = \begin{pmatrix} 0 & 0 & \hat{\boldsymbol{d}}_{13} \cdot \boldsymbol{E}\ e^{\iota\omega_1 t} \\ 0 & \delta & \hat{\boldsymbol{d}}_{23} \cdot \boldsymbol{E}\ e^{-\iota\omega_2 t} \\ \left[\hat{\boldsymbol{d}}_{13} \cdot \boldsymbol{E}\ e^{-\iota\omega_1 t}\right]^* & \left[\hat{\boldsymbol{d}}_{23} \cdot \boldsymbol{E}\ e^{-\iota\omega_2 t}\right]^* & \Delta \end{pmatrix}, \tag{1.32}$$

where $\delta = \epsilon_2 - (\omega_1 - \omega_2)$ and $\Delta = \epsilon_3 - \omega_1$. As $|3\rangle$ is a bit far from the resonance, we may adiabatically eliminate state $|3\rangle$. For Eq. (1.32), the Schrödinger equation is $\iota\partial_t \boldsymbol{c} = H'\boldsymbol{c}$, where $\boldsymbol{c} = (c_1, c_2, c_3)^{\mathrm{T}}$. Using $c_3 \approx -\left(H'_{31}c_1 + H'_{32}c_2\right)/\Delta$, where $H^{'}_{ij}$ refers to the ij^{th} element of matrix $H^{'}$ in Eq. (1.32), in the Schrödinger equations for c_1 and c_2, one gets an effective 2×2 Hamiltonian

$$H_2 = \begin{pmatrix} -\frac{|H'_{13}|^2}{\Delta} & -\frac{H'_{13}{H'_{23}}^*}{\Delta} \\ -\frac{H'_{23}{H'_{13}}^*}{\Delta} & \delta - \frac{|H'_{23}|^2}{\Delta} \end{pmatrix}. \tag{1.33}$$

After neglecting the fast-oscillating terms using the rotating-wave approximation, the resultant Hamiltonian [4]

$$H_2 = \begin{pmatrix} -\frac{|\Omega_1|^2 + |\Omega_2|^2}{4\Delta} & \frac{\Omega_1\Omega_2^*}{4\Delta} e^{-\iota(\boldsymbol{k}_1 - \boldsymbol{k}_2)\cdot\boldsymbol{r}} \\ \frac{\Omega_2\Omega_1^*}{4\Delta} e^{\iota(\boldsymbol{k}_1 - \boldsymbol{k}_2)\cdot\boldsymbol{r}} & \delta - \frac{|\Omega_1|^2 + |\Omega_2|^2}{4\Delta} \end{pmatrix}, \tag{1.34}$$

where the diagonal term $(|\Omega_1|^2 + |\Omega_2|^2)/4\Delta$ is ac-stark shift, and the off-diagonal term characterizes the spin-flipping process with a momentum transfer of $(\boldsymbol{k}_1 - \boldsymbol{k}_2)$, which is fundamentally responsible for the manifestation of the SO coupling effect.

For counterpropagating Raman laser beams propagating along $x-$direction, the single-particle Hamiltonian is [4,75]

$$\hat{H}_0 = \frac{\hbar^2 \boldsymbol{k}^2}{2M} + \frac{\Omega_R}{2}[\cos(2k_L x)\sigma_x - \sin(2k_L x)\sigma_y] + \frac{\delta}{2}\sigma_z, \tag{1.35}$$

where $\Omega_R = -\Omega_1\Omega_2^*/2\Delta$, $\boldsymbol{k}_L = \boldsymbol{k}_1 - \boldsymbol{k}_2$, and $\boldsymbol{k} = -\imath\nabla$. To make the SO coupling even more transparent, we perform a unitary transformation using a unitary operator $U = \exp(-\imath k_L x \sigma_z)$, and the transformed Hamiltonian is [4,75]

$$\hat{H}_0 = \frac{\hbar^2 \boldsymbol{k}^2}{2M} + \frac{\hbar^2 k_L k_x}{M}\sigma_z + \frac{\Omega_R}{2}\sigma_x + \frac{\delta}{2}\sigma_z, \tag{1.36}$$

where the SO coupling is now evident from the term $\propto k_x\sigma_z$.

The remarkable achievement of the experimental realization of SO-coupled BECs [75] provides a perfect gateway to investigating novel exotic states of ultracold quantum gases, drawing insights from condensed matter physics [66,67]. These experimental advancements [73–77] led to many theoretical studies in spinor systems, including spin-spiral ordering [78], vortex and skyrmion crystal [79], ferromagnetic and antiferromagnetic phases [80], ground-state phases like plane-wave, stripe or standing-wave, vortex-lattice, zero-momentum phases, etc. [48,81–83]. Besides these unusual phases, self-trapped vortex solitons [84–87], knotted vortices [88], super-stripes and super-lattices [89,90] can also emerge as the ground-state solutions of the SO-coupled spinor BECs in different parameter domains. The specific phases and the transitions among them in the ground-state phase diagram depend on various factors, such as the strength and nature of the SO coupling and the interactions between the atoms [48,91].

1.3 Rotating spinor condensates

Following the observation of a trapped BEC in ^{87}Rb and ^{23}Na alkali atoms at ultra-low temperature [20,21], experiments were conducted to generate rotating trapped condensates supporting quantized vortices [18] and extensive vortex lattices [19,27] under controlled conditions for both small and large angular frequencies of rotation. As proposed by Onsager [92], Feynman [13], and Abrikosov [16], these vortices exhibit quantized circulation similar to that observed in liquid He II [33]. The quantized circulation can be expressed as

$$\frac{M}{2\pi\hbar}\oint \mathbf{v}.d\mathbf{r} = \pm l, \tag{1.37}$$

where $\mathbf{v}$ denotes the superfluid velocity field, l is orbital angular momentum, and M is the mass of the atom. The $l \neq 0$ means a topological defect within the closed path, manifesting as a quantized vortex line [33]. The observation of unit angular momentum quantized vortices was initially reported in a uniform superfluid He II within a rotating bucket [93,94]. The curl of the velocity field, $\nabla \times \mathbf{v}(\mathbf{r}, t)$, determines vorticity and indicates the direction of the angular momentum vector.

The spinor BECs can exhibit a diverse range of topological excitations [1,95–97], which are not achievable in scalar BECs. Depending upon the nature of spin-exchange interactions, values of longitudinal magnetization f_z and rotational frequency $\Omega_{\rm rot}$, a wide assortment of topological structures can appear in the ground states of the spin-1 BEC [95,96,98]. Among these are thermodynamically stable Mermin-Ho and Anderson-Toulouse coreless vortices in a ferromagnetic spin-1 BEC [95,96]. The phase diagram in f_z-$\Omega_{\rm rot}$ plane reveals that the spin-1 BECs can host different types of both axisymmetric as well as asymmetric vortices [95]. The stability of former types with a phase-winding number of individual components between -1 to 1 has also been studied in f_z-$\Omega_{\rm rot}$ plane [99]. The two distinct vortex-lattice phases of a rotating ferromagnetic spin-1 BEC are a lattice of coreless vortices with non-singular spin-texture and a lattice with polar cores [98]. Coreless axisymmetric and non-axisymmetric vortices with spin-texture, respectively, corresponding to a skyrmion and a meron-pair also emerge in pseudospin-1/2 BECs under rotation [100]. As the rotation frequency approaches the trapping frequency, the BEC enters into a regime where the non-interacting part of the Hamiltonian becomes equivalent to the Hamiltonian of a charged particle with mass M and charge q in a magnetic field of magnitude $B = 2M\Omega_{\rm rot}/q$ [101]. In this regime, where mean-field interaction energy is smaller than $2\hbar\Omega_{\rm rot}$ and coherence length is of the order of inter-vortex separation; the bosons occupy the single-particle states corresponding to the lowest Landau level [101–103] and the GP approximation is valid [45]. With a further increase in rotation frequency, mean-field interaction energy becomes much smaller than $\hbar\Omega_{\rm rot}$, resulting in highly correlated vortex-liquid states which are no longer described by the mean-field GP equation [102–105]. An important parameter which characterizes the transition between these two regimes is the ratio of the number of bosons to the number of vortices termed as *filling fraction* [104]. In a single-component scalar BEC, a zero-temperature phase transition corresponding to the transition from vortex-lattice phase to an incompressible vortex-liquid phase occurs when the filling fraction approximately falls below six [104]. On the experimental front, the interlaced square vortex lattice in a rotating two-component pseudospin-1/2 BEC has been experimentally observed [106]. The experiment also confirmed the stability of the square vortex lattice by exciting Tkachenko modes [16] and their subsequent relaxation [106]. Spin-1 bosons under fast rotations in the lowest Landau level regime have been theoretically investigated [107,108], and it has been demonstrated that, similar to scalar BECs, a transition from vortex-lattice phase to quantum Hall liquid states at ultra-fast rotations occurs [107,108].

As discussed in Sec. 1.2.1, realization of SO coupling in spin-1 BECs, results in various ground-state phases like plane-wave, stripe or standing-wave, vortex-lattice, zero-momentum phases, etc [48,81–83,109]. The realization of the SO coupling has made it possible to explore the interplay of synthetic non-Abelian and Abelian gauge potential arising due to rotation [110,111], e.g. in the two-component SO-coupled [112–116] or coherently-coupled pseudospin-1/2 BECs [117]. In spin-1 BECs, the interaction between Rashba SO coupling and rotation under rapid quenching leading to half-skyrmion excitations [118], hexagonal lattice of skyrmions and a square lattice of half-quantized vortices [119] has already been theoretically investigated. It has also been shown numerically that a rotating spin-1 BEC with anisotropic SO coupling can support vortex-chain solutions [120], whereas the presence of an isotropic Rashba SO coupling may result in a vortex lattice with a hexagonal or an approximate square-lattice pattern [121].

1.4 Spin-orbital-angular-momentum-coupled spinor condensates

Spin-orbital-angular-momentum (SOAM) coupling, which represents the interaction between the spin and the orbital motion, is a fundamental phenomenon in nature. In the field of atomic physics, the relativistic interaction between spin and orbital angular momentum contributes to the fine structure observed in energy levels within hydrogen atoms [122]. A similar effect is observed for protons and neutrons as they move within the atomic nucleus, causing shifts in their energy levels within the nuclear shell model [123]. In condensed-matter physics, a similar interaction arises between the electron spin and its velocity, known as the spin-linear-momentum or SO coupling, which has already been discussed in Sec. 1.2. Although SO coupling has been extensively investigated in the ultra-cold atoms' field [109,111,124–126], it differs from the actual meaning of SO coupling in atomic physics, which signifies the interaction between spin and orbital angular momentum. During the second half of the last decade, a novel coupling, namely the SOAM coupling, which does couple the spin with the orbital angular momentum of the atom, was theoretically proposed in cold atoms, significantly enhancing our understanding of quantum many-body physics [127–134]. These proposals inspired the experimental realization of SOAM coupling in the spin-1 spinor BEC of ^{87}Rb atoms [135,136], using a Gaussian and a Laguerre-Gaussian beam co-propagating along the z-direction (which leads to an orbital angular-momentum transfer of $\hbar$ to the atoms) [135,136]. This was followed by the experimental demonstration of spin-polarized and zero-momentum phases in an SOAM-coupled pseudospin-1/2 BEC of ^{87}Rb atoms [5]; the work also demonstrated that Raman-induced gauge fields can lead to an effective rotation.

To understand the SOAM coupling, which connects the two hyperfine states of atoms by copropagating Laguerre-Gaussian beams, we consider a scenario illustrated in Fig. 1.4. The distinct orbital angular momentum carried by these beams induces a change in the orbital angular momentum of atoms during the transition between the two ground hyperfine states. The Hamiltonian describing an atom influenced by a pair of Raman Laguerre-Gaussian beams as per the semiclassical theory of atom-light interaction is

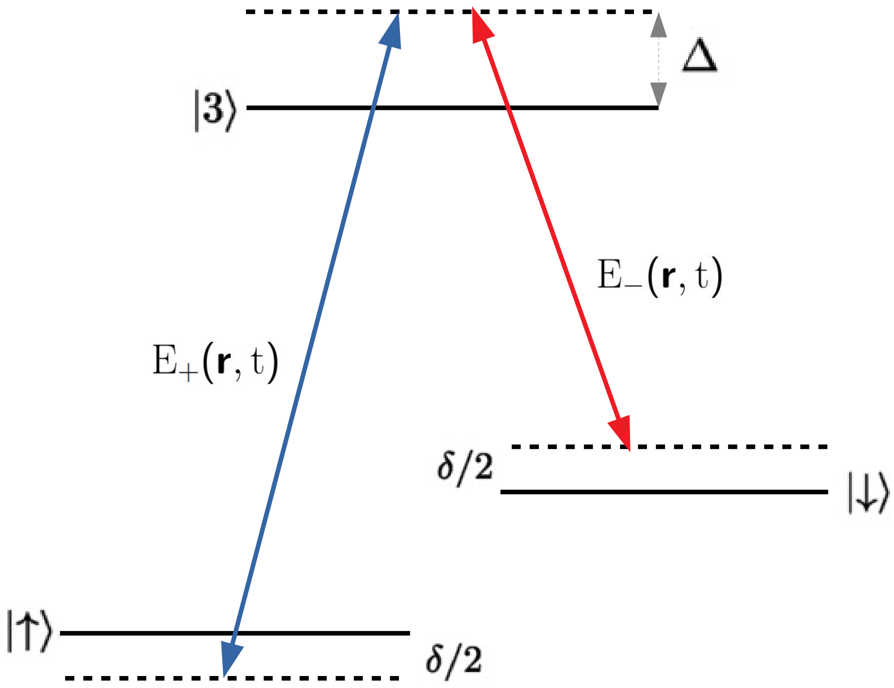

Figure 1.4: Figure illustrates two hyperfine states of atoms $|\uparrow\rangle$, $|\downarrow\rangle$ which are connected to the excited state $|3\rangle$ via a pair of copropagating Laguerre-Gaussian beams $E_\pm$. The Δ is representing single-photon detuning and δ is two-photon detuning [5,6].

written as [6,127]

$$H_{\text{AL}} = \begin{pmatrix} \hbar\omega_\uparrow & 0 & V_{\uparrow 3} \\ 0 & \hbar\omega_\downarrow & V_{\downarrow 3} \\ \hbar\omega_\downarrow & V_{\downarrow 3} & \hbar\omega_3 \end{pmatrix}, \tag{1.38}$$

where $|\uparrow\rangle$, $|\downarrow\rangle$, and $|3\rangle$ are the basis states associated with energies $\hbar\omega_\uparrow, \hbar\omega_\downarrow$, and $\hbar\omega_3$, respectively. In Eq. (1.38), $V_{j,j'} = \langle j|\hat{\boldsymbol{d}}.\boldsymbol{E}_\pm|j'\rangle$, where $j, j' =\uparrow, \downarrow$, and 3, $\hat{\boldsymbol{d}}$ is the dipole operator, and $\boldsymbol{E}_\pm$ are electric fields, which can be expressed as

$$\boldsymbol{E}_\pm(\mathbf{r}, t) = \frac{1}{2}\hat{\mathbf{e}}_\pm[\varepsilon_\pm(\mathbf{r})e^{-\iota\omega_\pm t} + \varepsilon^*_\pm(\mathbf{r})e^{\iota\omega_\pm t}], \tag{1.39}$$

where $\hat{\mathbf{e}}_\pm$ represents the unit vectors indicating the polarization direction of light, $\varepsilon_\pm$ corresponds to the spatial complex amplitudes, and $\omega_\pm$ denote the angular frequencies of the Raman beams. Next, we apply a time-dependent unitary transformation to our system to move to the rotating frame of reference, where

$$\psi' = U\psi, \quad H' = UH_{AL}U^\dagger - \iota U\partial_t U^\dagger, \tag{1.40}$$

for

$$U = \begin{pmatrix} \exp(\iota\eta_\uparrow t) & 0 & 0 \\ 0 & \exp(\iota\eta_\downarrow t) & 0 \\ 0 & 0 & \exp(-\iota\eta_3 t) \end{pmatrix}. \tag{1.41}$$

This results in

$$H' = \begin{pmatrix} \hbar\omega_\uparrow - \hbar\eta_\uparrow & 0 & V_{13}\ e^{\iota(\eta_\uparrow - \eta_3)t} \\ 0 & \hbar\omega_\downarrow - \hbar\eta_\downarrow & V_{23}\ e^{\iota(\eta_\downarrow - \eta_3)t} \\ \hbar\omega_\downarrow e^{\iota(\eta_3 - \eta_\uparrow)t} & V_{23}\ e^{\iota(\eta_3 - \eta_\downarrow)t} & \hbar\omega_3 - \hbar\eta_3 \end{pmatrix}, \tag{1.42}$$

where η_j can be considered as [6]

$$\eta_\uparrow = \frac{1}{2}(-\omega_+ + \omega_- + \omega_\uparrow + \omega_\downarrow), \tag{1.43a}$$

$$\eta_\downarrow = \frac{1}{2}(\omega_+ - \omega_- + \omega_\uparrow + \omega_\downarrow), \tag{1.43b}$$

$$\eta_3 = \frac{1}{2}(\omega_+ + \omega_- + \omega_\uparrow + \omega_\downarrow). \tag{1.43c}$$

For the Hamiltonian in Eq. (1.42), the Schrödinger equation is $\iota\partial_t \boldsymbol{c} = H'\boldsymbol{c}$, where $\boldsymbol{c} = (c_\uparrow, c_\downarrow, c_3)^{\mathrm{T}}$, and under rotating-wave approximation [137], we obtain [6]

$$\iota\hbar\frac{\partial c_\uparrow}{\partial t} = \frac{\delta}{2}c_\uparrow + \frac{1}{2}\rho_+^*\varepsilon_+^*(\mathbf{r})c_3, \tag{1.44a}$$

$$\iota\hbar\frac{\partial c_\downarrow}{\partial t} = -\frac{\delta}{2}c_\downarrow + \frac{1}{2}\rho_-^*\varepsilon_-^*(\mathbf{r})c_3, \tag{1.44b}$$

$$\iota\hbar\frac{\partial c_3}{\partial t} = \rho_+\varepsilon_+(\mathbf{r})c_\uparrow + \frac{1}{2}\rho_-\varepsilon_-(\mathbf{r})c_\downarrow - \Delta c_3, \tag{1.44c}$$

where $\rho_+ = \langle 3|-\boldsymbol{d}.\hat{e}_+|\uparrow\rangle$ and $\rho_- = \langle 3|-\boldsymbol{d}.\hat{\boldsymbol{e}}_-|\downarrow\rangle$ represent the matrix elements of the electric dipole moment, $\delta = \hbar[(\omega_+ - \omega_-) - (\omega_\downarrow - \omega_\uparrow)]$ is two-photon detuning, and $\Delta = \hbar(\omega_+ + \omega_- + \omega_\downarrow + \omega_\uparrow - \omega_3)/2$ is single-photon detuning. As the excited state $|3\rangle$ is far from the resonance, we can adiabatically eliminate it by considering $\partial c_3/\partial t \approx 0$ in Eq. (1.44a) to obtain [6]

$$c_3 \approx \frac{\rho_+\varepsilon_+(\mathbf{r})}{2\Delta}c_\uparrow + \frac{\rho_-\varepsilon_-(\mathbf{r})}{2\Delta}c_\downarrow. \tag{1.45}$$

Using Eq. (1.45), Eqs.(1.44a) and (1.44b) can be written as

$$i\hbar\frac{\partial}{\partial t}\begin{pmatrix} c_\uparrow \\ c_\downarrow \end{pmatrix} = \begin{pmatrix} \chi_+(\mathbf{r}) + \delta/2 & \Omega(\mathbf{r}) \\ \Omega^*(\mathbf{r}) & \chi_-(\mathbf{r}) - \delta/2 \end{pmatrix}\begin{pmatrix} c_\uparrow \\ c_\downarrow \end{pmatrix}, \tag{1.46}$$

where

$$\chi_\pm(\mathbf{r}) \equiv \frac{|\rho_\pm\varepsilon_\pm(\mathbf{r})|^2}{4\Delta}, \quad \Omega(\mathbf{r}) \equiv \frac{\rho_+^*\rho_-\varepsilon_+^*(\mathbf{r})\varepsilon_-(\mathbf{r})}{4\Delta}.$$

The diagonal terms $\chi_\pm$, which represent the ac-stark shift in Eq. (1.46), can be eliminated by properly choosing a wavelength of Legurre-Gaussian beams in the experiment [5,138,139]. The off-diagonal ac-stark shift term $\Omega(\mathbf{r})$ leads to a space-dependent coupling between two hyperfine states $|\uparrow\rangle$ and $|\downarrow\rangle$, resulting in an SOAM coupling of atoms.

To make the connection with the experiment [5], we consider the pair of Raman beams applied along the $z-$direction with the amplitudes

$$\varepsilon_\pm(\mathbf{r}) = \sqrt{2I_0}e^{-\iota l_\pm\phi}\left(\frac{r}{w}\right)^{|l_\pm|} e^{\frac{-r^2}{w^2}} e^{\iota kz}, \tag{1.47}$$

where (r, ϕ, z) are the cylindrical coordinates, w is the width of the beam, and I_0 is the intensity of the beam. The phase winding of $e^{-\imath l_\pm \phi}$ reflects the orbital angular momentum of $-l_\pm$ carried by the beam. The single-particle Hamiltonian for the spin-1/2 system can be described as [5]

$$\hat{H}_0 = -\frac{\hbar^2}{2M}\nabla^2 + V(\mathbf{r}) + V_{\mathrm{LG}}(\mathbf{r}), \tag{1.48}$$

where $V(\mathbf{r})$ is the external trapping potential, and V_{LG} denotes the interaction between the Laguerre-Gaussian beam and the atoms, which can be represented as [129]

$$V_{\mathrm{LG}} = \begin{pmatrix} \chi(\mathbf{r}) + \delta/2 & \Omega(r)e^{-\imath l\phi} \\ \Omega(r)e^{\imath l\phi} & \chi(\mathbf{r}) - \delta/2 \end{pmatrix}. \tag{1.49}$$

The $l = (l_+ - l_-)$ is the angular momentum transfer to the atom and $\Omega(r) = \Omega_R \left(\frac{r}{w}\right)^{|l_+|+|l_-|} e^{\frac{-2r^2}{w^2}}$ is coupling strength, where $\Omega_R = |\rho_+^* \rho_-| I_0/2\Delta$ is Rabi frequency. For simplicity, we have $\chi(\mathbf{r}) = \chi_+(\mathbf{r}) = \chi_-(\mathbf{r})$. By introducing a unitary transformation $\hat{U} = \exp(\imath l\phi\hat{\sigma}_z)$, the single-particle Hamiltonian is transformed to

$$\hat{\mathcal{H}}_0 = \left[-\frac{\hbar^2}{2Mr}\frac{\partial}{\partial r}r\frac{\partial}{\partial r} - \frac{\hbar^2}{2M}\frac{\partial^2}{\partial z^2} + V(\mathbf{r}) + \chi(r)\right]\mathbf{I} + \frac{(\hat{L}_z - l\hbar\hat{\sigma}_z)^2}{2Mr^2} + \Omega(r)\hat{\sigma}_x + \frac{\delta}{2}\hat{\sigma}_z, \tag{1.50}$$

where $\hat{L}_z = -\imath\hbar\partial/\partial\phi$ and $\hat{\sigma}_{x,z}$ are Pauli matrices.

In spin-1 BEC, SOAM coupling has been realized by considering copropagating Gaussian and Laguerre-Gaussian laser beams with an angular momentum transfer of $l = \hbar$ [135,136]. The single-particle Hamiltonian for an SOAM-coupled spin-1 BEC in the cylindrical coordinate system can be written as [135]

$$\begin{aligned} \hat{H}_0 = &\left[-\frac{\hbar^2}{2M}\frac{\partial}{r\partial r}\left(r\frac{\partial}{\partial r}\right) + \frac{L_z^2}{2Mr^2} - \frac{\hbar^2}{2M}\frac{\partial^2}{\partial z^2} + V(\mathbf{r})\right]\mathbf{I} \\ &+ \hbar\Omega(r)\cos(\phi)S_x - \hbar\Omega(r)\sin(\phi)S_y + \hbar\delta S_z, \end{aligned} \tag{1.51}$$

where $\mathbf{I}$ is a 3×3 identity matrix, $\Omega(r) = \Omega_R\sqrt{e}(r/r_0)e^{-r^2/2r_0^2}$, and r_0 is the radius of maximum-intensity (cylindrical) surface [135,136], respectively, δ is the Raman detuning, and S_x, S_y, and S_z are spin-1 matrices.

Both SOAM and SO couplings can yield effective rotations or synthetic magnetic fields which can result in the ground-state with vortices. The ground states obtained with SOAM coupling usually have the cylindrical symmetry of the Hamiltonian and are characterized by angular momentum quantum numbers [135]. With SOAM coupling, the spin-textures of coreless vortices, skyrmions, monopoles, etc. exhibit cylindrical symmetry because the unit vector $\hat{\boldsymbol{F}}$ completes a full rotation of 2π as ϕ varies from 0 to 2π, whereas with SO coupling, $\hat{\boldsymbol{F}}$ projected on the $x - y$ plane helically precesses along the x-direction and hence, cannot result in cylindrical symmetry [135].

Among the theoretical studies on the SOAM-coupled pseudospin-1/2 BECs, a stripe, an annular-stripe, a two-vortex molecule, and a vortex-antivortex molecule ground-state phases [130,140–142] and the effects of the ring-trapping potential on the annular-stripe phase have been studied [129,143]. The ground-state phases of an SOAM-coupled spin-1/2 BEC has also been studied in a toroidal trap [143]. Furthermore, the angular stripe phase in SOAM-coupled systems started gaining attention [140–144]. However, due to the narrow range of parameters, this stripe phase has not yet been observed experimentally [142].

Along with the studies on equilibrium ground-state phase diagrams, spectroscopic studies have been carried out on the SOAM-coupled pseudospin-1/2 BECs [133,141,144]. In particular, the low-lying excitation spectrum, including breathing and dipole modes, have been studied for the half-skyrmion and vortex-antivortex phases [133,141]. The ground-state phases and excitation spectrum have also been studied for a pseudospin-1/2 BEC with higher order SOAM couplings [130,144]. The different considerations of angular-momentum transfer to the atoms by the pair of Laguerre-Gaussian beams yield different single-particle Hamiltonians and, consequently, different phase diagrams. In this context, considering a theoretical SOAM-coupled spin-1 model with an angular-momentum transfer of $2\hbar$ rather than $\hbar$ realized in the experiment [135,136], the ground-state phase diagram and the dynamics ensuing on sudden quench of the quadratic Zeeman terms have been studied [132].

1.5 Collective Excitations

Low-energy excitations of quantum gases, known as collective excitations, can provide crucial insight into aspects such as ground-state phase stability, fluctuations, and superfluidity [45,145]. However, this can be done by analyzing collective excitations, which aid in mapping out the phase boundaries [45,145].

The experimental investigation of BECs started by subjecting the condensate to extremely low temperatures, eliminating the thermal cloud associated with it. The collective oscillations were induced through the modulation of the external trapping potential [146–150], especially a small time-dependent perturbation to the trapping potential was used to excite the shape oscillations of the condensate [146,147].

Innovative theoretical approaches have been formulated to describe the collective modes of confined BECs to substantiate the progress in experimentation. Within the mean-field model, a study was conducted on the linearised GP equation around the ground state [151]. Remarkably, the experimentally measured frequencies [146,147,152] demonstrated excellent agreement with theoretical predictions [151,153–156], representing significant achievements in the field. Collective oscillations can be induced not only by modulating the external trapping potential [146,147,157–161] but also by modulating the $s-$wave scattering length [162–165] In the Thomas-Fermi limit, the frequencies of collective excitations can be calculated analytically [153]. Due to the inherent nonlinearity of the equation of motion, various interesting phenomena are observed in the collective excitations of BECs, including frequency shifts [159,163,166,167], mode coupling [159,166,167], damping [148,168], as well as the collapse and revival of oscillations [159,169,170]. The collective excitations of a system can be calculated by using the Bogoliubov-de-Gennes (BdG) equations. To introduce BdG equations, we consider the SOAM-coupled pseudospin-1/2 BEC as discussed in Sec. 1.4. Under the mean-field approximation, an interacting SOAM-coupled pseudospin-1/2 BEC can be described by following two dimensionless CGPEs

$$i\frac{\partial\psi_\uparrow}{\partial t} = \left(-\frac{1}{2r}\frac{\partial}{\partial r}r\frac{\partial}{\partial r} + \frac{r^2}{2} + \chi(r) + \frac{(\hat{L}_z - l)^2}{2r^2}\right)\psi_\uparrow + \Omega(r)\psi_\downarrow + g\left|\psi_\uparrow\right|^2\psi_\uparrow + g_{\uparrow\downarrow}\left|\psi_\downarrow\right|^2\psi_\uparrow, \tag{1.52a}$$

$$i\frac{\partial\psi_\downarrow}{\partial t} = \left(-\frac{1}{2r}\frac{\partial}{\partial r}r\frac{\partial}{\partial r} + \frac{r^2}{2} + \chi(r) + \frac{(\hat{L}_z + l)^2}{2r^2}\right)\psi_\downarrow + \frac{1}{2}\Omega(r)\psi_\uparrow + g\left|\psi_\downarrow\right|^2\psi_\downarrow + g_{\uparrow\downarrow}\left|\psi_\uparrow\right|^2\psi_\downarrow. \tag{1.52b}$$

where $g = g_{\uparrow\uparrow} = g_{\downarrow\downarrow}$ and $g_{\uparrow\downarrow}$ are intraspecies and interspecies interaction strengths, respectively, and $\psi_\uparrow$ ($\psi_\downarrow$) is the component wavefunction corresponding to ↑ (↓) spin. Under the Bogoliubov approach, we consider the fluctuations in the ground state by writing the perturbed order parameter as

$$\psi_j(\mathbf{r},t) = \left[R_j(r) + u_j(r)e^{\iota(l_q\phi-\omega t)} + v_j^*(r)e^{\iota(l_q\phi+\omega t)}\right]e^{\iota(l_z\phi-\mu t)}, \tag{1.53}$$

where $j =\uparrow,\downarrow$, μ is the chemical potential, u and v are the Bogoliubov quasi-particle amplitudes, ω is collective excitation frequency, $l_z = \langle\hat{L}_z\rangle$ is the magnetic quantum number of the ground state, and $l_q = 0, \pm1, \pm2, \cdots$, is the magnetic quantum number of the excitation. Linearization Eqs. (1.52a) and (1.52b) and the conjugate set of equations using perturbed order parameter (1.53) yields the following four coupled BdG equations

$$\begin{aligned}
\omega u_\uparrow &= \left[-\frac{1}{2r}\frac{\partial}{\partial r}r\frac{\partial}{\partial r} + \frac{r^2}{2} + \chi(r) + \frac{(l_q+l_z-l)^2}{2r^2} + 2g(R_\uparrow)^2 + g_{\uparrow\downarrow}(R_\downarrow)^2 - \mu\right]u_\uparrow && (1.54a)\\
&+ \frac{r^2}{2}\Omega(r)u_\downarrow + g\left(R_\uparrow\right)^2v_\uparrow + g_{\uparrow\downarrow}R_\uparrow R_\downarrow u_\downarrow + g_{\uparrow\downarrow}R_\uparrow R_\downarrow v_\downarrow,\\
-\omega v_\uparrow &= \left[-\frac{1}{2r}\frac{\partial}{\partial r}r\frac{\partial}{\partial r} + \frac{r^2}{2} + \chi(r) + \frac{(l_q+l_z-l)^2}{2r^2} + 2g(R_\uparrow)^2 + g_{\uparrow\downarrow}(R_\downarrow)^2 - \mu\right]v_\uparrow && (1.54b)\\
&+ \frac{r^2}{2}\Omega(r)v_\downarrow + g(R_\uparrow)^2u_\uparrow + g_{\uparrow\downarrow}R_\uparrow R_\downarrow v_\downarrow + g_{\uparrow\downarrow}R_\uparrow R_\downarrow u_\downarrow,\\
\omega u_\downarrow &= \left[-\frac{1}{2r}\frac{\partial}{\partial r}r\frac{\partial}{\partial r} + \frac{r^2}{2} + \chi(r) + \frac{(l_q+l_z+l)^2}{2r^2} + g_{\uparrow\downarrow}(R_\uparrow)^2 + 2g(R_\downarrow)^2 - \mu\right]u_\downarrow && (1.54c)\\
&+ \frac{r^2}{2}\Omega(r)u_\uparrow + g(R_\downarrow)^2v_\downarrow + g_{\uparrow\downarrow}R_\uparrow R_\downarrow v_\uparrow + g_{\uparrow\downarrow}R_\uparrow R_\downarrow u_\uparrow,\\
-\omega v_\downarrow &= \left[-\frac{1}{2r}\frac{\partial}{\partial r}r\frac{\partial}{\partial r} + \frac{r^2}{2} + \chi(r) + \frac{(l_q+l_z+l)^2}{2r^2} + g_{\uparrow\downarrow}(R_\uparrow)^2 + 2g(R_\downarrow)^2 - \mu\right]v_\downarrow && (1.54d)\\
&+ \frac{r^2}{2}\Omega(r)v_\uparrow + g_{\uparrow\downarrow}R_\uparrow R_\downarrow u_\uparrow + g_{\uparrow\downarrow}R_\downarrow R_\uparrow v_\uparrow + g(R_\downarrow)^2u_\downarrow.
\end{aligned}$$

This coupled set of BdG equations can be solved by employing the finite-difference method to discretize the equations over the spatial radial grid [171] or by using the basis expansion method where the BdG amplitudes are written as linear superpositions in terms of a complete set of suitably chosen orthonormal basis states [172].

1.6 Aims and Objectives

The realization of SO-coupling paved the way to explore the interplay of an artificial non-Abelian gauge field resulting in SO-coupling and rotation, which itself is equivalent to an Abelian gauge potential. In the literature on rotating SO-coupled spin-1 and spin-2 BECs, the rotation frequencies considered mostly have been within the range of small to moderate values. This thesis aims to investigate the combined effect of interactions and SO couplings, particularly at high rotation frequencies for spin-1 BECs with ferromagnetic or antiferromagnetic interactions and then broaden the investigation to a rotating SO-coupled spin-2 system with antiferromagnetic, cyclic, or ferromagnetic interactions. Specifically, we wish to investigate the various effective potentials an atom in these SO-coupled spinor BECs may experience under the combined effect of SO coupling and rotation.

As discussed in Sec. 1.4, the experimental realization of SOAM coupling represents a significant milestone in spinor BECs. For an SOAM-coupled spin-1 BEC with an angular-momentum transfer of $l = 2\hbar$ [132], the ground-state phase diagram and the dynamics ensuing on sudden quench of quadratic Zeeman terms have been studied as mentioned in Sec. 1.4. In this context, considering the experimentally realized SOAM coupling with $l = \hbar$ [135,136], the detailed phase diagrams and excitation spectrums of SOAM-coupled spin-1 BECs with polar and ferromagnetic spin-exchange interactions have not been yet theoretically studied. More importantly, collective excitations of the SOAM-coupled spin-1 BEC have not been studied, irrespective of the theoretical models employed. We aim to bridge the research gap by investigating the low-lying excitation spectrum of ground-state phases, specifically focusing on the coreless and polar-core vortex states of SOAM-coupled spin-1 condensates. We also aim to explore the annular-stripe phase and its excitation spectrum, which can appear as the ground-state phase in an SOAM-coupling model with a larger angular momentum transfer (say $4\hbar$) to the condensate atoms. We study the ground-state phases for the model with a larger value of $l = 4\hbar$ and their excitation spectrum using the Bogoliubov approach.

The main objectives of the thesis are listed below:

- To study the effective potentials experienced by a boson in rotating SO-coupled spinor condensates.
- To study the vortex-lattice formation in SO-coupled spin-1 and spin-2 BECs under rotation.
- To study the quantum phases and spectrum of collective modes in a spin-1 BEC with SOAM coupling.
- To study the collective excitation spectrum of an annular-stripe phase of an SOAM-coupled spin-1 BEC.

To achieve these goals of the thesis, we have to numerically solve the mean-field model for an SO-coupled spin-f BEC, a set of $2f+1$ coupled time-dependent partial differential equations with first-order time-derivative and first- and second-order spatial-derivative terms. These coupled equations cannot be solved analytically without relying on approximations, and hence one needs to solve the equations numerically. Various numerical techniques have been employed in the literature to investigate spinor BECs [173–175]. This necessitates the exploration of numerical techniques to study the ground states and/or the dynamics of homogeneous or trapped spin-f BECs with SO coupling using (a) Fourier pseudospectral method and (b) Time-splitting (implicit or semi-implicit) finite-difference methods (in the first chapter of this thesis). The Fourier pseudospectral method is ideally suited for systems with periodic boundary conditions, whereas the finite difference methods offer more flexibility to implement alternative boundary conditions.

1.7 Outline of the thesis

In the first part of **Chapter 2**, we discuss the time-splitting Fourier pseudospectral method to numerically solve the CGPEs (for SO-coupled spin-1 or spin-2 BECs) which can be employed to study the ground state solutions and/or the dynamics of homogeneous or trapped condensates. As the Fourier pseudospectral method implements the periodic boundary conditions, we discuss a couple of time-splitting finite-difference methods to study the SO-coupled spinor BECs in the second part of this chapter.

In **Chapter 3**, we investigate the combined effects of rotation and SO couplings in spin-1 and spin-2 BECs systematically using the non-interacting model. By using the single-particle Hamiltonian, which is exactly solvable for one-dimensional coupling, we illustrate that a boson in these rotating SO- and coherently-coupled condensates are subjected to various effective potentials under specific coupling and rotation strengths. In the presence of mean-field interactions, using the CGPEs at moderate to high rotation frequencies, we investigate a variety of vortex-lattice structures emerging as ground-state solutions as a result of the interplay between rotation frequency, SO couplings, and interatomic interactions. Furthermore, we gain insights into the behavior of both antiferromagnetic and ferromagnetic interacting spin-1 BECs by examining the spin expectation per particle at moderate to high rotation frequencies. Similarly, we investigate antiferromagnetic, cyclic, and ferromagnetic phases under rotation for spin-2 BEC.

In **Chapter 4**, we investigate the low-lying excitation spectrum of the ground-state phases of SOAM-coupled spin-1 condensates. Here, we observe that at vanishing detuning, a ferromagnetic SOAM-coupled spin-1 BEC can have two ground-state phases, namely, coreless and polar-core vortex states, whereas an antiferromagnetic BEC supports only polar-core vortex solutions. The phase boundary between the coreless and polar-core vortex phases is demarcated by changes in angular momentum per particle, longitudinal magnetization, and excitation frequencies. The low-lying excitation spectrum is evaluated by solving the BdG equations. The spectrum is further confirmed by the dynamical evolution of the ground state subjected to a perturbation suitable to excite a density or a spin mode and a variational analysis for the density-breathing mode. Additionally, we discuss the effect of detuning in the excitation spectrum.

In **Chapter 5**, we introduce the SOAM-coupled spin-1 system with a larger angular momentum transfer ($l = 4\hbar$) to the atoms. We explore the ground state phases of this model with antiferromagnetic interaction and incorporate detuning to obtain an annular stripe solution. We calculate and analyze the collective excitation spectrum of these solutions, with a particular emphasis on the annular stripe phase. To further understand the nature of low-lying collective excitations, we utilize the time evolution of relevant observables after suitably perturbing the Hamiltonian and validate our calculations of the excitation spectrum using the BdG equations.

Finally, in **Chapter 6**, we summarize the main results of the thesis and discuss possible future research directions.

The thesis has three appendices. In Appendix A, we discuss time-splitting finite difference methods to solve the CGPEs for an SO-coupled spin-1 BEC. In Appendix B, we outline the details of the finite difference scheme [171] to solve the (circularly-symmetric) BdG equations for an SOAM-coupled spin-1 BEC. Lastly, in Appendix C, we provide the essential details to numerically solve the two-dimensional BdG equations in Cartesian coordinates using the basis expansion method [172].

Chapter 2

Numerical Methods

In the absence of thermal and quantum fluctuations at $T = 0$ K, the mean-field approximation allows one to describe an SO-coupled spin-f BEC by a set of $2f+1$ coupled nonlinear Schrödinger equations [1,51,55–57]. In general, this coupled set of equations, termed as the mean-field model, is not analytically solvable without resorting to approximations. In this context, in the absence of SO coupling, a wide range of numerical techniques have been employed in the literature to study spinor BECs [175–179]. In the following thesis chapters, we need to solve the coupled Gross-Pitaevskii equations (CGPEs) for SO-coupled spin-f BECs. This necessitates exploring numerical techniques to study the ground states and/or the dynamics of homogeneous or trapped spin-f BECs with SO coupling.

In this chapter, first, we discuss the time-splitting Fourier pseudospectral (TSFP) method, in which we first split the CGPEs into four sub-sets of equations, where each set consists of $2f+1$ equations, using Lie operator splitting [180]. The method then involves solving the aforementioned four sets of equations one after the other over the same time interval, with a solution to each set serving as the input to the following set of equations. As the Fourier pseudospectral method implements the periodic boundary conditions, we discuss a couple of time-splitting finite-difference methods to study the SO-coupled spinor BECs, which offer more flexibility to implement the alternative boundary conditions.

The chapter is organized as follows. In Sec. 2.1, we present a generalized mean-field model matrix equation for an SO-coupled spin-f BEC. Sec. 2.2 provides a detailed discussion of Fourier pseudospectral method employed to solve the CGPEs for spin-2 BECs in three-dimensional (3D), quasi-two-dimensional (q2D), and quasi-one-dimensional (q1D) settings. Moreover, this section discusses the important conserved quantities of a spin-2 BEC in the presence and absence of SO coupling. In Sec. 2.3, we employ a time-splitting Backward–Euler (TSBE) or a time-splitting Crank–Nicolson (TSCN) finite-difference methods to solve the split equations corresponding to the kinetic energy and SO coupling operators for a pseudospin-1/2, spin-1, and spin-2 BECs. Furthermore, Sec. 2.4 presents a few sample results for comparing finite-difference methods with the Fourier pseudospectral method.

2.1 Mean-field model for a spin-f BEC

A generic spin$-f$ condensate with Rashba SO coupling at $T = 0$ K can be modelled with a matrix equation of the form [1,48]

$$\iota\frac{\partial\Psi}{\partial t} = (H_{\rm SP} + H_{\rm SE} + H_{\rm SOC} + H_{\rm KE})\Psi, \tag{2.1}$$

where Ψ is a $2f + 1$ component order parameter. In this chapter, we consider $f = 1/2, 1,$ and 2 corresponding, respectively, to pseudospin-1/2, spin-1, and spin-2 condensates. In Eq. (2.1), $H_{\rm KE}$ is a diagonal matrix consisting of kinetic energy operators, $H_{\rm SOC}$ is matrix operator corresponding to SO coupling, $H_{\rm SE}$ consists of off-diagonal interaction terms, and $H_{\rm SP}$ is a diagonal matrix consisting of trapping potential plus diagonal interaction terms. Eq. (2.1) is split into four equations by using the standard Lie splitting [180]. Solution to Eq. (2.1) after time step δt is given as

$$\Psi(t + \delta t) = \hat{U}\Psi(t), \tag{2.2}$$

which describes the evolution of the wave function by a unitary propagator $\hat{U}$ given as

$$\hat{U} = \exp\left[-\iota\delta t(H_{\rm SP} + H_{\rm SE} + H_{\rm SOC} + H_{\rm KE})\right]. \tag{2.3}$$

The split-operator technique approximates the propagator as

$$\hat{U} \approx \exp\left(-\iota\delta t H_{\rm SP}\right)\exp\left(-\iota\delta t H_{\rm SE}\right)\exp\left(-\iota\delta t H_{\rm SOC}\right)\exp\left(-\iota\delta t H_{\rm KE}\right). \tag{2.4}$$

Using (2.4), Eq. (2.2) is equivalent to solving following equations successively

$$\iota\frac{\partial\Psi}{\partial t} = H_{\rm KE}\Psi, \tag{2.5a}$$
$$\iota\frac{\partial\Psi}{\partial t} = H_{\rm SOC}\Psi, \tag{2.5b}$$
$$\iota\frac{\partial\Psi}{\partial t} = H_{\rm SE}\Psi, \tag{2.5c}$$
$$\iota\frac{\partial\Psi}{\partial t} = H_{\rm SP}\Psi, \tag{2.5d}$$

over the same period of $[t, t + \delta]$.

2.2 Fourier pseudospectral method

We discuss the Fourier pseudospectral method for an SO-coupled spin-2 BEC, which can be described by five CGPEs, and for a spin-1 BEC the method has been discussed in Ref. [181]. In our discussion, we transform the CGPEs into dimensionless form, where physical quantities such as length, time, energy, etc., are expressed in terms of natural scales within the system. This dimensionless representation aids in eliminating cumbersome constants inherent in the CGPEs, enhancing both the aesthetic simplicity and computational efficiency of the numerical solver through less intensive floating-point operations [182].

2.2.1 CGPEs for an SO-coupled spin-2 BEC: Mean-field model

The quantum and thermal fluctuations in an SO-coupled spin-2 BEC at $T = 0$ K can be neglected, and the system is very well described by the following set of CGPEs in dimensionless form [1,68]

$$\begin{aligned}
\iota\frac{\partial\psi_{\pm2}(\mathbf{x},t)}{\partial t} &= \mathcal{H}\psi_{\pm2}(\mathbf{x},t)+c_0\rho(\mathbf{x},t)\psi_{\pm2}(\mathbf{x},t)+c_1[F_{\mp}(\mathbf{x},t)\psi_{\pm1}(\mathbf{x},t)\\
&\quad \pm2F_z(\mathbf{x},t)\psi_{\pm2}(\mathbf{x},t)]+c_2\frac{\Theta(\mathbf{x},t)\psi^*_{\mp2}(\mathbf{x},t)}{\sqrt{5}}+\Gamma_{\pm2}(\mathbf{x},t), &&\text{(2.6a)}\\
\iota\frac{\partial\psi_{\pm1}(\mathbf{x},t)}{\partial t} &= \mathcal{H}\psi_{\pm1}(\mathbf{x},t)+c_0\rho(\mathbf{x},t)\psi_{\pm1}(\mathbf{x},t)+c_1\Bigg[\sqrt{\frac{3}{2}}F_{\mp}(\mathbf{x},t)\psi_0(\mathbf{x},t)\\
&\quad +F_{\pm}(\mathbf{x},t)\psi_{\pm2}(\mathbf{x},t)\pm F_z(\mathbf{x},t)\psi_{\pm1}(\mathbf{x},t)\Bigg]-c_2\frac{\Theta(\mathbf{x},t)\psi^*_{\mp1}(\mathbf{x},t)}{\sqrt{5}}\\
&\quad +\Gamma_{\pm1}(\mathbf{x},t), &&\text{(2.6b)}\\
\iota\frac{\partial\psi_{0}(\mathbf{x},t)}{\partial t} &= \mathcal{H}\psi_{0}(\mathbf{x},t)+c_0\rho(\mathbf{x},t)\psi_{0}(\mathbf{x},t)+c_1\sqrt{\frac{3}{2}}[F_{-}(\mathbf{x},t)\psi_{-1}(\mathbf{x},t)\\
&\quad +F_{+}(\mathbf{x},t)\psi_{1}(\mathbf{x},t)]+c_2\frac{\Theta(\mathbf{x},t)\psi^*_{0}(\mathbf{x},t)}{\sqrt{5}}+\Gamma_{0}(\mathbf{x},t), &&\text{(2.6c)}
\end{aligned}$$

where suppressing the explicit dependence of component wavefunction ψ_j on $\mathbf{x}$ and t,

$$\begin{aligned}
\mathcal{H} &= -\frac{\nabla^2}{2}+V(\mathbf{x}),\quad \Theta=\frac{2\psi_2\psi_{-2}-2\psi_1\psi_{-1}+\psi_0^2}{\sqrt{5}},\quad F_z=\sum_{j=-2}^{2}j|\psi_j|^2, &&\text{(2.7a)}\\
F_- &= F_+^* = 2\psi^*_{-2}\psi_{-1}+\sqrt{6}\psi^*_{-1}\psi_0+\sqrt{6}\psi^*_0\psi_1+2\psi_2\psi^*_1, &&\text{(2.7b)}
\end{aligned}$$

and $\rho=\sum_{j=-2}^{2}|\psi_j|^2$ is the total density. In 3D setting, $\mathbf{x}$, Laplacian, trapping potential $V(\mathbf{x})$, interaction parameters (c_0, c_1, c_2), and SO-coupling terms Γ are defined as

$$\begin{aligned}
\mathbf{x} &\equiv (x,y,z),\ \nabla^2=\left(\frac{\partial}{\partial x^2}+\frac{\partial}{\partial y^2}+\frac{\partial}{\partial z^2}\right),\ V(\mathbf{x})=\frac{\alpha_x^2x^2+\alpha_y^2y^2+\alpha_z^2z^2}{2}, &&\text{(2.8a)}\\
c_0 &= \frac{4\pi N(4a_2+3a_4)}{7a_{\text{osc}}},\ c_1=\frac{4\pi N(a_4-a_2)}{7a_{\text{osc}}},\ c_2=\frac{4\pi N(7a_0-10a_2+3a_4)}{7a_{\text{osc}}}, &&\text{(2.8b)}\\
\Gamma_{\pm2} &= -\iota\left(\gamma_x\frac{\partial\psi_{\pm1}}{\partial x}\mp\iota\gamma_y\frac{\partial\psi_{\pm1}}{\partial y}\pm2\gamma_z\frac{\partial\psi_{\pm2}}{\partial z}\right), &&\text{(2.8c)}\\
\Gamma_{\pm1} &= -\iota\left(\gamma_x\frac{\partial\psi_{\pm2}}{\partial x}+\sqrt{\frac{3}{2}}\gamma_x\frac{\partial\psi_0}{\partial x}\pm\iota\gamma_y\frac{\partial\psi_{\pm2}}{\partial y}\mp\iota\sqrt{\frac{3}{2}}\gamma_y\frac{\partial\psi_0}{\partial y}\pm\gamma_z\frac{\partial\psi_{\pm1}}{\partial z}\right), &&\text{(2.8d)}\\
\Gamma_0 &= -\iota\left(\sqrt{\frac{3}{2}}\gamma_x\frac{\partial\psi_1}{\partial x}+\sqrt{\frac{3}{2}}\gamma_x\frac{\partial\psi_{-1}}{\partial x}+\iota\sqrt{\frac{3}{2}}\gamma_y\frac{\partial\psi_1}{\partial y}-\iota\sqrt{\frac{3}{2}}\gamma_y\frac{\partial\psi_{-1}}{\partial y}\right), &&\text{(2.8e)}
\end{aligned}$$

where α_ν and γ_ν with $\nu = x, y, z$ are the anisotropy parameters of trapping potential and SO coupling, respectively; N is the total number of atoms; $a_{\rm osc}$ (oscillator length) is chosen as a unit of length; and a_0, a_2, a_4 are the s-wave scattering lengths in total spin 0, 2 and 4 channels, respectively.

When a spin-2 BEC is strongly confined along one direction, say z, as compared to other two, i.e. $\omega_z \gg \omega_x \approx \omega_y$, then one can approximate Eqs. (2.6a)-(2.6c) by two-dimensional equations which can obtained by substituting [183]

$$\begin{aligned}
\mathbf{x} &\equiv (x,y), \quad \nabla^{\mathbf{2}} = \left(\frac{\partial}{\partial x^2} + \frac{\partial}{\partial y^2}\right), \quad V(\mathbf{x}) = \frac{\alpha_x^2 x^2 + \alpha_y^2 y^2}{2}, && (2.9a)\\
c_0 &= \sqrt{\frac{\alpha_z}{2\pi}} \frac{4\pi N(4a_2 + 3a_4)}{7a_{\rm osc}}, \quad c_1 = \sqrt{\frac{\alpha_z}{2\pi}} \frac{4\pi N(a_4 - a_2)}{7a_{\rm osc}}, && (2.9b)\\
c_2 &= \sqrt{\frac{\alpha_z}{2\pi}} \frac{4\pi N(7a_0 - 10a_2 + 3a_4)}{7a_{\rm osc}}, \quad \Gamma_{\pm 2} = -\iota\left(\gamma_x \frac{\partial \psi_{\pm 1}}{\partial x} \mp \iota\gamma_y \frac{\partial \psi_{\pm 1}}{\partial y}\right), && (2.9c)\\
\Gamma_{\pm 1} &= -\iota\left(\gamma_x \frac{\partial \psi_{\pm 2}}{\partial x} + \sqrt{\frac{3}{2}}\gamma_x \frac{\partial \psi_0}{\partial x} \pm \iota\gamma_y \frac{\partial \psi_{\pm 2}}{\partial y} \mp \iota\sqrt{\frac{3}{2}}\gamma_y \frac{\partial \psi_0}{\partial y}\right), && (2.9d)\\
\Gamma_0 &= -\iota\left(\sqrt{\frac{3}{2}}\gamma_x \frac{\partial \psi_1}{\partial x} + \sqrt{\frac{3}{2}}\gamma_x \frac{\partial \psi_{-1}}{\partial x} + \iota\sqrt{\frac{3}{2}}\gamma_y \frac{\partial \psi_1}{\partial y} - \iota\sqrt{\frac{3}{2}}\gamma_y \frac{\partial \psi_{-1}}{\partial y}\right). && (2.9e)
\end{aligned}$$

Similarly, if the BEC is strongly confined along two directions, say y and z, as compared to third one, i.e. $\omega_y = \omega_z \gg \omega_x$, then one can approximate Eqs. (2.6a)-(2.6c) by one-dimensional equations which can be obtained by substituting [183]

$$\begin{aligned}
\mathbf{x} &\equiv x, \quad \nabla^{\mathbf{2}} = \frac{\partial}{\partial x^2}, \quad V(\mathbf{x}) = \frac{\alpha_x^2 x^2}{2}, && (2.10a)\\
c_0 &= \sqrt{\alpha_y \alpha_z} \frac{2N(4a_2 + 3a_4)}{7a_{\rm osc}}, \quad c_1 = \sqrt{\alpha_y \alpha_z} \frac{2N(a_4 - a_2)}{7a_{\rm osc}}, && (2.10b)\\
c_2 &= \sqrt{\alpha_y \alpha_z} \frac{2N(7a_0 - 10a_2 + 3a_4)}{7a_{\rm osc}}, \quad \Gamma_{\pm 2} = -\iota\gamma_x \frac{\partial \psi_{\pm 1}}{\partial x}, && (2.10c)\\
\Gamma_{\pm 1} &= -\iota\left(\gamma_x \frac{\partial \psi_{\pm 2}}{\partial x} + \sqrt{\frac{3}{2}}\gamma_x \frac{\partial \psi_0}{\partial x}\right), && (2.10d)\\
\Gamma_0 &= -\iota\left(\sqrt{\frac{3}{2}}\gamma_x \frac{\partial \psi_1}{\partial x} + \sqrt{\frac{3}{2}}\gamma_x \frac{\partial \psi_{-1}}{\partial x}\right). && (2.10e)
\end{aligned}$$

The energy of an SO-coupled spin-2 BEC is given as

$$E = \int d\mathbf{x} \left[\left\{\sum_{j=-2}^{+2} \psi_j^* \left(-\frac{1}{2}\nabla^2 + V\right)\psi_j\right\} + \frac{c_0}{2}\rho^2 + \frac{c_1}{2}|\mathbf{F}|^2 + \frac{c_2}{2}|\Theta|^2 + \sum_{j=-2}^{+2} \psi_j^* \Gamma_j\right], \quad (2.11)$$

where $|\mathbf{F}|^2 = F_+ F_- + F_z^2$. The energy, along with the norm $\mathcal{N} = \int \rho d\mathbf{x}$ are two conserved quantities of an SO-coupled spin-2 BEC. The dimensionless formulation of the mean-field model, i.e. Eqs. (2.6a)-(2.6c), ensures that $\mathcal{N}$ is set to unity. In the absence of SO coupling, one more quantity longitudinal magnetization $f_z = \int F_z d\mathbf{x}$ is also conserved. The time-independent variant of Eqs. (2.6a)-(2.6c) can be obtained by substituting $\psi_j(\mathbf{x}, t) =$

$\psi_j(\mathbf{x})e^{-i\mu_j t}$, where μ_j are the chemical potentials of the individual components.

2.2.2 Fourier pseudospectral methods for a spin-2 BEC

The CGPEs (2.6a)-(2.6c) can be written in matrix form and four operators in Eq. (2.1) are defined as

$$\begin{aligned}
H_{\mathrm{SOC}} &= -i\gamma_x\partial_x S_x - i\gamma_y\partial_y S_y, \quad H_{\mathrm{SE}} = \begin{pmatrix} 0 & H_{12} & H_{13} & 0 & 0 \\ H_{12}^* & 0 & H_{23} & 0 & 0 \\ H_{13}^* & H_{23}^* & 0 & H_{34} & H_{35} \\ 0 & 0 & H_{34}^* & 0 & H_{45} \\ 0 & 0 & H_{35}^* & H_{45}^* & 0 \end{pmatrix}, && (2.12a)\\
H_{\mathrm{SP}} &= \mathrm{diag}\left(H_{+2}, H_{+1}, H_0, H_{-1}, H_{-2}\right), && (2.12b)\\
H_{\mathrm{KE}} &= \mathrm{diag}\Bigg(-\frac{\nabla^2}{2} - 2\iota\gamma_z\partial_z, -\frac{\nabla^2}{2} - \iota\gamma_z\partial_z, -\frac{\nabla^2}{2}, -\frac{\nabla^2}{2} + \iota\gamma_z\partial_z, \\
&\quad -\frac{\nabla^2}{2} + 2\iota\gamma_z\partial_z\Bigg), && (2.12c)
\end{aligned}$$

where S_x and S_y are irreducible representations of spin-2 matrices, $H_{\pm 2} = V + c_0\rho \pm 2c_1F_z + (2/5)c_2|\psi_{\mp 2}|^2$, $H_0 = V + c_0\rho + (1/5)c_2|\psi_0|^2$, $H_{\pm 1} = V + c_0\rho \pm c_1F_z + (2/5)c_2|\psi_{\mp 1}|^2$, $H_{12} = c_1F_- - (2/5)c_2\psi_{-1}\psi_{-2}^*$, $H_{13} = (1/5)c_2\psi_0\psi_{-2}^*$, $H_{23} = (\sqrt{6}/2)c_1F_- - (1/5)c_2\psi_0\psi_{-1}^*$, $H_{34} = (\sqrt{6}/2)c_1F_- - (1/5)c_2\psi_1\psi_0^*$, $H_{35} = (1/5)c_2\psi_2\psi_0^*$, and $H_{45} = c_1F_- - (2/5)c_2\psi_2\psi_1^*$. To solve the equations Eqs. (2.5a)-(2.5d) employing the Fourier pseudospectral method, split equations involving kinetic energy and SO-coupling operators are dealt with in the Fourier space. The Eq. (2.5a) can be expressed as the following set of decoupled equations

$$\begin{aligned}
\iota\frac{\partial\psi_j(x,y,z,t)}{\partial t} &= -\frac{\partial^2\psi_j(x,y,z,t)}{2\partial x^2} - \frac{\partial^2\psi_j(x,y,z,t)}{2\partial y^2} - \frac{\partial^2\psi_j(x,y,z,t)}{2\partial z^2} \\
&\quad + j\iota k_z\frac{\partial\psi_j(x,y,z,t)}{\partial z}, \qquad (2.13)
\end{aligned}$$

where $j = +2, +1, 0, -1, -2$. Solution of Eq. (2.13) in Fourier space is given as

$$\begin{aligned}
\hat{\psi}_{\pm 2}(k_x,k_y,k_z,t+\delta t) &= \hat{\psi}_{\pm 2}(k_x,k_y,k_z,t)\exp[-\iota(k_x^2+k_y^2+k_z^2 \pm 2\gamma_z k_z)\delta t], && (2.14a)\\
\hat{\psi}_{\pm 1}(k_x,k_y,k_z,t+\delta t) &= \hat{\psi}_{\pm 1}(k_x,k_y,k_z,t)\exp[-\iota(k_x^2+k_y^2+k_z^2 \pm \gamma_z k_z)\delta t], && (2.14b)\\
\hat{\psi}_0(k_x,k_y,k_z,t+\delta t) &= \hat{\psi}_0(k_x,k_y,k_z,t)\exp[-\iota(k_x^2+k_y^2+k_z^2)\delta t], && (2.14c)
\end{aligned}$$

where $\hat{\psi}_j$ is the Fourier transform of ψ_j and k_x, k_y, k_z are the corresponding Fourier frequencies. Now $\hat{\psi}_j(k_x,k_y,k_z,t+\delta t)$, the transient wave function in Fourier space is the initial value of the wave function for the Fourier transform of Eq. (2.5b), which in the Fourier space is given as

$$\iota\frac{\partial\hat{\Psi}(k_x,k_y,k_z,t)}{\partial t} = \hat{H}_{\mathrm{SOC}}\hat{\Psi}(k_x,k_y,k_z,t), \qquad (2.15)$$

where

$$\hat{H}_{\rm SOC} = \begin{pmatrix} 0 & \gamma_x k_x - \iota\gamma_y k_y & 0 & 0 & 0 \\ \gamma_x k_x + \iota\gamma_y k_y & 0 & \sqrt{\frac{3}{2}}(\gamma_x k_x - \iota\gamma_y k_y) & 0 & 0 \\ 0 & \sqrt{\frac{3}{2}}(\gamma_x k_x + \iota\gamma_y k_y) & 0 & \sqrt{\frac{3}{2}}(\gamma_x k_x - \iota\gamma_y k_y) & 0 \\ 0 & 0 & \sqrt{\frac{3}{2}}(\gamma_x k_x + \iota\gamma_y k_y) & 0 & \gamma_x k_x - \iota\gamma_y k_y \\ 0 & 0 & 0 & \gamma_x k_x + \iota\gamma_y k_y & 0 \end{pmatrix}, \tag{2.16}$$

and the formal solution of Eq. (2.15) is

$$\begin{aligned} \hat{\Psi}(k_x, k_y, k_z, t+\delta t) &= \exp(-\iota\delta t\hat{H}_{\rm SOC})\hat{\Psi}(k_x, k_y, k_z, t), \\ &= \exp(-\iota\delta t\hat{P}\hat{D}\hat{P}^{-1})\hat{\Psi}(k_x, k_y, k_z, t), \\ &= \hat{P}\exp(-\iota\delta t\hat{D})\hat{P}^{-1}\hat{\Psi}(k_x, k_y, k_z, t), \end{aligned} \tag{2.17}$$

where $\hat{P}$ is 5×5 matrix defined as $\hat{P} = (A_1,\ A_2,\ A_3,\ A_4,\ A_5)$ and $\hat{D}$ is a diagonal matrix. The A_j with $j = 1, 2, 3, 4, 5$ are normalised eigenvectors defined as

$$A_1 = \left\{\frac{1}{4}e^{-2\iota\beta}, -\frac{1}{2}e^{-\iota\beta}, \frac{\sqrt{3}}{2\sqrt{2}}, -\frac{e^{\iota\beta}}{2}, \frac{1}{4}e^{2\iota\beta}\right\}^T, \tag{2.18a}$$

$$A_2 = \left\{-\frac{1}{2}e^{-2\iota\beta}, \frac{e^{-\iota\beta}}{2}, 0, -\frac{e^{\iota\beta}}{2}, \frac{1}{2}e^{2\iota\beta}\right\}^T, \tag{2.18b}$$

$$A_3 = \left\{\frac{1}{2}\sqrt{\frac{3}{2}}e^{-2\iota\beta}, 0, -\frac{1}{2}, 0, \frac{1}{2}\sqrt{\frac{3}{2}}e^{2\iota\beta}\right\}^T, \tag{2.18c}$$

$$A_4 = \left\{-\frac{1}{2}e^{-2\iota\beta}, -\frac{1}{2}e^{-\iota\beta}, 0, \frac{e^{\iota\beta}}{2}, \frac{1}{2}e^{2\iota\beta}\right\}^T, \tag{2.18d}$$

$$A_5 = \left\{\frac{1}{4}e^{-2\iota\beta}, \frac{e^{-\iota\beta}}{2}, \frac{\sqrt{3}}{2\sqrt{2}}, \frac{e^{\iota\beta}}{2}, \frac{1}{4}e^{2\iota\beta}\right\}^T, \tag{2.18e}$$

and $\hat{D} = {\rm diag}\,(-2\alpha,\ -\alpha,\ 0,\ \alpha,\ 2\alpha)$ where

$$\alpha = \sqrt{(\gamma_x k_x)^2 + (\gamma_y k_y)^2} \quad \text{and} \quad \beta = \tan^{-1}\left(\frac{\gamma_y k_y}{\gamma_x k_x}\right). \tag{2.19}$$

For a q1D condensate, α and β reduce to $\gamma_x k_x$ and 0, respectively. The solution of split equation for $H_{\rm SE}$ is approached similarly with one difference that $H_{\rm SE}$ is time-dependent. Taking this into account, solution to equation for $H_{\rm SE}$ is [177]

$$\begin{aligned} \Psi(x, t+\delta t) &= \exp\left(-\iota\int_t^{t+\delta t} H_{\rm SE}(x,t)dt\right)\Psi(x,t), \\ &\approx \exp\left[-\iota\delta t\frac{\left\{H_{\rm SE}(x,t) + H_{\rm SE}^{fE}(x,t+\delta t)\right\}}{2}\right]\Psi(x,t), \end{aligned}$$

$$
\begin{aligned}
&= \exp(-\iota\delta t BQB^{-1})\Psi(x,t),\\
&= B\exp(-\iota\delta t Q)B^{-1}\Psi(x,t), \qquad (2.20)
\end{aligned}
$$

where $H_{\mathrm{SE}}^{fE}(x,t+\delta t)$ is estimated by the forward Euler (fE) method, and Q is the diagonal matrix. The diagonalization of $H_{\mathrm{SE}}(x,t)+H_{\mathrm{SE}}^{fE}(x,t+\delta t)$ is performed numerically using the external subroutine ZHEEV of LAPACK software package [184]. In the case of the Intel compiler, LAPACK libraries are included in the Intel Math Kernel Library (MKL) and can be linked from there also. H_{SP} being diagonal, the solution to Eq. (2.5d) can be calculated analytically as

$$
\Psi(x,y,z,t+\delta t) = \exp\left(-\iota\delta t H_{\mathrm{SP}}\right)\Psi(x,y,z,t). \qquad (2.21)
$$

This final wave function is the solution of Eq. (2.2) after time δt for this system. For a q2D and q1D condensates, the four operators are defined similarly.

2.2.3 Conservation/Non-conservation of Magnetization

In the absence of spin-orbit coupling, $\Gamma_{\pm2}(\mathbf{x},t)=\Gamma_{\pm1}(\mathbf{x},t)=\Gamma_0(\mathbf{x},t)=0$,

$$
\begin{aligned}
\frac{df_z}{dt} &= \int \left(2|\psi_{+2}(\mathbf{x},t)|^2+|\psi_{+1}(\mathbf{x},t)|^2-|\psi_{-1}(\mathbf{x},t)|^2-2|\psi_{-2}(\mathbf{x},t)|^2\right)d\mathbf{x},\\
&= \int \Bigg(2\frac{\partial\psi_{+2}}{\partial t}\psi_{+2}^*+2\psi_{+2}\frac{\partial\psi_{+2}^*}{\partial t}+\frac{\partial\psi_{+1}}{\partial t}\psi_{+1}^*+\psi_{+1}\frac{\partial\psi_{+1}^*}{\partial t}-\frac{\partial\psi_{-1}}{\partial t}\psi_{-1}^*\\
&\quad -\psi_{-1}\frac{\partial\psi_{-1}^*}{\partial t}-2\frac{\partial\psi_{-2}}{\partial t}\psi_{-2}^*-2\psi_{-2}\frac{\partial\psi_{-2}^*}{\partial t}\Bigg)d\mathbf{x}. \qquad (2.22)
\end{aligned}
$$

Using Eqs. (2.6a)-(2.6c) in Eq. (2.22), we obtain

$$
\begin{aligned}
\frac{df_z}{dt} &= -\iota c_1\int\Bigg(F_-\psi_{+1}\psi_{+2}^*-F_+\psi_{+1}^*\psi_{+2}-F_+\psi_{-1}\psi_{-2}^*+F_-\psi_{-1}^*\psi_{-2}+\sqrt{\frac{3}{2}}F_-\psi_0\psi_{+1}^*\\
&\quad -\sqrt{\frac{3}{2}}F_+\psi_0^*\psi_{+1}-\sqrt{\frac{3}{2}}F_+\psi_0\psi_{-1}^*+\sqrt{\frac{3}{2}}F_-\psi_0^*\psi_{-1}\Bigg)d\mathbf{x},\\
&= -\iota c_1\int\Bigg[F_-\left(\psi_{+1}\psi_{+2}^*+\psi_{-1}^*\psi_{-2}+\sqrt{\frac{3}{2}}\psi_0^*\psi_{-1}+\sqrt{\frac{3}{2}}\psi_0\psi_{+1}^*\right)\\
&\quad -F_+\left(\psi_{+1}^*\psi_{+2}+\psi_{-1}\psi_{-2}^*+\sqrt{\frac{3}{2}}\psi_0^*\psi_{+1}+\sqrt{\frac{3}{2}}\psi_0\psi_{-1}^*\right)\Bigg]d\mathbf{x},\\
&= -\iota c_1\int\left(F_-\frac{F_+}{2}-F_+\frac{F_-}{2}\right)d\mathbf{x}\\
&= 0. \qquad (2.23)
\end{aligned}
$$

In the presence of SO coupling, combining Eqs. (2.6a)-(2.6c) with Eq. (2.22) leads to

$$
\begin{aligned}
\frac{df_z}{dt} &= -\iota\int\left(2\psi_{+2}^*\Gamma_{+2}+2\psi_{+2}\Gamma_{+2}^*+\psi_{+1}^*\Gamma_{+1}+\psi_{+1}\Gamma_{+1}^*-2\psi_{-2}^*\Gamma_{-2}+2\psi_{-2}\Gamma_{-2}^*\right.\\
&\quad \left.+\psi_{-1}^*\Gamma_{-1}+\psi_{-1}\Gamma_{-1}^*\right)d\mathbf{x},
\end{aligned}
$$

$$\neq \quad 0, \tag{2.24}$$

in general. Therefore, f_z is conserved in the absence of SO coupling but not so generally in the presence of SO coupling.

Simultaneous conservation of Norm and Magnetization

We use the imaginary time propagation method, where t is replaced by $-\iota\tau$ in CGPEs (2.6a)-(2.6c), to determine the stationary states of the system. As the imaginary time propagation is used to calculate the system's ground state under the constraint of fixed norm and magnetization, it conserves neither of the two; one needs to renormalize the component wavefunctions after each time iteration. This means after each imaginary-time step $\delta\tau$, the component wavefunctions are rescaled as $\psi_j(\mathbf{x}, \tau + \delta t) = \sigma_j \psi_j(\mathbf{x}, \tau)$, where σ_j are renormalization factors. These renormalization factors σ_j satisfy the following relationships among them [185]

$$\sigma_1\sigma_{-1} = \sigma_0^2, \tag{2.25a}$$
$$\sigma_2\sigma_{-2} = \sigma_0^2, \tag{2.25b}$$
$$\sigma_2\sigma_{-1}^2 = \sigma_0^3, \tag{2.25c}$$

and

$$u^4\mathcal{N}_2 + u^3v\mathcal{N}_1 + u^2v^2\mathcal{N}_0 + uv^3\mathcal{N}_{-1} + v^4\mathcal{N}_{-2} = \mathcal{N}u^2v, \tag{2.26a}$$
$$2u^4\mathcal{N}_2 + u^3v\mathcal{N}_1 - uv^3\mathcal{N}_{-1} - 2v^4\mathcal{N}_{-2} = f_z u^2 v, \tag{2.26b}$$

with norm and magnetization, where $u = \sigma_1^2$ and $v = \sigma_0^2$ and $\mathcal{N}_j = \int |\psi_j(\mathbf{x}, \tau)|^2 d\mathbf{x}$ are the component norms at (imaginary) time τ. In this thesis, we solve Eqs. (2.26a) and (2.26b) using Newton-Raphson method after each iteration in imaginary time. The σ_1 and σ_0 so obtained can be substituted back in Eqs. (2.25a)-(2.25c) to determine the remaining renormalization factors σ. The simultaneous fixing of norm and magnetization is only implemented in the absence of SO coupling.

2.3 Time-splitting finite-difference methods

To enhance the mean-field model's generality for a spin-f spinor BEC, we incorporate the coherent coupling strength absent in the discussion of the Fourier pseudospectral method. Hence, the set of Eqs. (2.5a)-(2.5d) can be redefined as

$$\iota\frac{\partial\Psi}{\partial t} = H_{\rm p}\Psi = (H_{\rm KE} + H_{\rm SOC})\Psi, \tag{2.27a}$$
$$\iota\frac{\partial\Psi}{\partial t} = H_{\rm SE+}\Psi = (H_{\rm SE} + H_{\rm coh})\Psi, \tag{2.27b}$$
$$\iota\frac{\partial\Psi}{\partial t} = H_{\rm SP}\Psi. \tag{2.27c}$$

The $H_{\rm p}$ in Eq. (2.27a) and $H_{\rm coh}$ in Eq. (2.27b) are $2f+1\times 2f+1$ matrix operators defined as

$$\begin{aligned} H_{\rm p} &= \mathbf{1}\frac{\hat{p}_x^2+\hat{p}_y^2+\hat{p}_z^2}{2}+\gamma(S_x\hat{p}_y-S_y\hat{p}_x), & (2.28)\\ H_{\rm coh} &= \frac{\Omega_{\rm coh}}{2}S_x, & (2.29)\end{aligned}$$

where $\mathbf{1}$ represents a $2f+1\times 2f+1$ identity matrix, γ and $\Omega_{\rm coh}$ are the strengths of SO and coherent couplings, respectively, $\hat{p}_\nu=-\iota\partial/\partial\nu$ with $\nu=x,y,z$, and and S_x and S_y are spin matrices in Eqs. (1.9a)-(1.9c). As the $H_{\rm coh}=\Omega_{\rm coh}S_x/2$ also includes off-diagonal terms, we merge it into the $H_{\rm SE}$ matrix in Eq. (2.27b).

The matrix $H_{\rm SE}$ and $H_{\rm SP}$ in Eqs. (2.27b) and (2.27c), respectively, for a pseudospin-1/2 condensate are [48]

$$H_{\rm SP} = \begin{pmatrix} V+\sum_{l=1}^{2}g_{1l}|\psi_l|^2 & 0\\ 0 & V+\sum_{l=1}^{2}g_{2l}|\psi_l|^2\end{pmatrix}, \quad H_{\rm SE}=0, \tag{2.30}$$

where

$$V=\frac{1}{2}\sum_\nu \alpha_\nu^2\nu^2, \quad g_{ll}=\frac{4\pi N a_{ll}}{a_{\rm osc}}, \quad g_{l,3-l}=\frac{4\pi N a_{l,3-l}}{a_{\rm osc}},$$

where g_{ll} and $g_{l,3-l}$ with $l=1,2$ are intra- and inter-species interaction strengths, respectively. The intra-species interaction strengths g_{11} and g_{22} are proportional, respectively, to intra-species s-wave scattering lengths a_{11} and a_{22}, and the total number of condensate atoms. Similarly, the inter-species interaction strength g_{12} is proportional to inter-species s-wave scattering length a_{12} and the total number of condensate atoms. The equality $a_{12}=a_{21}$ implies that $g_{12}=g_{21}$.

The order parameter for three spin systems is normalized to unity as

$$\int\sum_l|\psi_l(\mathbf{x},t)|^2 d\mathbf{x}=\sum_l\mathcal{N}_l=\mathcal{N}=1. \tag{2.31}$$

The order parameter's norm, along with the energy of these SO-coupled spinor condensate, which is defined as

$$E=\int\left[\sum_{l,m}\psi_l^*\left(H_{\rm p}+H_{\rm SP}+H_{\rm SE+}\right)_{lm}\psi_m\right]d\mathbf{x}, \tag{2.32}$$

where l,m run over species' labels, are the two conserved quantities for an SO-coupled condensate.

2.3.1 TSBE and TSCN methods for spin-1/2 BEC

We describe the (semi)-implicit finite-difference schemes to numerically solve the CGPEs for SO-coupled spinor condensates. We use TSBE and TSCN methods to solve the coupled sets of non-linear partial differential equations describing SO-coupled pseudospin-1/2

BECs. The implementation is explained in detail for an SO-coupled pseudospin-1/2 condensate and then extended to higher spin condensates in Appendix A. The results obtained with these finite difference schemes are compared with results from the Fourier pseudospectral method.

2.3.2 Quasi-one-dimensional SO-coupled pseudospin-1/2 BEC

We consider a two-component pseudospin-1/2 BEC confined by a harmonic trapping potential with Rashba SO and coherent couplings. We first elaborate the method for solving one-dimensional CGPEs, which describe an SO-coupled pseudospin-1/2 BEC trapped by a q1D trapping potential. In such a trap, the y and z coordinates can be integrated out and after a rotation by $\pi/2$ about z-axis in spin-space, which changes S_y to $-S_x$, the resultant matrix operator H_p is

$$H_\mathrm{p} = \mathbf{1}\frac{\hat{p}_x^2}{2} - \gamma S_y \hat{p}_x \equiv \mathbf{1}\frac{\hat{p}_x^2}{2} + \gamma S_x \hat{p}_x, \tag{2.33}$$

where $\mathbf{1}$ is a 2×2 identity matrix. The form of H_coh, H_SP, and H_SE remain same as in Eqs. (2.29) and (2.30) with

$$\mathbf{x} = x, \quad V = \frac{1}{2}\alpha_x^2 x^2, \quad g_{ll} = \frac{2Na_{ll}\sqrt{\alpha_y \alpha_z}}{a_\mathrm{osc}}, \quad g_{l,3-l} = \frac{2Na_{l,3-l}\sqrt{\alpha_y \alpha_z}}{a_\mathrm{osc}},$$

where the terms have the same meanings as described in the previous section, and $\mathbf{x} = x$ is in the units of a_osc. The order parameter for this system is $\Psi(\mathbf{x}, t) = [\psi_1(\mathbf{x}, t), \psi_2(\mathbf{x}, t)]^T$ with T denoting the transpose. Using Eq. (2.33), the matrix Eq. (2.27a) in terms of coupled component equations are

$$\iota \frac{\partial \psi_l(x,t)}{\partial t} = -\frac{1}{2}\frac{\partial^2 \psi_l(x,t)}{\partial x^2} - \iota\gamma \frac{\partial \psi_{3-l}(x,t)}{\partial x}, \tag{2.34a}$$

where $l = 1, 2$ is species' label. The spatial domain $x \in [-L_x/2, L_x/2)$ is discretized via N_x uniformly spaced points with a spacing of Δx. The resulting one-dimensional space grid is $x_i = -L_x/2 + (i-1)\Delta x$ where $i = 1, 2, \ldots, N_x$. Using Δt as the time-step to discretize time, the discrete analogue of $\psi_l(x,t)$ is $\phi^n_{(i,l)}$ which represents the value of l^th component of the order parameter at a spatial coordinate x_i at time $n\Delta t$. The discretization scheme employs either (a) the periodic boundary condition

$$\phi^n_{(1,l)} = \phi^n_{(N_x+1,l)}, \quad \phi^n_{(0,l)} = \phi^n_{(N_x,l)}, \tag{2.35}$$

or (b) homogeneous Dirichlet boundary condition

$$\phi^n_{(0,l)} = \phi^n_{(N_x+1,l)} = 0. \tag{2.36}$$

In this chapter, from this point forward, indices l and m are exclusively used for species' labels, indices i, j, and k are used to denote only space-grid points, n is the index used for time, and $\nu = x, y, z$. With periodic boundary condition (2.35), the discrete analogue of Eq. (2.34a) using Forward-Euler or Backward-Euler or Crank-Nicolson discretization schemes [186] is

$$\begin{aligned}\phi^{n+1}_{(i,l)} - \phi^{n}_{(i,l)} = \frac{\iota\Delta t}{4\Delta x^2}\left[\alpha\left(\phi^{n+1}_{(i+1,l)} - 2\phi^{n+1}_{(i,l)} + \phi^{n+1}_{(i-1,l)}\right) + \beta\left(\phi^{n}_{(i+1,l)} - 2\phi^{n}_{(i,l)} + \phi^{n}_{(i-1,l)}\right)\right] \\ - \frac{\gamma\Delta t}{4\Delta x}\left[\alpha\left(\phi^{n+1}_{(i+1,3-l)} - \phi^{n+1}_{(i-1,3-l)}\right) + \beta\left(\phi^{n}_{(i+1,3-l)} - \phi^{n}_{(i-1,3-l)}\right)\right], \qquad (2.37)\end{aligned}$$

where $\alpha = 0, \beta = 2$ for Forward-Euler, $\alpha = 2, \beta = 0$ for Backward-Euler, and $\alpha = \beta = 1$ for Crank-Nicolson discretization. The local truncation error incurred in Backward-Euler and Crank-Nicolson discretizations are, respectively, of the order $O(\Delta x^2 + \Delta t)$ and $O(\Delta x^2 + \Delta t^2)$, and the methods are unconditionally stable [186]. The explicit Forward-Euler discretization scheme with the same local truncation error as the implicit Backward-Euler is trivial to implement but is only conditionally stable [186]. The solution of Eq. (2.34a) using Forward-Euler is

$$\phi^{n+1}_{(i,l)} = \frac{\iota\Delta t}{2\Delta x^2}\left[\phi^{n}_{(i+1,l)} - 2\phi^{n}_{(i,l)} + \phi^{n}_{(i-1,l)}\right] - \frac{\gamma\Delta t}{2\Delta x}\left[\phi^{n}_{(i+1,3-l)} - \phi^{n}_{(i-1,3-l)}\right] + \phi^{n}_{(i,l)}. \qquad (2.38)$$

The conditional stability of the Forward-Euler method makes it the least desirable among the three methods. Now, considering *Backward-Euler* discretization, Eq. (2.37) is

$$\iota\frac{\phi^{n+1}_{(i,l)} - \phi^{n}_{(i,l)}}{\Delta t} = -\frac{\phi^{n+1}_{(i+1,l)} - 2\phi^{n+1}_{(i,l)} + \phi^{n+1}_{(i-1,l)}}{2\Delta x^2} - \iota\gamma\frac{\phi^{n+1}_{(i+1,3-l)} - \phi^{n+1}_{(i-1,3-l)}}{2\Delta x}.$$

For $l = 1, 2$, the time evolution as per Backward-Euler is equivalent to

$$\begin{bmatrix}\phi^{n+1}_{(i,1)} \\ \phi^{n+1}_{(i,2)}\end{bmatrix} = (\mathbf{1} + \iota H_p\Delta t)^{-1}\begin{bmatrix}\phi^{n}_{(i,1)} \\ \phi^{n}_{(i,2)}\end{bmatrix}, \qquad (2.39)$$

where

$$H_p\begin{bmatrix}\phi^{n+1}_{(i,1)} \\ \phi^{n+1}_{(i,2)}\end{bmatrix} = \begin{bmatrix}-\frac{\phi^{n+1}_{(i+1,1)} - 2\phi^{n+1}_{(i,1)} + \phi^{n+1}_{(i-1,1)}}{2\Delta x^2} - \iota\gamma_x\frac{\phi^{n+1}_{(i+1,2)} - \phi^{n+1}_{(i-1,2)}}{2\Delta x} \\ -\frac{\phi^{n+1}_{(i+1,2)} - 2\phi^{n+1}_{(i,2)} + \phi^{n+1}_{(i-1,2)}}{2\Delta x^2} - \iota\gamma_x\frac{\phi^{n+1}_{(i+1,1)} - \phi^{n+1}_{(i-1,1)}}{2\Delta x}\end{bmatrix}. \qquad (2.40)$$

As H_p is a Hermitian operator, the time evolution operator $(\mathbf{1} + \iota H_p\Delta t)^{-1}$ in Backward-Euler discretization is not unitary, leading to the norm not being conserved. Similarly, time evolution using Forward-Euler discretization in (2.38) is equivalent to

$$\begin{bmatrix}\phi^{n+1}_{(i,1)} \\ \phi^{n+1}_{(i,2)}\end{bmatrix} = (\mathbf{1} - \iota H_p\Delta t)\begin{bmatrix}\phi^{n}_{(i,1)} \\ \phi^{n}_{(i,2)}\end{bmatrix}, \qquad (2.41)$$

corresponding to a non-Hermitian operator $(\mathbf{1} - \iota H_p\Delta t)$. In contrast to this, the time evolution as per Crank-Nicolson is equivalent to

$$\begin{bmatrix}\phi^{n+1}_{(i,1)} \\ \phi^{n+1}_{(i,2)}\end{bmatrix} = \frac{\mathbf{1} - \iota H_p\Delta t}{\mathbf{1} + \iota H_p\Delta t}\begin{bmatrix}\phi^{n}_{(i,1)} \\ \phi^{n}_{(i,2)}\end{bmatrix}, \qquad (2.42)$$

which corresponds to a unitary operator $(\mathbf{1}-\iota H_p\Delta t)/(\mathbf{1}+\iota H_p\Delta t)$. The Backward-Euler method is, therefore, not suitable for realtime evolution in contrast to the Crank-Nicolson method. Nonetheless, in imaginary time evolution, a non-unitary time evolution used to obtain the stationary state solutions, both Backward-Euler or Crank-Nicolson methods can be used. Rewriting Eq. (2.37) as

$$\begin{aligned}
&-\frac{\iota\alpha\Delta t}{4\Delta x^2}\left[\phi^{n+1}_{(i-1,l)}+\phi^{n+1}_{(i+1,l)}\right]+\left(1+\frac{\iota\alpha\Delta t}{2\Delta x^2}\right)\phi^{n+1}_{(i,l)}+\frac{\gamma\alpha\Delta t}{4\Delta x}\left(\phi^{n+1}_{(i+1,3-l)}-\phi^{n+1}_{(i-1,3-l)}\right)\\
&=\frac{\iota\beta\Delta t}{4\Delta x^2}\left[\phi^{n}_{(i-1,l)}+\phi^{n}_{(i+1,l)}\right]+\left(1-\frac{\iota\beta\Delta t}{2\Delta x^2}\right)\phi^{n}_{(i,l)}\\
&\quad-\frac{\gamma\beta\Delta t}{4\Delta x}\left(\phi^{n}_{(i+1,3-l)}-\phi^{n}_{(i-1,3-l)}\right),
\end{aligned}\tag{2.43}$$

and then using Eq. (2.35) in Eq. (2.43) with $i=1,2,\ldots,N_x$ and $l=1,2$, the resulting set of $2N_x$ coupled linear algebraic equations can be written in matrix form as

$$A\Phi^{n+1}_l+B\Phi^{n+1}_{3-l}=D_l,\tag{2.44}$$

where A, B are circulant $N_x\times N_x$ matrices and Φ^{n+1}_l, D_l are $N_x\times 1$ matrices. These matrices can be expressed as

$$A(i,:)=\left(1+\frac{\iota\alpha\Delta t}{2\Delta x^2},\ -\frac{\iota\alpha\Delta t}{4\Delta x^2},\ 0,\ \cdots,\ 0,\ -\frac{\iota\alpha\Delta t}{4\Delta x^2}\right)(C^{i-1})^T,\tag{2.45a}$$

$$B(i,:)=\left(0,\ \frac{\alpha\Delta t\gamma}{4\Delta x},\ 0,\ \cdots,\ 0,\ -\frac{\alpha\Delta t\gamma}{4\Delta x}\right)(C^{i-1})^T,\tag{2.45b}$$

$$\Phi^{n+1}_l=\left(\phi^{n+1}_{(1,l)},\ \phi^{n+1}_{(2,l)},\ \phi^{n+1}_{(3,l)},\ \cdots\ \phi^{n+1}_{(N_x,l)}\right)^T,\tag{2.45c}$$

$$\begin{aligned}d_l(i)=&\left[\frac{\iota\beta\Delta t}{4\Delta x^2}\left\{\phi^{n}_{(i-1,l)}+\phi^{n}_{(i+1,l)}\right\}+\left(1-\frac{\iota\beta\Delta t}{2\Delta x^2}\right)\phi^{n}_{(i,l)}\right.\\
&\left.-\frac{\gamma\beta\Delta t}{4\Delta x}\left(\phi^{n}_{(i+1,3-l)}-\phi^{n}_{(i-1,3-l)}\right)\right],\end{aligned}\tag{2.45d}$$

where $A(i,:)$ and $B(i,:)$ are the ith rows of A and B, respectively, $d_l(i)$ is the ith element of column matrix D_l, and C is defined as

$$C=\begin{bmatrix}0&0&\ldots&1\\1&0&\ldots&0\\\vdots&\ddots&&\vdots\\0&\ldots&1&0\end{bmatrix}.\tag{2.46}$$

For $l=1,2$, Eq. (2.44) represents two coupled matrix equations which can be decoupled to yield

$$(B^2-A^2)\Phi^{n+1}_l=BD_{3-l}-AD_l,\tag{2.47}$$

which for $l = 1$ and 2 represents two decoupled linear circulant systems of equations. Now, $B^2 - A^2$ being a circulant matrix can be diagonalised using Fourier matrix as [187]

$$\begin{aligned} B^2 - A^2 &= F^{-1}\Lambda F, \quad \text{where} && \text{(2.48a)} \\ F_{i,j} &= \frac{1}{\sqrt{N_x}} \exp\left[-\frac{2\pi\iota}{N_x}(i-1)(j-1)\right], \quad \text{and} && \text{(2.48b)} \\ \Lambda &= \text{diag}[\sqrt{N_x} F\{B^2(:,1) - A^2(:,1)\}]. && \text{(2.48c)} \end{aligned}$$

The product of the Fourier matrix (F) with a one-dimensional array is equal to the discrete Fourier transform of the array, and hence the solution to Eq. (2.47) using Eqs. (2.48a)-(2.48c) is [187]

$$\Phi_l^{n+1} = \text{IDFT}\left(\text{DFT}(BD_{3-l} - AD_l)./\text{DFT}(B^2(:,1) - A^2(:,1))\right), \tag{2.49}$$

where DFT and IDFT stand for discrete forward Fourier and inverse discrete Fourier transforms, respectively, $A^2(:,1)$ and $B^2(:,1)$ denote the first columns of A^2 and B^2, and ./ indicates the element-wise division.

With homogeneous Dirichlet boundary condition (2.36), the discretization of Eq. (2.34a) using Backward-Euler or Crank-Nicolson schemes yields

$$\begin{aligned} \phi_{(1,l)}^{n+1} - \phi_{(1,l)}^{n} &= \frac{\iota\Delta t}{4\Delta x^2}\left[\alpha\left(\phi_{(2,l)}^{n+1} - 2\phi_{(1,l)}^{n+1}\right) + \beta\left(\phi_{(2,l)}^{n} - 2\phi_{(1,l)}^{n}\right)\right] \\ &\quad - \frac{\gamma\Delta t}{4\Delta x}\left[\alpha\phi_{(2,3-l)}^{n+1} + \beta\phi_{(2,3-l)}^{n}\right], && \text{(2.50a)} \\ \phi_{(i,l)}^{n+1} - \phi_{(i,l)}^{n} &= \frac{\iota\Delta t}{4\Delta x^2}\left[\alpha\left(\phi_{(i+1,l)}^{n+1} - 2\phi_{(i,l)}^{n+1} + \phi_{(i-1,l)}^{n+1}\right) + \beta\left(\phi_{(i+1,l)}^{n} - 2\phi_{(i,l)}^{n}\right.\right. \\ &\quad \left.\left.+\phi_{(i-1,l)}^{n}\right)\right] - \frac{\gamma\Delta t}{4\Delta x}\left[\alpha\left(\phi_{(i+1,3-l)}^{n+1} - \phi_{(i-1,3-l)}^{n+1}\right) + \beta\left(\phi_{(i+1,3-l)}^{n}\right.\right. \\ &\quad \left.\left.-\phi_{(i-1,3-l)}^{n}\right)\right], \quad \text{for } i = 2, 3, \ldots N_x - 1, && \text{(2.50b)} \\ \phi_{(N_x,l)}^{n+1} - \phi_{(N_x,l)}^{n} &= \frac{\iota\Delta t}{4\Delta x^2}\left[\alpha\left(-2\phi_{(N_x,l)}^{n+1} + \phi_{(N_x-1,l)}^{n+1}\right) + \beta\left(-2\phi_{(N_x,l)}^{n}\phi_{(N_x-1,l)}^{n}\right)\right] \\ &\quad + \frac{\gamma\Delta t}{4\Delta x}\left[\alpha\phi_{(N_x-1,3-l)}^{n+1} + \beta\phi_{(N_x-1,3-l)}^{n}\right]. && \text{(2.50c)} \end{aligned}$$

Defining $\iota\Delta t/(4\Delta x^2) = \eta$ and $\gamma\Delta t/(4\Delta x) = \kappa$, Eqs. (2.50a)-(2.50c) can be written as a matrix equation

$$\begin{pmatrix} \mathcal{A} & \mathcal{B} \\ \mathcal{B} & \mathcal{A} \end{pmatrix} \begin{pmatrix} \Phi_1^{n+1} \\ \Phi_2^{n+1} \end{pmatrix} = \begin{pmatrix} \mathcal{D}_1 \\ \mathcal{D}_2 \end{pmatrix}, \tag{2.51}$$

where $\mathcal{A}$ and $\mathcal{B}$ are defined as

$$\mathcal{A} = \begin{pmatrix} 1+2\alpha\eta & -\alpha\eta & 0 & \cdots & 0 \\ -\alpha\eta & 1+2\alpha\eta & -\alpha\eta & \cdots & 0 \\ \vdots & \vdots & \ddots & \vdots & \vdots \\ 0 & \cdots & -\alpha\eta & 1+2\alpha\eta & -\alpha\eta \\ 0 & \cdots & 0 & -\alpha\eta & 1+2\alpha\eta \end{pmatrix}, \tag{2.52}$$

$$\mathcal{B} = \begin{pmatrix} 0 & \alpha\kappa & 0 & \cdots & 0 \\ -\alpha\kappa & 0 & \alpha\kappa & \cdots & 0 \\ \vdots & \vdots & \ddots & \vdots & \vdots \\ 0 & \cdots & -\alpha\kappa & 0 & \alpha\kappa \\ 0 & \cdots & 0 & -\alpha\kappa & 0 \end{pmatrix}, \tag{2.53}$$

and Φ_l^{n+1} is defined in Eq. (2.45c). The elements of column vectors $\mathcal{D}_l$ with $l = 1, 2$ in Eq. (2.51) are defined as

$$\tilde{d}_l(1) = (1 - 2\beta\eta)\phi^n_{(1,l)} + \beta\eta\phi^n_{(2,l)} - \beta\kappa\phi^n_{(2,3-l)}, \tag{2.54}$$

$$\tilde{d}_l(i) = \beta\eta\left[\phi^n_{(i+1,l)} + \phi^n_{(i-1,l)}\right] + (1 - 2\beta\eta)\phi^n_{(i,l)} - \beta\kappa\left[\phi^n_{(i+1,3-l)} - \phi^n_{(i-1,3-l)}\right]$$
$$\text{for } i = 2, 3 \ldots N_x - 1, \tag{2.55}$$

$$\tilde{d}_l(N_x) = \beta\eta\phi^n_{(N_x-1,l)} + (1 - 2\beta\eta)\phi^n_{(N_x,1)} + \beta\kappa\phi^n_{(N_x-1,3-l)}, \tag{2.56}$$

where $\tilde{d}_l(i)$ denotes the ith element of $\mathcal{D}_l$. The Eq. (2.51) is a sparse linear system of $2N_x$ equations and can be solved by iterative solvers [186,188] or direct solvers like Intel® oneAPI Math Kernel Library PARDISO [189]. The ease of applying different boundary conditions is one of the advantages of the finite difference method over the Fourier pseudospectral method. The Fourier pseudospectral method used to solve mean-field models of SO-coupled spinor BECs [181] naturally implements periodic boundary condition (2.35). To the best of our knowledge, the implementation of homogeneous Dirichlet boundary condition (2.36) is not available with the Fourier pseudospectral method when applied to SO-coupled spinor BECs. The homogeneous Dirichlet boundary conditions are the apt boundary for the BEC in an optical box trapping potential, which has already been experimentally realized [190]. Now, Eq. (2.27b) is evolved in time from $t_n = n\Delta t$ to $t_{n+1} = (n+1)\Delta t$ considering Eq. (2.49) as the solution at t_n if periodic boundary conditions are used; with homogeneous Dirichlet boundary conditions the input solution at t_n is the solution to Eq. (2.51). The exact analytic solution to Eq. (2.27b) is

$$\Psi(\mathbf{x}, t_{n+1}) = \exp[-\iota H_{\mathrm{SE+}}\Delta t]\Psi(\mathbf{x}, t_n) = \left[\mathbf{1}\cos\left(\frac{\Omega_{\mathrm{coh}}\Delta t}{2}\right) - \iota S_x \sin\left(\frac{\Omega_{\mathrm{coh}}\Delta t}{2}\right)\right]\Psi(\mathbf{x}, t_n). \tag{2.57}$$

The last step involves solving Eq. (2.27c) over the same period treating the solution in Eq. (2.57) as the solution at $t_n = n\Delta t$. The exact solution of Eq. (2.27c) is

$$\Psi(\mathbf{x}, t_{n+1}) = \exp[-\iota H_{\mathrm{SP}}\Delta t]\Psi(\mathbf{x}, t_n). \tag{2.58}$$

In the rest of this chapter, we will assume periodic boundary conditions to apply TSBE and TSCN discretization schemes.

2.3.3 Quasi-two-dimensional SO-coupled pseudospin-1/2 BEC

In a q2D trap with tight confinement along the z axis, the form of matrix operator $H_{\rm p}$ after integrating out the z coordinate becomes

$$H_{\rm p} = \mathbf{1}\frac{\hat{p}_x^2 + \hat{p}_y^2}{2} + \gamma(S_x\hat{p}_y - S_y\hat{p}_x), \tag{2.59}$$

and the form $H_{\rm coh}$, $H_{\rm SP}$, again remain unchanged from those in Eqs. (2.29) and (2.30) with

$$\mathbf{x} \equiv (x, y), \quad V = \frac{1}{2}(\alpha_x^2 x^2 + \alpha_y^2 y^2), \quad g_{lm} = \frac{2Na_{lm}\sqrt{2\pi\alpha_z}}{a_{osc}}. \tag{2.60}$$

For this q2D system, Eq. (2.27a) is further split into following two subequations

$$\iota\frac{\partial\Psi}{\partial t} = H_{p_x}\Psi, \tag{2.61a}$$

$$\iota\frac{\partial\Psi}{\partial t} = H_{p_y}\Psi, \tag{2.61b}$$

where H_{p_x} and H_{p_y} are defined as

$$H_{p_x} = \mathbf{1}\frac{\hat{p}_x^2}{2} - \gamma S_y\hat{p}_x, \quad H_{p_y} = \mathbf{1}\frac{\hat{p}_y^2}{2} + \gamma S_x\hat{p}_y. \tag{2.62}$$

The time evolution of the condensate from t_n to t_{n+1} is approximated by successive solutions to the Eqs. (2.27b), (2.27c), (2.61a), and (2.61b) over the same period. Here, we consider a two-dimensional spatial grid defined as $\nu_i = -L_\nu/2 + (i-1)\Delta\nu$, where $i = 1, 2, \ldots, N_\nu$, $\nu = x, y$ in units of $a_{\rm osc}$, and $\Delta\nu$ is spatial-step size. The discrete analogue of component wavefunction is $\phi^n_{(i,j,l)}$ which is equal to value of the lth wavefunction at a space point (x_i, y_j) at t_n time. Similar to q1D condensates, finite difference equivalents of each of Eqs. (2.61a) and (2.61b) can be simplified to two decoupled matrix equations

$$({B_x}^2 + {A_x}^2)X_l^{n+1} = A_x D_l^x + (-1)^l B_x D_{3-l}^x, \tag{2.63a}$$

$$({B_y}^2 - {A_y}^2)Y_l^{n+1} = B_y D_{3-l}^y - A_y D_l^y, \tag{2.63b}$$

where A_ν, B_ν (with $\nu = x, y$), $X_l^{n+1}, Y_l^{n+1}, D_l^\nu$ are defined

$$A_\nu(i,:) = \left(1 + \frac{\iota\alpha\Delta t}{2\Delta\nu^2},\ -\frac{\iota\alpha\Delta t}{4\Delta\nu^2},\ 0,\ \cdots,\ 0,\ -\frac{\iota\alpha\Delta t}{4\Delta\nu^2}\right)(C^{i-1})^T, \tag{2.64a}$$

$$B_x(i,:) = \left(0,\ \frac{\iota\alpha\Delta t\gamma}{4\Delta x},\ 0,\ \cdots,\ 0, -\frac{\iota\alpha\Delta t\gamma}{4\Delta x}\right)(C^{i-1})^T, \tag{2.64b}$$

$$B_y(i,:) = \left(0,\ \frac{\alpha\Delta t\gamma}{4\Delta y},\ 0,\ \cdots,\ 0,\ -\frac{\alpha\Delta t\gamma}{4\Delta y}\right)(C^{i-1})^T, \tag{2.64c}$$

$$X_l^{n+1} = \left(\phi^{n+1}_{(1,j,l)}\quad \phi^{n+1}_{(2,j,l)}\quad \phi^{n+1}_{(3,j,l)}\quad \cdots\quad \phi^{n+1}_{(N_x,j,l)}\right)^T, \tag{2.64d}$$

$$Y_l^{n+1} = \left(\phi^{n+1}_{(i,1,l)},\ \phi^{n+1}_{(i,2,l)},\ \phi^{n+1}_{(i,3,l)},\ \cdots\ \phi^{n+1}_{(i,N_y,l)}\right)^T, \tag{2.64e}$$

$$
\begin{aligned}
d_l^x(i) &= \left[\frac{\iota\beta\Delta t}{4\Delta x^2}\left\{\phi^n_{(i-1,j,l)}+\phi^n_{(i+1,j,l)}\right\}+\left(1-\frac{\iota\beta\Delta t}{2\Delta x^2}\right)\phi^n_{(i,j,l)}\right.\\
&\left.+\frac{(-1)^l\iota\gamma\beta\Delta t}{4\Delta x}\left(\phi^n_{(i+1,j,3-l)}-\phi^n_{(i-1,j,3-l)}\right)\right], \qquad (2.64\text{f})\\
d_l^y(i) &= \left[\frac{\iota\beta\Delta t}{4\Delta y^2}\left\{\phi^n_{(i,j-1,l)}+\phi^n_{(i,j+1,l)}\right\}+\left(1-\frac{\iota\beta\Delta t}{2\Delta y^2}\right)\phi^n_{(i,j,l)}\right.\\
&\left.-\frac{\gamma\beta\Delta t}{4\Delta y}\left(\phi^n_{(i,j+1,3-l)}-\phi^n_{(i,j-1,3-l)}\right)\right], \qquad (2.64\text{g})
\end{aligned}
$$

where $A_\nu(i,:)$ and $B_\nu(i,:)$ are the ith row of A_ν and B_ν, respectively, $d_l^\nu(i)$ is the ith element of column matrix D_l^ν, and C is defined in Eq. (2.46). For a fixed value of j (y-index) and l (species index), Eqs. (2.63a) is a linear circulant system of equations which can be solved by the same procedure as discussed to solve Eq. (2.47). The solution to Eq. (2.61a) is obtained by solving Eq. (2.63a) for all j and l values following the same procedure as discussed in Sec. 2.3.2. This solution, then, is considered as an input solution at t_n while solving another set of linear circulant systems of Eqs. (2.63b) over the same period, from t_n to $t_n+\Delta t$. The solutions to the Eqs. (2.27b) and (2.27c) for this case are again given as in Eqs. (2.57) and (2.58) with $\Psi(\mathbf{x},t_n)=[\psi_1(x,y,t_n),\psi_2(x,y,t_n)]^T$ where T stands for transpose.

2.3.4 Three-dimensional SO-coupled pseudospin-1/2 BEC

Here, we illustrate the extension of the TSBE and TSCN to a three-dimensional SO-coupled pseudospin-1/2 BEC. In this case, the form of matrix operators H_p, H_coh, H_SP are defined in Eqs. (2.28)-(2.30) and Eq. (2.27a) is further split into following three subequations

$$
\begin{aligned}
\iota\frac{\partial\Psi}{\partial t} &= H_{p_x}\Psi, \qquad (2.65\text{a})\\
\iota\frac{\partial\Psi}{\partial t} &= H_{p_y}\Psi, \qquad (2.65\text{b})\\
\iota\frac{\partial\Psi}{\partial t} &= H_{p_z}\Psi, \qquad (2.65\text{c})
\end{aligned}
$$

H_{p_x}, H_{p_y}, and H_{p_z} are defined as

$$
H_{p_x}=\mathbf{1}\frac{\hat{p}_x^2}{2}-\gamma S_y\hat{p}_x,\quad H_{p_y}=\mathbf{1}\frac{\hat{p}_y^2}{2}+\gamma S_x\hat{p}_y,\quad H_{p_z}=\mathbf{1}\frac{\hat{p}_z^2}{2}. \qquad (2.66)
$$

The time evolution of the condensate from t_n to t_{n+1} is approximated by successive solutions to the set of Eqs. (2.27b), (2.27c), (2.65a), (2.65b), and (2.65c) over the same period. The 3D spatial grid is defined as $\nu_i=-L_\nu/2+(i-1)\Delta\nu$, where $i=1,2,\ldots,N_\nu$, $\nu=x,y,z$, and $\Delta\nu$ is the spatial-step size along ν direction. The discrete analogue of component wavefunctions is $\phi^n_{(i,j,k,l)}$, which is equal to value of the lth wavefunction at a spatial point (x_i,y_j,z_k) at t_n time. Similar to a q1D condensate, finite difference equivalents of Eqs. (2.65a)-(2.65c) can be simplified to two decoupled matrix equations corresponding to $l = 1, 2$

$$\begin{aligned}
({B_x}^2 + {A_x}^2)X_l^{n+1} &= A_x D_l^x + (-1)^l B_x D_{3-l}^x, \qquad (2.67a)\\
({B_y}^2 - {A_y}^2)Y_l^{n+1} &= B_y D_{3-l}^y - A_y D_l^y, \qquad (2.67b)\\
A_z Z_l^{n+1} &= D_l^z, \qquad (2.67c)
\end{aligned}$$

where A_ν (with $\nu = x, y, z$), B_x and B_y are same as given in Eqs. (2.64a)-(2.64c), respectively, and $X_l^{n+1}, Y_l^{n+1}, Z_l^{n+1}, D_l^\nu$ are defined as

$$\begin{aligned}
X_l^{n+1} &= \left(\phi^{n+1}_{(1,j,k,l)} \quad \phi^{n+1}_{(2,j,k,l)} \quad \phi^{n+1}_{(3,j,k,l)} \quad \cdots \quad \phi^{n+1}_{(N_x,j,k,l)}\right)^T, \qquad (2.68a)\\
Y_l^{n+1} &= \left(\phi^{n+1}_{(i,1,k,l)}, \quad \phi^{n+1}_{(i,2,k,l)}, \quad \phi^{n+1}_{(i,3,k,l)}, \quad \cdots \quad \phi^{n+1}_{(i,N_y,k,l)}\right)^T, \qquad (2.68b)\\
Z_l^{n+1} &= \left(\phi^{n+1}_{(i,j,1,l)}, \quad \phi^{n+1}_{(i,j,2,l)}, \quad \phi^{n+1}_{(i,j,3,l)}, \quad \cdots \quad \phi^{n+1}_{(i,j,N_z,l)}\right)^T, \qquad (2.68c)\\
d_l^x(i) &= \left[\frac{\iota\beta\Delta t}{4\Delta x^2}\left\{\phi^n_{(i-1,j,k,l)} + \phi^n_{(i+1,j,k,l)}\right\} + \left(1 - \frac{\iota\beta\Delta t}{2\Delta x^2}\right)\phi^n_{(i,j,k,l)}\right.\\
&\quad \left. + \frac{(-1)^l \iota\gamma\beta\Delta t}{4\Delta x}\left(\phi^n_{(i+1,j,k,3-l)} - \phi^n_{(i-1,j,k,3-l)}\right)\right], \qquad (2.68d)\\
d_l^y(i) &= \left[\frac{\iota\beta\Delta t}{4\Delta y^2}\left\{\phi^n_{(i,j-1,k,l)} + \phi^n_{(i,j+1,k,l)}\right\} + \left(1 - \frac{\iota\beta\Delta t}{2\Delta y^2}\right)\phi^n_{(i,j,k,l)}\right.\\
&\quad \left. - \frac{\gamma\beta\Delta t}{4\Delta y}\left(\phi^n_{(i,j+1,k,3-l)} - \phi^n_{(i,j-1,k,3-l)}\right)\right], \qquad (2.68e)\\
d_l^z(i) &= \left[\frac{\iota\beta\Delta t}{4\Delta z^2}\left\{\phi^n_{(i,j,k-1,l)} + \phi^n_{(i,j,k+1,l)}\right\} + \left(1 - \frac{\iota\beta\Delta t}{2\Delta z^2}\right)\phi^n_{(i,j,k,l)}\right], \qquad (2.68f)
\end{aligned}$$

here $d_l^\nu(i)$ is the ith element of column matrix D_l^ν. The solution of Eq. (2.65a) is obtained by solving Eq. (2.67a) for all j, k, and l values following exactly the same procedure as discussed Sec. 2.3.2. Then, this solution is considered as an input while solving another set of linear circulant systems Eq. (2.67b), and then Eq. (2.67c). The solutions to Eqs. (2.27b) and (2.27c) for this system are again given as in Eqs. (2.57) and (2.58) with $\Psi(\mathbf{x}, t_n) = [\psi_1(x, y, z, t_n), \psi_2(x, y, z, t_n)]^T$.

We have considered standard Rashba coupling in the present chapter. The theoretical scheme to realize 3D analogue of Rashba coupling has also been proposed [191], and the finite difference method discussed in this section can be trivially extended to such a coupling.

2.4 Numerical Results

Here, we present the numerical results with TSFP, TSBE and TSCN methods for pseudospin-1/2, BECs in the presence as well as the absence of coherent coupling. The ground-state solution of an SO-coupled BEC can be achieved by considering an initial guess solution to the CGPEs and replacing t by $-\iota t = \tilde{t}$ to solve CGPEs. The resultant imaginary time evolution is not norm preserving, and hence, the total norm needs to be fixed to unity after each time iteration. The quantity $\tau = \max|\phi^{n+1}_{(i,j,l)} - \phi^n_{(i,j,l)}|/\Delta\tilde{t}$ serves

Table 2.1: Comparison of ground state energies of a pseudospin-1/2 BEC of ^{87}Rb obtained with TSFP, TSBE, and TSCN for different values of γ in the absence of coherent coupling Ω_{coh}. The interaction strength parameters are $g_{11} = 446.95$, $g_{22} = 402.26$, and $g_{12} = g_{21} = 491.65$ for the q1D BEC, whereas the same for q2D BEC are $g_{11} = 250.52$, $g_{22} = 225.47$, and $g_{12} = g_{21} = 275.57$.

		$\Delta x = 0.1, \Delta\tilde{t} = 0.01$			$\Delta x = 0.1, \Delta\tilde{t} = 0.005$		
	γ	TSFP	TSBE	TSCN	TSFP	TSBE	TSCN
q1D	0.5	21.4357	21.4357	21.4357	21.4357	21.4357	21.4357
	1.0	21.4186	21.4186	21.4186	21.4186	21.4186	21.4186
	1.5	21.3333	21.3334	21.3333	21.3324	21.3324	21.3324
	2.0	20.7018	20.7035	20.7022	20.7001	20.7014	20.7011
q2D	0.5	5.7201	5.7201	5.7201	5.7201	5.7201	5.7201
	1.0	5.4707	5.4707	5.4707	5.4707	5.4707	5.4707
	1.5	4.8520	4.8520	4.8520	4.8518	4.8518	4.8518
	2.0	3.9783	3.9786	3.9787	3.9883	3.9786	3.9786

as the convergence criterion to quantify convergence in imaginary time propagation. The stationary state solutions reported in this section have been obtained with $\tau = 10^{-6}$. In contrast to imaginary time evolution, realtime dynamics of the spinor BECs can be studied with TSCN and not with TSBE, as the latter does not conserve norm as was discussed in Sec. 2.3.2.

Pseudospin-1/2 BEC

We choose an experimentally realizable ^{87}Rb pseudospinor-1/2 BEC with scattering length $a_{11} = 101.8a_B$, interaction strengths $g_{12} = 1.1g_{11}$, $g_{22} = 0.9g_{11}$ and $g_{12} = g_{21}$ [192], where a_B is the Bohr radius. We consider 5000 atoms trapped in a q1D trapping potential with $\omega_x = 2\pi \times 20\text{Hz}$, $\omega_y = 2\pi \times 400\text{Hz}$ and $\omega_z = 2\pi \times 400\text{Hz}$. The interaction strengths in dimensionless units are given as

$$(g_{11},\ g_{22},\ g_{12}) = (446.95,\ 402.26,\ 491.65), \tag{2.69}$$

with $g_{12} = g_{21}$. As a q2D BEC, we consider 5000 atoms of ^{87}Rb in a trap with trapping frequencies $\omega_x = \omega_y = 2\pi \times 20\text{Hz}$, $\omega_z = 2\pi \times 400\text{Hz}$. In this case, the interaction strengths $g_{22} = 0.9g_{11}$, $g_{12} = 1.1g_{11}$, and $g_{12} = g_{21}$ for $a_{11} = 101.8a_B$ are given as

$$(g_{11},\ g_{22},\ g_{12}) = (250.52,\ 225.47,\ 275.57). \tag{2.70}$$

In both these cases, we compare the results from TSFP, TSBE and TSCN in the presence as well as the absence of coherent coupling and find an excellent agreement. The comparison of the ground state energies obtained with three methods for different values of γ are given in Table-2.1 for $\Omega_{\mathrm{coh}} = 0$ and Table-2.2 for $\Omega_{\mathrm{coh}} = 0.5$. The results with TSBE and TSCN are in very good agreement with those from TSFP. The component densities

Table 2.2: Comparison of ground state energies of a pseudospin-1/2 BEC obtained with TSFP, TSBE, and TSCN for $\Omega_{\text{coh}} = 0.5$ and different values of γ. The results have been obtained with $\Delta x = 0.1$ and $\Delta\tilde{t} = 0.01$. The interaction strength parameters considered for the q1D BEC are $g_{11} = 446.95$, $g_{22} = 402.26$, and $g_{12} = g_{21} = 491.65$, whereas the same for q2D BEC are $g_{11} = 250.52$, $g_{22} = 225.47$, and $g_{12} = g_{21} = 275.57$.

	γ	TSFP	TSBE	TSCN
q1D	0.5	21.4231	21.4231	21.4231
	1.0	21.4002	21.4002	21.4002
	1.5	21.3033	21.3034	21.3033
	2.0	20.6711	20.6727	20.6715
q2D	0.5	5.6457	5.6457	5.6457
	1.0	5.3339	5.3339	5.3339
	1.5	4.7181	4.7181	4.7181
	2.0	3.8434	3.8438	3.8438

corresponding to the ground state solutions obtained with TSBE and TSCN methods for q1D ^{87}Rb BEC are also in excellent agreement (not shown here).

We also study the variation of the convergence criterion as a function of $\tilde{t}$ in imaginary-time propagation with TSBE, TSCN, and TSFP to obtain the ground-state solution. As an example, in the imaginary-time propagation to obtain the ground state of the q1D pseudospin-1/2 BEC of ^{87}Rb starting with normalized Gaussian initial guess wavefunctions for the two components, the variations of τ as a function of $\tilde{t}$, obtained with three methods, are shown in Fig. 2.1(a) for $\Delta x = 0.1$ and $\Delta\tilde{t} = 0.01$ and in Fig. 2.1(b) for $\Delta x = 0.2$ and $\Delta\tilde{t} = 0.02$. It is evident that TSFP and TSCN shows faster convergence than TSBE. As discussed in Sec. 2.3.2, the TSBE does not lead to a unitary time evolution in contrast to TSCN. In order to confirm this, we consider the real-time evolution of the ground state solution of the q1D ^{87}Rb with TSFP, TSCN and TSBE. For this we consider the ground state solution corresponding to interaction parameters in Eq. (2.69) with

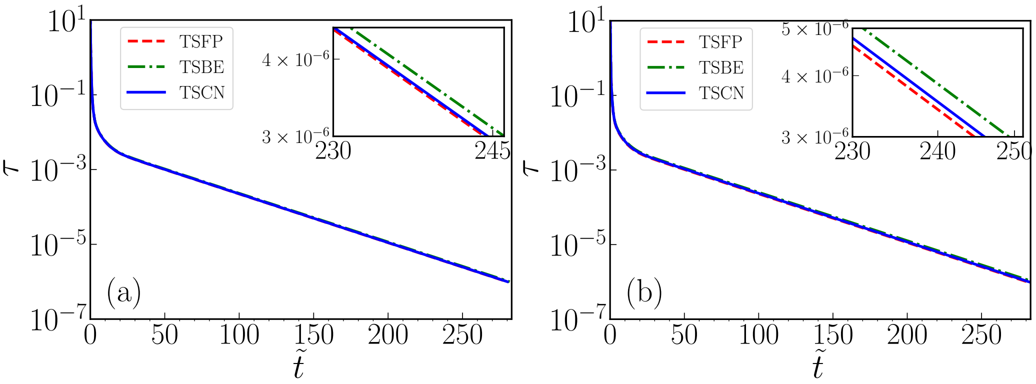

Figure 2.1: The variation of convergence criterion during an imaginary-time propagation to calculate the ground state of a q1D pseudospin-1/2 ^{87}Rb BEC with $g_{11} = 446.95$, $g_{22} = 402.26$, and $g_{12} = g_{21} = 491.65$. In (a), we have chosen $\Delta x = 0.1$ and $\Delta\tilde{t} = 0.01$, whereas for (b) $\Delta x = 0.2$ and $\Delta\tilde{t} = 0.02$.

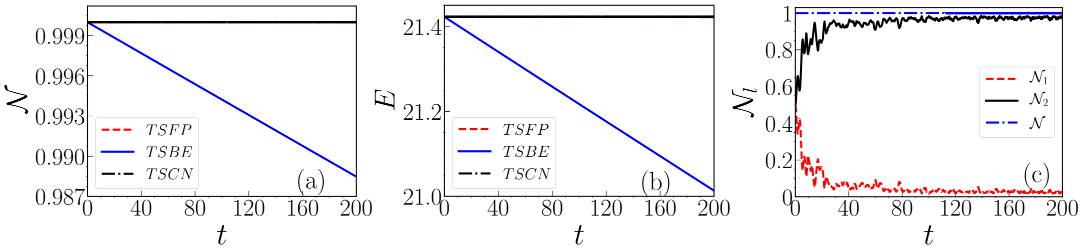

Figure 2.2: (a) Norm $\mathcal{N}$ as a function of time and (b) energy E as a function of time for the ground state solution of pseudospin-1/2 BEC of ^{87}Rb with $\gamma = \Omega_{\rm coh} = 0.5$. (c) Norm $\mathcal{N}$ and $\mathcal{N}_l$ as a function of time in realtime obtained for non-stationary initial solution using TSCN. The real-time evolution of the initial solution has been obtained using TSFP, TSBE, and TSCN with $\Delta x = 0.1$, $\Delta t = 0.005$, and the interaction parameters of the pseudospin-1/2 BEC are $g_{11} = 446.95$, $g_{22} = 402.26$, and $g_{12} = g_{21} = 491.65$.

$\gamma = \Omega_{\rm coh} = 0.5$ as the initial solution at $t = 0$ in real-time evolution. The variation of total norm and energy as a function of time obtained using TSFP, TSBE, and TSCN are shown in Fig. 2.2(a) and 2.2(b), respectively. The non-conservation of norm and hence energy in TSBE makes the method unsuitable to study any real-time dynamics. The dynamics of the ground state, a stationary state, is trivial in the sense that besides norm and energy, the expectation values of various operators are also conserved. Next, we consider the dynamics of a non-stationary state using TSCN. We first obtain a non-stationary state by solving CGPEs for the q1D ^{87}Rb with interaction strengths as defined in Eq. (2.69) and $\gamma = \Omega_{\rm coh} = 0.5$ under the constraint of zero polarization. The solution thus obtained is non-stationary and is then evolved in realtime (without any additional constraint) using TSCN. The variation of component norms and total norm as a function of time is shown in Fig. 2.2(c). The total norm $\mathcal{N}$ in TSCN is again conserved, illustrating the unitary time evolution.

2.5 Summary

In the first part of this chapter, we discussed the numerical algorithm using the Fourier pseudospectral method to solve the CGPEs for an SO-coupled spin-2 BEC which can be used to calculate the ground state solutions and/or the dynamics of homogeneous or trapped condensates. In the second part of the chapter, we discussed time-splitting Backward-Euler and Crank-Nicolson methods to study the SO-coupled CGPEs for pseudospinor BEC. Depending on the nature of the problem, without any loss of generality, we employed the Cartesian grid spanning either three-, two-, or one-dimensional space for numerical discretization. For some cases, we compared the ground state energies and the component density profiles calculated using the TSFP, TSBE, and TSCN methods. The numerical results for stationary states obtained with the three methods agree very well. In imaginary-time propagation, TSFP and TSCN exhibit faster convergence compared to TSBE. Moreover, the time evolution per TSCN is unitary, consistent with the underlying Hermitian Hamiltonian. This is not the case with TSBE, which results in non-unitary time evolution and thus renders the method unsuitable for studying any real-time dynamics. The numerical methods developed in this chapter can be easily extended to higher spin systems. The numerical methods provided in this chapter are discussed in Refs. [193,194].

Chapter 3

Rotating spin-orbit-coupled spinor BECs

As discussed in Sec. 1.2.1, one of the most important advances in the field of cold atom physics in the last decade has been an experimental demonstration of synthetic SO coupling in a spinor quantum gas [73–77], which has opened up new research direction in the field of quantum degenerate gases. The realization of SO-coupling paved the way to explore the interplay of an artificial non-Abelian gauge field resulting in SO-coupling and rotation, which itself is equivalent to an Abelian gauge potential. For an SO-coupled BEC, merely rotating the trapping potential will result in a time-dependent Hamiltonian, which can not have stationary vortex-lattice solutions [4]. This can be remedied by rotating both the (anisotropic) trap and the laser fields responsible for the creation of SO and coherent couplings, in which case the Hamiltonian in the rotating frame is time-independent [4].

In the literature on rotating SO-coupled spin-1 and spin-2 BECs discussed in Sec. 1.3, the rotation frequencies considered mostly have been within the range of small to moderate values. In this chapter, we aim to investigate the combined effect of interactions and SO couplings, particularly at high rotation frequencies for these higher spin systems. We examine systematically the combined effect of rotation and SO coupling in the spin-1 BECs with ferromagnetic or antiferromagnetic interactions and then broaden the investigation to a rotating SO-coupled spin-2 system with antiferromagnetic, cyclic, or ferromagnetic interactions. Specifically, we investigate the various effective potentials an atom in these SO-coupled spinor BECs may experience under the combined effect of SO coupling and rotation.

This chapter is organized as follows. The analytic solutions of the single-particle Hamiltonian corresponding to the SO-coupled spin-1 and spin-2 BECs under rotation are provided in Sec. 3.1. We present the mean-field CGPEs for a rotating SO-coupled spin-1 BEC in Sec. 3.2. The stationary-state solutions for the interacting SO-coupled ^{87}Rb and ^{23}Na spin-1 BECs in a rotating frame are discussed in Sec. 3.2.1. The response of the system is further explored through the computation of the spin expectation per particle as a function of rotation frequency in Sec. 3.3. The CGPEs for an SO-coupled spin-2 BEC in the rotating frame and the numerical solutions have been discussed in Sec. 3.4. In Sec. 3.5, we present a summary of the chapter.

3.1 Single-particle Hamiltonian

Under a q2D harmonic confinement, the Hamiltonian of an SO-coupled spin-f boson in the rotating frame in the dimensionless form is given by [113]

$$H_0 = \left[\frac{\hat{p}_x^2 + \hat{p}_y^2}{2} + V(x,y) - \Omega_{\rm rot} L_z\right]\mathbf{I} + \gamma_x S_x \hat{p}_x + \gamma_y S_y \hat{p}_y + \Omega_{\rm coh} S_x, \tag{3.1}$$

where $\hat{p}_\nu = -\imath\partial/\partial_\nu$ with $\nu = (x,y)$, $V(x,y) = (x^2+y^2)/2$ is an isotropic harmonic trapping potential, $\Omega_{\rm rot}$ is the angular frequency of rotation around z axis, γ_x and γ_y are the SO-coupling strengths, $\Omega_{\rm coh}$ is the coherent-coupling strength, $L_z = (x\hat{p}_y - y\hat{p}_x)$ is the z component of the angular-momentum operator, $\mathbf{I}$ is a $(2f+1)\times(2f+1)$ identity matrix, and S_ν is the irreducible representations of the angular momentum operator for a spin-f system. The units of length, time, energy, and energy eigenfunctions are considered to be $a_{\rm osc} = \sqrt{\hbar/(M\omega_x)}$, ω_x^{-1}, $\hbar\omega_x$, and $a_{\rm osc}^{-1}$, respectively, where M is the mass of the boson and ω_x is the harmonic oscillator frequency along x-direction. To delineate the combined effect of rotation, SO, and coherent couplings, we calculate the minimum-energy eigenfunctions and eigenenergies of the Hamiltonian for two analytically tractable cases:

$$\gamma_x \neq 0, \ \Omega_{\rm coh} \neq 0, \tag{3.2a}$$

$$\gamma_x = \gamma_y = \gamma \neq 0, \ \Omega_{\rm coh} = 0, \tag{3.2b}$$

where (3.2a) represents an experimentally realizable equal-strength mixture of Rashba and Dresselhaus couplings [75,76], which couples the spin with the linear momentum along the x-direction and the latter (3.2b) employs the Rashba SO coupling [68,195] which couples the spin with linear momentum along x-y plane.

3.1.1 Equal-strength mixture of Rashba and Dresselhaus couplings

The calculation of the eigen-spectrum of H_0 in the former case (3.2a) is facilitated by a unitary transformation, $H_0 \to U^\dagger H_0 U$ with

$$U = \frac{1}{2}\begin{pmatrix} 1 & -\sqrt{2} & 1 \\ \sqrt{2} & 0 & -\sqrt{2} \\ 1 & \sqrt{2} & 1 \end{pmatrix} \text{ and} \tag{3.3a}$$

$$U = \frac{1}{4}\begin{pmatrix} 1 & -2 & \sqrt{6} & -2 & 1 \\ 2 & -2 & 0 & 2 & -2 \\ \sqrt{6} & 0 & -2 & 0 & \sqrt{6} \\ 2 & 2 & 0 & -2 & -2 \\ 1 & 2 & \sqrt{6} & 2 & 1 \end{pmatrix}, \tag{3.3b}$$

for spin-1 and spin-2 systems, respectively. The operator U rotates the spin state about y axis in an anticlockwise direction by an angle $\pi/2$ [196]. The transformed Hamiltonian

$U^\dagger H_0 U = \mathrm{diag}\,(h_f, h_{f-1}, \ldots, h_{-f})$, where $\mathrm{diag}\,(\ldots)$ stands for a $2f+1 \times 2f+1$ diagonal matrix (operator). The operators h_j are

$$\begin{aligned} h_j =& \frac{(\hat{p}_x + \frac{j\gamma_x}{1-\Omega_{\rm rot}^2} + \Omega_{\rm rot}\bar{y})^2}{2} + \frac{(\hat{p}_{\bar{y}} - \Omega_{\rm rot}x)^2}{2} + (1-\Omega_{\rm rot}^2)\frac{(x^2+\bar{y}^2)}{2} \\ & - \frac{j^2\gamma_x^2}{2(1-\Omega_{\rm rot}^2)} + j\Omega_{\rm coh}, \end{aligned} \tag{3.4}$$

where $j = f, f-1, \ldots, -f$, $\bar{y} = y - j\gamma_x\Omega_{\rm rot}/(1-\Omega_{\rm rot}^2)$ and $\hat{p}_{\bar{y}} = -\iota\partial/\partial\bar{y}$ is the canonical conjugate momentum of $\bar{y}$. The decoupled eigenvalue equation for h_j is $h_j\phi_j(x,\bar{y}) = E_j\phi_j(x,\bar{y})$ which can be simplified by substituting $\phi_j(x,\bar{y}) = \bar{\phi}_j(x,\bar{y})\exp[-\iota j\gamma_x x/(1-\Omega_{\rm rot}^2)]$ to obtain

$$\left[\frac{\hat{p}_x^2+\hat{p}_{\bar{y}}^2}{2} + \frac{x^2+\bar{y}^2}{2} - \Omega_{\rm rot}(x\hat{p}_{\bar{y}} - \bar{y}\hat{p}_x) + j\Omega_{\rm coh}\right]\bar{\phi}_j(x,\bar{y}) \;=\; E_j\bar{\phi}_j(x,\bar{y}). \tag{3.5}$$

The Hamiltonian on the left-hand side of Eq. (3.5), barring the constant terms, is that of a two-dimensional isotropic harmonic oscillator under rotation. It is to be noted that the eigenfunctions of this Hamiltonian are also the eigenfunctions of the Hamiltonian representing an isotropic harmonic oscillator in the absence of rotation, which commutes with L_z [196]. The ground state eigenenergy is, therefore, given by

$$E_j = \frac{2(1+j\Omega_{\rm coh})(1-\Omega_{\rm rot}^2) - j^2\gamma_x^2}{2(1-\Omega_{\rm rot}^2)}, \tag{3.6}$$

and the corresponding eigenstate is $\bar{\phi}_j(x,\bar{y}) = \exp[(-x^2-\bar{y}^2)/2]/\sqrt{\pi}$. On the x-y plane, we thus obtain

$$\phi_j(x,y) = \frac{1}{\sqrt{\pi}}\exp\left[-\frac{x^2 + \left(y - \frac{j\gamma_x\Omega_{\rm rot}}{1-\Omega_{\rm rot}^2}\right)^2}{2} - \iota\frac{j\gamma_x}{1-\Omega_{\rm rot}^2}x\right]. \tag{3.7}$$

The $2f+1$ minimum-energy vector eigenfunctions of the original Hamiltonian H_0 with eigenenergies E_j can now simply be written as $\Phi_j(x,y) = \phi_j(x,y)U\zeta_j$, where U and $\phi_j(x,y)$ are defined in Eqs. (3.3a), (3.3b) and (3.7), respectively. Here ζ_j are the $2f+1$ eigenvectors of S_z. In the absence of coherent coupling, $\Omega_{\rm coh} = 0$, the eigenfunctions $\Phi_{-f}(x,y)$ and $\Phi_{+f}(x,y)$ become degenerate having the least energy. Under these considerations, the principle of linear superposition further admits $c_+\Phi_{+f} + c_-\Phi_{-f}$ to be a possible degenerate eigenfunction subject to the constraint $|c_+|^2 + |c_-|^2 = 1$. In the presence of infinitesimally small repulsive interactions, say spin-independent interactions, the interaction energy is minimized if $|c_+| = |c_-| = 1/\sqrt{2}$ resulting in a equal-strength mixture of $\Phi_{\pm f}(x,y)$. The resultant density, $\left[|\phi_{+f}(x,y)|^2 + |\phi_{-f}(x,y)|^2\right]/2$, is bimodal with equal-height peaks at $(0, \pm\gamma_x f\Omega_{\rm rot}/(1-\Omega_{\rm rot}^2))$; this is indeed reflective of an effective two-well potential experienced by the boson. The presence of coherent coupling $\Omega_{\rm coh} \neq 0$, however, results in the lifting of the degeneracy between $\Phi_{-f}(x,y)$ and $\Phi_{+f}(x,y)$ with

$\Delta E = E_{+f} - E_{-f} = 2f\Omega_{\rm coh}$.

The exact effective potential experienced by the boson can also be computed through vector and scalar potentials [112]. To identify these potentials for the former case (3.2a), we rewrite h_j in Eq. (3.4) as

$$h_j = \frac{(p_x - A_x^j)^2}{2} + \frac{(p_y - A_y^j)^2}{2} + W_j(x,y) + V(x,y), \tag{3.8}$$

where $A_x^j = -j\gamma_x - \Omega_{\rm rot} y$, $\quad A_y^j = \Omega_{\rm rot} x$ are the x and y components of the vector potential, and the scalar potential $W_j(x,y) = \left[2j\Omega_{\rm coh} - j^2\gamma^2 - 2j\gamma\Omega_{\rm rot} y - \Omega_{\rm rot}^2\left(x^2+y^2\right)\right]/2$. With these definitions, the effective potentials [112] for $j = f, f-1, \ldots, -f$ magnetic sublevels are given as

$$V_{\rm eff}^j(x,y) = \frac{1}{2}\left[(1-\Omega_{\rm rot}^2)(x^2+y^2) - j^2\gamma_x^2 + 2j\Omega_{\rm coh} - 2j\gamma_x\Omega_{\rm rot} y\right]. \tag{3.9}$$

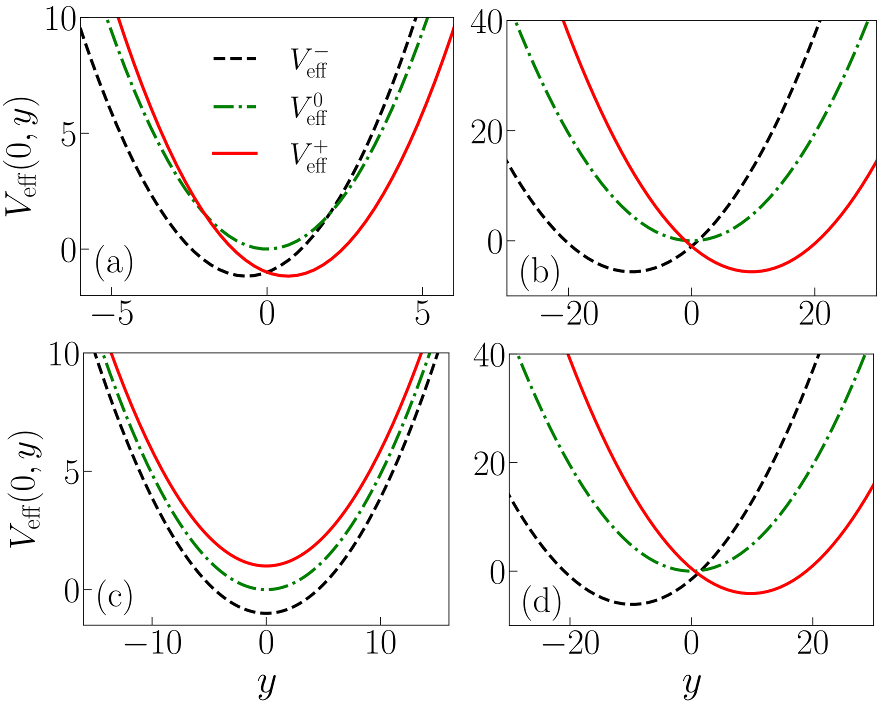

Figure 3.1: Sketch of the effective potential $V_{\rm eff}^j$ (experienced by the three eigenvectors of S_z), viz. Eq. (3.9), along y-axis: (a) $\gamma_x = 1,\ \gamma_y = 0,\ \Omega_{\rm coh} = 0$, and $\Omega_{\rm rot} = 0.5$, (b) $\gamma_x = 1,\ \gamma_y = 0,\ \Omega_{\rm coh} = 0$, and $\Omega_{\rm rot} = 0.95$, (c) $\gamma_x = 0,\ \gamma_y = 0,\ \Omega_{\rm coh} = 1$, and $\Omega_{\rm rot} = 0.95$, and (d) $\gamma_x = 1,\ \gamma_y = 0,\ \Omega_{\rm coh} = 1$, and $\Omega_{\rm rot} = 0.95$.

From Eq. (3.9), for $f = 1$, the $V_{\rm eff}^{+1}(x,y)$ and $V_{\rm eff}^{-1}(x,y)$ cross at $y = \Omega_{\rm coh}/\gamma_x\Omega_{\rm rot}$ for $\gamma_x \neq 0$ and $\Omega_{\rm rot} \neq 0$. In the region, $y < \Omega_{\rm coh}/\gamma_x\Omega_{\rm rot}$, $V_{\rm eff}^{-1}$ is lower than than the other two and with a minima at $\gamma_x\Omega_{\rm rot}/(1-\Omega_{\rm rot}^2)$, whereas for $y > \Omega_{\rm coh}/\gamma_x\Omega_{\rm rot}$, $V_{\rm eff}^{+1}$ is the low lying potential curve with a minima at $-\gamma_x\Omega_{\rm rot}/(1-\Omega_{\rm rot}^2)$. Which are also the positions of the density maxima of $|\Phi_{\pm 1}(x,y)|^2$, as discussed earlier. We illustrate the effective potential energy curves for the two representative cases with $\gamma_x = 1$ and

$\gamma_y = \Omega_{\rm coh} = 0$: under a moderate rotation frequency ($\Omega_{\rm rot} = 0.5$) in Fig. 3.1(a) and a high rotation frequency ($\Omega_{\rm rot} = 0.95$) in Fig. 3.1(b) . The potentials thus experienced by the boson are effectively equivalent to symmetric double-well potentials with minima occurring at ($x = 0, y = \mp 0.67$) and ($x = 0, y = \mp 9.74$), respectively. Depending on the values of γ_x and γ_y, the presence of the coherent coupling modifies the effective potential landscape in different ways, for example, with $\Omega_{\rm coh} = 1$ it is harmonic potential for $\gamma_x = \gamma_y = 0$ with minima at origin and an asymmetric double-well potential for $\gamma_x = 1$ and $\gamma_y = 0$ with a global minima at ($x = 0, y = -9.74$). These are, respectively, shown in Figs. 3.1(c) and (d). From Eq. (3.9), for $f = 2$, $V_{\rm eff}^{+2}(x, y)$ and $V_{\rm eff}^{-2}(x, y)$ overlap at ($x = 0, y = 0$) for

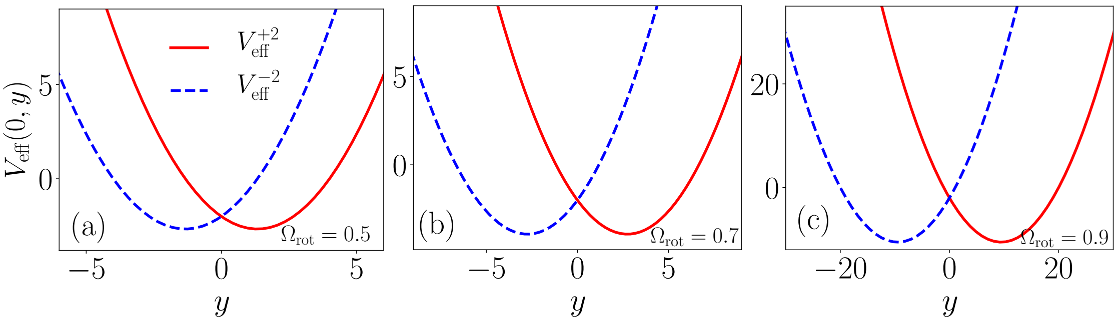

Figure 3.2: Effective potentials $V_{\rm eff}^{\pm 2}(0, y)$ for $\gamma_x = 1$, $\Omega_{\rm coh} = 0$: (a) $\Omega_{\rm rot} = 0.5$, (b) $\Omega_{\rm rot} = 0.7$, and (c) $\Omega_{\rm rot} = 0.9$. The potentials incurred by boson are effectively equivalent to symmetric double-well potentials with minima at ($x = 0, y = \mp 1.33$), ($x = 0, y = \mp 2.74$), and ($x = 0, y = \mp 9.47$) for $\Omega_{\rm rot} = 0.5, 0.7$, and 0.9, respectively.

$\Omega_{\rm coh} = 0$ as shown in Figs. 3.2(a)-(c) for $\Omega_{\rm rot} = 0.5, 0.7$, and 0.9, respectively.

3.1.2 Rashba SO coupling

For the latter case (3.2b), namely $\gamma \neq 0$ and $\Omega_{\rm coh} = 0$, the eigenvalue problem for the Hamiltonian H_0 is not exactly solvable. We, therefore, use the variational method to calculate an approximate minimum-energy solution. For that, we consider the following variational *ansatz* in polar coordinates for the spin-1 system

$$\Phi_{\rm var}(r, \phi) = \frac{\exp\left(-\frac{r^2}{2\sigma^2}\right)}{\sqrt{\pi\sigma^{2n+4}\Gamma(n+2)}} \times (\iota A_1 r^{|n|} e^{\iota n\phi}, -A_2 r^{|n+1|} e^{\iota(n+1)\phi}, \iota A_3 r^{|n+2|} e^{\iota(n+2)\phi})^T, \tag{3.10}$$

where A_1, A_2, A_3 are the variational amplitudes, σ is the variational width of the *ansatz*, and n is a variational integer. In the absence of rotation, the ground state of the single particle Hamiltonian is a circularly symmetric $(-1, 0, +1)$ type multi-ring solution with ± 1 components hosting ∓ 1 phase-singularities [81,82]. This allows us to fix the integer $n >= -1$. The normalization condition imposes the constraint

$$\left[\frac{A_1^2\Gamma(|n|+1)}{\sigma^{2(1-|n|+n)}\Gamma(n+2)}\right] + \left[A_3^2(n+2)\sigma^2 + A_2^2\right] = 1, \tag{3.11}$$

on the variational parameters $A_1, A_2, A_3, n,$ and σ. The variational energy in this case is

$$E_{\rm var}(A_1, A_2, A_3, n, \sigma) = \frac{\sigma^{-2(n+2)}}{2\Gamma(n+2)}[(\sqrt{2}A_1A_2\gamma(-|n|+3n+2)\sigma^{|n|+n+2}\Gamma\left(\frac{1}{2}\{n+|n|+2\}\right)$$
$$+ A_1^2\sigma^{2|n|}\Gamma(|n|+1)\{(\sigma^4+1)|n| - 2n\sigma^2\Omega_{\rm rot} + \sigma^4 + 1\} + (n+1)\sigma^{2n+2}\Gamma(n+1)$$
$$\{-2\sqrt{2}A_2A_3\gamma(n+2)\sigma^2 + A_3^2(n+2)\sigma^2(n\sigma^4 - 2n\sigma^2\Omega_{\rm rot} + n + 3\sigma^4 - 4\sigma^2\Omega + 3)$$
$$+ A_2^2(n\sigma^4 - 2n\sigma^2\Omega_{\rm rot} + n + 2\sigma^4 - 2\sigma^2\Omega_{\rm rot} + 2)\}]. \quad (3.12)$$

This energy can be minimized with respect to all variational parameters subject to the constraint in Eq. (3.11) to fix the variational parameters. To illustrate the validity of the variational method in this case, we consider three sets of parameters

$$\gamma = 0.5, \quad \Omega_{\rm coh} = 0, \quad \Omega_{\rm rot} = 0.95, \quad (3.13a)$$
$$\gamma = 1, \quad \Omega_{\rm coh} = 0, \quad \Omega_{\rm rot} = 0.5, \quad (3.13b)$$
$$\gamma = 1, \quad \Omega_{\rm coh} = 0, \quad \Omega_{\rm rot} = 0.95. \quad (3.13c)$$

The minimization of (3.12) results in $(A_1, A_2, A_3, n, \sigma) =$ $(-2.463,\ 0.707,\ 0.099,\ 24,\ 0.975)$ for parameters' set (3.13a), $(A_1, A_2, A_3, n, \sigma) = (0.517,\ -0.675,\ -0.336,\ 0,\ 0.828)$ for (3.13b), and $(A_1, A_2, A_3, n, \sigma) = (-4.861,\ 0.707,\ 0.051,\ 98,\ 0.975)$ for (3.13c). The comparison of variational, $\rho_{\rm var}(r) = |\Phi_{\rm var}(r,\phi)^2|$, and exact numerically evaluated single-particle density profiles, $\rho_{\rm num}(r)$, for (3.13a), (3.13b), and (3.13c) are shown in Figs. 3.3(a), 3.3(b), and 3.3(c), respectively. The charges of phase singularities in the component wavefunctions obtained with the variational analysis, i.e., $(+24, +25, +26)$ for set (3.13a), $(0, +1, +2)$ for set (3.13b) and $(+98, +99, +100)$ for (3.13c) match with the exact numerical results. For the sets (3.13a), (3.13b), and (3.13c), the peaks of total variational densities lie along circles of radii 4.88, 0.40 and 9.70, respectively, and are reflective of the effective toroidal

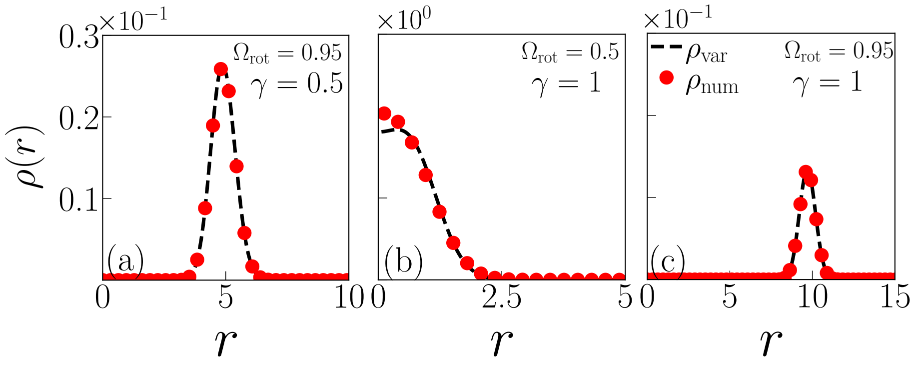

Figure 3.3: Total single-particle densities corresponding to variational ($\rho_{\rm var}$) and exact numerical solution ($\rho_{\rm num}$) of the eigen-value problem for (a) $\gamma = 0.5$, $\Omega_{\rm coh} = 0$, $\Omega_{\rm rot} = 0.95$; (b) $\gamma = 1$, $\Omega_{\rm coh} = 0$, $\Omega_{\rm rot} = 0.5$; and (c) $\gamma = 1$, $\Omega_{\rm coh} = 0$, $\Omega_{\rm rot} = 0.95$. The charges of phase singularities in the component wavefunctions corresponding to the total densities in (a), (b) and (c) are (+24,+25,+26), (0,+1,+2), and (+98,+99,+100), respectively.

potential experienced by the boson.

For a spin-2 BEC, we consider Rashba SO coupling as $\gamma(S_x\hat{p}_y - S_y\hat{p}_x)$, which under a unitary transformation transforming $S_x \rightarrow -S_y$ and $S_y \rightarrow S_x$ is equivalent to the $\gamma(S_x\hat{p}_x + S_y\hat{p}_y)$ [109]. The suitable variational *ansatz* in polar coordinates is

$$\Phi_{\text{var}}(r,\phi) = \frac{\exp\left(\frac{r^2}{2\sigma^2}\right)}{\sqrt{\pi\sigma^{2n+4}\Gamma(n+2)}} \times (A_1 r^{|n|} e^{\iota n\phi}, A_2 r^{|n+1|} e^{\iota(n+1)\phi}, A_3 r^{|n+2|} e^{\iota(n+2)\phi},$$
$$A_4 r^{|n+3|} e^{\iota(n+3)\phi}, A_5 r^{|n+4|} e^{\iota(n+4)\phi})^T, \tag{3.14}$$

where the various symbols have the same meaning as in Eq. (3.10).

The normalization condition and the variational energy are

$$(n+2)\sigma^2[(n+3)\sigma^2\{A_5^2(n+4)\sigma^2 + A_4^2\} + A_3^2] + A_2^2 + \frac{A_1^2}{(n+1)\sigma^2} = 1, \tag{3.15}$$

$$E_{\text{var}}(A_1,A_2,A_3,A_4,A_5,n,\sigma) = \frac{1}{2(n+1)\sigma^4}[4A_1A_2\gamma(n+1)\sigma^2 + (n+1)\sigma^2\{2\sqrt{6}A_2A_3\gamma(n+2)\sigma^2$$
$$+ (n+2)\sigma^2(2\sqrt{6}A_3A_4\gamma(n+3)\sigma^2 + (n+3)\sigma^2(4A_4A_5\gamma(n+4)\sigma^2 + A_5^2(n+4)\sigma^2(\{n+5\}$$
$$(\sigma^4+1) - 2(n+4)\sigma^2\Omega_{\text{rot}}) + A_4^2\{(n+4)(\sigma^4+1) - 2(n+3)\sigma^2\Omega_{\text{rot}}\}) + A_3^2\{(n+3)(\sigma^4+1) -$$
$$2(n+2)\sigma^2\Omega_{\text{rot}}\}) + A_2^2(\{n+2\}(\sigma^4+1) - 2(n+1)\sigma^2\Omega_{\text{rot}})\} + A_1^2\{(n+1)(\sigma^4+1) - 2n\sigma^2\Omega_{\text{rot}}\}]. \tag{3.16}$$

As an example, to check the validity of the variational method, we choose $(\gamma = 1, \Omega_{\text{rot}} = 0.9)$, and the minimization of (3.16) gives $(A_1, A_2, A_3, A_4, A_5, n, \sigma) = (-2.3728, 0.5012, -0.0645, 0.0055, -0.0002, 98, 0.9491)$. The variational $\rho_{\text{var}}(r)$, and exact single-particle density profile $\rho_{\text{num}}(r)$ agree with each other; the peak of total variational density lies along a circle of radius 9.47 (not shown here).

Although, the variational *ansatz* are reminiscent of the vortex-bright solitons which emerge as the ground states of SO-coupled spinor BECs with attractive mean-field interactions [84,85], the nature of the mean-field interactions (whether attractive or repulsive) and the emergent solutions (whether self-trapped or confined by a net trapping potential) are starkly different. In this chapter, we consider the SO-coupled spin-f BECs interacting with net repulsive mean-field interactions under net harmonic confinement. Hence, the single-particle solutions discussed in this section and the multi-particle solutions of the CGPEs in the following Section are not self-trapped or bright solitons.

3.2 Rotating SO-coupled spin-1 BEC

In a typical experiment, the BEC can have atom numbers ranging from a few thousand to up to a few tens of a million, which primarily interact via s-wave scattering. At temperatures very close to absolute zero, this ultra-dilute quantum degenerate system is usually studied using a mean-field approximation that neglects quantum and thermal fluctuations. In the mean-field approximation, a rotating SO-coupled spin-1 BEC in a q2D harmonic trapping potential $V(x, y)$ can be described by three CGPEs [1,81], which in the dimensionless form are

$$\begin{aligned}\iota\frac{\partial\psi_{\pm1}}{\partial t} &= \mathcal{H}\psi_{\pm1} + c_1(\rho_0 \pm \rho_-)\psi_{\pm1} + c_1\psi_{\mp1}^*\psi_0^2 - \frac{\iota}{\sqrt{2}}\left(\gamma_x\partial_x\psi_0 \mp \iota\gamma_y\partial_y\psi_0\right)\\ &\quad + \frac{\Omega_{\rm coh}}{\sqrt{2}}\psi_0, \qquad (3.17a)\\ \iota\frac{\partial\psi_0}{\partial t} &= \mathcal{H}\psi_0 + c_1\rho_+\psi_0 + 2c_1\psi_{+1}\psi_{-1}\psi_0^* - \iota\frac{\gamma_x}{\sqrt{2}}\partial_x\left(\psi_{+1}+\psi_{-1}\right) + \frac{\gamma_y}{\sqrt{2}}\partial_y\left(\psi_{+1}-\psi_{-1}\right)\\ &\quad + \frac{\Omega_{\rm coh}}{\sqrt{2}}(\psi_{+1}+\psi_{-1}), \qquad (3.17b)\end{aligned}$$

where

$$\mathcal{H} = \sum_{\nu=x,y}\frac{\hat{p}_\nu^2}{2} + V(x,y) + c_0\rho - \Omega_{\rm rot}L_z, \rho = \sum_{j=\pm1,0}\rho_j,\ \rho_j = |\psi_j|^2,\ \rho_\pm = \rho_{+1} \pm \rho_{-1}, \tag{3.18}$$

c_0 and c_1 are interaction parameters defined as

$$c_0 = \sqrt{8\pi\alpha}\frac{N(a_0+2a_2)}{3a_{\rm osc}},\ c_1 = \sqrt{8\pi\alpha}\frac{N(a_2-a_0)}{3a_{\rm osc}}, \tag{3.19}$$

where α is the ratio of trapping frequency along the axial direction to the radial x direction, N is the total number of atoms in the BEC, and a_0 and a_2 are the s-wave scattering lengths in total spin 0 and 2 channels, respectively. The CGPEs, viz. (3.17a) and (3.17b), can be numerically solved using, for instance, time-splitting methods discussed in the previous chapter.

3.2.1 Numerical solutions of CGPEs

We consider 10^5 atoms of spin-1 BECs like ^{87}Rb and ^{23}Na in an isotropic q2D harmonic trap with $\alpha = 10$. The trapping frequencies are $\omega_x = \omega_y = 2\pi \times 10$ Hz resulting in $a_{\rm osc}^{\rm Rb} = 3.41\ \mu$m and $a_{\rm osc}^{\rm Na} = 6.63\ \mu$m, respectively, for ^{87}Rb and ^{23}Na spinor BECs. The ferromagnetic ^{87}Rb has $a_0 = 101.8a_B$ and $a_2 = 101.4a_B$ [197], and anti-ferromagnetic ^{23}Na has $a_0 = 50a_B$ and $a_2 = 55.01a_B$ [198], where a_B is the Bohr radius. The resultant dimensionless interaction strengths for ^{87}Rb are $c_0 = 2482.21$ and $c_1 = -11.47$, and the same for ^{23}Na are $c_0 = 674.91$ and $c_1 = 21.12$. As $c_0 \gg c_1$, both the systems are repulsively interacting spinor BECs. We solve CGPEs (3.17a) and (3.17b) on a two-dimensional 512×512 spatial grid with a spatial-step size $\Delta x = \Delta y = 0.1$ and a temporal step size $\Delta t = 0.005$ using a time-splitting Fourier pseudospectral method discussed in the previous chapter. We calculate the stationary-state solutions by solving the CGPEs in imaginary time with an apt initial guess solution. In order to study the vortex-lattice states that can emerge as the minimum energy solutions of an SO-coupled spin-1 BEC in a rotating frame, we consider the following SO-coupling strengths

$$\gamma_x = 1, \gamma_y = 0; \quad \gamma = 0.5; \quad \gamma = 1, \tag{3.20}$$

where as defined earlier $\gamma = \gamma_x = \gamma_y$.

We first study the rotating SO-coupled ^{87}Rb and ^{23}Na spinor BECs with these SO-coupling strengths *without* coherent coupling. For this, we use the non-rotated ground states as the apt initial guess solutions to evolve the CGPEs (3.17a) and (3.17b) in imaginary time with $\Omega_{\rm rot} \neq 0$. For $\gamma_x = 1$, $\gamma_y = 0$, the ground state is a plane-wave phase [81] for ^{87}Rb and a stripe phase for ^{23}Na [199]. The plane-wave phase, whose phase structure is identical to a single plane-wave is the ground state phase for $c_1 < 0$ as it ensures $|\mathbf{f}(\mathbf{r})|^2 = 1$, where $\mathbf{f}(\mathbf{r}) = \mathbf{F}(\mathbf{r})/\rho(\mathbf{r})$. In contrast to the plane-wave phase the stripe phase corresponds to the superposition of the two plane waves yielding zero magnetization, i.e. $|\mathbf{f}(\mathbf{r})|^2 = 0$ [81]. At small rotation frequencies for $\gamma_x = 1$ and $\gamma_y = 0$, the phase-singularities (vortices) in the component wave functions exclusively align along the x-axis. The central chain of holes in the individual component densities arising due to these phase-singularities with $\Omega_{\rm rot} = 0.5$ is evident in Fig. 3.4(A) for ^{87}Rb and Fig. 3.4(C) for ^{23}Na.

At still higher rotation frequency of $\Omega_{\rm rot} = 0.95$, the majority of vortices arrange themselves on both sides of the central chain of vortices as shown in Figs. 3.4(B) and 3.4(D) for ^{87}Rb and ^{23}Na, respectively. The appearance of central chain of vortices, which appears along the line of the intersection of $V_{\rm eff}^{+1}(x, y)$ and $V_{\rm eff}^{-1}(x, y)$, is a generic feature of these systems with a sufficiently strong one-dimensional SO coupling [120,200]. The density is lower along this line of intersection of the effective potential curves, and it is energetically favorable for the vortices to align along this line, especially at the lower rotation frequencies. In both systems, the symmetric effective double-well potential leads to the condensate occupying the pairs of potential minima at $(x = 0, y = \pm 0.67)$ and $(x = 0, y = \pm 9.74)$, respectively, when rotated with $\Omega_{\rm rot} = 0.5$ and 0.95. This can be seen more vividly in the coarse-grained total density defined as $\tilde{\rho}(\mathbf{r}) = \int C(\mathbf{r} - \mathbf{r}')\rho(\mathbf{r}')d\mathbf{r}'$, where $C(\mathbf{r} - \mathbf{r}')$ is a normalized Gaussian with a width larger than the average inter-vortex separation. The coarse-grained total density peaks at the minima of the effective potentials. To illustrate, we refer the reader to $\tilde{\rho}(\mathbf{r})$ in Figs. 3.5(A) and 3.5(B) corresponding to the total density in Figs. 3.4(A) and 3.4(B), respectively. The $\tilde{\rho}(\mathbf{r})$ peaks at $(x = 0, y = \pm 0.6)$ and $(x = 0, y = \pm 9.7)$, respectively, in the two cases. The role of effective potential on the ground-state solution, say $(\psi_{+1}, \psi_0, \psi_{-1})^T$, becomes obvious if one considers the unitary transformation $(\phi_{+1}, \phi_0, \phi_{-1})^T = U^\dagger(\psi_{+1}, \psi_0, \psi_{-1})^T$, where component wave-function ϕ_j is subjected to an effective potential $V_{\rm eff}^j(x, y)$ as discussed in Sec. 3.1. The component densities obtained by transforming the solutions shown in Figs. 3.4(C) and 3.4(D) for ^{23}Na, for instance, are shown in Figs. 3.6(A) and 3.6(B), which as discussed in the Sec. 3.1 are the solutions corresponding to $\gamma_x S_z p_x$ coupling in the mean-field model. The coarse-grained peak values of densities of $j = \pm 1$ components (which are not shown here) occur at $(0, \pm 0.6)$ and $(0, \pm 9.7)$ when rotated with

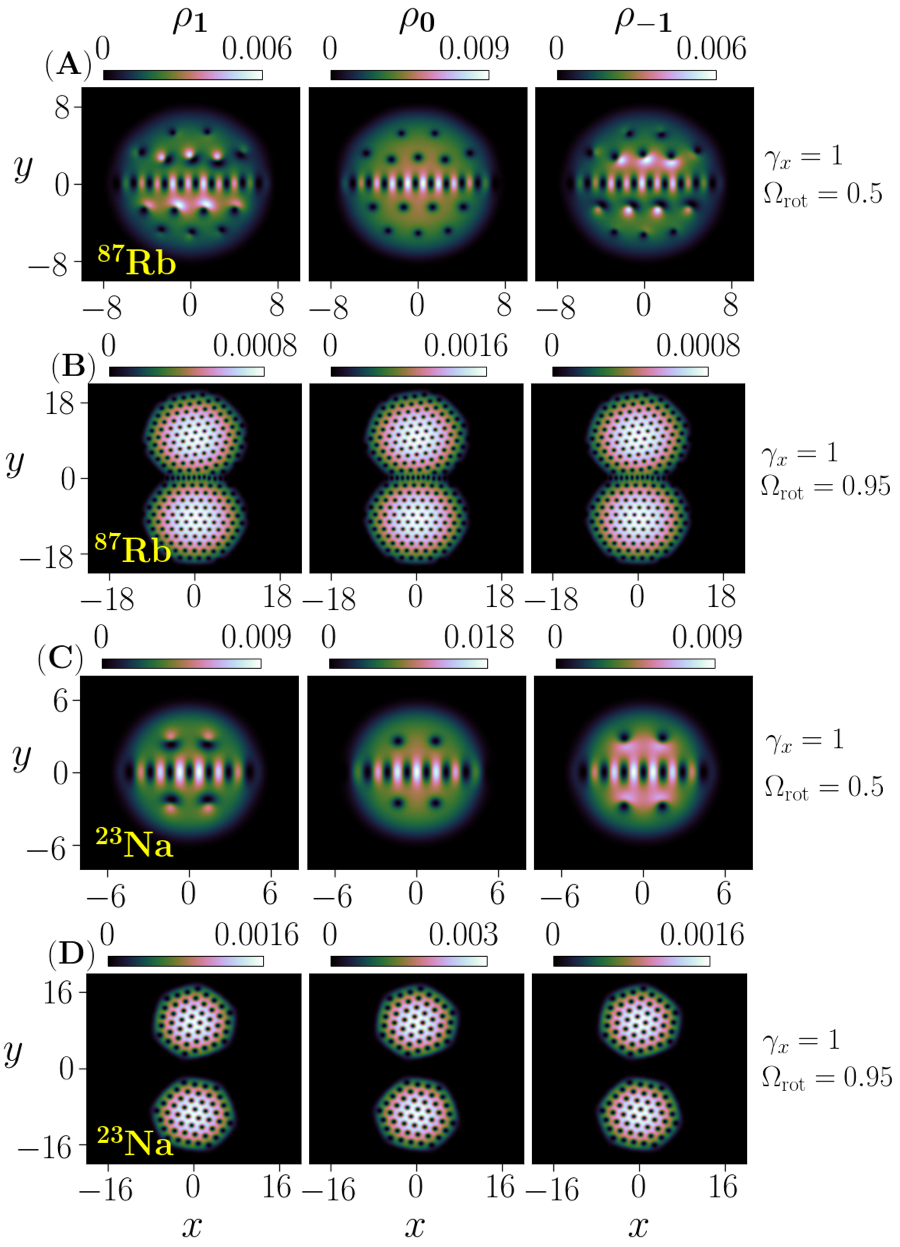

Figure 3.4: Equilibrium density profiles of the individual components of the SO-coupled ^{87}Rb spin-1 BEC with $c_0 = 2482.21$, $c_1 = -11.47$, $\gamma_x = 1$, and $\gamma_y = \Omega_{\rm coh} = 0$: (A) with $\Omega_{\rm rot} = 0.5$ and (B) with $\Omega_{\rm rot} = 0.95$. Similarly, (C) and (D) show the component densities for ^{23}Na with $c_0 = 674.91$ and $c_1 = 21.12$. The spatial coordinates and densities are in the units of $a_{\rm osc}$ and $a_{\rm osc}^{-2}$, respectively, where $a_{\rm osc} = 3.41$ μm for ^{87}Rb and 6.63 μm for ^{23}Na.

$\Omega_{\rm rot} = 0.5$ and 0.95 are in agreement with the effective potentials in Figs. 3.1(a) and 3.1(b), respectively. In the absence of rotation, $\gamma_x S_z p_x$ SO coupling favors miscibility of $j = \pm 1$ components for anti-ferromagnetic interactions, whereas it leads to phase-separation if the coupling strength is above a critical value for ferromagnetic interactions [199]. In the presence of rotation, the effective potential can lead to the phase-separation not only for a ferromagnetic ^{87}Rb (not shown here) but also for an antiferromagnetic ^{23}Na as is seen in the component density profiles in Figs. 3.6(A) and 3.6(B) for ^{23}Na. The $j = 0$ component

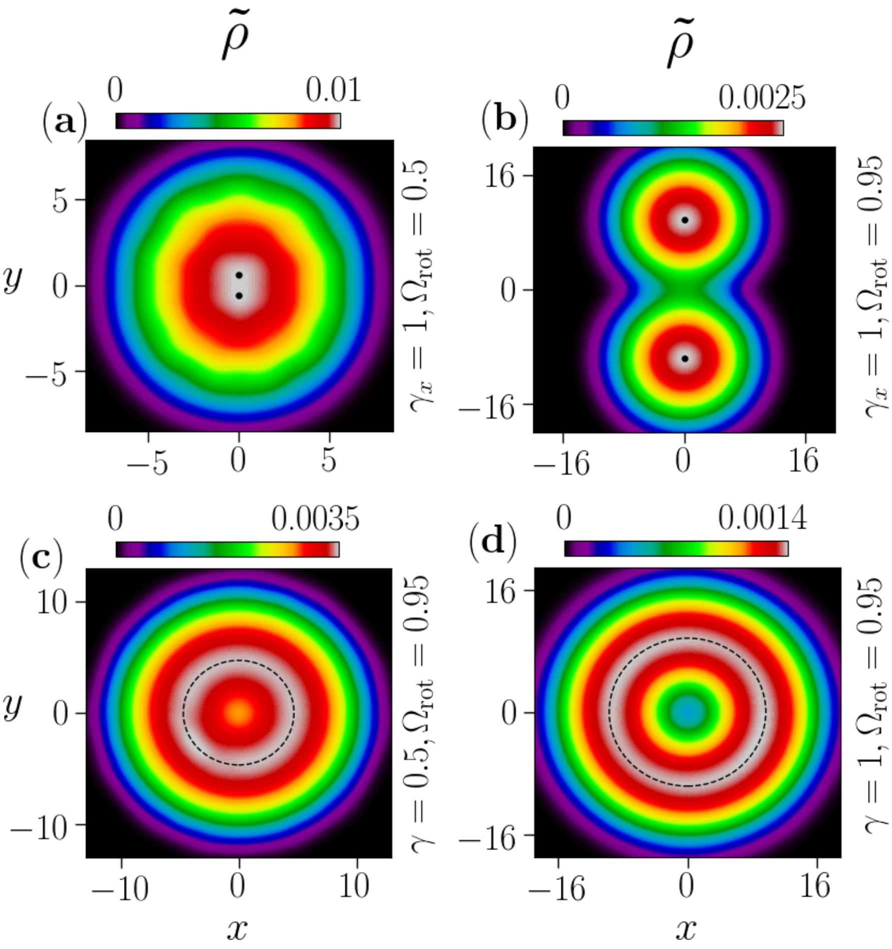

Figure 3.5: (a) and (b), respectively, show the coarse-grained densities $\tilde{\rho}(\mathbf{r})$ corresponding to the total densities in Figs. 3.4(A) and (B); the peak values of the coarse-grained densities at $(x = 0, y = \pm 0.6)$ and $(x = 0, y = \pm 9.7)$ are marked by dots. Similarly, (c) and (d), respectively, show $\tilde{\rho}(\mathbf{r})$ corresponding to the solutions in Figs. 3.7(B) and (D) and the respective peaks of $\tilde{\rho}(\mathbf{r})$ are marked by dashed circles of radii 4.7 and 9.7. The spatial coordinates and densities are in the units of $a_{\rm osc}$ and $a_{\rm osc}^{-2}$, respectively, where $a_{\rm osc} = 3.41$ μm.

occupies the cores of vortices in $j = \pm 1$ component at $\Omega_{\rm rot} = 0.5$ in Fig. 3.6(A). With an increase in rotation frequency, the number of atoms in $j = \pm 1$ components keeps on increasing at the cost of atoms in $j = 0$ component. Hence, at a larger rotation frequency of $\Omega_{\rm rot} = 0.95$ in Fig. 3.6(B), there are no atoms in the $j = 0$ component. Another consequence of the phase-separation is that the spin expectation per particle (which is independent of rotation in spin space) tends to approach one for all the results shown in Fig. 3.6 and consequently in Fig. 3.4. Thus, $\gamma_x S_z p_x$ SO coupling provides a simpler description of the results in Fig. 3.4.

Next for isotropic SO coupling with $\gamma = 0.5$ and $\Omega_{\rm rot} = 0.5$, the small number of vortices which nucleate are unable to crystallize in a triangular vortex-lattice pattern as shown in Figs. 3.7(A) and 3.7(E) for ^{87}Rb and ^{23}Na, respectively, which are consistent with the observations in Refs. [19,121]. The vortex patterns in the component densities near

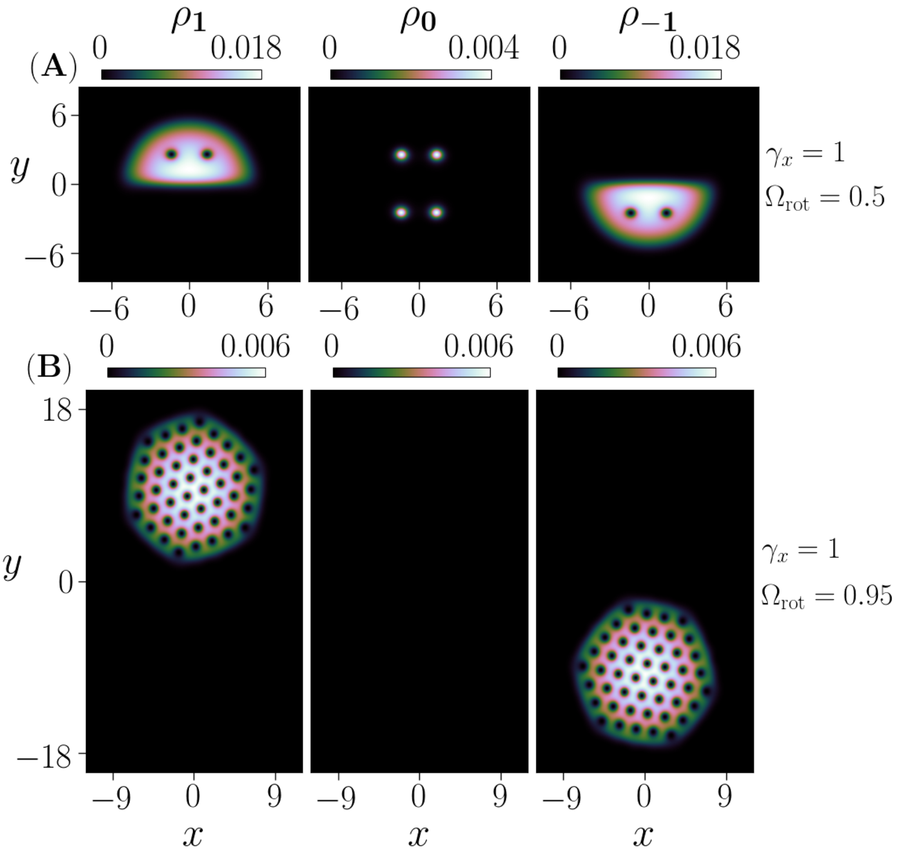

Figure 3.6: (A) and (B) are the individual component densities of the stationary SO-coupled spin-1 BECs of ^{23}Na corresponding to $H_{\text{SOC}} = \gamma_x p_x S_z$ for $\gamma_x = 1$ with $\Omega_{\text{rot}} = 0.5$ and $\Omega_{\text{rot}} = 0.95$, respectively. The $j = 0$ component is fully absent in (B). These solutions have been obtained by operating $U^\dagger$ on the solutions corresponding to $H_{\text{SOC}} = \gamma_x p_x S_x$ shown in Figs. 3.4(C) and Figs. 3.4(D) for ^{23}Na BEC. The spatial coordinates and densities are in the units of a_{osc} and a_{osc}^{-2}, respectively, where $a_{\text{osc}} = 6.63\ \mu$m for ^{23}Na.

the center in Fig. 3.7(E) resemble square lattices consistent with a similar observation in Ref. [121]. The two condensates rotated at a high rotation frequency $\Omega_{\text{rot}} = 0.95$ are shown in Figs. 3.7(B) and 3.7(F); here, the phase profiles of both the condensates (which are not shown) reveal that the center of the condensates have phase singularities of charges $(0, +1, +2)$ in $j = +1$, 0, and -1 components, respectively. At this large rotation frequency, more vortices are created in condensates, which relax in a triangular lattice pattern. The coarse-grained peak value of the total densities for the two condensates lie along a circle of radius 4.7, e.g. $\tilde{\rho}(\mathbf{r})$ corresponding to the solution in Figs. 3.7(B) is shown in Fig. 3.5(C), which is in a decent agreement with the variational single-particle density maxima position at 4.88 in Fig. 3.3(a). The circle encloses approximately 24 phase singularities, which agrees with phase-winding numbers calculated using variational analysis of the single-particle Hamiltonian. Next with $\gamma = 1$ and $\Omega_{\text{rot}} = 0.5$, the component ground-state densities are shown in Figs. 3.7(C) and 3.7(G). The centers of both the condensates, in this case, have phase singularities of charges $(0, +1, +2)$, respectively, in

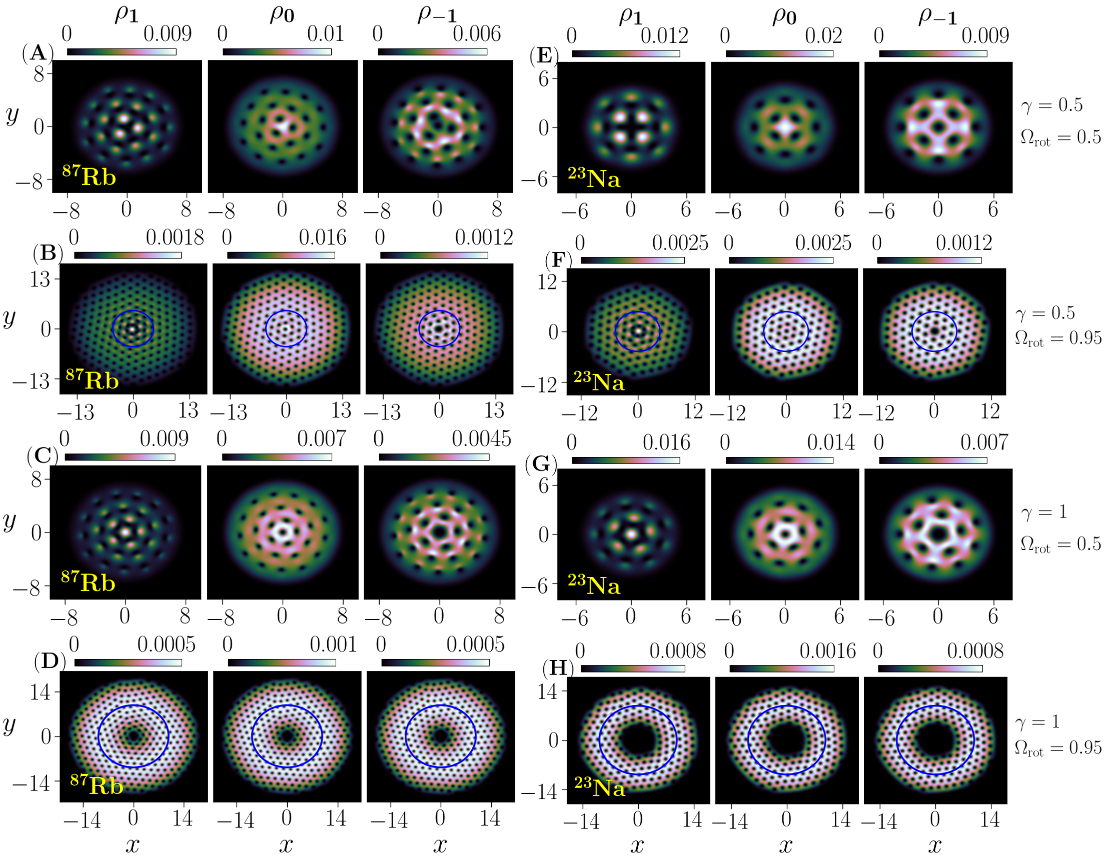

Figure 3.7: Equilibrium density profiles of the individual component densities of the SO-coupled spin-1 BECs: (A)-(D) ^{87}Rb with $c_0 = 2482.21$, $c_1 = -11.47$ and (E)-(H) ^{23}Na spin-1 BEC with $c_0 = 674.91$ and $c_1 = 21.12$. (A) and (B) have been obtained with $\Omega_{\rm rot} = 0.5, 0.95$, respectively, and SO-coupling strength of $\gamma = 0.5$. Similarly, (C) and (D) correspond to SO-coupling strength of $\gamma = 1$ with $\Omega_{\rm rot} = 0.5$, and 0.95, respectively. For SO-coupled ^{23}Na, the plots (E) and (F) correspond to $\gamma = 0.5$ and $\Omega_{\rm rot}$ =0.5,0.95, respectively, and (G) and (H) correspond to $\gamma = 1$ with $\Omega_{\rm rot} = 0.5, 0.95$, respectively. Blue circles in (B), (F), (D) and (H) correspond to the peak in coarse-grained total density $\tilde{\rho}(\mathbf{r})$. The spatial coordinates and densities are in the units of $a_{\rm osc}$ and $a_{\rm osc}^{-2}$, respectively, where $a_{\rm osc} = 3.41$ μm and 6.63 μm for ^{87}Rb and ^{23}Na, respectively.

$j = +1$, 0, and -1 components, respectively. When rotated with a higher frequency of $\Omega_{\rm rot} = 0.95$, the condensate densities acquire a giant hole at the center as shown in Figs. 3.7(D) and 3.7(H) with an annulus of triangular vortex-lattice pattern in each component. The coarse-grained peak values of the total densities in this case, too, are along a circle of radius 9.7 as is seen in Fig. 3.5(D) for ^{87}Rb, which agrees well with the variational single-particle density peak in Fig. 3.3(c). The circle contains approximately 100 phase singularities in each component in agreement with the single particle. The appearance of a giant vortex at the trap center in the component densities surrounded by singly charged vortices arranged in an annulus for sufficiently strong isotropic SO-coupling strengths at fast rotations is a generic feature of these systems [113,116]. The quantitative differences in respective component densities of ^{87}Rb and ^{23}Na when rotated with $\Omega_{\rm rot} = 0.95$ is primarily a consequence of c_0 for the two BECs being 2482.21 and 674.91, respectively.

3.2.2 Effect of coherent coupling

To highlight the effects which can solely be attributed to an interplay of rotation, coherent coupling, and interactions, we first consider ^{23}Na BEC without and with coherent coupling at a rotation frequency of $\Omega_{\rm rot} = 0.95$ in the absence of SO coupling. Here, without coherent coupling, the BEC supports an array of double-core vortices [30] in each component, which arrange themselves in a square-lattice pattern as is shown in Figs. 3.8(A). Each double-core vortex core consists of two non-overlapping phase singularities of unit charge, each marked with white dots in Fig. 3.8(A). With coherent coupling of $\Omega_{\rm coh} = 1$, the system at the same rotation frequency of $\Omega_{\rm rot} = 0.95$ hosts a triangular-lattice pattern in each component as shown in Fig. 3.8(B), where a typical vortex core in each component consists of a single phase singularity. Here the effective potential is an isotropic harmonic potential $V_{\rm eff}^{-1}$ as shown in shown in Fig. 3.1(c).

Next, we consider the combined effect of SO and coherent couplings on the ground-state vortex configurations. Here, we consider two parameter sets- first with $\gamma_x = \gamma_y = 1$, $\Omega_{\rm coh} = 1$, and second with $\gamma_x = 1, \gamma_y = 0$, $\Omega_{\rm coh} = 1$. In the former case, the ground state density has a hole whose center is shifted along $+y$ direction as shown in Fig. 3.8(C). In the latter, the component densities distribute in two unequal triangular lattice patterns above and below the x-axis, as shown in Fig. 3.8(D), and with an increase in $\Omega_{\rm coh}$, the size of the smaller triangular lattice pattern in the upper-half plane decreases further with a corresponding increase in the size of one in the lower-half plane. The splitting of the component densities into two unequal parts can be attributed to the effective potential experienced by the system, which is an asymmetric double-well potential created by $V_{\rm eff}^{-1}(x,y)$ and $V_{\rm eff}^{+1}(x,y)$ with a global minima at $(x = 0, y = -9.7)$ and a local minima at $(x = 0, y = +9.7)$ as shown in Fig. (3.1)(d). We obtain similar results for ^{87}Rb spin-1 BEC at $\Omega_{\rm rot} = 0.95$ which have not been shown here.

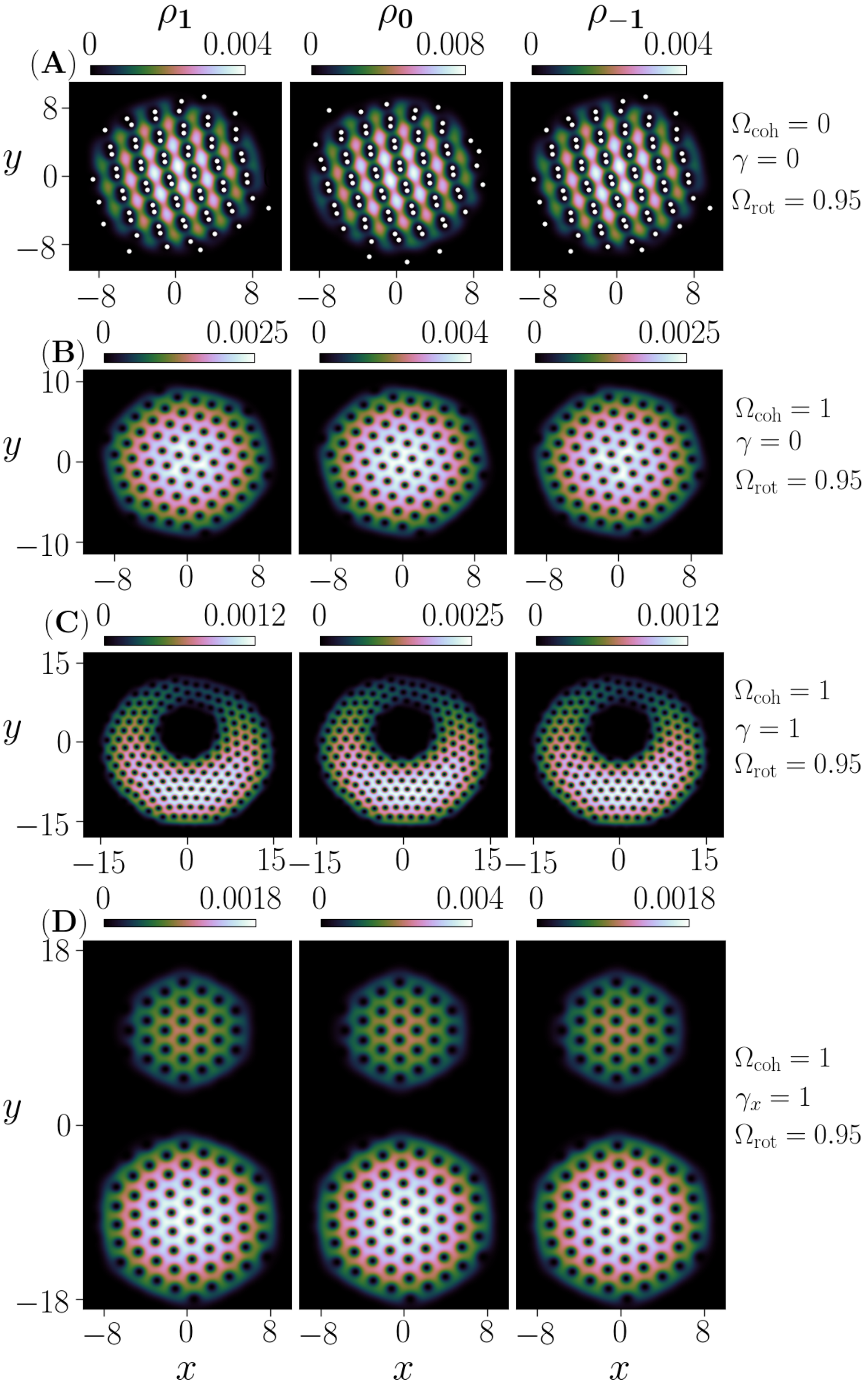

Figure 3.8: Equilibrium density profiles of the individual components of ^{23}Na spin-1 BEC with interaction parameters $c_0 = 674.91$, $c_1 = 21.12$, when rotated with $\Omega_{\rm rot} = 0.95$. (A) has been obtained for $\Omega_{\rm coh} = \gamma_x = \gamma_y = 0$ and $\Omega_{\rm rot} = 0.95$, whereas (B), (C), and (D) have been obtained with coherent-coupling strength $\Omega_{\rm coh} = 1$ and SO-coupling strengths of $\gamma_x = \gamma_y = 0$, $\gamma_x = \gamma_y = 1$, and $\gamma_x = 1, \gamma = 0$, respectively. The spatial coordinates and densities are in the units of $a_{\rm osc}^{\rm Na}$ and $\left[a_{\rm osc}^{\rm Na}\right]^{-2}$ respectively, where $a_{\rm osc}^{\rm Na} = 6.63$ μm.

3.2.3 Stability and expansion dynamics

All the stationary states discussed in the present work correspond to repulsively interacting spinor BECs subjected to rotation and SO coupling and are dynamically stable in the rotating frame. As an illustration of this, we consider the real-time dynamics of the solutions in Figs. 3.4(C) and 3.4(D) with a random (complex) Gaussian noise $\delta\psi_j(x,y)$ added to each component wavefunction $\psi_j(x,y)$ at $t=0$, which then are taken as initial solutions to solve CGPEs. (3.17a) and (3.17b) in real time. We consider $\delta\psi_j(x,y) = 10^{-2}\eta_j(x,y)$, where $\eta_j(x,y)$ is a distribution of complex Gaussian random numbers. We observe that the condensates retain their structure including the lattice patterns during the real-time evolution. This is evident from the component densities in Figs. 3.9(A) and 3.9(B) corresponding to solutions in Figs. 3.4(C) and 3.4(D), respectively. It is to be noted that anomalous flux created by SO coupling plays an important role in stabilising the q2D SO-coupled spinor BEC interacting with attractive mean-field interactions against collapse instability [201]. The condensates considered in the present work are interacting by net repulsive mean-field interactions and hence are not expected to have any collapse instability. Nonetheless, in the experiments, the vortex lattice in the BECs are imaged after releasing the condensate from the trap, and in this context, for the solutions in the present work, such an expansion dynamics on switching off the trap in the lab frame will be dictated primarily by an interplay of the anomalous flux and the centrifugal flux due to the angular momentum in the system. As an example, we consider the expansion dynamics of the solution in Fig. 3.6(B) with $\gamma S_z p_x$ SO coupling, when $V(x,y)$ and $\Omega_{\rm rot}$ are both set to zero at $t=0$, thus mimicking the expansion dynamics in the experiments. The ensuing evolution of the total density is shown via the images of the total density at three instants in Fig. 3.10, where $j=+1$ ($j=-1$) component contributes to the density above (below) y axis. In this case, the center of mass of $j=\pm 1$ component moves with velocity $\mathbf{v} = \mp 9.3\hat{\mathbf{x}}$ in the dimensionless units. Using the minimum energy single particle solutions $\Phi = (\phi_{+1},0,0)^T$ and $\Phi = (0,0,\phi_{-1})^T$, where ϕ_j are defined in Eq. (3.7), the velocity [201]

$$
\begin{aligned}
\mathbf{v} &= \frac{1}{\Phi^\dagger\Phi}\left[\frac{\iota}{2}\left(\Phi\nabla\Phi^\dagger - \Phi^\dagger\nabla\Phi\right) + \Phi^\dagger(\gamma S_z)\Phi\right],\\
&= \left(\mp\frac{\gamma}{1-\Omega_{\rm rot}^2} + \gamma\right)\hat{\mathbf{x}}, \qquad (3.21)
\end{aligned}
$$

where $-$ sign corresponds to $(\phi_{+1},0,0)^T$ and $+$ to $(0,0,\phi_{-1})^T$. The anomalous velocity contribution to the velocity is γ, which is consistent with Ref. [201], and the remaining is arising as an interplay of coupling and rotation. For $\gamma=1$ and $\Omega_{\rm rot}=0.95$, Eq. (3.21) yields $\mathbf{v} = \mp 9.25\hat{\mathbf{x}}$ in agreement with results in Fig. 3.10. Similarly, we observe that with two-dimensional Rashba SO coupling too the centrifugal flux during the expansion dynamics (results not shown here) is created by an interplay of SO coupling and rotation.

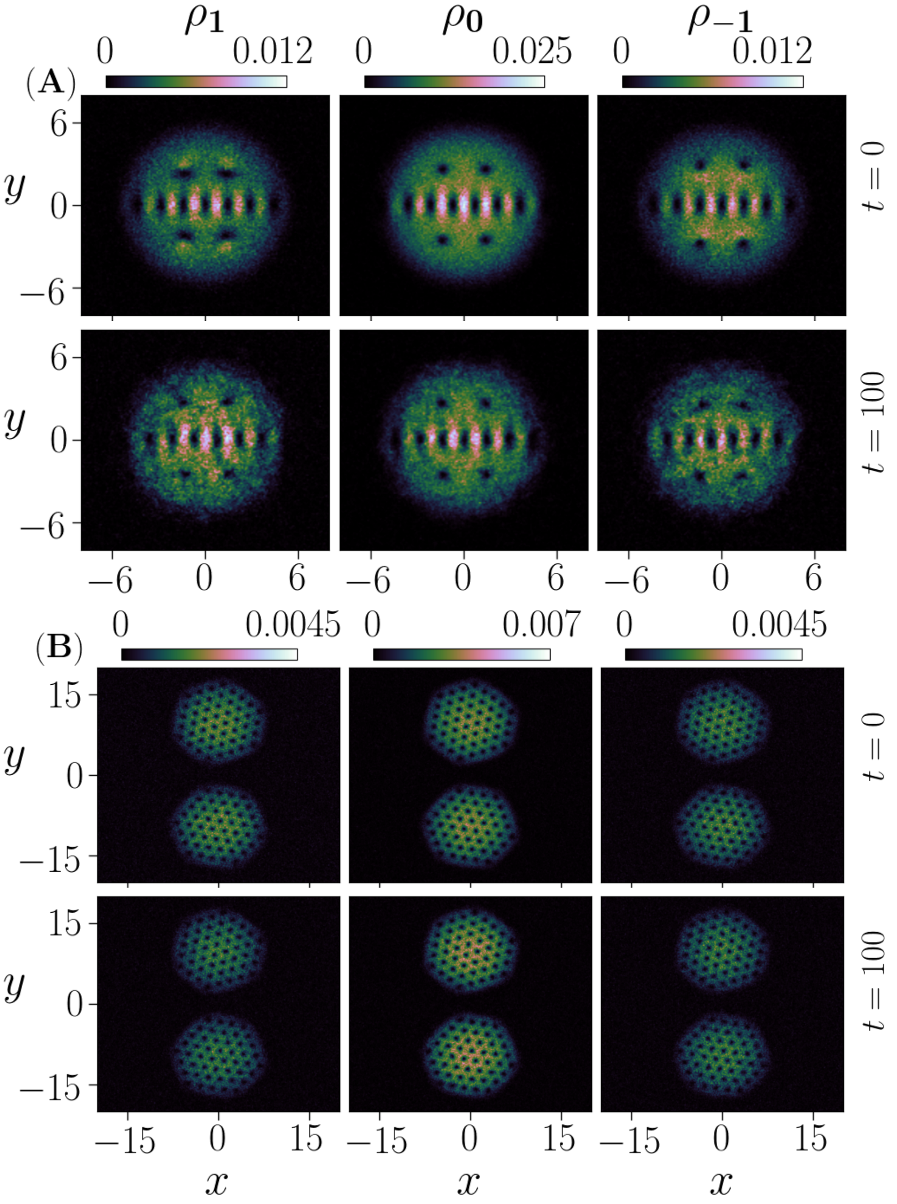

Figure 3.9: Realtime evolution of the stationary states perturbed with an addition of a random complex (Gaussian) noise at $t = 0$: (A) $\rho_j(x, y, t)$ corresponding to the solution in Fig. 3.4(C) with $c_0 = 674.91$, $c_1 = 21.12$, $\gamma_x = 1$ and $\Omega_{\rm rot} = 0.5$ at $t = 0$ and $t = 100$, and (B) corresponding to the solution in Fig. 3.4(D) with $\Omega_{\rm rot} = 0.95$ with same interaction and SO coupling.

3.3 Spin-expectation per particle and spin-texture for spin-1 BECs

As noted in Sec. 3.2.1, the ground state solutions of the rotating SO-coupled ^{87}Rb and ^{23}Na BECs at moderate to high rotation frequencies are qualitatively similar, and the quantitative differences stem from the different magnitudes of c_0. To ascertain this further, here we consider SO-coupled ^{87}Rb and ^{23}Na spin-1 BECs with $\gamma = 0.5$ or 1, $\Omega_{\rm coh} = 0$ and

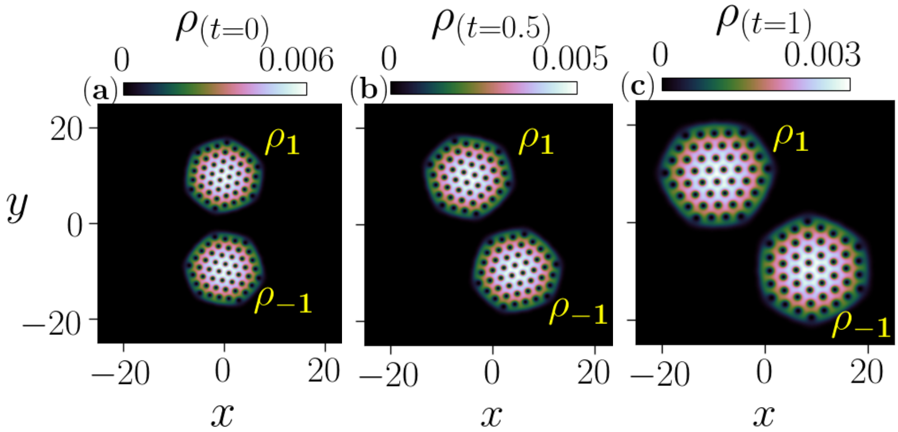

Figure 3.10: Expansion dynamics of the solution in Fig. 3.6(B) with $c_0 = 674.91$, $c_1 = 21.12$, and $\gamma_x = 1$ in absence of trapping potential and rotation: (a) $\rho(x, y, t = 0)$, (b) $\rho(x, y, t = 0.5)$ and (c) $\rho(x, y, t = 1)$. The component densities $\rho_{\pm1}(x, y, t)$ are moving with speed 9.3 along $\mp x$ directions.

(approximately) same c_0 but with different atom numbers. For ^{87}Rb, we again consider $c_0 = 2482.21$ and $c_1 = -11.47$ corresponding to 10^5 atoms, whereas for ^{23}Na we consider 3.68×10^5 atoms resulting in $c_0 = 2482.35$ and $c_1 = 77.68$. We define the spin-density vector $\mathbf{F} = (F_x, F_y, F_z)$ where

$$F_\nu(x, y) = \sum_{m,m'} \psi_m^*(x, y)(S_\nu)_{mm'}\psi_{m'}(x, y), \tag{3.22}$$

and $f = \int |\mathbf{F}(x, y)|d\mathbf{r}/\int \rho(x, y)d\mathbf{r}$, which serves as a measure of spin-expectation per particle for an inhomogeneous system. We examine the angular momentum per particle, f, and spin-texture [1] $\mathbf{f}(x, y) = \mathbf{F}(x, y)/\rho(x, y)$ as a function of rotation frequency. In the absence of rotation, the ^{87}Rb and ^{23}Na spin-1 BECs have $f = 1$ and 0, respectively [1]. The f as a function of rotation frequency $\Omega_{\rm rot}$ for the two systems is shown in Fig. 3.11, which illustrates that with increase in $\Omega_{\rm rot}$, $f \to 1$ for ^{23}Na whereas it remains close to 1 for ^{87}Rb. We also analyse spin-expectation per particle using the single-particle variational solution $\Phi_{\rm var}$ in Eq. (3.14) to evaluate f. The variational analysis predicts $f \approx 1$ for $\gamma = 0.5$ (1) and $\Omega_{\rm rot} \geqslant 0.6$ (0.4), which is consistent with the numerical results for ^{87}Rb and ^{23}Na BECs at moderate to high rotations as is shown in Fig. 3.11. The differences in numerical and variational f values for $\Omega_{\rm rot} \leqslant 0.6$ (0.4) are mainly because of spin-dependent interactions, which expectedly become increasingly less important with an increase in rotation frequency. Next, we consider the spin-texture of ^{87}Rb and ^{23}Na BEC with $\gamma = 0.5, \Omega_{\rm coh} = 0$ when rotated with $\Omega_{\rm rot} = 0.1$ and 0.95. The component densities for ^{87}Rb and ^{23}Na when rotated with $\Omega_{\rm rot} = 0.1$ are shown in Figs. 3.12(A) and 3.12(B), respectively, and the corresponding spin textures are in Figs. 3.12(a) and 3.12(b). At this frequency ^{87}Rb hosts three skyrmions in Fig. 3.12(a) as compared to two for ^{23}Na in Fig. 3.12(b) (near the center of the trap). The generation of skyrmion and half-skyrmion

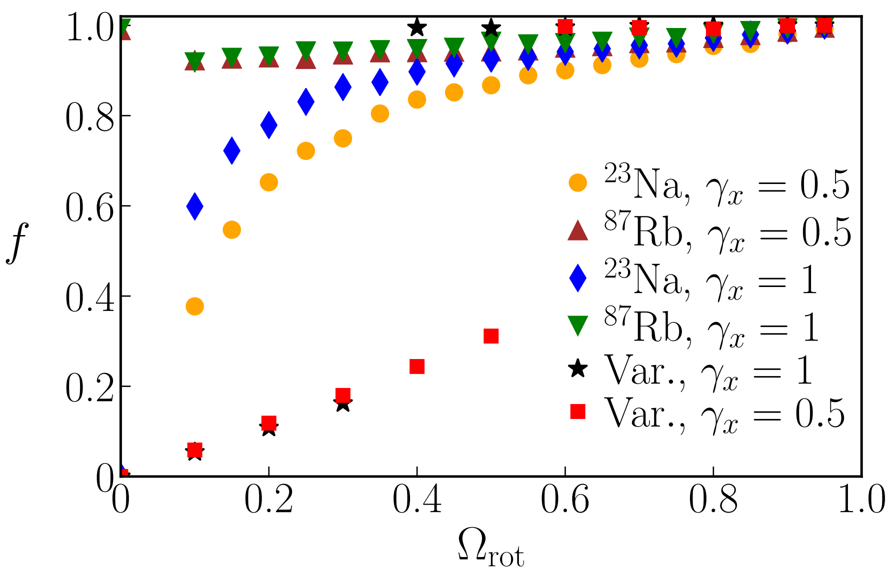

Figure 3.11: Variation of spin-expectation per particle f with rotation frequency obtained from the variational method discussed in Sec. 3.1 and the numerical solutions of the CGPEs for the SO-coupled ^{87}Rb and ^{23}Na BECs.

excitations in rotating SO-coupled BECs is discussed in Refs. [115,118]. The spin-textures at $\Omega_{\rm rot} = 0.95$ are shown in Fig. 3.13(a) for ^{87}Rb and Fig. 3.13(b) for ^{23}Na, here both the systems have a skyrmion at the center surrounded by a lattice of half-skyrmions. The spin-texture of ^{87}Rb corresponds to the component densities shown in Fig. 3.7(B), whereas the component densities of ^{23}Na which are indistinguishable ^{87}Rb are not shown here. The similarity of the two systems at faster rotation is also reflected in the spin-textures. The similarity in the response of the two systems at fast rotations has also been confirmed based upon their mass and spin currents.

3.4 Rotating SO-coupled spin-2 BEC

Under a q2D harmonic confinement, a rotating SO-coupled spin-2 BEC under mean-field approximation can be described by a set of five CGPEs [1]

$$\iota\frac{\partial\psi_{\pm2}}{\partial t} = \mathcal{H}\psi_{\pm2} + c_1(F_\mp\psi_{\pm1} \pm 2F_z\psi_{\pm2}) + c_2\frac{\Theta\psi^*_{\mp2}}{\sqrt{5}} + \Gamma_{\pm2}, \tag{3.23a}$$

$$\iota\frac{\partial\psi_{\pm1}}{\partial t} = \mathcal{H}\psi_{\pm1} + c_1\left(\sqrt{\frac{3}{2}}F_\mp\psi_0 + F_\pm\psi_{\pm2} \pm F_z\psi_{\pm1}\right) - c_2\frac{\Theta\psi^*_{\mp1}}{\sqrt{5}} + \Gamma_{\pm1}, \tag{3.23b}$$

$$\iota\frac{\partial\psi_0}{\partial t} = \mathcal{H}\psi_0 + c_1\sqrt{\frac{3}{2}}(F_-\psi_{-1} + F_+\psi_1) + c_2\frac{\Theta\psi^*_0}{\sqrt{5}} + \Gamma_0, \tag{3.23c}$$

where $\Psi = (\psi_{+2}, \psi_{+1}, \psi_0, \psi_{-1}, \psi_{-2})^T$ is a five component order parameter, $\mathcal{H}$ is same in Eq. (3.18). In Eqs. (3.23a)-(3.23c), Γ_j for an equal-strength mixture of Rashba and

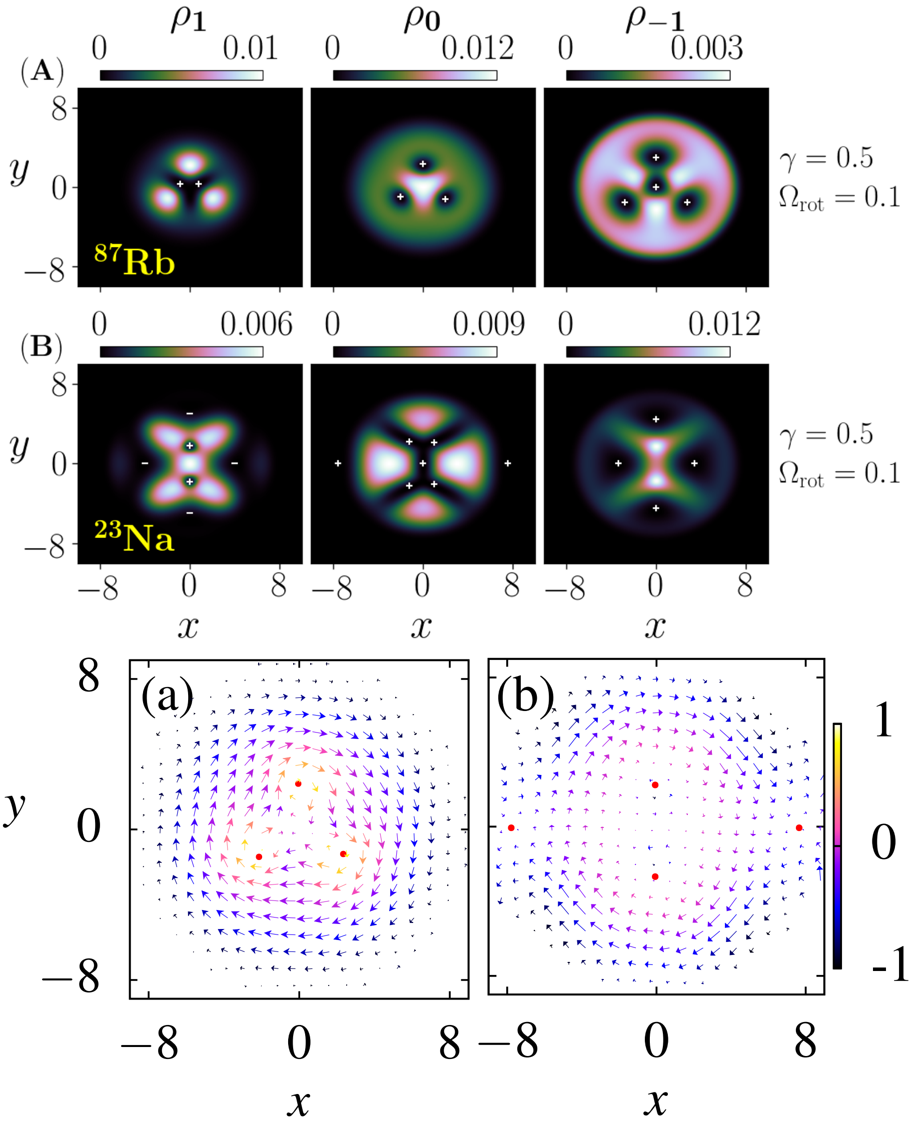

Figure 3.12: (A) displays the component density of the SO-coupled ^{87}Rb BEC with $\gamma_x = \gamma_y = 0.5$ when rotated with $\Omega_{\rm rot} = 0.1$ and (B) displays the same for ^{23}Na BEC. The interaction strengths for ^{87}Rb and ^{23}Na are $c_0 = 2482.21$, $c_1 = -11.47$ and $c_0 = 2482.35$, $c_1 = 77.68$, respectively. The locations and signs of phase-singularities in each component are marked with ± signs. (a) and (b), respectively, show the spin-textures corresponding to the densities in (A) and (B), where (a) has the three skyrmions (marked by red dots), and (b) has two near the center of the trap in addition to two cross-disgyrations in spin-texture along x-axis coinciding with +1 phase singularity in $j = 0$ component. The spatial coordinates and densities are in the units of $a_{\rm osc}$ and $a_{\rm osc}^{-2}$, respectively, where $a_{\rm osc} = 3.41$ μm and 6.63 μm for ^{87}Rb and ^{23}Na, respectively.

Dresselhaus couplings are

$$\Gamma_{\pm 2} = -\iota\gamma_x\frac{\partial\psi_{\pm 1}}{\partial x}, \quad \Gamma_{\pm 1} = -\iota\left(\gamma_x\frac{\partial\psi_{\pm 2}}{\partial x} + \sqrt{\frac{3}{2}}\gamma_x\frac{\partial\psi_0}{\partial x}\right),$$

$$\Gamma_0 = -\iota\left(\sqrt{\frac{3}{2}}\gamma_x\frac{\partial\psi_1}{\partial x} + \sqrt{\frac{3}{2}}\gamma_x\frac{\partial\psi_{-1}}{\partial x}\right),$$

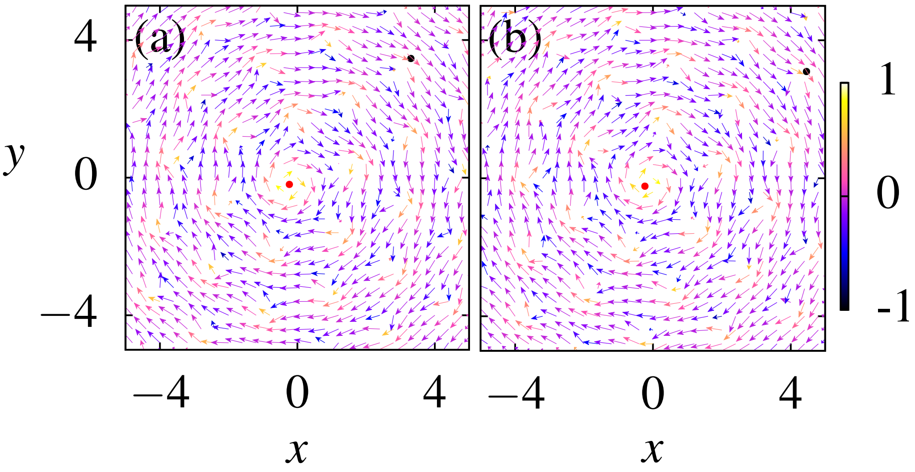

Figure 3.13: (a) shows the spin-texture for ^{87}Rb system and (b) shows the same for ^{23}Na system at rotation frequency $\Omega_{\text{rot}} = 0.95$. Both figures have a skyrmion at the centre (marked by a red dot) and in the rest of the regions, half-skyrmion lattice (black dot marks the center of one such half-skyrmion). The respective interaction parameters are the same as those considered in Fig. 3.12.

for Rashba coupling are

$$\Gamma_{\pm 2} = -\iota\gamma \left(\frac{\partial \psi_{\pm 1}}{\partial y} \pm \iota \frac{\partial \psi_{\pm 1}}{\partial x} \right),$$

$$\Gamma_{\pm 1} = -\iota\gamma \left(\frac{\partial \psi_{\pm 2}}{\partial y} + \sqrt{\frac{3}{2}} \frac{\partial \psi_0}{\partial y} \mp \iota \frac{\partial \psi_{\pm 2}}{\partial x} \pm \iota \sqrt{\frac{3}{2}} \frac{\partial \psi_0}{\partial x} \right),$$

$$\Gamma_0 = -\iota\gamma \left(\sqrt{\frac{3}{2}} \frac{\partial \psi_1}{\partial y} + \sqrt{\frac{3}{2}} \frac{\partial \psi_{-1}}{\partial y} - \iota \sqrt{\frac{3}{2}} \frac{\partial \psi_1}{\partial x} + \iota \sqrt{\frac{3}{2}} \frac{\partial \psi_{-1}}{\partial x} \right),$$

and rest of the quantities have the same definitions as in Eqs. (2.7a), (2.7b), (2.9a)-(2.9c).

3.4.1 Numerical Results for spin-2 BEC

We consider 50,000 atoms of spin-2 BECs like ^{23}Na and ^{87}Rb in an isotropic q2D trap with $\omega_x = \omega_y = 2\pi \times 10$ Hz and $\omega_z = 2\pi \times 100$ Hz. The oscillator lengths are 4.69μm and 2.41μm for ^{23}Na and ^{87}Rb, respectively. The three scattering lengths for ^{23}Na are $a_0 = 34.9a_B, a_2 = 45.8a_B$, and $a_4 = 64.5a_B$ [61] and the same for ^{87}Rb are $a_0 = 87.93a_B$, $a_2 = 91.28a_B$, and $a_4 = 99.18a_B$ [202]. The triplet of dimensionless interaction strengths are $(c_0,\ c_1,\ c_2) = (340.45,\ 16.90,\ -18.25)$ and $(c_0, c_1, c_2) = (1164.80, 13.88, 0.43)$ for ^{23}Na and ^{87}Rb, respectively. The SO-coupled spin-2 BEC can exhibit various ground-state solutions depending on the interaction parameters and the strength of the SO coupling in the absence of a rotation [185,203,204]. For example, the axisymmetric solution characterized by $(-2, -1, 0, +1, +2)$ charge phase singularities in the component wavefunction can arise from the equal-weight superposition of an infinite number of plane waves [90,203]. Additionally, other patterns such as stripe [90,203], square lattices [90,203], or triangular lattices [90,203] can arise through the superposition of counter-propagating

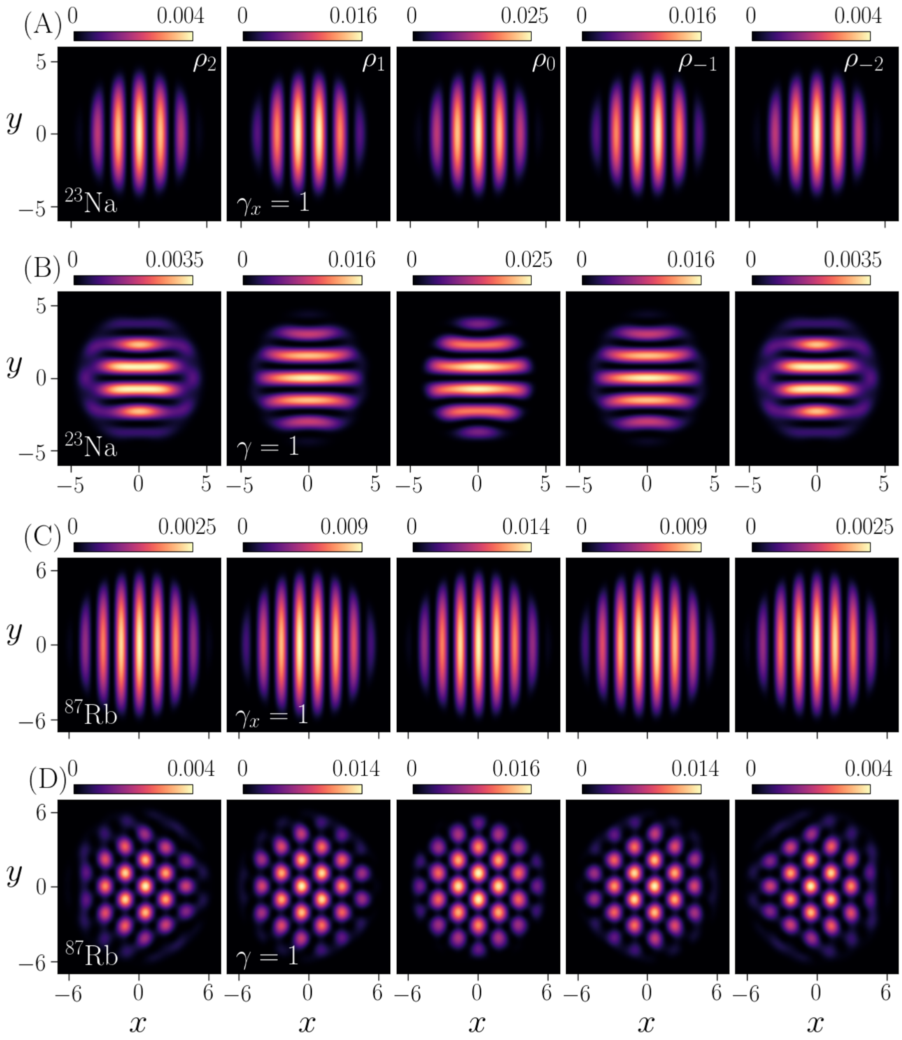

Figure 3.14: Ground-state component densities of an SO-coupled ^{23}Na BEC with $c_0 = 340.45, c_1 = 16.90$, and $c_2 = -18.25$ for (A) $\gamma_x = 1, \gamma_y = 0$ and (B) $\gamma = 1$. (C) and (D) show the same for ^{87}Rb with $c_0 = 1164.80, c_1 = 13.88$, and $c_2 = 0.43$.

plane waves, four plane waves with propagation vectors at a right angle to each other, or three plane waves with propagation vectors at an angle of $2\pi/3$ to each other, respectively.

In the absence of rotation, for an equal-strength mixture of Rashba and Dresselhaus couplings with $\gamma_x = 1$ and $\Omega_{\text{coh}} = 0$, the ground-state density profiles for both antiferromagnetic and cyclic interactions have vertical stripe patterns [see Figs. 3.14(A) and 3.14(C)]. For Rashba SO coupling with $\gamma = 1$ and $\Omega_{\text{coh}} = 0$, the ground-state density profiles for the two interactions are qualitatively different with a horizontal stripe for the antiferromagnetic and a triangular lattice for the cyclic interaction [cf. Figs. 3.14(B) and 3.14(D)].

Antiferromagnetic interactions

In the rotating frame, the component density profiles with rotation frequencies $\Omega_{\text{rot}} = 0.5, 0.7,$ and 0.9 are shown in Figs. 3.15(A)-3.15(C), respectively. With the increase

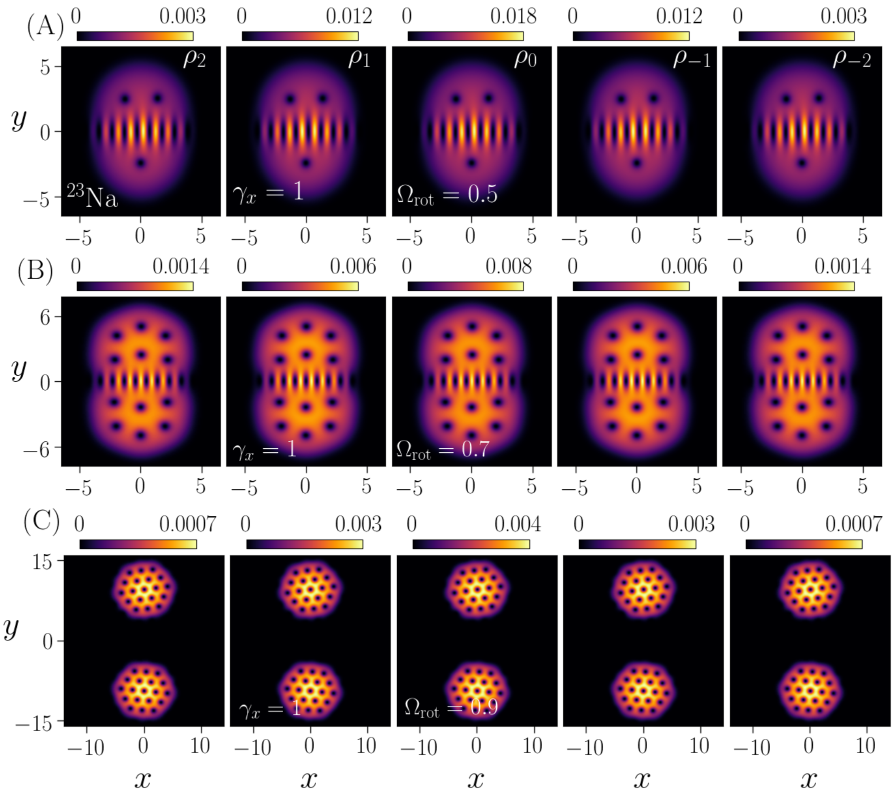

Figure 3.15: Ground-state component densities of an SO-coupled ^{23}Na BEC with $c_0 = 340.45$, $c_1 = 16.90$, $c_2 = -18.25$, $\gamma_x = 1, \gamma_y = 0$: (A) $\Omega_{\rm rot} = 0.5$, (B) $\Omega_{\rm rot} = 0.7$, and (C) $\Omega_{\rm rot} = 0.9$.

in rotation frequency, the asymmetric double-well potential experienced by the boson becomes apparent in Fig. 3.15(B) and 3.15(C), as was discussed in Sec. 3.2.1 for spin-1 BEC.

For Rashba SO coupling, the component density profiles for $\Omega_{\rm rot} = 0.5, 0.7$, and 0.9 are shown in Fig. 3.16. When rotated with $\Omega_{\rm rot} = 0.7$, the central region of the condensate has phase singularities with charges $(0, +1, +2, +3, +4)$, respectively [see Fig. 3.16(B)]. The charges of these singularities have been determined from the phase of the order parameter (not shown here). At a larger rotation frequency $\Omega_{\rm rot} = 0.9$, the component densities acquire a ring-type structure with a giant vortex at the center, which again is reminiscent of an effective toroidal potential as discussed in Sec. 3.2.1.

Cyclic interactions

The density profiles for different $\Omega_{\rm rot}$ are shown in Fig. 3.17 for the equal-strength mixture of Rashba and Dresselhaus couplings and in Fig. 3.18 for Rashba coupling. The density profiles for moderate to high rotation frequencies are qualitatively similar to ^{23}Na with antiferromagnetic interactions; the minor differences in density profiles may be attributed to different values of c_0.

The rotational energy of a scalar BEC (with a large number of vortices) in the rotating frame, $E(\Omega_{\rm rot} \neq 0) - E(\Omega_{\rm rot} = 0)$, is comparable to the energy of a rigid body under

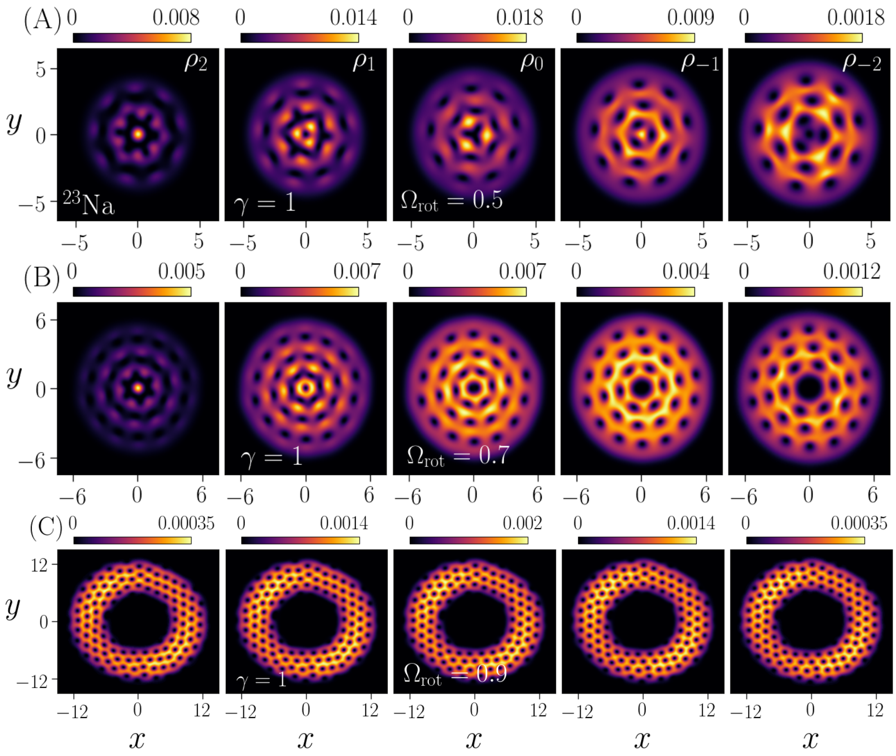

Figure 3.16: Ground-state component densities of an SO-coupled ^{23}Na with $c_0 = 340.45, c_1 = 16.90, c_2 = -18.25$, $\gamma = 1$: (A) $\Omega_{\rm rot} = 0.5$, (B) $\Omega_{\rm rot} = 0.7$, and (C) $\Omega_{\rm rot} = 0.9$.

rotation, i.e. $-I\Omega_{\rm rot}^2/2$, where I is the moment of inertia of the condensate [33,121]. We illustrate in Fig. 3.19 the rotational energy as a function of $\Omega_{\rm rot}$ for SO-coupled BECs with both antiferromagnetic and cyclic interactions. The rotational energy for both systems decreases as $-\Omega_{\rm rot}^2$.

The SO-coupled BEC with realistic ferromagnetic interactions under moderate to high rotation frequencies behaves similarly to the BECs with antiferromagnetic/cyclic interactions and has similar equilibrium density profiles (not shown here).

3.5 Summary

We have studied the stationary-state vortex lattice configurations of rotating SO-coupled spin-1 and spin-2 BECs trapped in q2D harmonic potentials. Using exact numerical solutions complemented by a variational analysis, we have shown that the non-interacting part of the Hamiltonian can be translated to the rotating effective potentials with symmetric, asymmetric double-well, and toroidal structures. We have illustrated using the mean-field GP formalism, employing the realistic experimental parameters, at moderate to high rotation frequencies, the analytically obtained effective potential minima and the numerically obtained coarse-grained density maxima's position are in excellent agreement. The effects of rotation are further elucidated by computing the spin expectation per particle for the ferro- as well as the antiferromagnetic BECs. For the former, the spin expectation is always close to unity, irrespective of the rotation

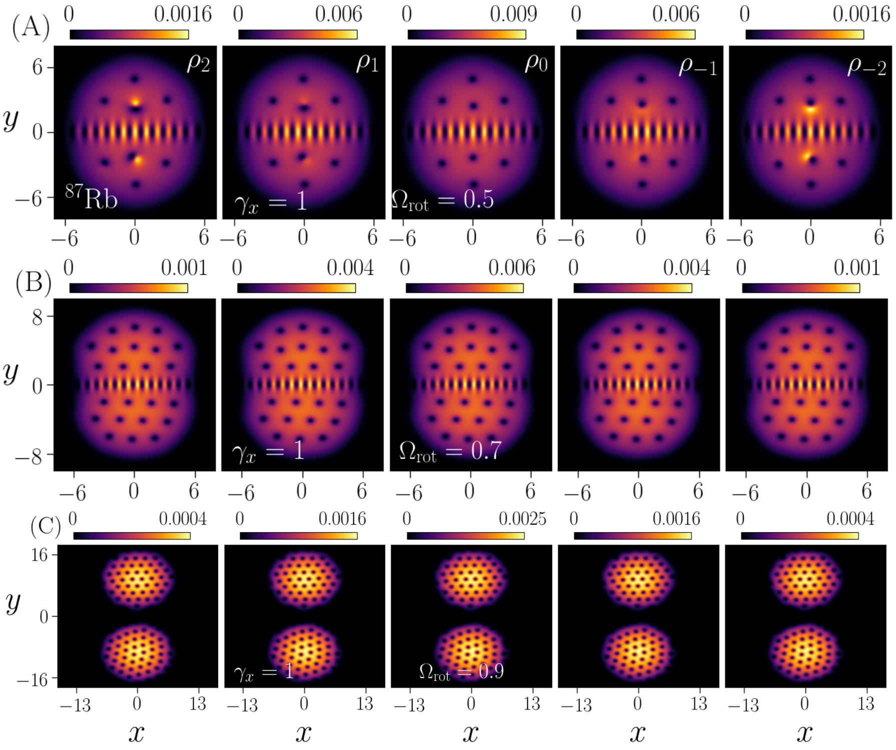

Figure 3.17: Ground-state component densities of an SO-coupled ^{87}Rb BEC with $c_0 = 1164.80$, $c_1 = 13.88$, $c_2 = 0.43$, $\gamma_x = 1, \gamma_y = 0$: (A) $\Omega_{\rm rot} = 0.5$, (B) $\Omega_{\rm rot} = 0.7$, and (C) $\Omega_{\rm rot} = 0.9$.

frequency. Meanwhile, for the latter, the spin-expectation value increases with an increase in rotation frequency and tends to approach one. For the simpler one-dimensional coupling ($\propto \gamma S_z p_x$), spatial segregation between the $j = \pm 1$ components results in spin-expectation per particle approaching one for the antiferromagnetic BEC; similarly, single-particle variational analysis with Rashba SO coupling also indicates the spin-expectation per particle approaching one irrespective of the spin-exchange interactions with increasing rotational frequency. The similarity in the response of the fast-rotating spin-1 BECs with ferromagnetic and antiferromagnetic interactions, and similarly, the response of spin-2 BECs with ferromagnetic, antiferromagnetic, and cyclic interactions highlights the much-diminished role of the spin-exchange interactions vis-à-vis the other competing terms in the system's Hamiltonian. The results reported in this chapter are discussed in Refs. [205,206].

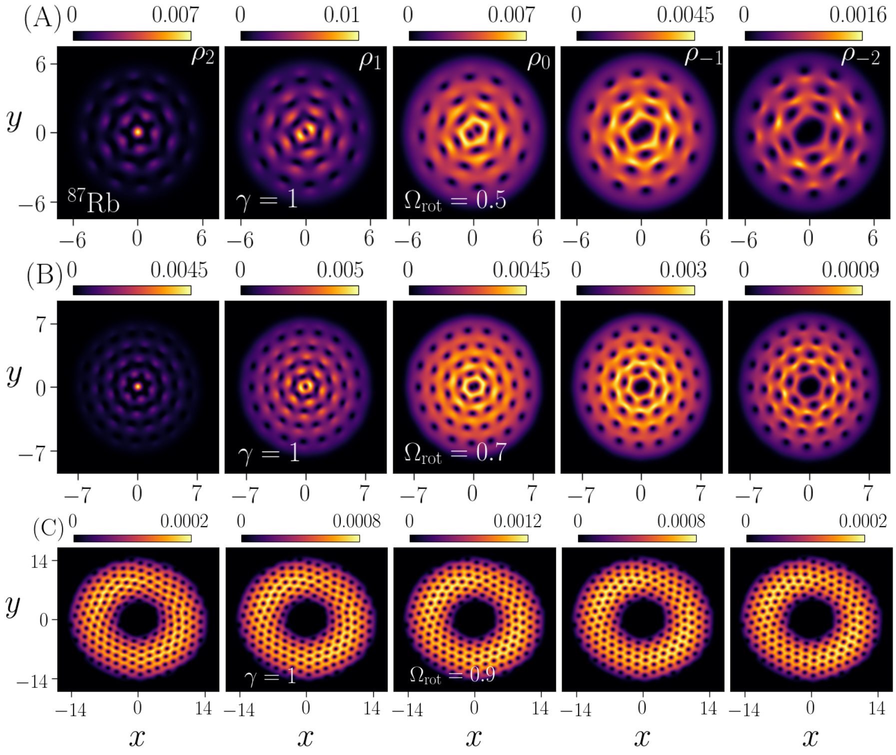

Figure 3.18: Ground-state component densities of an SO-coupled ^{87}Rb BEC with $c_0 = 1164.80,\ c_1 = 13.88,\ c_2 = 0.43,\ \gamma = 1$: (A) $\Omega_{\rm rot} = 0.5$, (B) $\Omega_{\rm rot} = 0.7$, and (C) $\Omega_{\rm rot} = 0.9$.

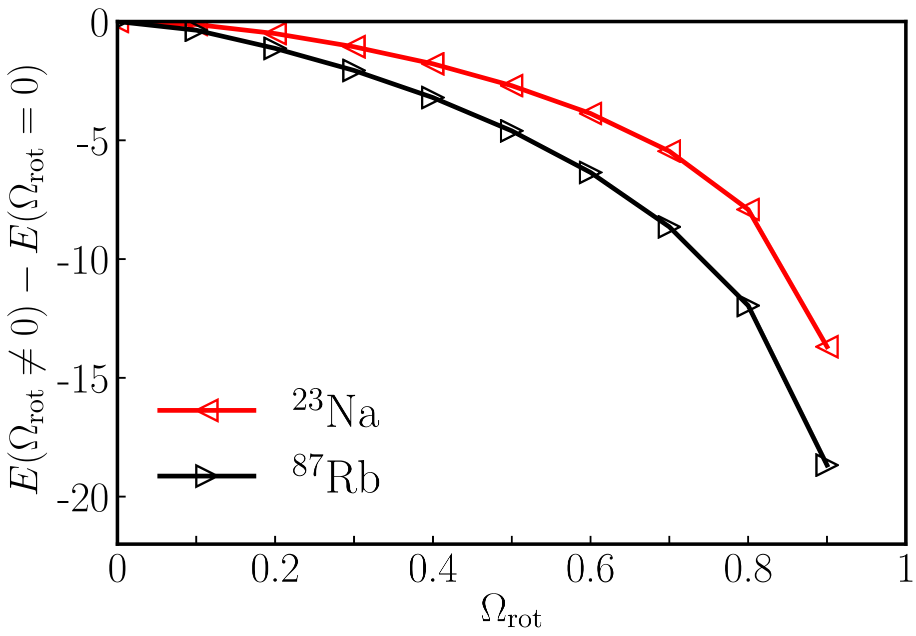

Figure 3.19: Rotational energy $E(\Omega_{\rm rot} \neq 0) - E(\Omega_{\rm rot} = 0)$ as a function of $\Omega_{\rm rot}$ for Rashba SO-coupled ^{23}Na and ^{87}Rb BECs.

Chapter 4

Quantum phases and the excitation spectrum of an SOAM-coupled spin-1 BEC

As discussed in Sec. 1.4, the experimental realization of SOAM coupling represents a significant milestone in the research field of spinor BECs [6]. In this chapter, we calculate the low-lying excitation spectrum of ground-state phases, specifically focusing on the coreless and polar-core vortex states of SOAM-coupled spin-1 condensates. These two solutions are circularly symmetric and have been experimentally realized [136] by employing a Gaussian and a Laguerre-Gaussian beam that co-propagate along the z-direction, resulting in an angular momentum transfer of $\hbar$ to the atom.

The chapter is organized as follows. In Sec. 4.1, we present the Hamiltonian describing an SOAM-coupled spin-1 BEC in cylindrical coordinates and the reduction to a q2D formulation through a set of CGPEs. In Sec. 4.2, we discuss the ground-state phases of SOAM-coupled ferromagnetic and polar BECs in the limit of vanishing detuning. In Sec. 4.3.1, we discuss the spectrum of the noninteracting SOAM-coupled spin-1 BEC, and follow it with the collective excitations of the interacting SOAM-coupled spin-1 BECs in 4.3.2. In Sec. 4.3.3, we explore the effect of detuning on the ground-state phases and excitation spectrum. In Sec. 4.3.4, starting with the ground state solution, we study the low-lying collective excitations which are excited with the addition of suitable perturbations to the Hamiltonian at $t = 0$. In Sec. 4.3.5, the variational method to study a few low-lying modes is discussed, which is followed by the summary of key results in Sec. 4.4.

4.1 Mean-field model for an SOAM-coupled spin-1 BEC

In this chapter, we consider SOAM-coupled spin-1 BECs in which the orbital angular momentum of the center of the mass of the atoms is synthetically coupled to their internal spin states [5,135]. In the cylindrical coordinate system, the non-interacting (single-particle) part of the Hamiltonian for the spinor BEC is [135,136]

$$H_{\mathrm{s}} = \left[-\frac{\hbar^2}{2M}\frac{\partial}{r\partial r}\left(r\frac{\partial}{\partial r}\right) + \frac{L_z^2}{2Mr^2} - \frac{\hbar^2}{2M}\frac{\partial^2}{\partial z^2} + V(\mathbf{r}) \right]\mathbf{I} \\ + \Omega(r)[\cos(\phi)S_x - \sin(\phi)S_y] + \delta S_z, \tag{4.1}$$

where $\mathbf{I}$ is a 3×3 identity matrix, $V(\mathbf{r}) = M(\omega_0^2 r^2/2 + \omega_z^2 z^2)/2$ constitutes the external harmonic potential to trap the atoms of mass M, $L_z = -\iota\hbar\partial/\partial\phi$ is the angular momentum operator, $\Omega(r) = \Omega_0\sqrt{e}(r/r_0)\exp[-r^2/2r_0^2]$ is the Raman-coupling strength with Ω_0 and r_0 as the Rabi frequency and the radius of the maximum-intensity (cylindrical) surface [135,136], respectively, δ is the Raman detuning, and S_x, S_y and S_z are irreducible representations of the spin-1 angular momentum operators. Under mean-field approximation, the interacting part of the Hamiltonian $H_{\rm int}$ is given by [1]

$$H_{\rm int} = \frac{c_0}{2}\rho + \frac{c_1}{2}\mathbf{F}.\mathbf{S} \tag{4.2}$$

with c_0 and c_1 as the mean-field interaction parameters. The total density of the system is given by ρ, $\mathbf{F} = (F_x, F_y, F_z)$ is the spin-density vector, and $\mathbf{S} = (S_x, S_y, S_z)$. Since the SOAM coupling is restricted to the radial plane, and we consider $\omega_z \gg \omega_0$, the dominant dynamics is constrained to the same plane with frozen axial degrees of freedom. We can then integrate out the z degree of freedom from the condensate wave function and describe the system as q2D on the radial r-ϕ plane. Starting from the Hamiltonian $H = H_{\rm s} + H_{\rm int}$, in polar coordinates, we obtain the following coupled q2D CGPEs in dimensionless form

$$\iota\frac{\partial\psi_{\pm1}}{\partial t} = \mathcal{H}\psi_{\pm1} + c_1(\rho_0 \pm \rho_-)\psi_{\pm1} + c_1\psi_{\mp1}^*\psi_0^2 \pm \delta\psi_{\pm1} + \frac{\Omega(r)}{\sqrt{2}}e^{\pm\iota\phi}\psi_0, \tag{4.3a}$$

$$\iota\frac{\partial\psi_0}{\partial t} = \mathcal{H}\psi_0 + c_1\rho_+\psi_0 + 2c_1\psi_{+1}\psi_{-1}\psi_0^* + \frac{\Omega(r)}{\sqrt{2}}(e^{-\iota\phi}\psi_{+1} + e^{\iota\phi}\psi_{-1}), \tag{4.3b}$$

where

$$\mathcal{H} = -\frac{1}{2}\frac{\partial}{r\partial r}\left(r\frac{\partial}{\partial r}\right) + \frac{L_z^2}{2r^2} + \frac{r^2}{2} + c_0\rho,\ \rho = \sum_{j=\pm1,0}\rho_j,\ \rho_j = |\psi_j|^2,\ \rho_\pm = \rho_{+1} \pm \rho_{-1}.$$

Under geometric renormalization, in terms of s-wave scattering lengths a_0 and a_2 in the total spin 0 and 2 channels, respectively, c_0 and c_1 take the form

$$c_0 = \sqrt{8\pi\alpha}\frac{N(a_0+2a_2)}{3a_{\rm osc}}, \quad c_1 = \sqrt{8\pi\alpha}\frac{N(a_2-a_0)}{3a_{\rm osc}}, \tag{4.4}$$

denoting the spin-independent and spin-dependent interactions, respectively. The anisotropy parameter $\alpha = \omega_z/\omega_0$ is defined to be the trapping frequency ratio along the axial to the radial direction, and N is the total number of atoms. The units of length, time, energy, and energy eigenfunctions are considered to be $a_{\rm osc} = \sqrt{\hbar/(M\omega_0)}$, ω_0^{-1}, $\hbar\omega_0$, and $a_{\rm osc}^{-1}$, respectively, and $\int r\rho(r)drd\phi = 1$.

4.2 Ground-state quantum phases of SOAM coupled spinor BEC

To understand the intercomponent phase relationship imposed by various competing terms in the Hamiltonian, we consider a generic circularly symmetric *ansatz*, $\psi_j =$

$f_j(r)e^{\iota(w_j\phi+\beta_j)}$, for the component wavefunctions, where w_j and β_j are, respectively, the phase-winding number and constant phase associated with the radially-symmetric real function f_j. The phase-dependent part of the interaction energy is minimized, provided [99]

$$w_{+1} - 2w_0 + w_{-1} = 0, \tag{4.5a}$$

$$\beta_{+1} - 2\beta_0 + \beta_{-1} = \begin{cases} 2n\pi & \text{for } c_1 < 0, \\ (2n'+1)\pi & \text{for } c_1 > 0, \end{cases} \tag{4.5b}$$

where n and n' are integers. Similarly, the SOAM-part of the energy is minimized if

$$w_{+1} - w_0 = 1, \quad w_0 - w_{-1} = 1, \tag{4.6a}$$

$$\beta_{+1} - \beta_0 = (2p+1)\pi, \quad \beta_0 - \beta_{-1} = (2p'+1)\pi, \tag{4.6b}$$

where p and p' are again integers. If the conditions on the winding numbers in Eq. (4.6a) are satisfied, the condition in Eq. (4.5a) is satisfied too. On the other hand, conditions between the constant phase factors in Eqs. (4.5b) and (4.6b) can be simultaneously satisfied for $c_1 < 0$ only.

To further substantiate the intercomponent phase relationships imposed by SOAM-coupling, we extract $\mathcal{S} = S_x \cos\phi - S_y \sin\phi$ [140] from the single-particle Hamiltonian H_s. In the limit when Ω_0 is large, c_1-dependent part of the Hamiltonian can be neglected, and the phase structure of the emergent ground-state solution is mainly determined by $\mathcal{S}$ via its minimum energy eigen spinor. The normalized eigen spinor of $\mathcal{S}$ with minimum eigen energy -1 can be written as $(e^{\iota(m+1)\phi},\ -\sqrt{2}e^{\iota m\phi},\ e^{\iota(m-1)\phi})^T/2$ with m being any integer. The phase structure of this eigenspinor is consistent with phase relations in Eqs. (4.6a) and (4.6b). With an increase in m, there is an energy cost from the phase-dependent part of the kinetic energy, suggesting that only small values of phase-winding numbers may emerge. Numerical results confirm this, where we obtain a solution corresponding to $m = 0$ in large Ω_0 limit irrespective of the nature of spin-exchange interactions. The spinor part of the ground state in this limit tends to approach the aforementioned eigenstate of $\mathcal{S}$ with $m = 0$.

Various numerical techniques have been employed in the literature to study spinor BECs in q1D, q2D, and 3D settings as discussed in Chapter 2 [172,181,207]. In practice, we choose the time-splitting finite-difference method and choose different initial guess solutions as an input to Eqs. (4.3a) and (4.3b) to arrive at ground-state solutions. As an example, we take initial states $\Psi \sim e^{-r^2/2} \times (e^{\iota(m+1)\phi},\ -\sqrt{2}e^{\iota m\phi},\ e^{\iota(m-1)\phi})^T/2$, with different values of m. Besides these initial states, we consider a random initial guess where $\psi_j(r)$ are complex Gaussian random numbers.

At the outset, motivated by the experimental realization of the SOAM-coupled BECs [135,136] using spin-1 ^{87}Rb atoms, we validate our numerical simulations to study and emulate the observed ground-state quantum phases of the ferromagnetic system in the absence of detuning $\delta = 0$ first and later with $\delta \neq 0$. It is to be noted that in the experiments [136], both zero and non-zero values of detuning have been considered. Similar to the experiment, we consider the ^{87}Rb atoms confined in an anisotropic harmonic trap with $\omega_0 = 2\pi \times 140$ Hz and $r_0 = 15$ μm [136]. However, we take $\omega_z = 2\pi \times 2400$ Hz, enabling us to perform q2D simulations. Here $a_0 = 101.8a_B$ and $a_2 = 101.4a_B$ with a_B as the Bohr radius [197]. The ground-state densities and phase distributions, obtained numerically by solving the CGPEs (4.3a) and (4.3b) with imaginary-time propagation, for given Ω_0 and N, are in qualitative agreement with the experimental results. The ground-state densities calculated for a pair of Ω_0 values with $N = 5000$ are shown in Figs. 4.1(a) and 4.1(b). For $\Omega_0 = 0.25$, the solutions with $(+2, +1, 0)$ and $(0, -1, -2)$ phase-winding numbers are two degenerate ground states, and with $\Omega_0 = 1$, $(+1, 0, -1)$ state is obtained as the ground state solution. As we vary Ω_0 from 0 to 20, at small Ω_0, due to the co-action of spin-dependent interaction term and SOAM coupling, (+2,+1,0)-type solution appears as the ground state. After a critical value of coupling strength (say Ω_0^c), $\Omega\mathcal{S}$ primarily dictates the nature of the solution to result in $(+1, 0, -1)$-type phase. The condition $\langle\mathcal{S}\rangle \approx -1$ is satisfied in this latter phase for sufficiently large Ω_0 as shown in Fig. 4.2(a), which indicates that no further phase can be expected with higher Ω_0. We term these two phases I and II. In contrast to ^{87}Rb, $(+1, 0, -1)$-type is the single ground state phase for ^{23}Na with $c_1 > 0$. In this case too, $\langle\mathcal{S}\rangle \approx -1$ at large Ω_0 as shown in Fig. 4.2(a).

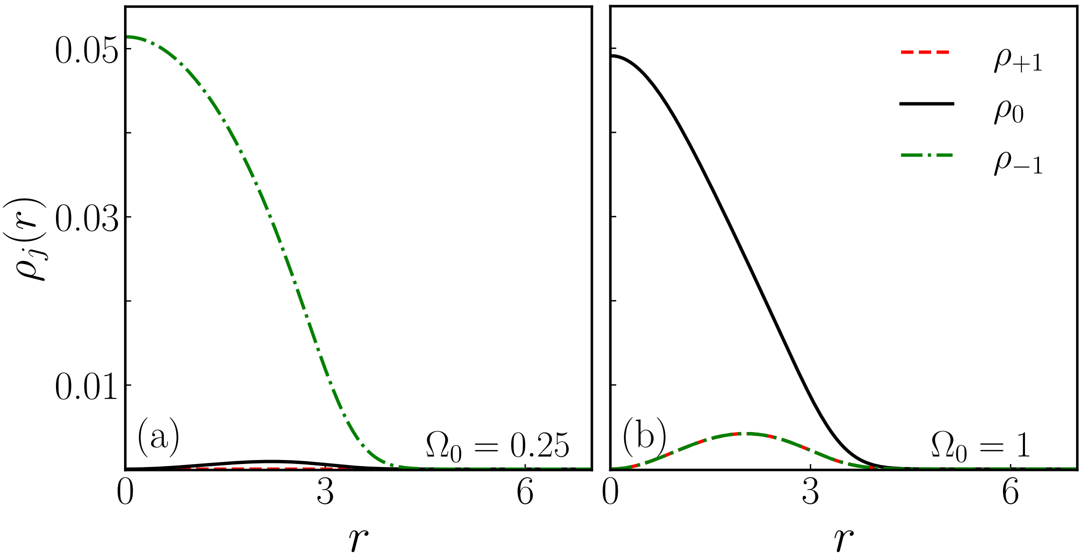

Figure 4.1: Ground-state densities of the SOAM-coupled ^{87}Rb spin-1 BEC with $c_0 = 121.28$ and $c_1 = -0.56$ corresponding to $N = 5000$ for (a) $\Omega_0 = 0.25$ and (b) $\Omega_0 = 1$. The $j = +1, 0$, and -1 spin components carry phase winding numbers of $+2, +1$, and 0, respectively, in (a) and $+1, 0$, and -1, respectively, in (b). As discussed in the text, the various quantities in this and the rest of the figures are dimensionless.

Longitudinal magnetization per particle $f_z = \int F_z d\mathbf{r}$, spin expectation per particle $f = \int |\mathbf{F}| d\mathbf{r}$ where $|\mathbf{F}| = \sqrt{F_x^2 + F_y^2 + F_z^2}$, and angular momentum per particle $\langle L_z\rangle$ can

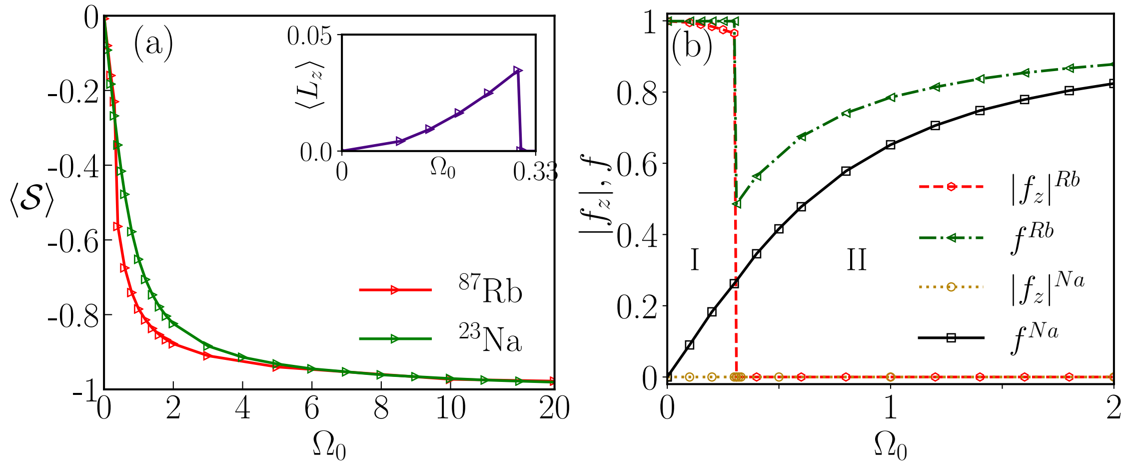

Figure 4.2: (a) $\langle\mathcal{S}\rangle$ as a function of SOAM-coupling strength Ω_0 for ^{87}Rb with $c_0 = 121.28$ and $c_1 = -0.56$ and ^{23}Na with $c_0 = 121.35$ and $c_1 = 3.80$. Inset in (a): $\langle L_z\rangle$ for ^{87}Rb as a function of Ω_0. (b) $|f_z|$ and f for ^{87}Rb and ^{23}Na as a function of SO coupling strength Ω_0. The c_0 and c_1 for ^{87}Rb and ^{23}Na are the same as those in (a).

be used to characterize these ground-state phases. In the ferromagnetic domain with $c_0 = 121.28$ and $c_1 = -0.56$, for $\Omega_0 <= \Omega_0^c = 0.3$, i.e. in phase I, $\langle L_z\rangle \neq 0$ and increases continuously as shown in the inset of Fig. 4.2(a), whereas $|f_z| \approx 1$ and $f = 1$ as shown in Fig. 4.2(b). For $\Omega_0 > \Omega_0^c$, the transition to phase II is accompanied by discontinuities in $\langle L_z\rangle, |f_z|$, and f, where the former two reduce to zero, the latter becomes less than one. In the antiferromagnetic domain, e.g. with $c_0 = 121.35$ and $c_1 = 3.8$, there is no phase transition with an increase in Ω_0 resulting in smooth behaviour of the same quantities. Here f asymptotically approaches one, whereas $|f_z|$ and $\langle L_z\rangle$, expectantly, remain zero.

Furthermore, we calculate the ground state phase diagrams in c_1/c_0-Ω_0 plane, where we fix $c_0 = 121.28$ and vary c_1, and N-Ω_0 plane for fixed $c_1/c_0 = -0.0046$ which corresponds to ^{87}Rb. The ratio c_1/c_0 may be manipulated experimentally by tuning one of the scattering lengths by optical Feshbach resonance [208]. These two are respectively shown in Figs. 4.3(a) and 4.3(b), thus again illustrating that an antiferromagnetic BEC has one ground-state phase in contrast to the ferromagnetic one. It can be seen that with a decrease in c_1 (keeping c_0 fixed) in the ferromagnetic phase, the domain of phase I increases, whereas with an increase in the number of atoms (keeping c_1/c_0 fixed), it decreases. Phase I and II also have distinctive topological spin textures $\mathbf{F} = (F_x, F_y, F_z)$. For the solutions in Figs. 4.1(a) and 4.1(b) spin-textures are shown in Figs. 4.4(a) and 4.4(b), respectively. The spin-textures in Figs. 4.4(a) and 4.4(b) are in agreement with those reported in Ref. [136]; at the centre, $\mathbf{F}$ points along negative z direction in Fig. 4.4(a), whereas it is zero in Fig. 4.4(b). The details of the spin-textures allow the identification of phases I and II with the coreless vortex and polar-core vortex states, respectively. It is to be noted that in Ref. [132], the two reported circularly symmetric phases correspond to $(-4, -2, 0)$- and $(-2, 0, +2)$-type solutions distinct from phases I and II in the present work.

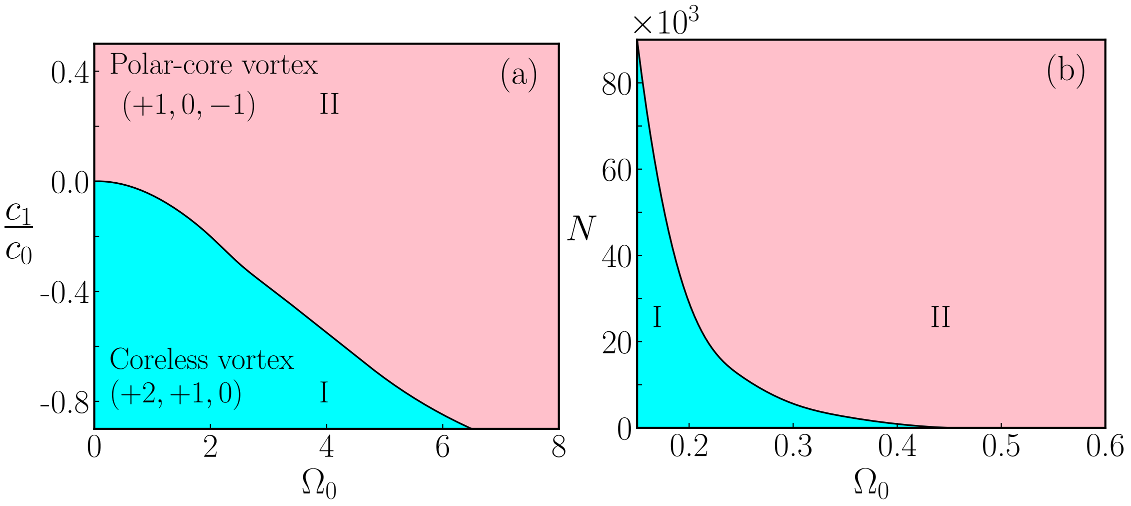

Figure 4.3: The ground-state phase diagrams in (a) c_1/c_0-Ω_0 and (b) N-Ω_0 planes. In (a) c_0 was kept fixed at 121.28 while varying c_1. In (b) $c_1/c_0 = -0.0046$ corresponding to ^{87}Rb.

4.3 Collective excitation spectrum

To study the excitation spectrum, we exploit the innate circular symmetry of the Hamiltonian. To this end, we perform a local spin rotation about $\hat{z}$ by the azimuthal angle -ϕ to remove the ϕ dependence from the Hamiltonian. As a result, the order parameter $\Psi = (\psi_{+1}, \psi_0, \psi_{-1})^T$ is transformed to $e^{-\iota S_z \phi}\Psi = (e^{-\iota\phi}\psi_{+1}, \psi_0, e^{\iota\phi}\psi_{-1})^T$, and the transformed Hamiltonian takes form

$$H = \left[-\frac{1}{2}\frac{\partial}{r\partial r}\left(r\frac{\partial}{\partial r}\right) + \frac{(L_z+S_z)^2}{2r^2} + V(r)\right]\mathbf{I} + \Omega(r)S_x + H_{\text{int}}, \tag{4.7}$$

where $H_{\text{int}} = c_0\rho/2 + c_1\mathbf{F}.\mathbf{S}/2$. The Hamiltonian in Eq. (4.7) is circularly symmetric, and one can seek the simultaneous eigenfunctions of H and L_z with fixed angular momentum $l_z = 0, 1, \ldots$. For example, the solutions presented in Figs. 4.1(a) and 4.1(b) can now be seen as corresponding to $l_z = 1$ and 0, respectively. The single-particle Hamiltonian in Eq. (4.1) is symmetric under the transformation defined by an operator $\mathcal{R} = \exp(-iS_x\pi)K$, where K is complex-conjugation operator. This implies that for any $l_z \neq 0$, there will be two degenerate solutions connected by $\mathcal{R}$. For example, for $l_z = 1$, the degenerate counterpart with $l_z = -1$ corresponds to $(0, -1, -2)$ phase-winding numbers in the component wavefunctions.

We use the Bogoliubov approach to study the excitation spectrum. In which we consider the fluctuations to the ground state by writing the perturbed order parameter as

$$\Psi(r,\phi,t) = e^{-\iota\mu t + \iota(l_z+S_z)\phi}[\Psi_{\text{eq}}(r) + \delta\Psi(r,t)e^{\iota l_q\phi}], \tag{4.8}$$

where $\Psi_{\text{eq}}(r) = [R_{+1}(r), R_0(r), R_{-1}(r)]^T$ is the radial part of the order parameter with R_j as the radial wavefunction corresponding to the j^{th} spin component, μ is the chemical

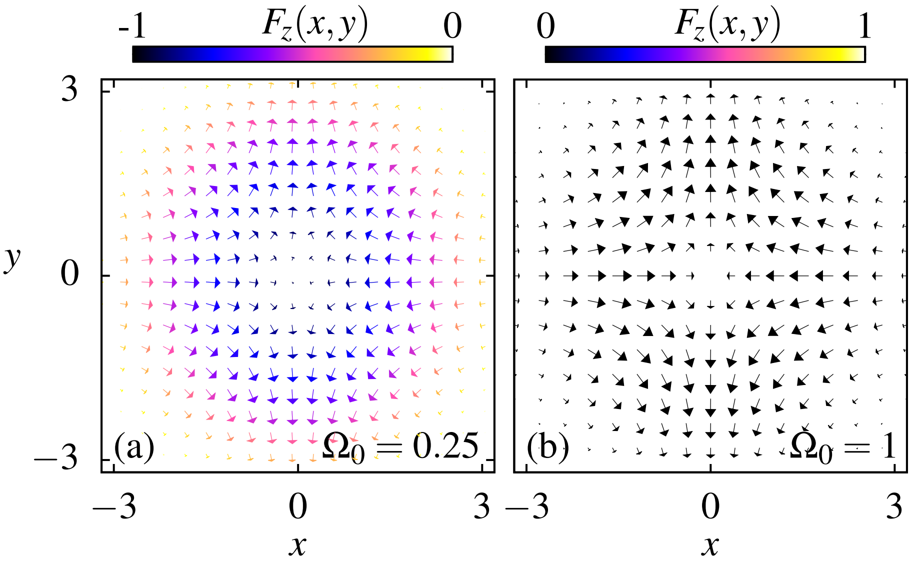

Figure 4.4: (a) and (b) show the spin-texture for 5000 atoms of ^{87}Rb system with the coupling strength $\Omega_0 = 0.25$ and $\Omega_0 = 1$, respectively. The length of the arrows shows the projection of $\mathbf{F}(x, y)$ on the x-y plane, and the colour bar indicates its component along z axis; $\mathbf{F}(x, y)$ vector field lies on the x-y plane in (b).

potential, and $l_q = 0, \pm1, \pm2, \ldots$ is the magnetic quantum number associated with the angular momentum of the quasiparticle excitations. The details of the BdG analysis are given in Appendix B.

4.3.1 Non-interacting system

To understand the effect of coupling strength, we first study the single-particle excitation spectrum. The ground-state solution has phase-winding numbers $(\pm1, 0)$ in $j = \pm1, 0$ spin states, respectively. The excitation spectrum is shown in Fig. 4.5. For $\Omega_0 = 0$, the n^{th} energy level is $3(n + 1)$-fold degenerate, as the single-particle Hamiltonian is identical to a system of three decoupled isotropic two-dimensional harmonic oscillators. For example, excitations with energies 0 and 1 are three- and six-fold degenerate, respectively. The SOAM-coupling lifts the degeneracies partially. For example, for $\Omega_0 \neq 0$, there is only one zero-energy excitation; similarly, the red lines in the spectrum in Fig. 4.5 correspond to non-degenerate excitations, whereas the black ones to two-fold degenerate modes. The non-degenerate modes have the magnetic quantum number of the excitation $l_q = 0$, whereas modes with two-fold degeneracy have $l_q \neq 0$.

4.3.2 Interacting spin-1 BEC

Here we study the excitation spectrum (a) as a function of Ω_0 for fixed c_0 and c_1 and (b) as a function of N for fixed Ω_0 and c_0/c_1 ratio. Both Ω_0 and N can be varied in an experiment [135,136]. As was discussed in Sec. 4.2, for $c_1 < 0$, both phases I and II can appear as the ground-state phases with a variation of either Ω_0 or N. We primarily consider ^{87}Rb BEC in the following discussion.

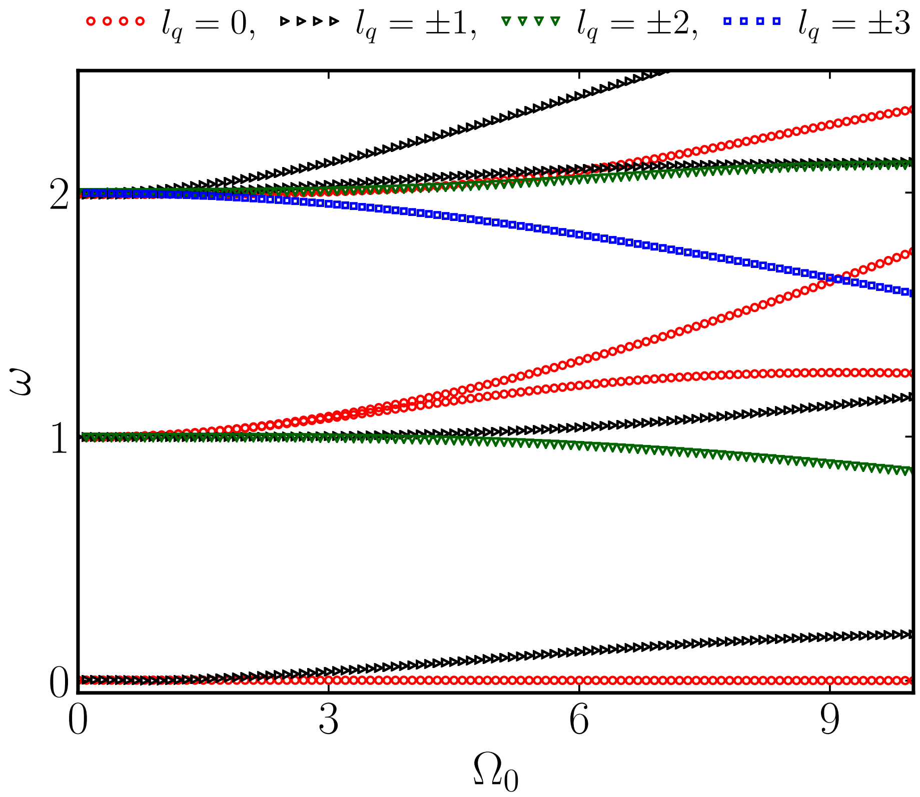

Figure 4.5: (Color online) Single particle excitation spectrum for spin-1 BEC as a function of SOAM coupling strength ω_0.

Phase I: Here we consider $c_0 = 121.18$ and $c_1 = -0.56$ and vary Ω_0. The excitation spectrum for phase I is shown in Fig. 4.6(a) for $l_q = 0, \pm 1$ and (b) for $|l_q| \geq 2$. The modes with frequencies 1 and 2 are, respectively, dipole and density-breathing modes in Fig. 4.6(a) . This identification of a mode is based on the real-time evolution of the expectation of a suitably chosen observable, as will be discussed in the next subsection. The presence of ferromagnetic interactions further aids the lifting of the degeneracy, in this case between the modes with magnetic quantum numbers $\pm l_q$, which are degenerate at the single-particle level. We have confirmed this, for example, by examining the excitation spectrum of a system with $c_0 = 121.18$ and $c_1 = -0.6c_0 \ll -0.56$ (not shown here), where the non-degenerate nature of the spectrum is clearly seen. In phase I, there are two zero-energy Goldstone modes corresponding to two broken continuous symmetries, namely gauge and rotational symmetry. The latter corresponds to the symmetry transformation generated by L_z.

Phase II: As already mentioned in Sec. 4.2, the transition from phase I to II occurs at $\Omega_0 > 0.3$ for $c_0 = 121.18$ and $c_1 = -0.56$. The transition is accompanied by the discontinuities in the excitation spectrum. The excitation spectrum for phase II is shown in Fig. 4.6(c). Here, among the low-lying modes are dipole and breathing modes corresponding to both density and spin channels. Both density- and spin-dipole modes are doubly degenerate, corresponding to magnetic quantum number $l_q = \pm 1$. On the other hand, both density- and spin-breathing modes are non-degenerate with $l_q = 0$.

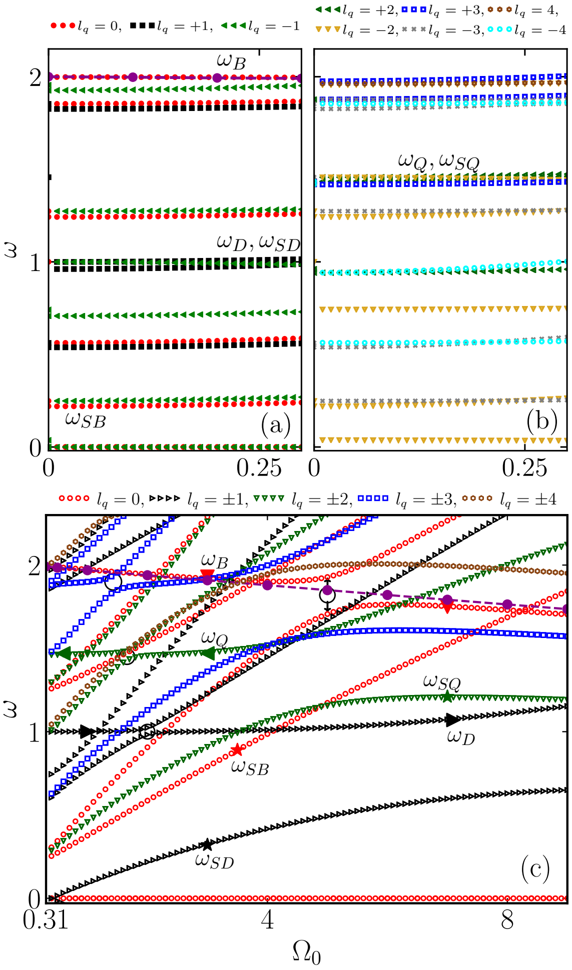

Figure 4.6: Low-lying excitation spectrum of ^{87}Rb SOAM-coupled spin-1 BEC with $c_0 = 121.18$ and $c_1 = -0.56$ as a function of coupling strength Ω_0 of phase I with $l_q = 0, \pm 1$ in (a) and $l_q = \pm 2, \pm 3, \pm 4, \ldots$ in (b); among the named modes, $l_q = 0$ for density- and spin-breathing, $l_q = +1$ for density-dipole, $l_q = -1$ for spin-dipole, $l_q = +2$ for density-quadrupole, and $l_q = -2$ for spin-quadrupole modes. (c) shows the same for phase II, where $l_q = 0$ for density- and spin-breathing, $l_q = \pm 1$ for density- and spin-dipole, $l_q = \pm 2$ for density- and spin-quadrupole modes. In (a) and (c), the dashed magenta-colored line is the variational estimate for the density-breathing mode.

At small values of Ω_0, the energies of the spin modes are less than their density-mode analogues. There is a single zero-energy mode due to the broken gauge symmetry in this phase. Besides these modes, the density- and spin-quadrupole modes are also marked in the excitation spectrum in Figs. 4.6(a)-4.6(c). As the collective excitations characterize a system's response to small perturbations, these can be experimentally studied using Bragg spectroscopy [209,210].

Additionally, the variation in SOAM-coupling strength leads to avoided crossings between the pairs of excitations, a few of which are identified by the black circles in Fig. 4.6(c). We observe that the avoided crossing occur between the density and spin oscillations associated with the same magnetic quantum number l_q. In the vicinity of the avoided crossing, the roles of the density and spin modes are interchanged as shown in Fig. 4.6(c). We study this mode mixing by examining the density ($\delta\rho$) and spin fluctuations

$(\delta F_x, \delta F_y, \delta F_z)$ yielded by the perturbed order parameter and defined as

$$\begin{aligned}
\delta\rho =& 2\mathrm{Re}\sum_j \psi_j \delta\psi_j^*, && (4.9a)\\
\delta F_x =& \sqrt{2}\mathrm{Re}(\psi_{+1}\delta\psi_0^* + \psi_0\delta\psi_{+1}^* + \psi_{-1}\delta\psi_0^* + \psi_0\delta\psi_{-1}^*), && (4.9b)\\
\delta F_y =& -\sqrt{2}\mathrm{Im}(-\psi_{+1}\delta\psi_0^* + \psi_0\delta\psi_{+1}^* + \psi_{-1}\delta\psi_0^* - \psi_0\delta\psi_{-1}^*), && (4.9c)\\
\delta F_z =& 2\mathrm{Re}(\psi_{+1}\delta\psi_{+1}^* - \psi_{-1}\delta\psi_{-1}^*), && (4.9d)
\end{aligned}$$

where 'Re' and 'Im' denote the real and imaginary part, respectively. For a pure density mode, one would expect that $\delta\rho \neq 0$ and $\delta F_\nu = 0$, similarly for a pure spin mode one would expect that $\delta\rho = 0$ and at least one of the $\delta F_\nu \neq 0$. The order-parameter fluctuation $\delta\Psi(r, \phi, t)$, and hence density and spin fluctuations, can be constructed with the Bogoliubov quasiparticle amplitudes u and v corresponding to the frequency ω of the mode as $\delta\psi_j(r, \phi, t) \propto e^{\iota(l_z+j+l_q)\phi}\left[u_j(r)e^{-\iota\omega t} - v_j^*(r)e^{\iota\omega t}\right]$. In the excitation spectrum in

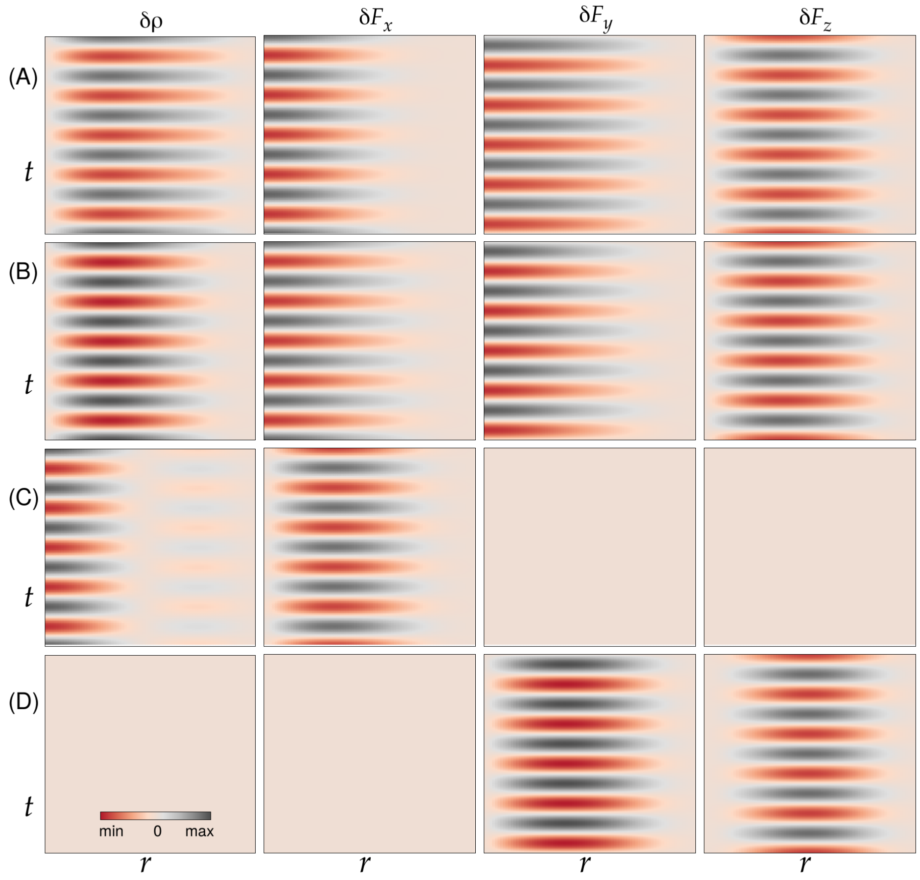

Figure 4.7: (A) shows the density fluctuations, $\delta\rho(r, \phi = 0, t)$, and spin-density fluctuations, $\delta F_\nu(r, \phi = 0, t)$, with $\nu = x, y, z$ corresponding to $\omega_D = 1$. (B)-(D) present the same for $\omega_{SD} = 0.08$, $\omega_B = 1.97$, $\omega_{SB} = 0.37$, respectively. The radial and time extents, along horizontal and vertical directions, respectively, in each subfigure are $4a_{\mathrm{osc}}$ and $5T$, respectively, where $T = 2\pi/\omega$ is the time period of the corresponding mode with ω frequency. The presence of both density and spin fluctuations in (A)-(C) is an outcome of the avoided crossing between the pairs of modes in the excitation spectrum shown in Fig. 4.6(c).

Fig. 4.6(c) at $\Omega_0 = 1$, the density- and spin-dipole modes' frequencies are $\omega_D = 1$ and $\omega_{SD} = 0.08$, respectively, and the density- and spin-breathing modes' frequencies are $\omega_B = 1.97$ and $\omega_{SB} = 0.37$, respectively. One can see that the density-dipole, density-breathing, and spin-dipole modes encounter avoided crossings, whereas the spin-breathing mode does not. This observation agrees with the density and spin-density fluctuations evaluated along the $\phi = 0$ line and shown in Figs. 4.7(A)-4.7(D). For the density-dipole mode with $\omega_D = 1$, both density and spin channels are excited as is seen from $\delta\rho(r, \phi = 0, t)$ and $\delta F_\nu(r, \phi = 0, t)$ in Fig. 4.7(A), where $\nu = x, y, z$. Similarly, number density, longitudinal (F_z), and transverse magnetization (F_x, F_y) densities oscillate in time, corresponding to the spin-dipole mode in Fig. 4.7(B), and density-breathing mode ends up exciting both the number and transverse magnetization densities in Fig. 4.7(C). On the other hand, the spin-breathing mode excites the spin channel alone in Fig. 4.7(D). The density and spin-quadrupole modes also excite the density and spin fluctuations, which are not shown. This mode mixing indicated by both density and spin fluctuations is absent in q1D SO-coupled BECs where any collective excitation yields either density or spin fluctuations [211]. The nomenclature of the modes in Figs. 4.6(a)-4.6(c) is consistent with the density, $\delta\rho(x, y, t)$, and longitudinal magnetization density, $\delta F_z(x, y, t)$, fluctuations corresponding to density, breathing, and quadrupole modes in Fig. 4.8 shown at $t = 0, T/4, T/2, 3T/4$, and T instants, where T is the period of the collective excitation.

Next, we study the excitation spectrum as a function of N for $c_1/c_0 = -0.0046$. Here first, we fix Ω_0 to 0.3, where a phase transition from phase I to II occurs at $N = 5700$. The excitation spectrum, in this case, for phase I and II are shown in Figs. 4.9(a) and 4.9(b). The same for $\Omega_0 = 3$ is shown in Fig. 4.9(c), where phase II is the ground state phase with no phase transition. The modes in phase II are, again, either non-degenerate or with two-fold degeneracy. For SOAM-coupled ^{23}Na BEC with $c_0 = 121.35$ and $c_1 = 3.8$ the excitation spectrum, which is not shown here, is similar to the spectrum in Fig. 4.9(c) with some quantitative differences attributable to different c_1 values.

4.3.3 Non-zero detuning

In this subsection, we consider the effects of the detuning on the phase diagram and excitation spectrum. In Fig. 4.10, we show the phase diagram in the number of atoms versus the detuning (N-δ) plane for a constant coupling strength of $\Omega_0 = 5$ and $c_1/c_0 = -0.0046$ corresponding to ^{87}Rb. We observe for a small value of δ, the polar-core vortex (phase II) emerges as the ground-state solution. However, at a critical detuning δ_c, a phase transition from (+1,0,-1)-type solution (phase II) to (+2,+1,0)-type solution (phase I) occurs. For example, for $\Omega_0 = 5$ and $N = 5000$ corresponding to $c_0 = 121.18$, $c_1 = -0.56$, the phase transition occurs at $\delta_c = 0.3$. Phase II at smaller detuning and phase I at larger detuning values in Fig. 4.10 is in qualitative agreement with the experimental findings [136]. It is worth noting that the presence of δ in the Hamiltonian leads to the breakdown of the symmetry defined by $\mathcal{R}$. As a result, (+2,+1,0) and (0,-1,-2)-type solutions corresponding to $l_z = 1$ and -1, respectively, are no longer degenerate. To

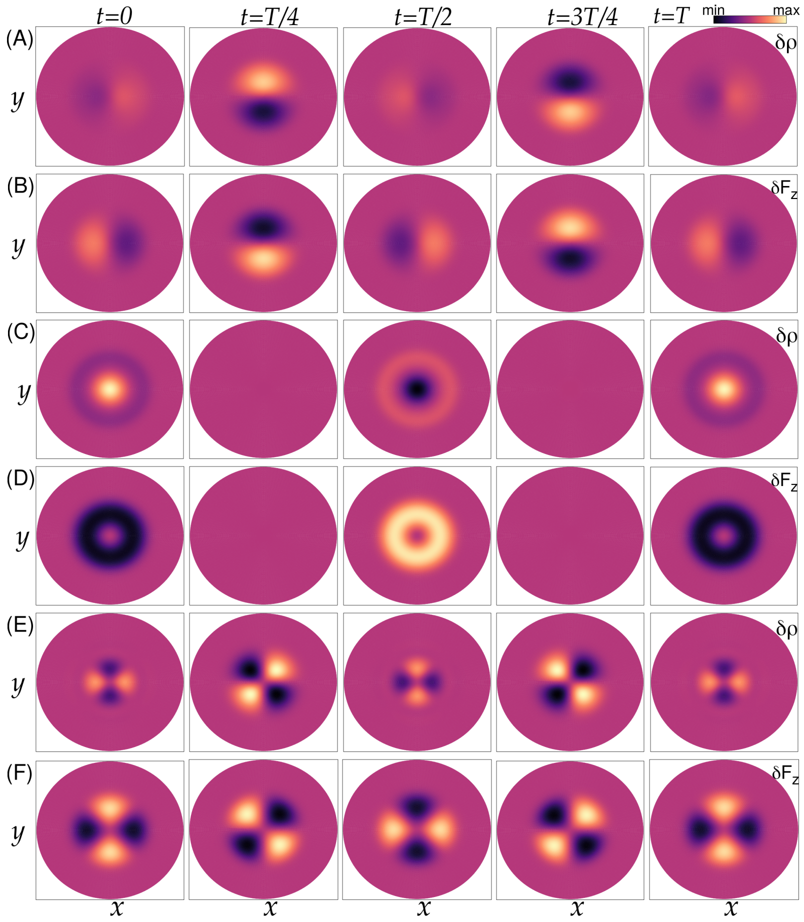

Figure 4.8: Density and longitudinal magnetization density fluctuations at $t = 0, T/4, T/2, 3T/4$, and T where $T = 2\pi/\omega$ with ω as the mode-frequency: (A) $\delta\rho(x, y, t)$ for the density-dipole mode with $\omega_D = 1$, (B) $\delta F_z(x, y, t)$ for the spin-dipole mode with $\omega_{SD} = 0.08$, (C) $\delta\rho(x, y, t)$ for the density-breathing mode with $\omega_B = 1.97$, (D) $\delta F_z(x, y, t)$ for the spin-breathing modes with $\omega_{SB} = 0.37$, (E) $\delta\rho(x, y, t)$ for the density-quadrupole mode with $\omega_Q = 1.46$, and (F) $\delta F_z(x, y, t)$ for the spin-quadrupole mode with $\omega_{SQ} = 0.46$. The box size in each subfigure is $6.4a_{\mathrm{osc}} \times 6.4a_{\mathrm{aosc}}$.

illustrate the effect of detuning on the excitation spectrum, we contrast the collective excitation spectrum of the condensate with $N = 5000$, $\Omega_0 = 5$ for (a) $\delta = 0$ and (b) $\delta = 0.2$. The ground-state phase in both these cases is phase II, as can be seen from the phase diagram in Fig. 4.10. The excitation frequencies as a function of l_q for these two cases are shown in Figs. 4.11(a) and 4.11(b). As discussed in Appendix B, the presence of detuning leads to the lifting of the degeneracies in the excitation spectrum about $l_q = 0$. The low-lying modes have been identified in Figs. 4.11(a) and 4.11(b). In Fig. 4.11(a), the density-dipole, spin-dipole, density-quadrupole, and spin-quadrupole exhibit two-fold degeneracies corresponding to $\pm l_q$. However, in the presence of δ, all these modes become non-degenerate and are highlighted in Fig. 4.11(b).

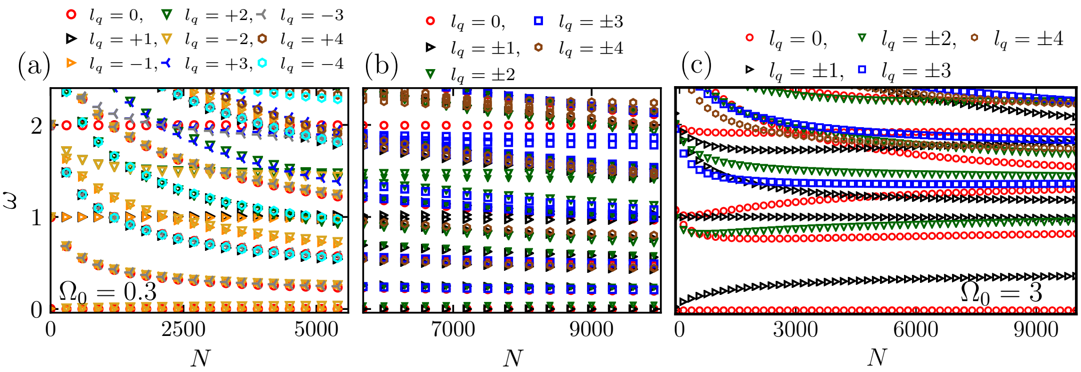

Figure 4.9: Low-lying excitation spectrum for ^{87}Rb spin-1 BEC with $c_1/c_0 = -0.0046$ as a function of the number of atoms N: (a)-(b) for $\Omega_0 = 0.3$ with a phase transition from phase I to II at $N = 5700$ and (c) $\Omega_0 = 3$. (a) corresponds to the spectrum of phase I, whereas (b) and (c) correspond to the spectrum of phase II. The different point styles in (a) signify non-degenerate modes with different l_q, while in (b) and (c), 'red circle', 'black right-pointing triangle, 'green down-pointing triangle', and 'blue square' correspond, respectively to the modes with $l_q = 0, \pm 1, \pm 2, \pm 3$, and so on.

4.3.4 Dynamics

We examine the nature of low-lying collective excitations through the time evolution of the expectation of physical observables, which also serves to validate our calculation of the excitation spectrum from the BdG equations. Here, we consider the Hamiltonian with an appropriately chosen time-independent perturbation, say $H'_{\rm s}$ added to its single-particle part $H_{\rm s}$. This modifies the CGPEs (4.3a) and (4.3b) with an added term corresponding to $H'_{\rm s}\Psi(r, \phi, t)$ in each equation. We then solve these resultant CGPEs over a finite period of time by considering previously obtained ground-state solutions as the initial solutions at $t = 0$. Numerically, one needs to consider a two-dimensional spatial grid over here, for which we choose the Cartesian x-y grid.

We consider $c_0 = 121.28$, $c_1 = -0.56$, and $\Omega_0 = 1$, which yielded the ground-state phase in Fig. 4.1(b) as an example set of parameters to study the dynamics. To excite the density-dipole mode, we take the perturbation $H'_{\rm s} = \lambda x$, where $\lambda \ll 1$. We then examine the dynamics of the center of mass of the BEC via $x_{\rm cm}(t) = \langle x \rangle = \sum_{j=\pm1,0} \int x\rho_j(x, y, t)dxdy$ which is plotted in Fig. 4.12(a). We also compute its Fourier transform $\widehat{x}_{\rm cm}(\omega)$ to demonstrate that the dominant frequency resonates at $\omega = 1$ as can be seen in Fig. 4.12(b) and matches with $\omega_{\rm D} = 1$ in the BdG spectrum in Fig. 4.6(c). We could have chosen $H'_s = \lambda y$ and then calculated $y_{\rm cm}(t)$ giving us the same excitation frequency. This is a consequence of the two-fold degeneracy in the density-dipole mode. We have checked that this mode can also be excited by shifting the minima of the external trapping potential. This particular way of exciting this mode has direct relevance from an experimental point of view, where the minima of potential can be easily shifted. Similarly, to examine the excitation of the density-breathing mode with $H'_{\rm s} = \lambda(x^2 + y^2)$, where the relevant observable is $r^2 = x^2 + y^2$, we calculate mean square radius $r^2_{\rm ms}(t) = \langle r^2 \rangle$

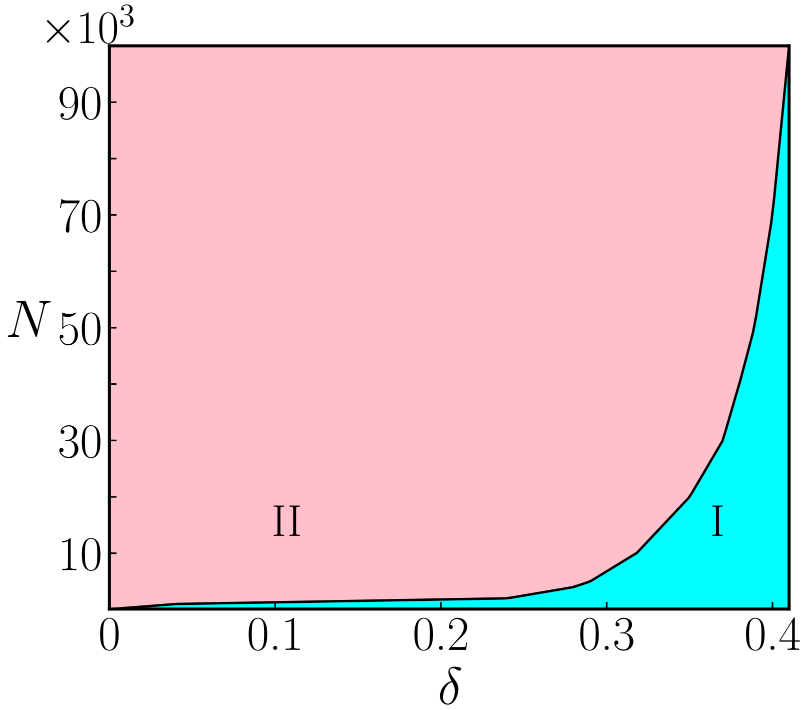

Figure 4.10: The ground-state phase diagrams in N-δ plane for $c_1/c_0 = -0.0046$ corresponding to ^{87}Rb spin-1 BEC and $\Omega_0 = 5$.

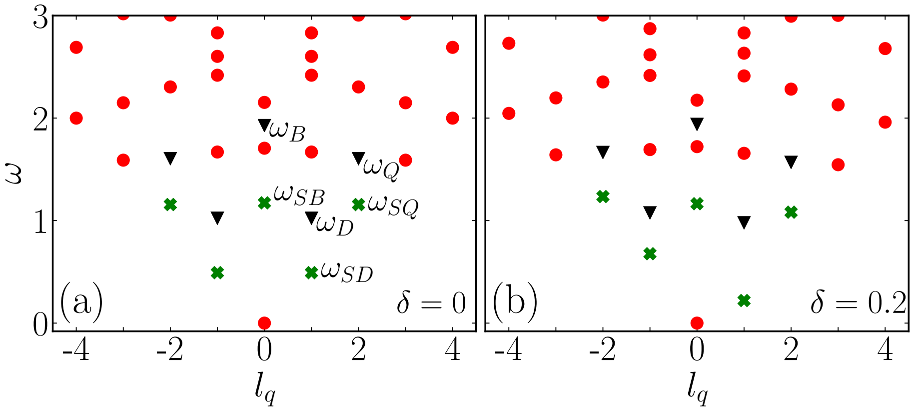

Figure 4.11: Collective excitation spectrum for ferromagnetic ^{87}Rb spin-1 BEC with interaction parameters $c_0 = 121.28$, $c_1 = -0.56$, and coupling stength $\Omega_0 = 5$ for (a) $\delta = 0$ and (b) $\delta = 0.2$. The 'black down-pointing triangles' and 'green crosses' denote the density and spin modes, respectively.

as a function of time, which is plotted in Fig. 4.12(c). The Fourier transform $\widehat{r^2_{\rm ms}}(\omega)$ of $r^2_{\rm ms}(t)$ reveals a dominant peak at $\omega = 1.99$ in Fig. 4.12(d) which is close to BdG result of $\Omega_{\rm B} = 1.97$. This mode, again, can be excited by perturbing the trap strength, which can be achieved in an experiment with ease and thus giving access to this mode. Similarly, the spin-dipole mode can be excited by adding a perturbation $H' = \lambda x S_z$ or $\lambda y S_z$ with xS_z or yS_z as the pertinent observable corresponding to the spin-dipole mode. The two possible observables again reflect the two-fold degeneracy of spin-dipole

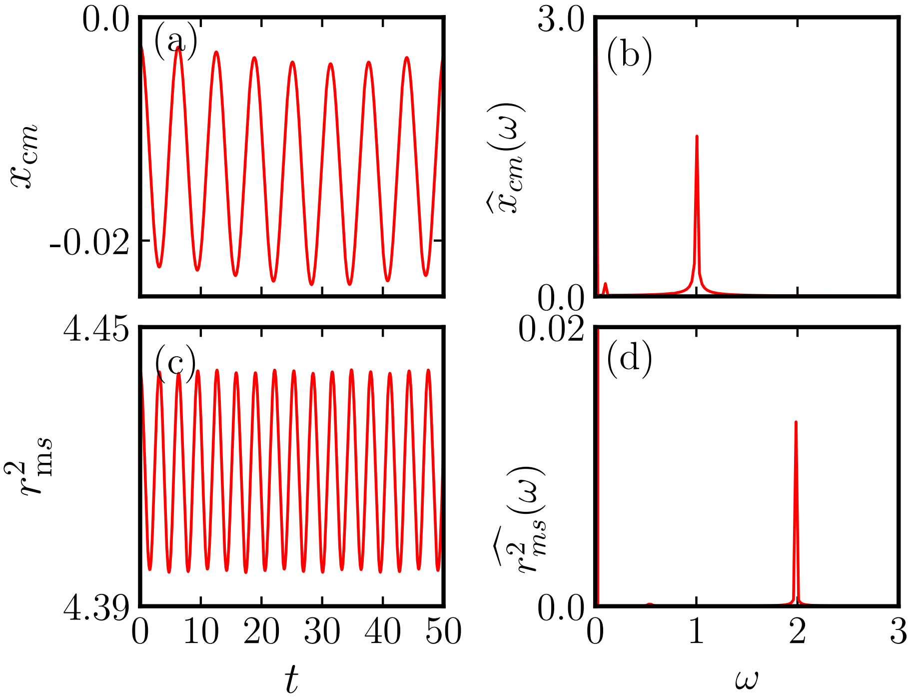

Figure 4.12: (a) shows the center of mass oscillations, i.e. $x_{\rm cm}(t)$ as a function of time and (b) corresponding Fourier transform with a dominant peak at $\omega = 1$ for ^{87}Rb spin-1 BEC with $c_0 = 121.28$, $c_1 = -0.56$, and $\Omega_0 = 1$. (c) shows the oscillations in the mean square size of the system $r^2_{\rm ms}(t)$ and (d) the corresponding Fourier transform with a dominant peak at $\omega = 1.99$ for the same interaction and coupling strengths.

modes. The time-variation of $d_x(t) = \langle xS_z\rangle = \sum_{j=+1,-1}\int x\rho_j(x,y,t)dxdy$ is shown in Fig. 4.13(a) and its Fourier transform in Fig. 4.13(b) has a dominant peak at $\omega = 0.1$, which corresponds to the spin-dipole mode labelled in Fig. 4.6(c) with $\omega_{\rm SD} = 0.08$. Similarly, the spin-breathing mode corresponds to observable r^2S_z. In Figs. 4.13(c) and 4.13(d), we show the dynamics of $d_r^2(t) = \langle r^2S_z\rangle$, i.e. the relative difference in the mean-square radii of the $j = \pm1$ components and the associated Fourier transform, respectively, with a dominant peak at $\omega = 0.37$, in agreement with $\omega_{\rm SB}$ in Fig. 4.6(c). The very small secondary peaks present in Fig. 4.12(b) and 4.12(d) correspond to the spin-dipole and spin-breathing modes, respectively. These peaks become prominent when subjected to appropriate perturbations and are observed through relevant observables, as shown in Fig. 4.13. Likewise, the small peaks appearing in Fig. 4.13(b) and 4.13(d) also signify modes present in the BdG spectrum. Finally, the density- and spin-quadrupole modes' frequencies calculated from the time evolution of $\langle xy\rangle$ and $\langle xyS_z\rangle$ are in agreement with the numbers in Fig. 4.6(c).

4.3.5 Variational analysis

For an SOAM-coupled spin-1 system, a few low-lying modes can be studied using a time-dependent variational method [212]. For example, to calculate the density-breathing

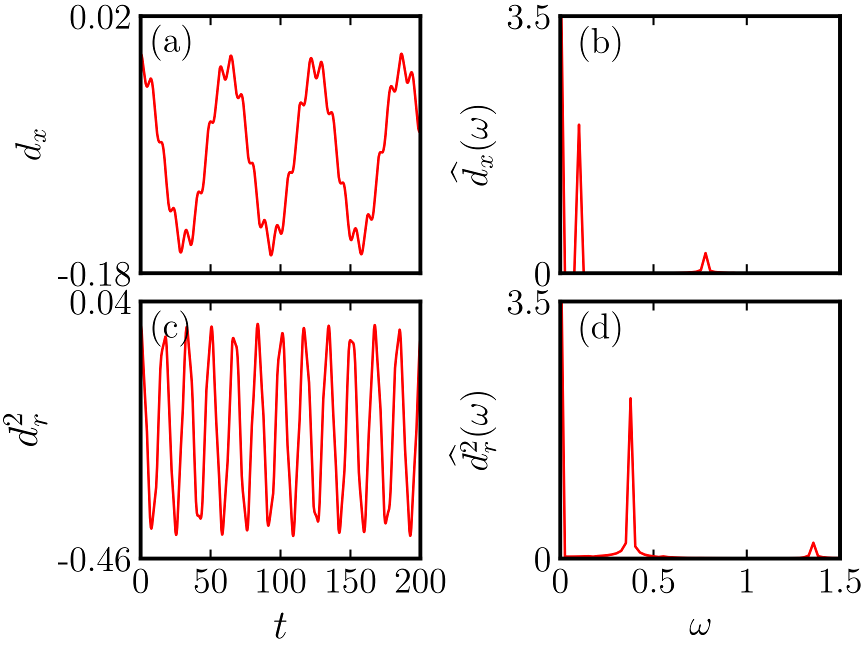

Figure 4.13: (a) shows $d_x(t)$ as a function of time and (b) corresponding Fourier transform with a dominant peak at $\omega = 0.1$ for ^{87}Rb spin-1 BEC with $c_0 = 121.28$, $c_1 = -0.56$, and $\Omega_0 = 1$. Similarly, (c) and (d) show the $d_x^2(t)$ and its Fourier transform with a dominant peak at $\omega = 0.37$ for the same interaction and coupling strengths.

mode in the absence of detuning, we consider the following variational ansatz

$$\Psi = \frac{r}{2\sqrt{\pi}\sigma(t)^2} \exp\left[-\frac{r^2}{2\sigma(t)^2} + \iota\alpha(t)r^2\right] \times \begin{pmatrix} e^{\iota(m+1)\phi} \\ -\sqrt{2}e^{\iota m\phi} \\ e^{\iota(m-1)\phi}, \end{pmatrix} \tag{4.10}$$

where $\sigma(t)$ and $\alpha(t)$ are time-dependent variational parameters used to denote the width of condensate and chirp of Gaussian pulse, respectively, and $m = \pm 1$ for phase I or 0 for phase II. The Lagrangian of the system is given by

$$L = \sum_j \int dr d\phi \frac{\iota}{2}\left(\psi_j^* \frac{\partial \psi_j}{\partial t} - \psi_j \frac{\partial \psi_j^*}{\partial t}\right) - E, \tag{4.11}$$

where energy E is defined as

$$\begin{aligned} E = \iint \Bigg[& \sum_j \psi_j^* \left\{-\frac{1}{2r}\frac{\partial}{\partial r}\left(r\frac{\partial}{\partial r}\right) + \frac{L_z^2}{2r^2} + \frac{r^2}{2}\right\}\psi_j + \frac{c_0}{2}\rho^2 + \frac{c_1}{2}(\rho_{+1} + \rho_0 - \rho_{-1})\rho_{+1} \\ & + \frac{c_1}{2}(\rho_{+1} + \rho_{-1})\rho_0 + \frac{c_1}{2}(\rho_{-1} + \rho_0 - \rho_{+1})\rho_{-1} + \sqrt{2}\Omega(r)\mathrm{Re}(\psi_{+1}^* e^{i\phi}\psi_0 + \psi_{-1}^* e^{-i\phi}\psi_0) \\ & + 2c_1\mathrm{Re}(\psi_{-1}^*\psi_0^2\psi_{+1}^*)\Bigg] dr d\phi. \end{aligned} \tag{4.12}$$

For $m = \pm 1$, the (coupled) Euler-Lagrange equations are

$$\ddot{\sigma}(t) = \frac{\sigma}{2}\left(\frac{6\sqrt{2\pi}\sqrt{e}\Omega_0\sqrt{\frac{1}{r_0^2}+\frac{2}{\sigma^2}}\left(r_0^7 - 2r_0^5\sigma^2\right)}{\left(2r_0^2+\sigma^2\right)^4} - 2\right) + \frac{c_0+c_1+10\pi}{8\pi\sigma^3}, \tag{4.13a}$$

$$\alpha = \frac{\dot{\sigma}}{2\sigma}, \tag{4.13b}$$

where $\dot{}$ denotes the time derivative. The equilibrium width σ_0 of the condensate satisfies

$$\frac{c_0+c_1+10\pi}{4\pi\sigma_0^4} + \frac{6\sqrt{2\pi}\sqrt{e}\Omega_0\sqrt{\frac{1}{r_0^2}+\frac{2}{\sigma_0^2}}\left(r_0^7 - 2r_0^5\sigma_0^2\right)}{\left(2r_0^2+\sigma_0^2\right)^4} = 2.$$

The frequency of the oscillation in width calculated by linearizing Eq. (4.13a) about equilibrium width σ_0 is

$$\omega_B^{\mathrm{I}} = \left[\frac{15\sqrt{2\pi}r_0^4\sqrt{e}\sigma_0\Omega_0(3r_0^2-2\sigma_0^2)\sqrt{2r_0^2+\sigma_0^2}+1}{(2r_0^2+\sigma_0^2)^5} + \frac{3(c_0+c_1+10\pi)}{8\pi\sigma_0^4}\right]^{1/2}. \tag{4.14}$$

Similarly, for $m = 0$ in Eq. (4.10), the density breathing mode is

$$\omega_B^{\mathrm{II}} = \left[\frac{15\sqrt{2\pi}r_0^4\sqrt{e}\sigma_0\Omega_0(3r_0^2-2\sigma_0^2)\sqrt{2r_0^2+\sigma_0^2}+1}{(2r_0^2+\sigma_0^2)^5} + \frac{3(c_0+c_1+6\pi)}{8\pi\sigma_0^4}\right]^{1/2}. \tag{4.15}$$

The variationally calculated density-breathing mode's frequency agrees with the values in the BdG spectrum as demonstrated in Figs. 4.6(a) and 4.6(c) for phases I and II, respectively. As mentioned in Sec. 4.3.4, density breathing mode can be easily excited by modulating the trapping potential strength in an experiment.

4.4 Summary

We have investigated the low-lying collective excitations of the coreless and the polar-core vortex phases supported by the spin-1 BECs with SOAM coupling. The existence of the two phases is seen in the full phase diagrams in the *ratio of interaction strengths* versus *coupling strength* and also the *number of atoms* versus *coupling strength* planes. We have studied the excitation spectrum as a function of two experimentally controllable parameters, namely coupling strength and the number of atoms. The excitation spectrums are characterized by the discontinuities across the phase boundary between the two phases and within a phase by avoided crossings between the modes with the same magnetic quantum number of excitations. The avoided crossings signal the hybridization of the density and spin channels; the nature of spin and density fluctuations has indeed confirmed this. Among the low-lying modes, we identify dipole, breathing, and quadrupole modes for density and spin channels. The frequencies of these named modes are further validated from the time evolution of the expectations of the physical observables when an apt time-independent perturbation is added to the system's Hamiltonian. An analytic estimate for the density-breathing modes has also been obtained using the variational analysis. Our results can serve as a benchmark to compute the finite-temperature phase diagram and spin dynamics. With the experimental observation of collective excitation, dispersion (excitation energies as a function of wavenumber) in Raman-induced SO-coupled BECs [209,210], we expect that our results can also be verified in future SOAM-coupled experiments. The results reported in this chapter are discussed in Ref. [213].

Chapter 5

Excitation spectrum of an annular-stripe phase in an SOAM-coupled spin-1 BEC

With the SOAM-coupling models corresponding to larger orbital angular momentum imparted by the pair of Laguerre-Gaussian beams to the BEC atoms, the annular stripe phase can emerge as one of the ground state phases [142,143]. With such an SOAM-coupling model, in this chapter, we study the ground-state phases and their collective excitation spectrums with a special focus on the the annular stripe phase, which spontaneously breaks two continuous symmetries: rotational and U(1) gauge symmetry.

The chapter is organized as follows. In Sec. 5.1, we discuss the ground-state solutions and excitation spectrum of the single particle Hamiltonian for an SOAM-coupled spin-1 system. In Sec. 5.2, we describe the interacting mean-field model and discuss ground-state phases of an SOAM-coupled antiferromagnetic BEC. In Sec. 5.3, we discuss collective excitations of the interacting SOAM-coupled spin-1 BEC and calculate some low-lying modes by using real-time dynamics, which is followed by the summary of key results in Sec. 5.4.

5.1 Single-particle Hamiltonian

For an orbital angular momentum transfer of l by the Laguerre-Gaussian beams, the single-particle SOAM-coupled Hamiltonian is [135,136]

$$H_0 = \left[-\frac{1}{2}\frac{\partial}{r\partial r}\left(r\frac{\partial}{\partial r}\right) + \frac{\hat{L}_{\mathrm{z}}^2}{2r^2} + \frac{\partial^2}{\partial z^2} + V(\mathbf{r})\right]\mathbf{I} + \Omega(r)[\cos(l\phi)S_x - \sin(l\phi)S_y] + \delta S_z, \quad (5.1)$$

where $\Omega(r) = \Omega_0 e^{l/2}(r/w)^l \exp[-lr^2/2w^2]$, is the Raman-coupling strength [142] with Ω_0 and w as the Rabi frequency and beam waist, respectively, and rest of the quantities having the same definitions as in Eq. (4.1). As was done in Chapter 4 to obtain Eq. (4.7), we consider the unitary transformation with unitary operator $e^{-\imath l S_z \phi}$ for arbitrary l. The transformed Hamiltonian is

$$H_0^{'} = \left[-\frac{1}{2}\frac{\partial}{r\partial r}\left(r\frac{\partial}{\partial r}\right) + \frac{(\hat{L}_z + lS_z)^2}{2r^2} + V(r)\right]\mathbf{I} + \Omega(r)S_x + \delta S_z, \quad (5.2)$$

with the transformed order parameter $(e^{-\iota l\phi}\psi_{+1}, \psi_0, e^{\iota l\phi}\psi_{-1})^T$. The simultaneous eigenstates of (5.2) and $\hat{L}_z$ are characterized by orbital angular momentum quantum number l_z, whose value is related to the angular momentum of each spin component l_j in the laboratory frame as $l_j = l_z + jl$ [6,132] in the presence of δ. The eigenstate of a single-particle Hamiltonian (5.2) can be defined as

$$\Psi(r,\phi) = e^{\iota l_z\phi}\Psi_{\rm eq}(r), \tag{5.3}$$

where $\Psi_{\rm eq}(r) = [\psi_{+1}(r), \psi_0(r), \psi_{-1}(r)]^T$ with $\psi_j(r)$ as the radial wavefunction corresponding to the $j^{\rm th}$ spin component. In order to obtain an annular stripe, we consider the orbital angular momentum transfers to the atoms $l = 4$ and beam waist $w = 5$. The energy spectra of the single-particle Hamiltonian (5.2) are shown in Figs. 5.1(a)-(d) for four pairs of coupling strengths and detuning. In the absence of detuning, the $l_z = 0$ is the ground state corresponding to the $(\pm 4, 0)$ charge singularities in component wavefunctions $j = \pm 1, 0$, respectively, [see Figs. 5.1(a) and 5.1(b)]. With non-zero detuning (however small it may be), the ground states correspond to $l_z = +4$ or -4, depending on whether δ is positive or negative; e.g. with $\Omega_0 = 10, \delta = 1$ and $\Omega_0 = 10, \delta = -1$, the ground state has $l_z = 4$ and -4, respectively [see Figs. 5.1(c) and 5.1(d)]. Like Hamiltonian (4.1), Hamiltonian (5.1) for $\delta = 0$ is symmetric under the transformation defined by the operator $\mathcal{R} = \exp(-\iota S_x\pi)K$, explaining the degeneracy of $\pm l_z$ solutions with $l_z \neq 0$; in the presence of detuning, the symmetry is no longer present, as evidenced by the non-degenerate $\pm l_z$ pair of solutions.

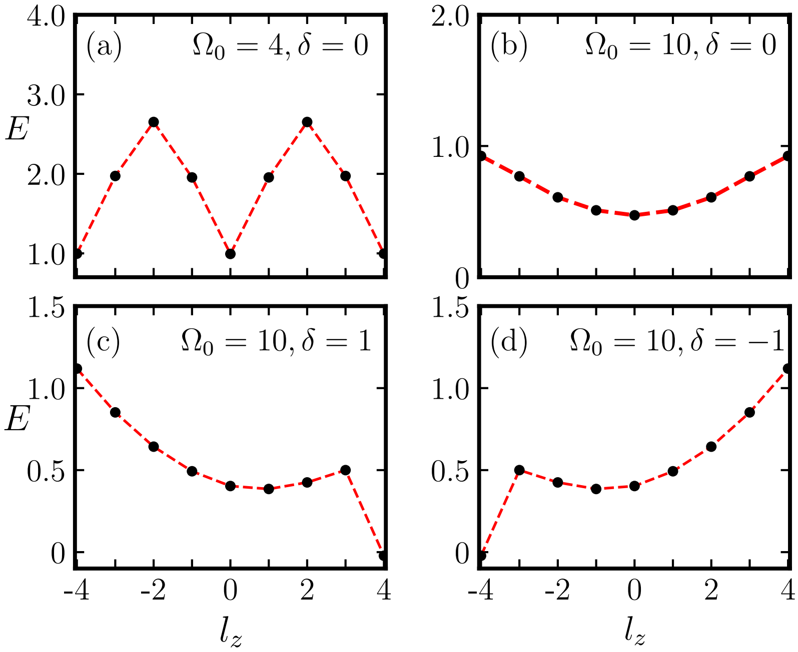

Figure 5.1: The single-particle energy spectrum for (a) $\Omega_0 = 4$, $\delta = 0$; (b) $\Omega_0 = 10$, $\delta = 0$; (c) $\Omega_0 = 10$, $\delta = 1$; and (d) $\Omega_0 = 10$ and $\delta = -1$.

We use the Bogoliubov approach to study the excitation spectrum of these circular-symmetric solutions, as discussed previously in Sec. 4.3. Fig. 5.2(a) shows the

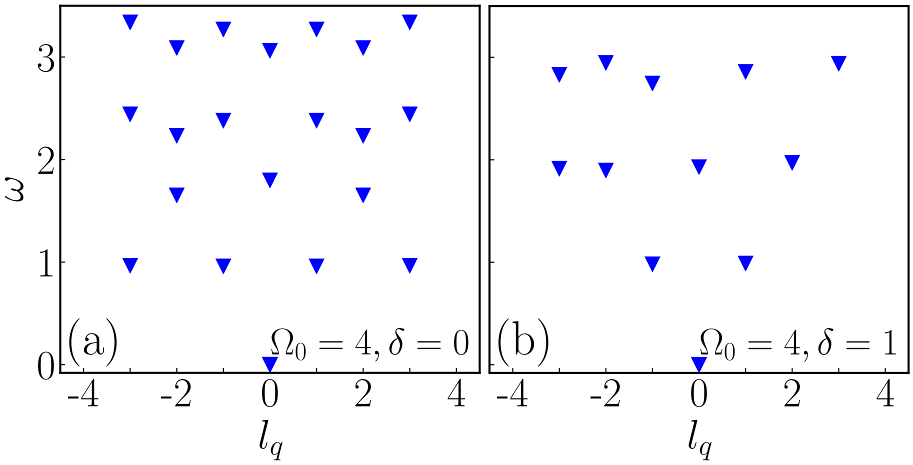

Figure 5.2: The single-particle excitation spectrum of an SOAM-coupled spin-1 BEC with (a) $\Omega_0 = 4$, $\delta = 0$ and (b) $\Omega_0 = 4$, $\delta = 1$. The ground state corresponds to $l_z = 0$ in (a) and $l_z = 4$ in (b).

excitation spectrum of the ground-state solution $l_z = 0$ obtained for $\Omega_0 = 4$ and $\delta = 0$, and (b) shows the same for $l_z = +4$ obtained with $\Omega_0 = 4$ and $\delta = 1$. For $\delta = 0$, all modes corresponding to $l_q \neq 0$ are doubly degenerate. However, with the introduction of δ, this degeneracy is lifted, and no mode remains degenerate [cf. Figs. 5.2(a) and 5.2(b)].

5.2 Ground-state phases of interacting system

Under mean-field approximation, the interacting system is described by the following set of three CGPEs

$$\iota\frac{\partial\psi_{\pm1}}{\partial t} = \mathcal{H}\psi_{\pm1} + c_1(\rho_0 \pm \rho_-)\psi_{\pm1} + c_1\psi_{\mp1}^*\psi_0^2 \pm \delta\psi_{\pm1} + \frac{\Omega(r)}{\sqrt{2}}e^{\pm\iota 4\phi}\psi_0, \quad (5.4a)$$

$$\iota\frac{\partial\psi_0}{\partial t} = \mathcal{H}\psi_0 + c_1\rho_+\psi_0 + 2c_1\psi_{+1}\psi_{-1}\psi_0^* + \frac{\Omega(r)}{\sqrt{2}}(e^{-\iota 4\phi}\psi_{+1} + e^{\iota 4\phi}\psi_{-1}), \quad (5.4b)$$

where $r = \sqrt{x^2 + y^2}$, $\phi = \tan^{-1}(y/x)$, and various other terms have the same definitions as in Eqs. (4.3a) and (4.3b).

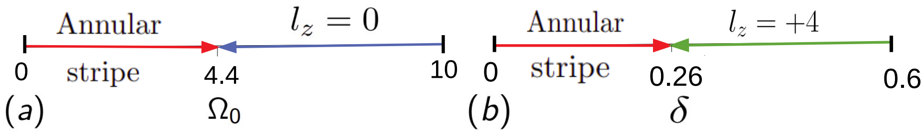

Figure 5.3: The ground-state phase diagrams of an SOAM-coupled spin-1 BEC with $c_0 = 10$ and $c_1 = 3$ (a) as a function of Ω_0 for $\delta = 0.1$ and (b) as a function of δ for $\Omega_0 = 5$. In (a), a phase transition from an annular stripe to $l_z = 0$ phase occurs when Ω_0 exceeds 4.4, and in (b), a phase transition from the annular stripe to $l_z = 4$ phase occurs when δ exceeds 0.26. In (a) and (b), Ω_0 and δ ranges are not-to-scale.

In the previous chapter, we focused on investigating the excitation spectrum of the emergent circularly-symmetric solutions of the mean-field model, which did not permit the

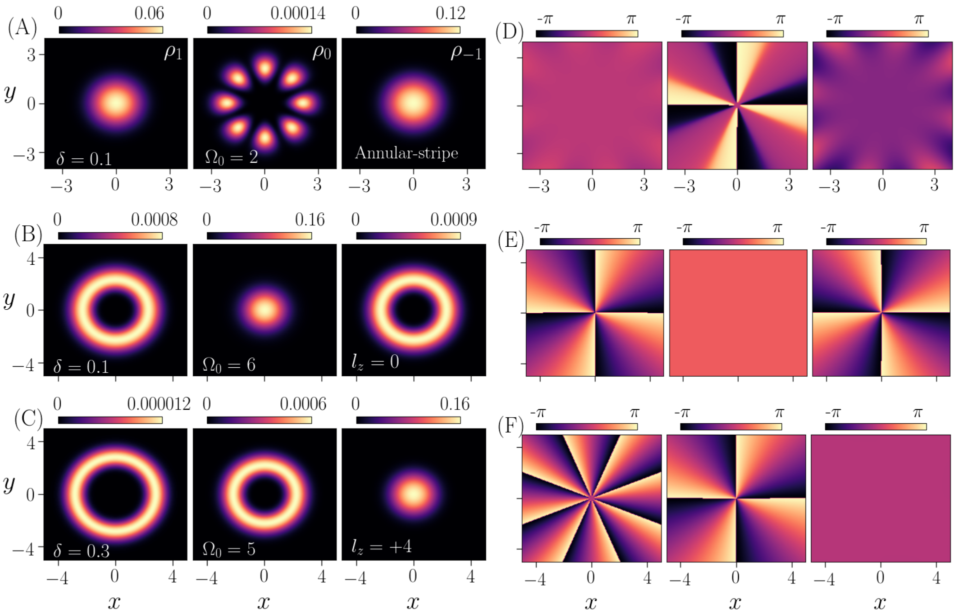

Figure 5.4: Ground states of the SOAM-coupled spin-1 BEC with $c_0 = 10$, $c_1 = 3$: (A) and (D) the component densities and phases, respectively, for $\delta = 0.1$ and $\Omega_0 = 2$; (B) and (E) the densities and phases, respectively, for $\delta = 0.1$ and $\Omega_0 = 6$; and (C) and (F) the densities and phases, respectively, for $\delta = 0.3$ and $\Omega_0 = 5$. In (E), $+1, 0$, and -1 components have phase singularities of charges $+4, 0$, and -4, respectively, and in (F), the corresponding charges are $+8, +4$, and 0.

annular-stripe phase as the ground-state solution. To achieve the annular-stripe phase with the mean-field model in Eqs (5.4a) and (5.4b), we consider the BEC with antiferromagnetic interactions with $c_0 = 10$ and $c_1 = 3$. We first calculate the ground-state phases for a fixed detuning value of $\delta = 0.1$. While varying the SOAM-coupling Ω_0 from 0 to 10, a phase transition from an annular-stripe phase to $l_z = 0$ phase occurs at $\Omega_0 = 4.4$. For an alternate set of parameters, we fixed Ω_0 to 5 and varied δ from 0 to 0.6. In this case, the phase transition from the annular-stripe phase to $l_z = 4$ occurs at $\delta = 0.26$ [see Figs. 5.3(a) and 5.3(b) for schematic illustrations of the phase diagrams]. We also examine the longitudinal magnetization $f_z = \int F_z dxdy$ and spin expectation per particle $f = \int |\mathbf{F}| dxdy$, where $|\mathbf{F}| = \sqrt{F_x^2 + F_y^2 + F_z^2}$, to ascertain the transition points between the annular-stripe and circularly-symmetric phases.

Annular-stripe phase

The interatomic interaction in the spinor BEC is one of the most important parameters to affect the parameter space in which the annular stripe phase is the ground state. This phenomenon closely resembles the emergence of the stripe phase in a linear SO-coupled BEC [214]. Fig. 5.4(A) displays the ground-state densities for a typical annular-stripe phase calculated with $\Omega_0 = 2$ and $\delta = 0.1$. In this phase, the orbital angular momentum is not a good quantum number, as evidenced by the absence of rotational symmetry [see top row of Fig. 5.4]. The longitudinal magnetization $|f_z|$, and and spin expectations per

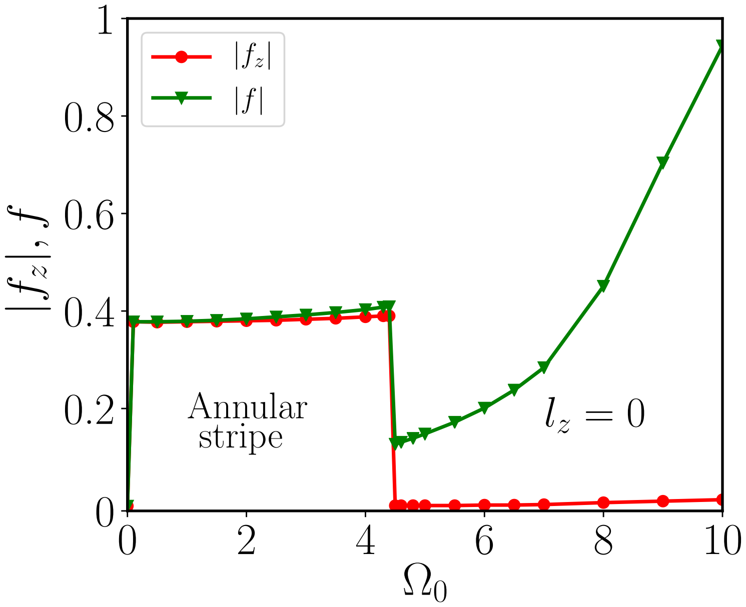

Figure 5.5: $|f_z|$ and f, as a function SOAM-coupling strength Ω_0, for a SOAM-coupled spin-1 BEC $c_0 = 10$, $c_1 = 3$, and $\delta = 0.1$.

particle f are both non-zero, as shown in Fig. 5.5.

Circular-symmetric phases

As discussed previously, a phase transition from the annular-stripe phase to $l_z = 0$ or 4 phase occurs above a critical coupling strength or detuning. The component densities and corresponding phases for a typical rotationally-symmetric $l_z = 0$ phase, which has $(\pm 4, 0)$ charge singularities in $j = \pm 1, 0$ components, respectively, are shown in the middle row of Fig. 5.4. As Ω_0 exceeds the critical coupling strength, the transition to $l = 0$ phase is characterized by the discontinuities in $|f_z|$ and f as shown in Fig. 5.5. Similarly, a typical rotationally-symmetric $l_z = +4$ phase is shown in the bottom row of Fig. 5.4. The three phases, namely annular-stripe, $l_z = 0$, and $l_z = +4$, are characterized by distinctive spin textures [cf. Figs. 5.6(a)-5.6(c)]. The spin-texture of the annular-stripe phase has spins pointing in opposite directions in the adjacent density petals (lobes); $F_z(x, y) = 0$ in the spin-texture of $l_z = 0$ phase; and $F_z(x, y) \neq 0$ in $l_z = +4$ phase.

5.3 Collective excitation spectrum

Using the Bogoliubov approach, we write the perturbed order parameter as

$$\Psi(x, y, t) = e^{-\iota\mu t}[\Psi_{\text{eq}}(x, y) + \delta\Psi(x, y, t)], \tag{5.5}$$

where $\Psi_{\text{eq}}(x, y) = [\psi_{+1}(x, y), \psi_0(x, y), \psi_{-1}(x, y)]^T$ is the equilibrium order parameter with $\psi_j(x, y)$ as the wavefunction corresponding to the j^{th} spin component, μ is the chemical potential. The fluctuation $\delta\Psi(x, y, t)$ to the equilibrium order parameter in Eq. (5.5) is written as $\delta\Psi(x, y, t) = u(x, y)e^{-\iota\omega t} + v^*(x, y)e^{\iota\omega t}$, where u and v are Bogoliubov

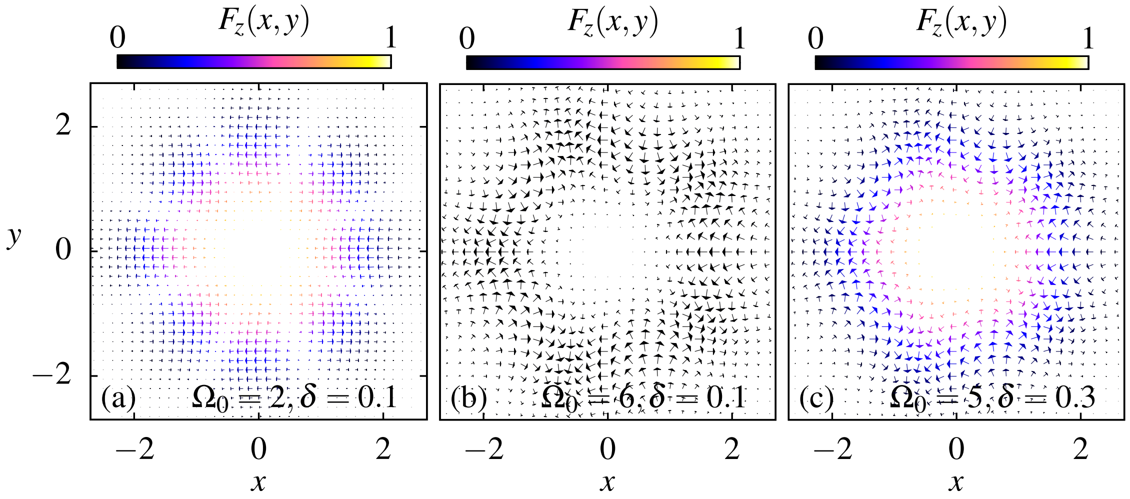

Figure 5.6: The spin-texture of SOAM-coupled spin-1 BEC for (a) $\delta = 0.1$ and $\Omega_0 = 2$, (b) $\delta = 0.1$ and $\Omega_0 = 6$, and (c) $\delta = 0.3$ and $\Omega_0 = 5$. In (a)-(c) $c_0 = 10$, $c_1 = 3$. The arrows show the projection of $\mathbf{F}(x, y)$ on the x-y plane, and the color indicates its component along z axis; $\mathbf{F}(x, y)$ vector field lies on the x-y plane in (b).

amplitudes and ω is the excitation frequency. Here, unlike in Chapter 4, $\Psi_{\rm eq}(x, y)$, $\Psi(x, y, t)$, $u(x, y)$, and $v(x, y)$ are not presumed to be circularly symmetric to accommodate the BdG analysis for the annular-stripe phase. The linearization of the three CGPEs (5.4a) and (5.4b) and the corresponding conjugate equations, using the perturbed order parameter as defined in Eq. (5.5), results in the set of coupled BdG equations; the details of the BdG analysis in this case are discussed in the Appendix C.

We study the collective excitation spectrum (a) as a function of Ω_0 for fixed interaction parameters and δ, and (b) as a function of δ for fixed interaction parameters and Ω_0. The collective excitation spectrum as a function of Ω_0 for $c_0 = 10$, $c_1 = 3$, and $\delta = 0.1$ is shown in Fig. 5.7. In the excitation spectrum, a few low-lying modes have been identified and labelled, such as density-dipole mode (ω_D) highlighted by filled red circles and density-breathing mode (ω_B) with asterisks. The methodology to identify the collective modes has been discussed previously in Chapter 4. In the annular-stripe phase, two continuous symmetries, namely gauge and rotational symmetry, are broken, which manifest as two zero-energy Goldstone modes in the excitation spectrum (see Fig. 5.7). When $\Omega_0 > 4.4$, the transition to phase $l_z = 0$ is accompanied by the discontinuities in the excitation spectrum in Fig. 5.7. There is a single zero-energy mode due to the broken gauge symmetry in this phase.

The collective excitation spectrum as a function of δ for $c_0 = 10, c_1 = 3$, and $\Omega_0 = 5$ is shown in Fig. 5.8. The transition from annular-stripe to $l_z = 4$ phase is discernible by the appearance of a roton mode, similar to the roton in the plane-wave phase with linear momentum SO coupling [209,210,215–217]. Within $l_z = 4$, phase the roton mode is softens with a decrease in δ and vanish at the transition point [141]. A few low-lying modes are marked in both the phases in the excitation spectrum in Fig. 5.8.

As discussed in Sec. 4.3, in this chapter, too, we validate our calculations of excitation

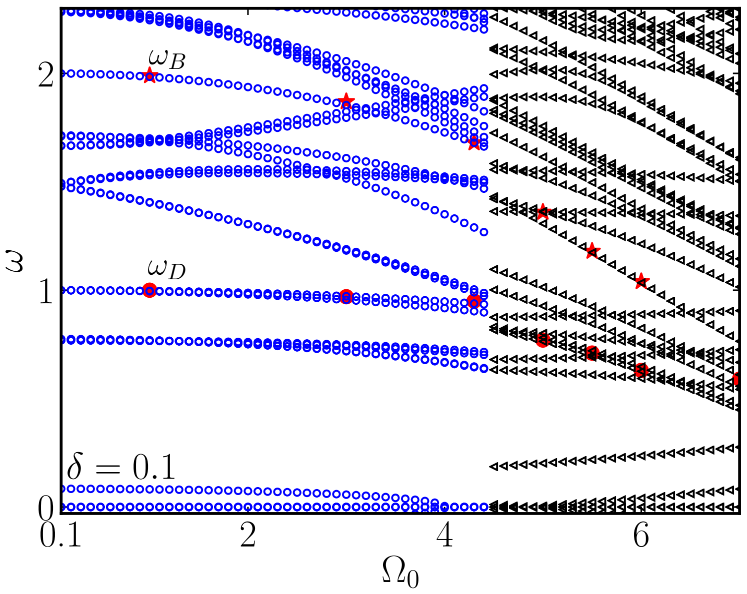

Figure 5.7: The excitation spectrum of the SOAM-coupled spin-1 BEC with $c_0 = 10$, $c_1 = 3$, and $\delta = 0.1$ as a function of Ω_0. The blue "circles" and black "triangles" correspond, respectively, to annular-stripe and $l_z = 0$ phases. For $\Omega_0 > 4.4$, there is a phase transition from the annular stripe to the circularly symmetric $l_z = 0$ phases. The density-dipole and density-breathing modes are, respectively, marked by red circles and stars.

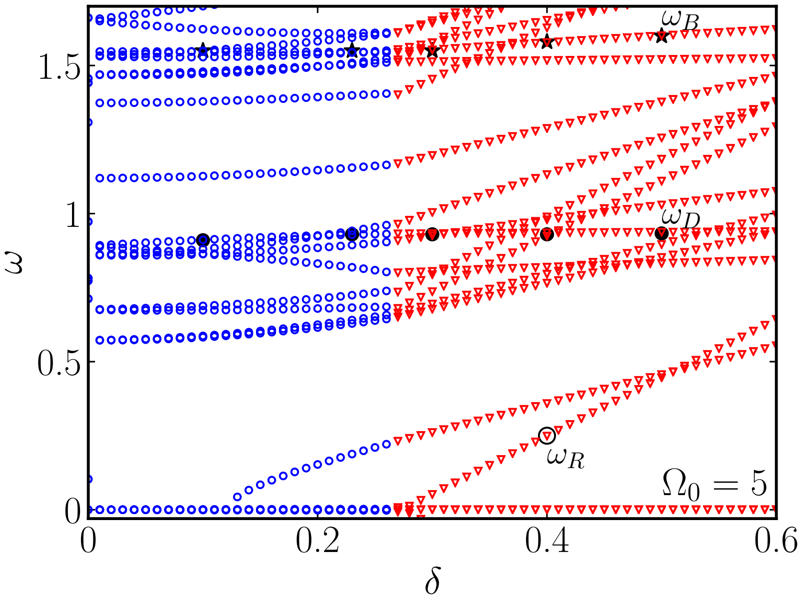

Figure 5.8: The excitation spectrum of the SOAM-coupled spin-1 BEC with $c_0 = 10$, $c_1 = 3$, and $\Omega_0 = 5$ as a function of δ. The blue "circles" and red "triangles" correspond, respectively, to the annular-stripe and $l_z = 4$ phases. For $\delta > 0.26$, there is a phase transition from the annular stripe phase and the circular symmetric $l_z = 4$ phase. The density-dipole and density-breathing modes are, respectively, marked by black circles and stars. The roton mode is highlighted by a black circle and labelled as ω_R.

spectrum and identify a few low-lying modes by adding a suitable time-independent perturbation $H^{'}$ to the Hamiltonian.

To excite the density-dipole mode, we choose $H^{'} = \lambda x$, where $\lambda \ll 1$, and study

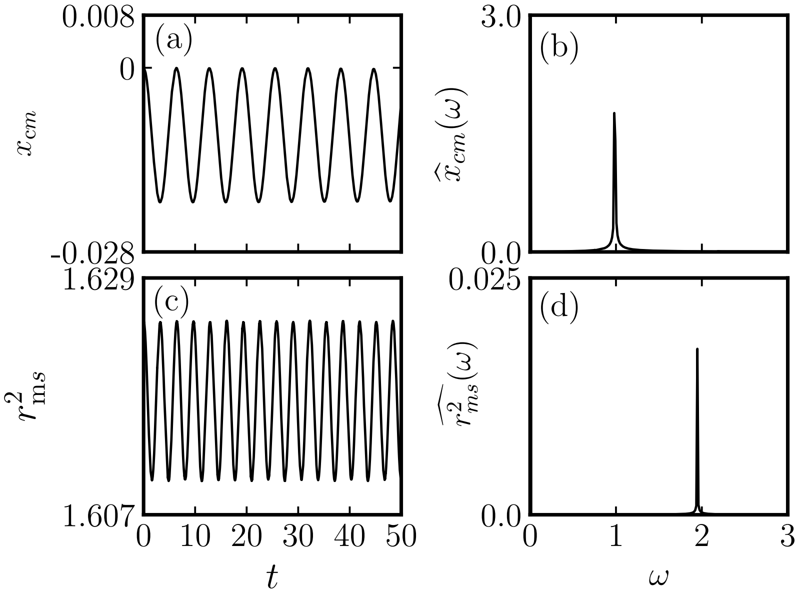

Figure 5.9: (a) shows the center of mass oscillations, i.e. $x_{\rm cm}(t)$ as a function of time and (b) corresponding Fourier transform with a peak at $\omega = 0.98$ for antiferromagnetic spin-1 BEC with $c_0 = 10$, $c_1 = 3$, $\delta = 0.1$, and $\Omega_0 = 2$. (c) shows the oscillations in the mean square size of the system $r^2_{\rm ms}(t)$ and (d) the corresponding Fourier transform peaks at $\omega = 1.95$ for the same interaction and coupling strengths.

the time evolution of the center of mass of the BEC. The time evolution of $x_{\rm cm}(t) = \langle x \rangle$ for $c_0 = 10$, $c_1 = 3$, $\delta = 0.1$, and $\Omega_0 = 2$ is shown in Fig. 5.9(a) and its Fourier transform in Fig. 5.9(b) peaks at 0.98, which matches with ω_D in Fig. 5.7. Similarly, we excite the density-breathing mode with $H' = \lambda(x^2 + y^2)$, and examine the mean square radius $r^2_{\rm ms}(t) = \langle x^2 + y^2 \rangle$ as a function of time and its Fourier transform $\widehat{r^2_{\rm ms}}(\omega)$ [see Figs. 5.9(c) and 5.9(d)]. The oscillation frequency of $r^2_{\rm ms}(t)$ matches with the frequency of density-breathing mode ($\omega_B = 1.95$).

5.4 Summary

We have investigated the ground-state phases and the low-lying excitation spectrum of an SOAM-coupled spin-1 BEC with antiferromagnetic interactions. We use the SOAM-coupled model corresponding to an angular momentum transfer of $l = 4\hbar$ to the atoms, which permits the annular stripe phase as one of the ground state phases. For the chosen set of interaction parameters ($c_0 = 10$ and $c_1 = 3$), we observed a phase transition from an annular stripe phase to a circularly symmetric $l_z = 0$ (or $l_z = +4$) phase as coupling strength (or detuning) exceeds a critical value. The circularly symmetric $l_z = 0$ phase is characterized by phase singularities of order $(+4, 0, -4)$ in $j = (+1, 0, -1)$ spin components, respectively. Similarly, for $l_z = +4$ phase, $(+8, +4, 0)$ are the respective charges of the phase singularities. Using the Bogoliubov approach, we have studied the excitation spectrum (a) as a function of Ω_0 for fixed interaction parameters and δ and (b) as a function of δ for fixed interaction parameters and Ω_0. For (a), the excitation spectrum shows discontinuities across the phase boundary between the annular stripe and $l_z = 0$ phases, and in (b), collective modes vary smoothly across the phase boundary between the annular stripe and $l_z = +4$ phases. We also identify a couple of low-lying density modes in the excitation spectrum using the perturbative dynamics discussed in Chapter 4.

Chapter 6

Summary and future directions

6.1 Thesis summary

In summary, we have studied the SO-coupled spin-1 and spin-2 BECs under rotation with an emphasis on moderate to high rotations using mean-field models. Our analysis of the eigenfunctions and eigenenergies of the non-interacting part of the Hamiltonian, using variational analysis and exact numerical solutions, shows that a boson in such BECs can be subjected to a variety of rotating effective potentials including symmetric, asymmetric double-well, and toroidal potentials.

For an SO-coupled spin-1 BEC under rotation, the shape of these effective potentials is consistent with the component density profiles for ^{87}Rb and ^{23}Na BECs with experimentally realizable interaction parameters. We show the spin expectation per particle for a ferromagnetic BEC stays close to one as a function of rotation frequency, whereas for an antiferromagnetic BEC it starts increasing with an increase in rotation frequency and tends to approach one at high rotations. For an SO coupling between the spin and the linear momentum along one direction, i.e., $\gamma_x S_x p_x$, spatial segregation of the eigenfunctions ($\Phi^{\pm}_{\rm var}$) of the single particle Hamiltonian in the presence of moderate to high rotations, which translates to a spatial segregation between $m_j = \pm 1$ components in an equivalent $\gamma_x S_z p_x$ coupling, can result in spin-expectation per particle approaching one for an antiferromagnetic BEC. For an isotropic SO coupling without coherent coupling, our variational analysis also predicts spin expectation per particle approaching one at moderate to high rotations. This results in a similar response of the two systems at moderate to large rotations, as exemplified in similar spin-texture, mass-current, etc., and component-density profiles of the two systems. Similarly, for SO-coupled spin-2 BECs under rotation, we illustrated using the mean-field CGPEs, employing the realistic experimental parameters, the spatial distribution of ^{87}Rb, ^{23}Na, and ^{85}Rb are consistent with the inhomogeneity of the effective potentials. The similarity in response of the fast-rotating cyclic phase ^{87}Rb, antiferromagnetic ^{23}Na and ferromagnetic ^{87}Rb highlights the much-diminished role of the spin-exchange interactions vis-à-vis the other competing terms in the system's Hamiltonian.

Motivated by the recent experiments [Chen *et al.*, Phys. Rev. Lett **121**, 113204 (2018), Chen *et al.*, Phys. Rev. Lett. **121**, 250401 (2018)], which demonstrated the coupling between the spin and orbital angular momentum of the atoms, we investigated the ground-state phases and low-lying excitation spectrum of the SOAM-coupled spin-1 condensates with both ferromagnetic and antiferromagnetic interactions. Without detuning with ferromagnetic interaction, the ground-state phase is either a coreless or a polar-core vortex state. In contrast, with antiferromagnetic interaction, it is the polar-core vortex. We calculated the phase diagrams in the ratio of interaction strengths versus coupling strength $(c_1/c_0 - \Omega_0)$ and the number of atoms versus coupling strength $(N - \Omega_0)$ planes. We studied the excitation spectrum of the system as a function of two experimentally controllable parameters, namely coupling strength and the number of atoms. The excitation spectrum of the coreless vortex phase is non-degenerate, whereas in the polar-core vortex phase, $\pm l_q$ modes with $l_q \neq 0$ are degenerate. The excitation spectrum is characterized by the discontinuities across the phase boundary between the two phases and within a phase by avoided crossings between the modes with the same magnetic quantum number of excitations. The avoided crossings signal the hybridization of the density and spin channels; the nature of spin and density fluctuations has confirmed this. Among the low-lying modes, we identify dipole, breathing, and quadrupole modes for density and spin channels. The frequencies of these named modes are further validated from the time evolution of the expectations of the physical observables when an apt time-independent perturbation is added to the system's Hamiltonian. For the density-dipole, density-breathing, and density-quadrupole modes, the perturbations considered are λx, λx^2, and λxy, respectively. For the spin-dipole, spin-breathing, and spin-quadrupole modes, the apt perturbations are $\lambda S_z x$, $\lambda S_z x^2$, and $\lambda S_z xy$, respectively. The corresponding physical observables are $\langle x\rangle, \langle x^2\rangle$, and $\langle xy\rangle$ for density modes and $\langle xS_z\rangle, \langle x^2 S_z\rangle$, and $\langle xyS_z\rangle$ for spin modes. An analytic estimate for the density-breathing modes has also been obtained using variational analysis. In the presence of detuning, $\pm l_q$ modes become non-degenerate in the polar-core vortex phase.

We consider an SOAM coupling model corresponding to an angular momentum transfer of $l = 4\hbar$ to the atoms, which permits the symmetry-breaking annular stripe phase as one of the ground state phases. For a chosen set of interaction parameters, we observed an annular-stripe phase along with two circular symmetric phases, namely $l_z = 0$ and $l_z = +4$ phase characterized by the charge singularities $(+4, 0, -4)$ and $(+8, +4, 0)$, respectively. We observed a phase transition from an annular stripe phase to a circularly symmetric $l_z = 0$ (or $l_z = +4$) phase as coupling strength (or detuning) exceeds a critical value. Using the Bogoliubov approach, we studied the excitation spectrum (a) as a function of Ω_0 for fixed interaction parameters and δ and (b) as a function of δ for fixed interaction parameters and Ω_0. For (a), the excitation spectrum shows discontinuities across the phase boundary between the annular stripe and $l_z = 0$ phases, and in (b) collective modes vary smoothly across the phase boundary between the annular stripe and $l_z = +4$ phases.

6.2 Future directions

In the near future, we aim to study the low-lying excitation spectrum and ground-state phase diagram of Raman-induced SO-coupled spin-1 BECs at zero and finite temperatures; the existing literature on this theme is primarily on pseudospin-1/2 BECs [218–220].

On the theme of SOAM-coupled spinor BECs the annular stripe phase has a semblance with the supersolid stripe phase in an SO-coupled BEC [81,214,216,221–224]; just like the supersolid stripe phase annular stripe breaks two continuous symmetries, namely rotational and gauge symmetry. Our work in this thesis also shows that the roton mode vanishes at the boundary of annular-stripe and $l_z = +4$ phases. Recently, a temperature-induced supersolidity has been proposed in an SO-coupled pseudospin-1/2 BEC [225]. This motivates us to study the fate of the annular-stripe phase at finite temperatures in future.

The single-particle SOAM-coupled Hamiltonians considered in this work are rotationally symmetric. If this rotational symmetry is explicitly broken by replacing the isotropic harmonic trapping potential with a box-trapping potential, the ground state phase diagram will change drastically. In this context, it will be interesting to study such a system's ground state phase diagram in the future, especially since the box-trapping potential is now experimentally realizable [190].

Appendix A

Time-splitting finite-difference methods for an SO-coupled spin-1 BEC

The H_{SP} and H_{SE} matrices in Eqs. (2.27b) and (2.27c) for a 3D spin-1 condensate are [1,55,56]

$$H_{\mathrm{SP}} = \begin{pmatrix} V + c_0\rho + c_1(\rho_0 + \rho_-) & 0 & 0 \\ 0 & V + c_0\rho + c_1\rho_+ & 0 \\ 0 & 0 & V + c_0\rho + c_1(\rho_0 - \rho_-) \end{pmatrix}, \tag{A.1a}$$

$$H_{\mathrm{SE}} = c_1 \begin{pmatrix} 0 & \psi_0\psi_{-1}^* & 0 \\ \psi_0^*\psi_{-1} & 0 & \psi_0^*\psi_1 \\ 0 & \psi_0\psi_1^* & 0 \end{pmatrix}, \tag{A.1b}$$

where $\rho_l = |\psi_l|^2$ with $l = 0, \pm1$, $\rho = \sum_l \rho_l$, $\rho_\pm = \rho_{+1} \pm \rho_{-1}$, and dimensionless interaction strength parameters are

$$c_0 = \frac{4\pi N(a_0 + 2a_2)}{3a_{\mathrm{osc}}} \text{ and } c_1 = \frac{4\pi N(a_2 - a_0)}{3a_{\mathrm{osc}}}. \tag{A.2}$$

In Eqs. (A.1a) and (A.1b), the $\mathbf{x}$ dependence of trapping potential, densities, and component wavefunctions has been suppressed.

A.1 Quasi-one-dimensional SO-coupled spin-1 BEC

In a q1D trap, H_{p} matrix in Eq. (2.27a) for SO-coupled spin-1 BEC takes the form

$$H_{\mathrm{p}} = \mathbf{1}\frac{\hat{p}_x^2}{2} + \gamma S_x \hat{p}_x, \tag{A.3}$$

where $\mathbf{1}$ is a 3×3 identity matrix, and S_x is the 3×3 spin-1 matrix. The form of H_{coh}, H_{SP}, and H_{SE}, respectively, in Eqs. (2.29), (A.1a), and (A.1b) remain unchanged, provided

$$\mathbf{x} = x, \quad V = \frac{1}{2}\alpha_x^2 x^2, \quad c_0 = \sqrt{\alpha_y\alpha_z}\frac{2N(a_0 + 2a_2)}{3a_{\mathrm{osc}}}, \quad c_1 = \sqrt{\alpha_y\alpha_z}\frac{2N(a_2 - a_0)}{3a_{\mathrm{osc}}}.$$

Using the first-order time-splitting, the solution of the Eq. (2.1) is equivalent to solving the set of Eqs. (2.27a)-(2.27c) successively. The $\Psi(\mathbf{x},t) = [\psi_1(\mathbf{x},t), \psi_0(\mathbf{x},t), \psi_{-1}(\mathbf{x},t)]^T$ is the order parameter for spin-1 system. We solve Eq. (2.27a) using finite difference schemes described in detail for pseudospin-1/2 BEC. Using Backward-Euler (and/or Crank-Nicolson) discretization schemes along with periodic boundary conditions, viz. Eq. (2.35), Eq. (2.27a) reduces to three coupled matrix equations

$$
\begin{aligned}
A\Phi_{\pm 1}^{n+1} + B\Phi_0^{n+1} &= D_{\pm 1}, && \text{(A.4a)}\\
A\Phi_0^{n+1} + B(\Phi_1^{n+1} + \Phi_{-1}^{n+1}) &= D_0. && \text{(A.4b)}
\end{aligned}
$$

Eqs. (A.4a)-(A.4b), can be decoupled into following three independent matrix equations,

$$
\begin{aligned}
(2B^2A - A^3)\Phi_{\pm 1}^{n+1} &= (B^2 - A^2)D_{\pm 1} + ABD_0 - B^2 D_{\mp 1}, && \text{(A.5a)}\\
(A^2 - 2B^2)\Phi_0^{n+1} &= AD_0 - B(D_1 + D_{-1}), && \text{(A.5b)}
\end{aligned}
$$

where A and Φ_l^{n+1} with $l = 1, 0, -1$ are same as in Eq. (2.45a) and Eq. (2.45c), respectively, whereas rows of B and elements of D_j are now defined as

$$
\begin{aligned}
B(i,:) &= \left(0,\ \frac{\alpha\Delta t\gamma}{4\sqrt{2}\Delta x},\ 0,\ \cdots,\ 0,\ -\frac{\alpha\Delta t\gamma}{4\sqrt{2}\Delta x}\right)(C^{i-1})^T, && \text{(A.6a)}\\
d_{\pm 1}(i) &= \left[\frac{\iota\beta\Delta t}{4\Delta x^2}\left\{\phi^n_{(i-1,\pm 1)} + \phi^n_{(i+1,\pm 1)}\right\} + \left(1 - \frac{\iota\beta\Delta t}{2\Delta x^2}\right)\phi^n_{(i,\pm 1)}\right.\\
&\quad \left. - \frac{\gamma\beta\Delta t}{4\sqrt{2}\Delta x}\left(\phi^n_{(i+1,0)} - \phi^n_{(i-1,0)}\right)\right], && \text{(A.6b)}\\
d_0(i) &= \left[\frac{\iota\beta\Delta t}{4\Delta x^2}\left\{\phi^n_{(i-1,0)} + \phi^n_{(i+1,0)}\right\} + \left(1 - \frac{\iota\beta\Delta t}{2\Delta x^2}\right)\phi^n_{(i,0)}\right.\\
&\quad \left. - \frac{\gamma\beta\Delta t}{4\sqrt{2}\Delta x}\left(\phi^n_{(i+1,1)} - \phi^n_{(i-1,1)} + \phi^n_{(i+1,-1)} - \phi^n_{(i-1,-1)}\right)\right]. && \text{(A.6c)}
\end{aligned}
$$

The decoupled matrix Eqs. (A.5a) -(A.5b) are linear circulant systems of equations which can be solved by using the method described for pseudospin-1/2 BEC. The analytic solution to Eq. (2.27b) is [181]

$$
\Psi(\mathbf{x}, t_{n+1}) \approx \left(\mathbf{1} + \frac{\cos\zeta - 1}{\zeta^2}\Delta t^2 H^2_{\mathrm{SE}+} - \iota\frac{\sin\zeta}{\zeta}\Delta t H_{\mathrm{SE}+}\right)\Psi(\mathbf{x}, t_n), \qquad \text{(A.7)}
$$

where $\zeta = \Delta t\sqrt{|c_1\psi_0\psi_{-1}^* + \frac{\Omega_{\mathrm{coh}}}{2\sqrt{2}}|^2 + |c_1\psi_0\psi_1^* + \frac{\Omega_{\mathrm{coh}}}{2\sqrt{2}}|^2}$. Finally, the solution to Eq. (2.27c) is again given as in Eq. (2.58) with the caveat that the various quantities are identified as those corresponding to spin-1 BEC.

A.2 Quasi-two-dimensional SO-coupled spin-1 BEC

Here the form of matrix operator H_{p} is same as in Eq. (2.59) with $\mathbf{1}$ representing a 3×3 identity matrix, and S_ν with $\nu = x, y$ denoting the spin-1 matrices. Also, the form of H_{coh},

$H_{\rm SP}$, and $H_{\rm SE}$ in Eqs. (2.29), (A.1a), (A.1b), respectively, remain unchanged, provided

$$\mathbf{x} \equiv (x, y), \quad V = \sum_{\nu=x,y} \frac{\alpha_\nu^2 \nu^2}{2}, \tag{A.8}$$

$$c_0 = \sqrt{2\pi\alpha_z}\frac{2N(a_0 + 2a_2)}{3a_{\rm osc}}, \quad c_1 = \sqrt{2\pi\alpha_z}\frac{2N(a_2 - a_0)}{3a_{\rm osc}}. \tag{A.9}$$

The CGPEs of a q2D spin-1 BEC with Rashba SO coupling, where H_p is further split into $H_{p_x} + H_{p_y}$, where H_{p_x} and H_{p_y} are defined in Eq. (2.62) with $\mathbf{1}$ and S_ν being identified as 3×3 identity and spin-1 matrices, respectively. Similar to a q2D pseudospin-1/2 BEC, each of Eq. (2.61a) and Eq. (2.61b) can be discretized into three decoupled matrix equations, such as

$$(A_x^3 + 2A_xB_x^2)X_{\pm1}^{n+1} = (A_x^2 + B_x^2)D_{\pm1}^x \mp A_xB_xD_0^x + B_x^2D_{\mp1}^x, \tag{A.10a}$$

$$(A_x^2 + 2B_x^2)X_0^{n+1} = A_xD_0^x + B_x(D_1^x - D_{-1}^x) \tag{A.10b}$$

for Eq. (2.61a), and

$$(2B_y^2A_y - A_y^3)Y_{\pm1}^{n+1} = (B_y^2 - A_y^2)D_{\pm1}^y + A_yB_yD_0^y - B_y^2D_{\mp1}^y, \tag{A.11a}$$

$$(A_y^2 - 2B_y^2)Y_0^{n+1} = A_yD_0^y - B_y(D_1^y + D_{-1}^y), \tag{A.11b}$$

for Eq. (2.61b). Here, A_ν (with $\nu = x, y$), X_l^{n+1}, Y_l^{n+1}, are defined as in Eq. (2.64a), Eq. (2.64d) and Eq. (2.64e) respectively, whereas B_ν, D_l^ν are now defined as

$$B_x(i,:) = \left(0,\ \frac{\iota\alpha\Delta t\gamma}{4\sqrt{2}\Delta x},\ 0,\ \cdots,\ 0,\ -\frac{\iota\alpha\Delta t\gamma}{4\sqrt{2}\Delta x}\right)(C^{i-1})^T, \tag{A.12a}$$

$$B_y(i,:) = \left(0,\ \frac{\alpha\Delta t\gamma}{4\sqrt{2}\Delta y},\ 0,\ \cdots,\ 0,\ -\frac{\alpha\Delta t\gamma}{4\sqrt{2}\Delta y}\right)(C^{i-1})^T, \tag{A.12b}$$

$$\begin{aligned} d_{\pm1}^x(i) = \Bigg[&\frac{\iota\beta\Delta t}{4\Delta x^2}\left\{\phi^n_{(i-1,j,\pm1)} + \phi^n_{(i+1,j,\pm1)}\right\} + \left(1 - \frac{\iota\beta\Delta t}{2\Delta x^2}\right)\phi^n_{(i,j,\pm1)} \\ &\mp\frac{\iota\gamma\beta\Delta t}{4\sqrt{2}\Delta x}\left(\phi^n_{(i+1,j,0)} - \phi^n_{(i-1,j,0)}\right)\Bigg], \end{aligned} \tag{A.12c}$$

$$\begin{aligned} d_0^x(i) = \Bigg[&\frac{\iota\beta\Delta t}{4\Delta x^2}\left\{\phi^n_{(i-1,j,0)} + \phi^n_{(i+1,j,0)}\right\} + \left(1 - \frac{\iota\beta\Delta t}{2\Delta x^2}\right)\phi^n_{(i,j,0)} \\ &+\frac{\iota\beta\Delta t\gamma}{4\sqrt{2}\Delta x}\left(\phi^n_{(i+1,j,1)} - \phi^n_{(i-1,j,1)} - (\phi^n_{(i-1,j,-1)} - \phi^n_{(i+1,j,-1)})\right)\Bigg], \end{aligned} \tag{A.12d}$$

$$\begin{aligned} d_{\pm1}^y(i) = \Bigg[&\frac{\iota\beta\Delta t}{4\Delta y^2}\left\{\phi^n_{(i,j-1,\pm1)} + \phi^n_{(i,j+1,\pm1)}\right\} + \left(1 - \frac{\iota\beta\Delta t}{2\Delta y^2}\right)\phi^n_{(i,j,\pm1)} \\ &-\frac{\gamma\beta\Delta t}{4\sqrt{2}\Delta y}\left(\phi^n_{(i,j+1,0)} - \phi^n_{(i,j-1,0)}\right)\Bigg], \end{aligned} \tag{A.12e}$$

$$\begin{aligned} d_0^y(i) = \Bigg[&\frac{\iota\beta\Delta t}{4\Delta y^2}\left\{\phi^n_{(i,j-1,0)} + \phi^n_{(i,j+1,0)}\right\} + \left(1 - \frac{\iota\beta\Delta t}{2\Delta y^2}\right)\phi^n_{(i,j,0)} \\ &-\frac{\gamma\beta\Delta t}{4\sqrt{2}\Delta y}\left(\phi^n_{(i,j+1,1)} - \phi^n_{(i,j-1,1)} + \phi^n_{(i,j+1,-1)} - \phi^n_{(i,j-1,-1)}\right)\Bigg]. \end{aligned} \tag{A.12f}$$

Eqs. (A.10a) and (A.10b), and (A.11a) and (A.11b) are linear circulant systems of equations, and thus can be solved as described for a pseudospin-1/2 condensate in Sec. 2.3.2. The solution to Eqs. (2.27a)-(2.27c) is also similar as described for a q1D spin-1 condensate.

A.3 Sample numerical results

We consider (1) ^{23}Na and (2) ^{87}Rb spin-1 BECs corresponding to antiferromagnetic and ferromagnetic phases. The scattering lengths corresponding to systems (1) and (2) are $a_0 = 50.00a_B$, $a_1 = 55.01a_B$ [198] and $a_0 = 101.8a_B$, $a_1 = 100.4a_B$ [192], respectively. We consider 10000 atoms trapped in a q1D trapping potential with $\omega_x = 2\pi \times 20$ Hz and $\omega_y = \omega_z = 2\pi \times 400$ Hz. The interaction strengths c_0 and c_2 in dimensionless units for aforementioned two systems are

Table A.1: Comparison of ground state energies of SO- and coherently-coupled spin-1 BECs using TSFP, TSBE, and TSCN methods with $\Delta x = 0.1$ and $\Delta\tilde{t} = 0.005$. The energies correspond to different values γ. The coherent coupling used for q1D and q2D systems are 0.5 and 0.1, respectively. The interaction strength parameters considered for the q1D BECs are $c_0 = 240.83$, $c_1 = 7.54$ for ^{23}Na and $c_0 = 885.72$, $c_1 = -4.09$ for ^{87}Rb, whereas the same for q2D BECs are $c_0 = 134.98$, $c_1 = 4.22$ and $c_0 = 248.22$, $c_1 = -1.15$, respectively.

	γ		^{23}Na			^{87}Rb	
		TSFP	TSBE	TSCN	TSFP	TSBE	TSCN
q1D	0.5	15.0623	15.0623	15.0623	35.7812	35.7812	35.7812
	1.0	14.6873	14.6873	14.6873	35.4062	35.4062	35.4062
	1.5	14.0623	14.0623	14.0623	34.7812	34.7812	34.7812
	2.0	13.1873	13.1876	13.1876	34.9062	33.9062	33.9065
q2D	0.5	4.3797	4.3797	4.3797	8.2638	8.2638	8.2638
	1.0	3.9602	3.9602	3.9601	7.8747	7.8747	7.8747
	1.5	3.3303	3.3303	3.3303	7.2435	7.2435	7.2435
	2.0	2.4486	2.4489	2.4489	6.3658	6.3661	6.3661

$$(1) \quad (c_0, c_1) = (240.83, 7.54), \tag{A.13a}$$

$$(2) \quad (c_0, c_1) = (885.72, -4.09). \tag{A.13b}$$

The same number of atoms trapped in a q2D trapping potential with $\omega_x = \omega_y = 2\pi \times 20$ Hz and $\omega_z = 2\pi \times 400$ Hz leads to following interaction strengths

$$(1) \quad (c_0, c_1) = (134.98, 4.22), \tag{A.14a}$$

$$(2) \quad (c_0, c_1) = (248.22, -1.15), \tag{A.14b}$$

for ^{23}Na and ^{87}Rb spin-1 BECs, respectively. The oscillator lengths for systems (1) and (2) are 4.69 μm and 2.41 μm, respectively. For these two cases, the comparison of ground state energies obtained from TSFP, TSBE and TSCN shows an excellent agreement as reported in Table-(A.1). The numerically obtained component densities in the ground states of harmonically trapped q1D ^{23}Na and ^{87}Rb spin-1 BECs with different values of γ and $\Omega_{\rm coh}$ are (not shown here) in an excellent agreement.

Appendix B

Solving BdG equations using finite difference method

The fluctuation $\delta\Psi(r,t) = [\delta\psi_{+1}(r,t), \delta\psi_0(r,t), \delta\psi_{-1}(r,t)]^T$ to the equilibrium order parameter in Eq. (4.8) is $\delta\psi_j(r,t) = u_j(r)e^{-i\omega t} + v_j^*(r)e^{i\omega t}$, where $u_j(r)$ and $v_j(r)$ are Bogoliubov quasi-particle amplitudes for j^{th} spin component and ω is the excitation frequency. Linearization of CGPEs (4.3a) and (4.3b) and the conjugate set of equations using the perturbed order parameter in Eq. (4.8) yields following six-coupled BdG equations:

$$\begin{aligned}
\omega u_{+1} = {} & \Bigg[-\frac{\nabla_r^2}{2} + \frac{r^2}{2} + \delta + \frac{(l_q+l_z+1)^2}{2} - \mu + c_0(2R_{+1}^2 + R_0^2 + R_{-1}^2) \\
& + c_1(2R_{+1}^2 + R_0^2 - R_{-1}^2)\Bigg] u_{+1} + \left[\frac{\Omega(r)}{\sqrt{2}} + R_{+1}R_0(c_0+c_1) + 2c_1R_0R_{-1}\right] u_0 \\
& + R_{+1}^2(c_0+c_1)v_{+1} + R_{+1}R_0(c_0+c_1)v_0 + R_{+1}R_{-1}(c_0-c_1)u_{-1} \\
& + [R_{+1}R_{-1}(c_0-c_1) + 2c_1R_0^2]v_{-1}, \qquad \text{(B.1a)}
\end{aligned}$$

$$\begin{aligned}
-\omega v_{+1} = {} & \Bigg[-\frac{\nabla_r^2}{2} + \frac{r^2}{2} + \delta + \frac{(l_q+l_z+1)^2}{2} - \mu + c_0(2R_{+1}^2 + R_0^2 + R_{-1}^2) \\
& + c_1(2R_{+1}^2 + R_0^2 - R_{-1}^2)\Bigg] v_{+1} + \left[\frac{\Omega(r)}{\sqrt{2}} + R_{+1}R_0(c_0+c_1) + 2c_1R_0R_{-1}\right] v_0 \\
& + R_{+1}^2(c_0+c_1)u_{+1} + R_{+1}R_0(c_0+c_1)u_0 + R_{+1}R_{-1}(c_0-c_1)v_{-1} \\
& + [R_{+1}R_{-1}(c_0-c_1) + 2c_1R_0^2]u_{-1}, \qquad \text{(B.1b)}
\end{aligned}$$

$$\begin{aligned}
\omega u_0 = {} & \left[-\frac{\nabla_r^2}{2} + \frac{r^2}{2} + \frac{(l_q+l_z)^2}{2} - \mu + c_0(R_{+1}^2 + 2R_0^2 + R_{-1}^2) - c_1(R_{+1}^2 + R_{-1}^2)\right] u_0 \\
& + \left[\frac{\Omega(r)}{\sqrt{2}} - R_{+1}^2(c_0+c_1)\right] u_{+1} + R_{+1}R_0(c_0+c_1)v_{+1} + (c_0R_0^2 + 2c_1R_{+1}R_{-1})v_0 \\
& + \left[\frac{\Omega(r)}{\sqrt{2}} + R_0R_{-1}(c_0+c_1) - 2c_2R_{+1}R_0\right] u_{-1} + R_{+1}R_{-1}(c_0+c_1)v_{-1}, \qquad \text{(B.1c)}
\end{aligned}$$

$$\begin{aligned}
-\omega v_0 = {} & \left[-\frac{\nabla_r^2}{2} + \frac{r^2}{2} + \frac{(l_q+l_z)^2}{2} - \mu + c_0(R_{+1}^2 + 2R_0^2 + R_{-1}^2) - c_1(R_{+1}^2 + R_{-1}^2)\right] v_0 \\
& + \left[\frac{\Omega(r)}{\sqrt{2}} - R_{+1}^2(c_0+c_1)\right] v_{+1} + R_{+1}R_0(c_0+c_1)u_{+1} + (c_0R_0^2 + 2c_1R_{+1}R_{-1})u_0 \\
& + \left[\frac{\Omega(r)}{\sqrt{2}} + R_0R_{-1}(c_0+c_1) - 2c_1R_{+1}R_0\right] v_{-1} + R_{+1}R_{-1}(c_0+c_1)u_{-1}, \qquad \text{(B.1d)}
\end{aligned}$$

$$\begin{aligned}
\omega u_{-1} &= \left[-\frac{\nabla_r^2}{2} + \frac{r^2}{2} - \delta + \frac{(l_q+l_z-1)^2}{2} - \mu + c_0(R_{+1}^2 + R_0^2 + 2R_{-1}^2) \right. \\
&\left. + c_1(2R_{-1}^2 + R_0^2 - R_{+1}^2) \right] u_{-1} + \left[\frac{\Omega(r)}{\sqrt{2}} + R_0 R_{-1}(c_0+c_1) + 2c_1 R_{+1} R_0 \right] u_0 \\
&+ (c_0-c_1) R_{+1} R_{-1} u_{+1} + [R_{+1} R_{-1}(c_0-c_1) + 2c_1 R_0^2] v_{+1} \\
&+ R_{-1}^2 (c_0+c_1) v_{-1} + R_{+1} R_0 (c_0+c_1) v_0, \qquad \text{(B.1e)} \\
-\omega v_{-1} &= \left[-\frac{\nabla_r^2}{2} + \frac{r^2}{2} - \delta + \frac{(l_q+l_z-1)^2}{2} - \mu + c_0(R_{+1}^2 + R_0^2 + 2R_{-1}^2) \right. \\
&\left. + c_1(2R_{-1}^2 + R_0^2 - R_{+1}^2) \right] v_{-1} + \left[\frac{\Omega(r)}{\sqrt{2}} + R_0 R_{-1}(c_0+c_1) + 2c_1 R_{+1} R_0 \right] v_0 \\
&+ (c_0-c_1) R_{+1} R_{-1} v_{+1} + [R_{+1} R_{-1}(c_0-c_1) + 2c_1 R_0^2] u_{+1} \\
&+ R_{-1}^2 (c_0+c_1) u_{-1} + R_{+1} R_0 (c_0+c_1) u_0, \qquad \text{(B.1f)}
\end{aligned}$$

where $\nabla_r^2/2 = \partial^2/(2\partial r^2) + \partial/(2r\partial r)$ and $l_z = 1$ for phase I (coreless vortex) and 0 for phase II (polar-core vortex). To solve coupled Eqs. (B.1a)-(B.1f), we use the finite-difference method to discretize these equations over the radial grid r_i consisting of N_r points with $i = 1, 2, \ldots, N_r$ [171]. To discretize the terms involving the kinetic energy operator, say $\nabla_r^2 f(r) = f''(r)$, we employ the finite difference approximation as follows

$$f''(r_i) \approx \begin{cases} \frac{f(r_{i+2})-2f(r_{i+1})+f(r_i)}{\Delta r^2} + \frac{f(r_{i+1})-f(r_i)}{r_i\Delta r} & \text{if } i=1 \\ \frac{f(r_{i+1})-2f(r_i)+f(r_{i-1})}{\Delta r^2} + \frac{f(r_{i+1})-f(r_{i-1})}{2r_i\Delta r} & \text{if } i=2 \text{ to } N_r-1 \\ \frac{f(r_i)-2f(r_{i-1})+f(r_{i-2})}{\Delta r^2} + \frac{f(r_i)-f(r_{i-1})}{r_i\Delta r} & \text{if } i=N_r, \end{cases} \qquad \text{(B.2a)}$$

where $f(r)$ is either $u_j(r)$ or $v_j(r)$, and Δr is radial step size. The discretization of each of the six BdG equations yields N_r equations corresponding to each grid point. These equations can now be combined as a single matrix eigenvalue equation, where the dimension of the matrix is $6N_r \times 6N_r$ with the eigenvector of the form

$$\begin{aligned}
&[u_{+1}(r_1), u_{+1}(r_2), \ldots, u_{+1}(r_{N_r}), v_{+1}(r_1), v_{+1}(r_2), \ldots, v_{+1}(r_{N_r}), \\
&u_0(r_1), u_0(r_2), \ldots, u_0(r_{N_r}), v_0(r_1), v_0(r_2), \ldots, v_0(r_{N_r}), \\
&u_{-1}(r_1), u_{-1}(r_2), \ldots, u_{-1}(r_{N_r}), v_{-1}(r_1), v_{-1}(r_2), \ldots, v_{-1}(r_{N_r})]^T. \qquad \text{(B.3)}
\end{aligned}$$

In this thesis, we used a radial grid consisting of $N_r = 256$ points with a radial step-size of $\Delta r = 0.05$, which results in a $6N_r \times 6N_r$ matrix eigenvalue problem, which can be solved using standard matrix diagonalization subroutines.

It is to noted that Eqs. (B.1a)-(B.1f) for $l_z = 0$ and $\delta = 0$, remain invariant if $l_q \neq 0$ is changed to $-l_q$ with simultaneous interchange of the $j = +1$ and $j = -1$ components. It implies that for non-zero magnetic quantum number of excitation ($l_q \neq 0$), $\pm l_q$ excitation modes in the single-particle excitation spectrum, viz. Fig. 4.5, will be degenerate. For the same reason, $\pm l_q$ modes with $l_q \neq 0$ of a polar-core vortex phase are also degenerate, for example in Fig. 4.6(c). In the presence of detuning ($\delta \neq 0$) or angular momentum ($l_z \neq 0$), this invariance is not there, and as a result, $\pm l_q$ excitations with $l_q \neq 0$ are no longer degenerate in the coreless vortex phase.

Appendix C

Solving two-dimensional BdG equations using basis expansion method

The linearization of the CGPEs (5.4a) and (5.4b) and the corresponding conjugate equations, using the perturbed order parameter as defined in Eq. (5.5), results in the following set of six-coupled two-dimensional BdG equations:

$$\begin{pmatrix} P_1 & P_2 \\ -P_2^* & -P_1^* \end{pmatrix} \begin{pmatrix} \mathbf{u}^\lambda \\ \mathbf{v}^\lambda \end{pmatrix} = \omega_\lambda \begin{pmatrix} \mathbf{u}^\lambda \\ \mathbf{v}^\lambda \end{pmatrix}, \tag{C.1}$$

where

$$P_1 = \begin{pmatrix} h_{+1,+1} & h_{+1,0} & (c_0 - c_1)(\psi_{-1}\psi_{+1}^*) \\ h_{+1,0}^* & h_{0,0} & h_{0,-1} \\ (c_0 - c_1)(\psi_{+1}^*\psi_{-1}) & h_{0,-1}^* & h_{-1,-1} \end{pmatrix},$$

$$P_2 = \begin{pmatrix} (c_0 + c_1)\psi_{+1}^2 & (c_0 + c_1)\psi_0\psi_{+1} & (c_0 - c_1)\psi_{-1}\psi_{+1} + c_1\psi_0^2 \\ (c_0 + c_1)\psi_{+1}\psi_0 & c_0\psi_0^2 + 2c_1\psi_{+1}\psi_{-1} & (c_0 + c_1)\psi_{-1}\psi_0 \\ (c_0 - c_1)\psi_{+1}\psi_{-1} + c_1\psi_0^2 & (c_0 + c_1)\psi_0\psi_{-1} & (c_0 + c_1)\psi_{-1}^2 \end{pmatrix},$$

with

$$\begin{aligned} h_0 &= \left(-\frac{1}{2}\partial_x^2 - \frac{1}{2}\partial_y^2 - \mu + V(x,y) + c_0\rho\right),\ h_{+1,+1} = h_0 + c_0\rho_{+1} + c_1(2\rho_{+1} + \rho_0 - \rho_{-1}), \\ h_{0,0} =& h_0 + c_0\rho_0 + c_1(\rho_{+1} + \rho_{-1}),\ h_{-1,-1} = h_0 + c_0\rho_{-1} + c_1(n_0 - \rho_{+1} + 2\rho_{-1}), \\ h_{+1,0} =& (c_0 + c_1)\psi_0^*\psi_{+1} + 2c_1\psi_{-1}^*\psi_0 + h_{\rm cc},\ h_{0,-1} = (c_0 + c_1)\psi_0\psi_{-1}^* + 2c_1\psi_{+1}\psi_0^* + h_{\rm cc}, \\ h_{\rm cc} =& \frac{\Omega(r)}{\sqrt{2}}e^{\imath l\phi},\ \rho_j = |\psi_j|^2,\ \mathbf{u}^\lambda = (u_{+1}^\lambda, u_0^\lambda, u_{-1}^\lambda)^T,\ \mathbf{v}^\lambda = (v_{+1}^\lambda, v_0^\lambda, v_{-1}^\lambda)^T. \end{aligned}$$

where the x, y dependence of various quantities has been suppressed. The BdG equations Eq. (C.1) can be solved using the finite difference method, as we discussed in Appendix B. The finite-difference method, in this case, yields a matrix eigenvalue problem of size $6(N_xN_y + 1) \times 6(N_xN_y + 1)$, where N_x and N_y are the numbers of grid points along

x and y directions on a rectangular spatial grid. As the matrix size is very large, solving it using standard matrix diagonalization subroutines is time-consuming. To avoid large matrix eigenvalue problems, we use the basis expansion method to solve the coupled BdG equations [172], where we first express $u_j(x,y)$ and $v_j(x,y)$ as a linear combination of the two-dimensional harmonic oscillator eigenstates, say $\phi_p(x,y)$. Specifically we write $u_j(x,y) = \sum_p m_p^j \phi_p(x,y)$ and similarly $v_j(x,y) = \sum_p n_p^j \phi_p(x,y)$, where m_p^j and n_p^j are the coefficients of the linear superposition. The resultant BdG equations are then successively projected on the N_b basis states. While implementing the projection, one typically needs to evaluate the following matrix elements:

$$\begin{aligned}
M_{11}^{pq} = \iint \phi_p(x,y)\Bigg[-\frac{1}{2}\partial_x^2 - \frac{1}{2}\partial_y^2 - \mu + V(x,y) + c_0(\rho + \rho_1) \\
+ c_1(2\rho_{+1} + \rho_0 - \rho_{-1})\Bigg]\phi_q(x,y)dxdy,
\end{aligned}$$

$$M_{12}^{pq} = \iint \phi_p(x,y)(c_0 + c_1)\psi_{+1}^2\phi_q(x,y)dxdy,$$

$$M_{13}^{pq} = \iint \phi_p(x,y)\Bigg[(c_0 + c_1)\psi_0^*\psi_{+1} + 2c_1\psi_{-1}^*\psi_0 + h_{\rm cc}\Bigg]\phi_q(x,y)dxdy,$$

$$M_{14}^{pq} = \iint \phi_p(x,y)(c_0 + c_1)\psi_0\psi_{+1}\phi_q(x,y)dxdy,$$

$$M_{15}^{pq} = \iint \phi_p(x,y)(c_0 - c_1)(\phi_{+1}\psi_{-1}^*)\phi_q(x,y)dxdy,$$

$$M_{16}^{pq} = \iint \phi_p(x,y)\Bigg[(c_0 - c_1)\psi_{-1}\psi_{+1} + c_1\psi_0^2\Bigg]\phi_q(x,y)dxdy,$$

$$M_{21}^{pq} = -\iint \phi_p(x,y)(c_0 + c_1)\psi_{+1}^{2*}\phi_q(x,y)dxdy,$$

$$\begin{aligned}
M_{22}^{pq} = -\iint \phi_p(x,y)\Bigg[-\frac{1}{2}\partial_x^2 - \frac{1}{2}\partial_y^2 - \mu + V(x,y) + c_0\rho + c_0\rho_1 \\
+ c_1(2\rho_{+1} + \rho_0 - \rho_{-1})\Bigg]\phi_q(x,y)dxdy,
\end{aligned}$$

$$M_{23}^{pq} = -\iint \phi_p(x,y)\Bigg[(c_0 + c_1)\psi_0^*\psi_{+1}^*\Bigg]\phi_q(x,y)dxdy,$$

$$M_{24}^{pq} = -\iint \phi_p(x,y)\Bigg[(c_0 + c_1)\psi_0^*\psi_{+1}^* + 2c_1\psi_0^*\psi_{-1}^* + cc^*\Bigg]\phi_q(x,y)dxdy,$$

$$M_{25}^{pq} = -\iint \phi_p(x,y)\Bigg[(c_0 - c_1)\phi_0^*\psi_{-1}^* + c_1\psi_0^{2*}\Bigg]\phi_q(x,y)dxdy,$$

$$M_{26}^{pq} = -\iint \phi_p(x,y)(c_0 - c_1)\psi_{-1}\psi_{+1}^*\phi_q(x,y)dxdy,$$

$$\begin{aligned}
M_{31}^{pq} =& \iint \phi_p(x,y)\Bigg[(c_0+c_1)\psi_0\psi_{+1}^* + 2c_1\psi_{-1}\psi_0^* + h_{\mathrm{cc}^*}\Bigg]\phi_q(x,y)dxdy,\\
M_{32}^{pq} =& \iint \phi_p(x,y)(c_0+c_1)\psi_{+1}\psi_0\phi_q(x,y)dxdy,\\
M_{33}^{pq} =& \iint \phi_p(x,y)\Bigg[-\frac{1}{2}\partial_x^2 - \frac{1}{2}\partial_y^2 - \mu + V(x,y) + c_0(\rho+\rho_0)\\
&+ c_1(\rho_{+1}-\rho_{-1})\Bigg]\phi_q(x,y)dxdy,\\
M_{34}^{pq} =& \iint \phi_p(x,y)\Bigg[c_0\psi_0^2 + 2c_1\psi_{-1}\psi_1\Bigg]\phi_q(x,y)dxdy,\\
M_{35}^{pq} =& \iint \phi_p(x,y)\Bigg[(c_0+c_1)\psi_{-1}^*\psi_0 + 2c_1\phi_0^*\psi_1 + cc\Bigg]\phi_q(x,y)dxdy,\\
M_{36}^{pq} =& \iint \phi_p(x,y)(c_0+c_1)\psi_{-1}\psi_0\phi_q(x,y)dxdy,
\end{aligned}$$

$$\begin{aligned}
M_{41}^{pq} =& -\iint \phi_p(x,y)(c_0+c_1)\psi_0^*\psi_{+1}^*\phi_q(x,y)dxdy,\\
M_{42}^{pq} =& -\iint \phi_p(x,y)\Bigg[(c_0+c_1)\psi_1\psi_0^* + 2c_1\psi_{-1}^*\psi_0 + cc\Bigg]\phi_q(x,y)dxdy,\\
M_{43}^{pq} =& -\iint \phi_p(x,y)\Bigg[c_0\psi_0^{2*} + 2c_1\psi_{-1}^*\psi_1^*\Bigg]\phi_q(x,y)dxdy,\\
M_{44}^{pq} =& -\iint \phi_p(x,y)\Bigg[-\frac{1}{2}\partial_x^2 - \frac{1}{2}\partial_y^2 - \mu + V(x,y) + c_0(\rho+\rho_0)\\
&+ c_1(\rho_{+1}-\rho_{-1})\Bigg]\phi_q(x,y)dxdy,\\
M_{45}^{pq} =& -\iint \phi_p(x,y)(c_0+c_1)\psi_{-1}^*\psi_0^*\phi_q(x,y)dxdy,\\
M_{46}^{pq} =& -\iint \phi_p(x,y)\Bigg[(c_0+c_1)\psi_0^*\psi_{-1} + 2c_1\psi_1^*\psi_0 + cc^*\Bigg]\phi_q(x,y)dxdy,
\end{aligned}$$

$$\begin{aligned}
M_{51}^{pq} =& \iint \phi_p(x,y)(c_0-c_1)\psi_1^*\psi_{-1}\phi_q(x,y)dxdy,\\
M_{52}^{pq} =& \iint \phi_p(x,y)\Bigg[(c_0-c_1)\psi_{-1}\psi_{+1} - c_1\psi_0^2\Bigg]\phi_q(x,y)dxdy,\\
M_{53}^{pq} =& \iint \phi_p(x,y)\Bigg[(c_0+c_1)\psi_{-1}\psi_0^* + 2c_1\psi_1^*\psi_0 + cc^*\Bigg]\phi_q(x,y)dxdy,\\
M_{54}^{pq} =& \iint \phi_p(x,y)(c_0^*+c_1^*)\psi_0\psi_{-1}\phi_q(x,y)dxdy,\\
M_{55}^{pq} =& \iint \phi_p(x,y)\Bigg[-\frac{1}{2}\partial_x^2 - \frac{1}{2}\partial_y^2 - \mu + V(x,y) + c_0(\rho+\rho_{-1})
\end{aligned}$$

$$
\begin{aligned}
&\quad + c_1(2\rho_{-1} + \rho_0 - \rho_1)\Bigg]\phi_q(x,y)dxdy,\\
M_{56}^{pq} &= \iint \phi_p(x,y)(c_0 + c_1)\psi_{-1}^2\phi_q(x,y)dxdy,
\end{aligned}
$$

$$
\begin{aligned}
M_{61}^{pq} &= -\iint \phi_p(x,y)\Bigg[(c_0 - c_1)\psi_{-1}^*\psi_{+1}^* + c_1\psi_0^{2*}\Bigg]\phi_q(x,y)dxdy,\\
M_{62}^{pq} &= -\iint \phi_p(x,y)(c_0 - c_1)\psi_{-1}^*\psi_1\phi_q(x,y)dxdy,\\
M_{63}^{pq} &= -\iint \phi_p(x,y)(c_0 + c_1)\psi_0^*\psi_{+1}^*\phi_q(x,y)dxdy,\\
M_{64}^{pq} &= -\iint \phi_p(x,y)\Bigg[(c_0 + c_1)\psi_0\psi_{-1}^* + 2c_1\psi_0^*\psi_1 + cc\Bigg]\phi_q(x,y)dxdy,\\
M_{65}^{pq} &= -\iint \phi_p(x,y)(c_0 + c_1)\psi_{-1}^{2*}\phi_q(x,y)dxdy,\\
M_{66}^{pq} &= -\iint \phi_p(x,y)\Bigg[-\frac{1}{2}\partial_x^2 - \frac{1}{2}\partial_y^2 - \mu + V(x,y) + c_0(\rho + \rho_{-1})\\
&\quad + c_1(2\rho_{-1} + \rho_0 - \rho_1)\Bigg]\phi_q(x,y)dxdy.
\end{aligned}
$$

The projection implementation allows one to cast the BdG equations as a $6N_b \times 6N_b$ matrix eigenvalue problem with the eigenvector of form

$$
\begin{aligned}
&[m_1^{+1}, m_2^{+1}, \ldots, m_{N_b}^{+1}, n_1^{+1}, n_2^{+1}, \ldots, n_{N_b}^{+1}, m_1^0, m_2^0, \ldots, m_{N_b}^0,\\
&n_1^0, n_2^0, \ldots, n_{N_b}^0, m_1^{-1}, m_2^{-1}, \ldots, m_{N_b}^{-1}, n_1^{-1}, n_2^{-1}, \ldots, n_{N_b}^{-1}]^T
\end{aligned} \tag{C.2}
$$

The $6N_b \times 6N_b$ matrix is a sparse matrix, and one can employ the sparse matrix representation in the ARPACK library for diagonalization [226]. For small N_b, LAPACK subroutines [184] can also efficiently handle the diagonalization of the matrix. This thesis considers $N_b = 900$, corresponding to 30 one-dimensional harmonic oscillator basis states, each along x and y direction; the matrix eigenvalue problem can be solved using the LAPACK software package.

List of Publications

Published Journal Articles:

1. **P. Banger**, Rajat, A. Roy, and S. Gautam, *Quantum phases and spectrum of collective modes in a spin-1 BEC with spin-orbital-angular-momentum coupling,* Phys. Rev. A, **108** (2023) 043310.
2. **P. Banger**, *Vortex-lattice formation in spin-orbit-coupled spin-2 Bose-Einstein Condensate under Rotation,* J. Low Temp. Phys., **213** (2023) 155170.
3. **P. Banger**, R. K. Kumar, A. Roy, and S. Gautam, *Effective potentials in a rotating spin-orbit-coupled spin-1 spinor condensate,* J. Phys.: Condens. Matter, **35** (2023) 045401.
4. **P. Banger**, P. Kaur, A. Roy, and S. Gautam, *FORTRESS: FORTRAN programs to solve coupled Gross-Pitaevskii equations for spin-orbit coupled spin-f Bose-Einstein condensates with spin $f = 1$ or 2,* Comput. Phys. Commun. **279** (2022) 108442.
5. **P. Banger**, P. Kaur, and S. Gautam, *Semi-implicit finite difference methods to study the spin-orbit- and coherently-coupled spinor Bose-Einstein condensates,* Int. J. Mod. Phys. C **33** (04) (2022) 2250046.

Manuscript Under Preparation:

1. **P. Banger**, Rajat, and S. Gautam, *Collective excitation spectrum of an annular-stripe of spin-orbital-angular-momentum coupled spin-1 BEC.*

Conference Presentations

Poster Presentations:

1. “Effective potentials in rotating spin-orbit-coupled BECs” at **Ultracold Quantum Matter: Basic Research and Applications**, Physikzentrum Bad Honnef, Germany, 12–16 Dec 2022.
2. “Effective potentials in a rotating spin-orbit-coupled spin-1 spinor condensate” at **Conference on Condensed Matter Physics (PRL CCMP 2023)**, Physical Research Laboratory, Ahmedabad, India, 6-8 February 2023.
3. “Effective potentials in a rotating spin-orbit-coupled spin-1 spinor condensate” at **Physics Day**, Indian Institute of Technology Ropar (IIT Ropar), India, 3rd March 2023.
4. “Effective potentials in a rotating spin-orbit-coupled spin-1 spinor condensate” at **School on Light and Cold Atoms**, ICTP-SAIFR/IFT-UNESP São Paulo, Brazil, 6-17 March 2023.
5. “Effective potentials in a rotating spin-orbit-coupled spin-1 spinor condensate” at **Workshop on Low Dimensional Quantum Gases**, Principia Institute, São Paulo, Brazil, 19-22 March 2023.
6. “Quantum phases and the spectrum of collective modes in a spin-1 Bose-Einstein condensate with spin-orbital-angular-momentum coupling” at **Annual Conference on Quantum Condensed Matter (QMAT2023)**, NISER Bhubaneswar, India, 27-30 November 2023.

Oral Presentation (Invited Talk)

1. “Quantum phases and the spectrum of collective modes in a spin-1 Bose-Einstein condensate with spin-orbital-angular-momentum coupling” at conference **Quantum Technologies using UltraCold atoms**, IISER Pune, India, 15–17 November 2023.

References

[1] Y. Kawaguchi and M. Ueda, "Spinor Bose-Einstein condensates," *Physics Reports*, vol. 520, p. 253, 2012.

[2] L. Tao and E. Y. Tsymbal, "Persistent spin texture enforced by symmetry," *Nature Communications*, vol. 9, p. 2763, 2018.

[3] I. B. Spielman, "Raman processes and effective gauge potentials," *Phys. Rev. A*, vol. 79, p. 063613, 2009.

[4] J. Radic, *Spin-Orbit-Coupled Qunatum Gases.* PhD thesis, University of Maryland, 2015.

[5] D. Zhang, T. Gao, P. Zou, L. Kong, R. Li, X. Shen, X.-L. Chen, S.-G. Peng, M. Zhan, H. Pu, and K. Jiang, "Ground-state phase diagram of a spin-orbital-angular-momentum coupled Bose-Einstein condensate," *Phys. Rev. Lett.*, vol. 122, p. 110402, 2019.

[6] S.-G. Peng, K. Jiang, X.-L. Chen, K.-J. Chen, P. Zou, and L. He, "Spin-orbital-angular-momentum-coupled quantum gases," *AAPPS Bulletin*, vol. 32, p. 36, 2022.

[7] Bose, "Plancks gesetz und lichtquantenhypothese," *Zeitschrift für Physik*, vol. 26, p. 178, 1924.

[8] A. Einstein, "Sitzungsber," *Kgl. Preuss. Akad. Wiss*, vol. 3, p. 261, 1925.

[9] A. Einstein, *Quantentheorie des einatomigen idealen gases, sitzungsberichte kgl*, vol. 261. 1924.

[10] J. Ranninger, A. Griffin, D. Snoke, and S. Stringari, *Bose-Einstein Condensation.* Cambridge University Press, 1995.

[11] F. London, "The λ-phenomenon of liquid helium and the Bose-Einstein degeneracy," *Nature*, vol. 141, p. 643, 1938.

[12] L. Onsager, "Statistical hydrodynamics," *II Nuovo Cimento (1943-1954)*, vol. 6, p. 279, 1949.

[13] R. P. Feynman, "Chapter II application of quantum mechanics to liquid helium," in *Progress in low temperature physics*, vol. 1, p. 17, Elsevier, 1955.

[14] H. E. Hall and W. F. Vinen, "The rotation of liquid helium II II. the theory of mutual friction in uniformly rotating helium II," *Proceedings of the Royal Society of London. Series A. Mathematical and Physical Sciences*, vol. 238, p. 215, 1956.

[15] H. E. Hall and W. F. Vinen, "The rotation of liquid helium II I. Experiments on the propagation of second sound in uniformly rotating helium II," *Proceedings of the Royal Society of London. Series A. Mathematical and Physical Sciences*, vol. 238, p. 204, 1956.

[16] V. Tkachenko, "On vortex lattices," *Sov. Phys. JETP*, vol. 22, p. 1282, 1966.

[17] M. R. Matthews, B. P. Anderson, P. Haljan, D. Hall, C. Wieman, and E. A. Cornell, "Vortices in a Bose-Einstein condensate," *Phys. Rev. Lett.*, vol. 83, p. 2498, 1999.

[18] K. W. Madison, F. Chevy, W. Wohlleben, and J. Dalibard, "Vortex formation in a stirred Bose-Einstein condensate," *Phys. Rev. Lett.*, vol. 84, p. 806, 2000.

[19] J. R. Abo-Shaeer, C. Raman, J. M. Vogels, and W. Ketterle, "Observation of vortex lattices in Bose-Einstein condensates," *Science*, vol. 292, p. 476, 2001.

[20] M. H. Anderson, J. R. Ensher, M. R. Matthews, C. E. Wieman, and E. A. Cornell, "Observation of Bose-Einstein condensation in a dilute atomic vapor," *Science*, vol. 269, p. 198, 1995.

[21] K. B. Davis, M.-O. Mewes, M. R. Andrews, N. J. van Druten, D. S. Durfee, D. Kurn, and W. Ketterle, "Bose-Einstein condensation in a gas of sodium atoms," *Phys. Rev. Lett.*, vol. 75, p. 3969, 1995.

[22] C. C. Bradley, C. Sackett, J. Tollett, and R. G. Hulet, "Evidence of Bose-Einstein condensation in an atomic gas with attractive interactions," *Phys. Rev. Lett.*, vol. 75, p. 1687, 1995.

[23] M. Andrews, C. Townsend, H.-J. Miesner, D. Durfee, D. Kurn, and W. Ketterle, "Observation of interference between two Bose condensates," *Science*, vol. 275, p. 637, 1997.

[24] M.-O. Mewes, M. Andrews, D. Kurn, D. Durfee, C. Townsend, and W. Ketterle, "Output coupler for Bose-Einstein condensed atoms," *Phys. Rev. Lett.*, vol. 78, p. 582, 1997.

[25] S. L. Cornish, N. R. Claussen, J. L. Roberts, E. A. Cornell, and C. E. Wieman, "Stable ^{85}Rb Bose-Einstein condensates with widely tunable interactions," *Phys. Rev. Lett.*, vol. 85, p. 1795, 2000.

[26] E. H. Lieb, R. Seiringer, and J. Yngvason, "Bosons in a trap: A rigorous derivation of the Gross–Pitaevskii energy functional," *Phys. Rev. A*, vol. 61, p. 043602, Mar 2000.

[27] I. Coddington, P. C. Haljan, P. Engels, V. Schweikhard, S. Tung, and E. A. Cornell, "Experimental studies of equilibrium vortex properties in a Bose-condensed gas," *Phys. Rev. A*, vol. 70, p. 063607, 2004.

[28] A. L. Fetter and A. A. Svidzinsky, "Vortices in a trapped dilute Bose-Einstein condensate," *J. Phys.: Condens. Matter*, vol. 13, p. R135, 2001.

[29] J. R. Abo-Shaeer, C. Raman, and W. Ketterle, "Formation and decay of vortex lattices in Bose-Einstein condensates at finite temperatures," *Phys. Rev. Lett.*, vol. 88, p. 070409, 2002.

[30] K. Kasamatsu, M. Tsubota, and M. Ueda, "Vortices in multicomponent Bose-Einstein condensates," *International Journal of Modern Physics B*, vol. 19, p. 1835, 2005.

[31] V. Schweikhard, I. Coddington, P. Engels, V. P. Mogendorff, and E. A. Cornell, "Rapidly rotating Bose-Einstein condensates in and near the lowest landau level," *Phys. Rev. Lett.*, vol. 92, p. 040404, 2004.

[32] V. Bretin, S. Stock, Y. Seurin, and J. Dalibard, "Fast rotation of a Bose-Einstein condensate," *Phys. Rev. Lett.*, vol. 92, p. 050403, 2004.

[33] A. L. Fetter, "Rotating trapped Bose-Einstein condensates," *Rev. Mod. Phys.*, vol. 81, p. 647, 2009.

[34] M.-S. Chang, C. D. Hamley, M. D. Barrett, J. A. Sauer, K. M. Fortier, W. Zhang, L. You, and M. S. Chapman, "Observation of spinor dynamics in optically trapped ^{87}Rb Bose-Einstein condensates," *Phys. Rev. Lett.*, vol. 92, p. 140403, 2004.

[35] J. Stenger, S. Inouye, D. Stamper-Kurn, H.-J. Miesner, A. Chikkatur, and W. Ketterle, "Spin domains in ground-state Bose-Einstein condensates," *Nature*, vol. 396, p. 345, 1998.

[36] A. Robert, O. Sirjean, A. Browaeys, J. Poupard, S. Nowak, D. Boiron, C. I. Westbrook, and A. Aspect, "A Bose-Einstein condensate of metastable atoms," *Science*, vol. 292, p. 461, 2001.

[37] F. P. Dos Santos, J. Léonard, J. Wang, C. Barrelet, F. Perales, E. Rasel, C. Unnikrishnan, M. Leduc, and C. Cohen-Tannoudji, "Bose-Einstein condensation of metastable helium," *Phys. Rev. Lett.*, vol. 86, p. 3459, 2001.

[38] G. Modugno, G. Ferrari, G. Roati, R. J. Brecha, A. Simoni, and M. Inguscio, "Bose-Einstein condensation of potassium atoms by sympathetic cooling," *Science*, vol. 294, p. 1320, 2001.

[39] T. Weber, J. Herbig, M. Mark, H.-C. Nagerl, and R. Grimm, "Bose-Einstein condensation of cesium," *Science*, vol. 299, p. 232, 2003.

[40] B. Pasquiou, E. Maréchal, G. Bismut, P. Pedri, L. Vernac, O. Gorceix, and B. Laburthe-Tolra, "Spontaneous demagnetization of a dipolar spinor Bose gas in an ultralow magnetic field," *Phys. Rev. Lett.*, vol. 106, p. 255303, 2011.

[41] P. M. Chaikin, T. C. Lubensky, and T. A. Witten, *Principles of condensed matter physics*, vol. 10. Cambridge University Press, 1995.

[42] L. P. Pitaevskii, "Vortex lines in an imperfect Bose gas," *Sov. Phys. JETP*, vol. 13, p. 451, 1961.

[43] E. P. Gross, "Structure of a quantized vortex in boson systems," *Il Nuovo Cimento (1955-1965)*, vol. 20, p. 454, 1961.

[44] F. Dalfovo, S. Giorgini, L. P. Pitaevskii, and S. Stringari, "Theory of Bose-Einstein condensation in trapped gases," *Rev. Mod. Phys.*, vol. 71, p. 463, 1999.

[45] C. J. Pethick and H. Smith, *Bose–Einstein Condensation in Dilute Gases.* Cambridge University Press, 2008.

[46] D. Stamper-Kurn, M. Andrews, A. Chikkatur, S. Inouye, H.-J. Miesner, J. Stenger, and W. Ketterle, "Optical confinement of a Bose-Einstein condensate," *Phys. Rev. Lett.*, vol. 80, p. 2027, 1998.

[47] M. R. Matthews, B. P. Anderson, P. C. Haljan, D. S. Hall, M. J. Holland, J. E. Williams, C. E. Wieman, and E. A. Cornell, "Watching a superfluid untwist itself: Recurrence of rabi oscillations in a Bose-Einstein condensate," *Phys. Rev. Lett.*, vol. 83, p. 3358, 1999.

[48] H. Zhai, "Degenerate quantum gases with spin–orbit coupling: a review," *Rep. Prog. Phys.*, vol. 78, p. 026001, 2015.

[49] H. Schmaljohann, M. Erhard, J. Kronjäger, M. Kottke, S. Van Staa, L. Cacciapuoti, J. Arlt, K. Bongs, and K. Sengstock, "Dynamics of $f = 2$ spinor Bose-Einstein condensates," *Phys. Rev. Lett.*, vol. 92, p. 040402, 2004.

[50] A. Griesmaier, J. Werner, S. Hensler, J. Stuhler, and T. Pfau, "Bose-Einstein condensation of chromium," *Phys. Rev. Lett.*, vol. 94, p. 160401, 2005.

[51] M. Koashi and M. Ueda, "Exact eigenstates and magnetic response of spin-1 and spin-2 Bose-Einstein condensates," *Phys. Rev. Lett.*, vol. 84, p. 1066, 2000.

[52] H. Saito and M. Ueda, "Diagnostics for the ground-state phase of a spin-2 Bose-Einstein condensate," *Phys. Rev. A*, vol. 72, p. 053628, 2005.

[53] K. Murata, H. Saito, and M. Ueda, "Broken-axisymmetry phase of a spin-1 ferromagnetic Bose-Einstein condensate," *Phys. Rev. A*, vol. 75, p. 013607, 2007.

[54] H. Mäkelä and K.-A. Suominen, "Ground states of spin-3 Bose-Einstein condensates for conserved magnetization," *Phys. Rev. A*, vol. 75, p. 033610, 2007.

[55] T.-L. Ho, "Spinor Bose condensates in optical traps," *Phys. Rev. Lett.*, vol. 81, p. 742, 1998.

[56] T. Ohmi and K. Machida, "Bose-Einstein condensation with internal degrees of freedom in alkali atom gases," *Journal of the Physical Society of Japan*, vol. 67, p. 1822, 1998.

[57] C. V. Ciobanu, S.-K. Yip, and T.-L. Ho, "Phase diagrams of $f = 2$ spinor Bose-Einstein condensates," *Phys. Rev. A*, vol. 61, p. 033607, 2000.

[58] N. N. Bogolyubov, "On the theory of superfluidity," *J. Phys. (USSR)*, vol. 11, p. 23, 1947.

[59] A. Griffin, "Conserving and gapless approximations for an inhomogeneous Bose gas at finite temperatures," *Phys. Rev. B*, vol. 53, p. 9341, 1996.

[60] H. Saito and M. Ueda, "Spontaneous magnetization and structure formation in a spin-1 ferromagnetic Bose-Einstein condensate," *Phys. Rev. A*, vol. 72, p. 023610, 2005.

[61] C. Ciobanu, S.-K. Yip, and T.-L. Ho, "Phase diagrams of $f = 2$ spinor Bose-Einstein condensates," *Phys. Rev. A*, vol. 61, p. 033607, 2000.

[62] M. Ueda and M. Koashi, "Theory of spin-2 Bose-Einstein condensates: Spin correlations, magnetic response, and excitation spectra," *Phys. Rev. A*, vol. 65, p. 063602, 2002.

[63] D. M. Stamper-Kurn and M. Ueda, "Spinor bose gases: Symmetries, magnetism, and quantum dynamics," *Rev. Mod. Phys.*, vol. 85, p. 1191, 2013.

[64] C. Chin, R. Grimm, P. Julienne, and E. Tiesinga, "Feshbach resonances in ultracold gases," *Rev. Mod. Phys.*, vol. 82, p. 1225, 2010.

[65] D. Xiao, M.-C. Chang, and Q. Niu, "Berry phase effects on electronic properties," *Rev. Mod. Phys.*, vol. 82, p. 1959, 2010.

[66] M. Z. Hasan and C. L. Kane, "Colloquium: topological insulators," *Rev. Mod. Phys.*, vol. 82, p. 3045, 2010.

[67] I. Žutić, J. Fabian, and S. D. Sarma, "Spintronics: Fundamentals and applications," *Rev. Mod. Phys.*, vol. 76, p. 323, 2004.

[68] Y. A. Bychkov and E. I. Rashba, "Oscillatory effects and the magnetic susceptibility of carriers in inversion layers," *Journal of physics C: Solid state physics*, vol. 17, p. 6039, 1984.

[69] G. Dresselhaus, "Spin-orbit coupling effects in zinc blende structures," *Phys. Rev.*, vol. 100, p. 580, 1955.

[70] S. D. Ganichev and L. E. Golub, "Interplay of Rashba/Dresselhaus spin splittings probed by photogalvanic spectroscopy-a review," *Phys. Status Solidi B*, vol. 251, p. 1801, 2014.

[71] M. Johanning, A. F. Varón, and C. Wunderlich, “Quantum simulations with cold trapped ions,” *Journal of Physics B: Atomic, Molecular and Optical Physics*, vol. 42, p. 154009, 2009.

[72] I. Bloch, J. Dalibard, and S. Nascimbene, “Quantum simulations with ultracold quantum gases,” *Nature Physics*, vol. 8, p. 267, 2012.

[73] Y.-J. Lin, R. L. Compton, K. Jiménez-García, J. V. Porto, and I. B. Spielman, “Synthetic magnetic fields for ultracold neutral atoms,” *Nature*, vol. 462, p. 628, 2009.

[74] Y.-J. Lin, R. L. Compton, K. Jimenez-Garcia, W. D. Phillips, J. V. Porto, and I. B. Spielman, “A synthetic electric force acting on neutral atoms,” *Nature Physics*, vol. 7, p. 531, 2011.

[75] Y.-J. Lin, K. Jiménez-García, and I. B. Spielman, “Spin–orbit-coupled Bose-Einstein condensates,” *Nature*, vol. 471, p. 83, 2011.

[76] D. Campbell, R. Price, A. Putra, A. Valdés-Curiel, D. Trypogeorgos, and I. Spielman, “Magnetic phases of spin-1 spin-orbit-coupled Bose gases,” *Nature Communications*, vol. 7, p. 10897, 2016.

[77] X. Luo, L. Wu, J. Chen, Q. Guan, K. Gao, Z.-F. Xu, L. You, and R. Wang, “Tunable atomic spin-orbit coupling synthesized with a modulating gradient magnetic field,” *Scientific Reports*, vol. 6, p. 18983, 2016.

[78] Z. Cai, X. Zhou, and C. Wu, “Magnetic phases of bosons with synthetic spin-orbit coupling in optical lattices,” *Phys. Rev. A*, vol. 85, p. 061605, 2012.

[79] W. S. Cole, S. Zhang, A. Paramekanti, and N. Trivedi, “Bose-hubbard models with synthetic spin-orbit coupling: Mott insulators, spin textures, and superfluidity,” *Phys. Rev. Lett.*, vol. 109, p. 085302, 2012.

[80] M. Gong, Y. Qian, M. Yan, V. W. Scarola, and C. Zhang, “Dzyaloshinskii-moriya interaction and spiral order in spin-orbit coupled optical lattices,” *Scientific Reports*, vol. 5, p. 10050, 2015.

[81] C. Wang, C. Gao, C.-M. Jian, and H. Zhai, “Spin-orbit coupled spinor Bose-Einstein condensates,” *Phys. Rev. Lett.*, vol. 105, p. 160403, 2010.

[82] E. Ruokokoski, J. A. Huhtamäki, and M. Möttönen, “Stationary states of trapped spin-orbit-coupled Bose-Einstein condensates,” *Phys. Rev. A*, vol. 86, p. 051607, 2012.

[83] G. I. Martone, F. V. Pepe, P. Facchi, S. Pascazio, and S. Stringari, “Tricriticalities and quantum phases in spin-orbit-coupled spin-1 Bose gases,” *Phys. Rev. Lett.*, vol. 117, p. 125301, 2016.

[84] H. Sakaguchi, E. Y. Sherman, and B. A. Malomed, “Vortex solitons in two-dimensional spin-orbit coupled Bose-Einstein condensates: Effects of the Rashba-Dresselhaus coupling and zeeman splitting,” *Phys. Rev. E*, vol. 94, p. 032202, 2016.

[85] S. Gautam and S. K. Adhikari, “Vortex-bright solitons in a spin-orbit-coupled spin-1 condensate,” *Phys. Rev. A*, vol. 95, p. 013608, 2017.

[86] S. Gautam and S. K. Adhikari, “Three-dimensional vortex-bright solitons in a spin-orbit-coupled spin-1 condensate,” *Phys. Rev. A*, vol. 97, p. 013629, 2018.

[87] S. Gautam and S. K. Adhikari, “Solitons in a spin-orbit-coupled spin-1 Bose-Einstein condensate,” *Brazilian Journal of Physics*, vol. 51, p. 298, 2021.

[88] Y.-K. Liu, Y. Liu, and S.-J. Yang, “Stable knotted structure in spin-1 Bose-Einstein condensates with spin-orbit coupling,” *Phys. Rev. A*, vol. 99, p. 063626, 2019.

[89] S. K. Adhikari, “Multiring, stripe, and superlattice solitons in a spin-orbit-coupled spin-1 condensate,” *Phys. Rev. A*, vol. 103, p. L011301, 2021.

[90] P. Kaur, S. Gautam, and S. K. Adhikari, “Supersolid-like solitons in a spin-orbit-coupled spin-2 condensate,” *Phys. Rev. A*, vol. 105, p. 023303, 2022.

[91] S. Zhang, W. S. Cole, A. Paramekanti, and N. Trivedi, “Spin-orbit coupling in optical lattices,” *Annual Review of Cold Atoms and Molecules*, vol. 3, p. 135, 2015.

[92] L. Onsager, P. C. Hemmer, and H. Holden, *Lars Onsager*, vol. 17. World Scientific, 1996.

[93] W. F. Vinen, “The detection of single quanta of circulation in liquid helium II,” *Proceedings of the Royal Society of London. Series A. Mathematical and Physical Sciences*, vol. 260, p. 218, 1961.

[94] M. Gordon, R. Packard, *et al.*, “Vortex photography: A progress report,” *Le Journal de Physique Colloques*, vol. 39, p. C6, 1978.

[95] T. Mizushima, K. Machida, and T. Kita, “Axisymmetric versus nonaxisymmetric vortices in spinor Bose-Einstein condensates,” *Phys. Rev. A*, vol. 66, p. 053610, 2002.

[96] T. Mizushima, K. Machida, and T. Kita, “Mermin-ho vortex in ferromagnetic spinor Bose-Einstein condensates,” *Phys. Rev. Lett.*, vol. 89, p. 030401, 2002.

[97] M. Ueda, “Topological aspects in spinor Bose-Einstein condensates,” *Rep. Prog. Phys.*, vol. 77, p. 122401, 2014.

[98] T. Mizushima, N. Kobayashi, and K. Machida, “Coreless and singular vortex lattices in rotating spinor Bose-Einstein condensates,” *Phys. Rev. A*, vol. 70, p. 043613, 2004.

[99] T. Isoshima and K. Machida, “Axisymmetric vortices in spinor Bose-Einstein condensates under rotation,” *Phys. Rev. A*, vol. 66, p. 023602, 2002.

[100] K. Kasamatsu, M. Tsubota, and M. Ueda, “Giant hole and circular superflow in a fast rotating Bose-Einstein condensate,” *Phys. Rev. A*, vol. 66, p. 053606, 2002.

[101] T.-L. Ho, “Bose-Einstein condensates with large issue of vortices,” *Phys. Rev. Lett.*, vol. 87, p. 060403, 2001.

[102] N. K. Wilkin and J. M. F. Gunn, “Condensation of “composite bosons” in a rotating BEC,” *Phys. Rev. Lett.*, vol. 84, p. 6, 2000.

[103] N. R. Cooper and N. K. Wilkin, “Composite fermion description of rotating Bose-Einstein condensates,” *Phys. Rev. B*, vol. 60, p. R16279, 1999.

[104] N. R. Cooper, N. K. Wilkin, and J. M. F. Gunn, “Quantum phases of vortices in rotating Bose-Einstein condensates,” *Phys. Rev. Lett.*, vol. 87, p. 120405, 2001.

[105] N. Regnault and T. Jolicoeur, “Quantum hall fractions in rotating Bose-Einstein condensates,” *Phys. Rev. Lett.*, vol. 91, p. 030402, 2003.

[106] V. Schweikhard, I. Coddington, P. Engels, S. Tung, and E. A. Cornell, “Vortex-lattice dynamics in rotating spinor Bose-Einstein condensates,” *Phys. Rev. Lett.*, vol. 93, p. 210403, 2004.

[107] J. W. Reijnders, F. J. M. van Lankvelt, K. Schoutens, and N. Read, “Quantum hall states and boson triplet condensate for rotating spin-1 bosons,” *Phys. Rev. Lett.*, vol. 89, p. 120401, 2002.

[108] K. V. Kavokin, I. A. Shelykh, A. V. Kavokin, G. Malpuech, and P. Bigenwald, “Quantum theory of spin dynamics of exciton-polaritons in microcavities,” *Phys. Rev. Lett.*, vol. 92, p. 017401, 2004.

[109] H. Zhai, “Spin-orbit coupled quantum gases,” *International Journal of Modern Physics B*, vol. 26, p. 1230001, 2012.

[110] N. Goldman, G. Juzeliūnas, P. Öhberg, and I. B. Spielman, “Light-induced gauge fields for ultracold atoms,” *Rep. Prog. Phys.*, vol. 77, p. 126401, 2014.

[111] J. Dalibard, F. Gerbier, G. Juzeliūnas, and P. Öhberg, “Colloquium: Artificial gauge potentials for neutral atoms,” *Rev. Mod. Phys.*, vol. 83, p. 1523, 2011.

[112] J. Radić, T. A. Sedrakyan, I. B. Spielman, and V. Galitski, “Vortices in spin-orbit-coupled Bose-Einstein condensates,” *Phys. Rev. A*, vol. 84, p. 063604, 2011.

[113] X.-Q. Xu and J. H. Han, “Spin-orbit coupled Bose-Einstein condensate under rotation,” *Phys. Rev. Lett.*, vol. 107, p. 200401, 2011.

[114] X.-F. Zhou, J. Zhou, and C. Wu, "Vortex structures of rotating spin-orbit-coupled Bose-Einstein condensates," *Phys. Rev. A*, vol. 84, p. 063624, 2011.

[115] C.-F. Liu, H. Fan, Y.-C. Zhang, D.-S. Wang, and W.-M. Liu, "Circular-hyperbolic skyrmion in rotating pseudo-spin-1/2 Bose-Einstein condensates with spin-orbit coupling," *Phys. Rev. A*, vol. 86, p. 053616, 2012.

[116] A. Aftalion and P. Mason, "Phase diagrams and Thomas-Fermi estimates for spin-orbit-coupled Bose-Einstein condensates under rotation," *Phys. Rev. A*, vol. 88, p. 023610, 2013.

[117] A. Aftalion and P. Mason, "Rabi-coupled two-component Bose-Einstein condensates: Classification of the ground states, defects, and energy estimates," *Phys. Rev. A*, vol. 94, p. 023616, 2016.

[118] C.-F. Liu and W. Liu, "Spin-orbit-coupling-induced half-skyrmion excitations in rotating and rapidly quenched spin-1 Bose-Einstein condensates," *Phys. Rev. A*, vol. 86, p. 033602, 2012.

[119] S.-W. Su, C.-H. Hsueh, I.-K. Liu, T.-L. Horng, Y.-C. Tsai, S.-C. Gou, and W. Liu, "Spontaneous crystallization of skyrmions and fractional vortices in fast-rotating and rapidly quenched spin-1 Bose-Einstein condensates," *Phys. Rev. A*, vol. 84, p. 023601, 2011.

[120] C.-F. Liu, Y.-M. Yu, S.-C. Gou, and W.-M. Liu, "Vortex chain in anisotropic spin-orbit-coupled spin-1 Bose-Einstein condensates," *Phys. Rev. A*, vol. 87, p. 063630, 2013.

[121] S. K. Adhikari, "Vortex-lattice formation in a spin-orbit coupled rotating spin-1 condensate," *J. Phys.: Condens. Matter*, vol. 33, p. 065404, 2020.

[122] L. D. Landau and E. M. Lifshitz, *Quantum mechanics: Non-relativistic Theory*, vol. 3. Elsevier, 2013.

[123] A. De-Shalit and I. Talmi, *Nuclear shell theory*, vol. 14. Academic Press, 2013.

[124] X. Zhou, Y. Li, Z. Cai, and C. Wu, "Unconventional states of bosons with the synthetic spin-orbit coupling," *Journal of Physics B: Atomic, Molecular and Optical Physics*, vol. 46, p. 134001, 2013.

[125] V. Galitski and I. B. Spielman, "Spin-orbit coupling in quantum gases," *Nature*, vol. 494, p. 49, 2013.

[126] S. Zhang and G.-B. Jo, "Recent advances in spin-orbit coupled quantum gases," *Journal of Physics and Chemistry of Solids*, vol. 128, p. 75, 2019.

[127] X.-J. Liu, H. Jing, X. Liu, and M.-L. Ge, "Generation of two-flavor vortex atom laser from a five-state medium," *The European Physical Journal D-Atomic, Molecular, Optical and Plasma Physics*, vol. 37, p. 261, 2006.

[128] M. DeMarco and H. Pu, “Angular spin-orbit coupling in cold atoms,” *Phys. Rev. A*, vol. 91, p. 033630, 2015.

[129] K. Sun, C. Qu, and C. Zhang, “Spin–orbital-angular-momentum coupling in Bose-Einstein condensates,” *Phys. Rev. A*, vol. 91, p. 063627, 2015.

[130] C. Qu, K. Sun, and C. Zhang, “Quantum phases of Bose-Einstein condensates with synthetic spin–orbital-angular-momentum coupling,” *Phys. Rev. A*, vol. 91, p. 053630, 2015.

[131] Y.-X. Hu, C. Miniatura, B. Gremaud, *et al.*, “Half-skyrmion and vortex-antivortex pairs in spinor condensates,” *Phys. Rev. A*, vol. 92, p. 033615, 2015.

[132] L. Chen, H. Pu, and Y. Zhang, “Spin-orbit angular momentum coupling in a spin-1 Bose-Einstein condensate,” *Phys. Rev. A*, vol. 93, p. 013629, 2016.

[133] I. Vasić and A. Balaž, “Excitation spectra of a Bose-Einstein condensate with an angular spin-orbit coupling,” *Phys. Rev. A*, vol. 94, p. 033627, 2016.

[134] J. Hou, X.-W. Luo, K. Sun, and C. Zhang, “Adiabatically tuning quantized supercurrents in an annular Bose-Einstein condensate,” *Phys. Rev. A*, vol. 96, p. 011603, 2017.

[135] H.-R. Chen, K.-Y. Lin, P.-K. Chen, N.-C. Chiu, J.-B. Wang, C.-A. Chen, P. Huang, S.-K. Yip, Y. Kawaguchi, and Y.-J. Lin, “Spin–orbital-angular-momentum coupled Bose-Einstein condensates,” *Phys. Rev. Lett.*, vol. 121, p. 113204, 2018.

[136] P.-K. Chen, L.-R. Liu, M.-J. Tsai, N.-C. Chiu, Y. Kawaguchi, S.-K. Yip, M.-S. Chang, and Y.-J. Lin, “Rotating atomic quantum gases with light-induced azimuthal gauge potentials and the observation of the Hess-Fairbank effect,” *Phys. Rev. Lett.*, vol. 121, p. 250401, 2018.

[137] M. Scully, M. Zubairy, *et al.*, *Quantum optics*. Cambridge University Press, 1997.

[138] W. F. Holmgren, R. Trubko, I. Hromada, and A. D. Cronin, “Measurement of a wavelength of light for which the energy shift for an atom vanishes,” *Phys. Rev. Lett.*, vol. 109, p. 243004, 2012.

[139] C. D. Herold, V. D. Vaidya, X. Li, S. L. Rolston, J. V. Porto, and M. S. Safronova, “Precision measurement of transition matrix elements via light shift cancellation,” *Phys. Rev. Lett.*, vol. 109, p. 243003, 2012.

[140] Y. Duan, Y. M. Bidasyuk, and A. Surzhykov, “Symmetry breaking and phase transitions in Bose-Einstein condensates with spin–orbital-angular-momentum coupling,” *Phys. Rev. A*, vol. 102, p. 063328, 2020.

[141] X.-L. Chen, S.-G. Peng, P. Zou, X.-J. Liu, and H. Hu, “Angular stripe phase in spin-orbital-angular-momentum coupled Bose condensates,” *Phys. Rev. Res.*, vol. 2, p. 033152, 2020.

[142] N. Chiu, Y. Kawaguchi, S. Yip, and Y. Lin, "Visible stripe phases in spin-orbital-angular-momentum coupled Bose-Einstein condensates," *New Journal of Physics*, vol. 22, p. 093017, 2020.

[143] Y. M. Bidasyuk, K. S. Kovtunenko, and O. O. Prikhodko, "Fine structure of the stripe phase in ring-shaped Bose-Einstein condensates with spin-orbital-angular-momentum coupling," *Phys. Rev. A*, vol. 105, p. 023320, 2022.

[144] K.-J. Chen, F. Wu, J. Hu, and L. He, "Ground-state phase diagram and excitation spectrum of a Bose-Einstein condensate with spin-orbital-angular-momentum coupling," *Phys. Rev. A*, vol. 102, p. 013316, 2020.

[145] L. Pitaevskii and S. Stringari, *Bose-Einstein condensation and superfluidity*, vol. 164. Oxford University Press, 2016.

[146] D. Jin, J. Ensher, M. Matthews, C. Wieman, and E. A. Cornell, "Collective excitations of a Bose-Einstein condensate in a dilute gas," *Phys. Rev. Lett.*, vol. 77, p. 420, 1996.

[147] M.-O. Mewes, M. Andrews, N. Van Druten, D. Kurn, D. Durfee, C. Townsend, and W. Ketterle, "Collective excitations of a Bose-Einstein condensate in a magnetic trap," *Phys. Rev. Lett.*, vol. 77, p. 988, 1996.

[148] D. Stamper-Kurn, H.-J. Miesner, S. Inouye, M. Andrews, and W. Ketterle, "Collisionless and hydrodynamic excitations of a Bose-Einstein condensate," *Phys. Rev. Lett.*, vol. 81, p. 500, 1998.

[149] F. Chevy, V. Bretin, P. Rosenbusch, K. Madison, and J. Dalibard, "Transverse breathing mode of an elongated Bose-Einstein condensate," *Phys. Rev. Lett.*, vol. 88, p. 250402, 2002.

[150] H. Ott, J. Fortágh, S. Kraft, A. Günther, D. Komma, and C. Zimmermann, "Nonlinear dynamics of a Bose-Einstein condensate in a magnetic waveguide," *Phys. Rev. Lett.*, vol. 91, p. 040402, 2003.

[151] M. Edwards, P. Ruprecht, K. Burnett, R. Dodd, and C. W. Clark, "Collective excitations of atomic Bose-Einstein condensates," *Phys. Rev. Lett.*, vol. 77, p. 1671, 1996.

[152] Y. Lu, W. Xiao-Rui, L. Ke, T. Xin-Zhou, X. Hong-Wei, and L. Bao-Long, "Low-energy collective excitation of Bose-Einstein condensates in an anisotropic magnetic trap," *Chinese Physics Letters*, vol. 26, p. 076701, 2009.

[153] S. Stringari, "Collective excitations of a trapped Bose-condensed gas," *Phys. Rev. Lett.*, vol. 77, p. 2360, 1996.

[154] M. Edwards, R. Dodd, C. W. Clark, and K. Burnett, "Zero-temperature, mean-field theory of atomic Bose-Einstein condensates," *Journal of research of the National Institute of Standards and Technology*, vol. 101, p. 553, 1996.

[155] K. Singh and D. Rokhsar, "Collective excitations of a confined Bose condensate," *Phys. Rev. Lett.*, vol. 77, p. 1667, 1996.

[156] L. You, W. Hoston, and M. Lewenstein, "Low-energy excitations of trapped Bose condensates," *Phys. Rev. A*, vol. 55, p. R1581, 1997.

[157] Y. Castin and R. Dum, "Bose-Einstein condensates in time dependent traps," *Phys. Rev. Lett.*, vol. 77, p. 5315, 1996.

[158] J. J. Garcia-Ripoll, V. M. Perez-Garcia, and P. Torres, "Extended parametric resonances in nonlinear schrödinger systems," *Phys. Rev. Lett.*, vol. 83, p. 1715, 1999.

[159] F. Dalfovo, C. Minniti, and L. Pitaevskii, "Frequency shift and mode coupling in the nonlinear dynamics of a Bose condensed gas," *Phys. Rev. A*, vol. 56, p. 4855, 1997.

[160] J. J. Ripoll and V. M. Perez-Garcia, "Barrier resonances in Bose-Einstein condensation," *Phys. Rev. A*, vol. 59, p. 2220, 1999.

[161] A. I. Nicolin, "Resonant wave formation in Bose-Einstein condensates," *Phys. Rev. E*, vol. 84, p. 056202, 2011.

[162] S. Pollack, D. Dries, R. Hulet, K. M. F. Magalhães, E. Henn, E. Ramos, M. Caracanhas, and V. S. Bagnato, "Collective excitation of a Bose-Einstein condensate by modulation of the atomic scattering length," *Phys. Rev. A*, vol. 81, p. 053627, 2010.

[163] I. Vidanović, A. Balaž, H. Al-Jibbouri, and A. Pelster, "Nonlinear Bose-Einstein condensate dynamics induced by a harmonic modulation of the s-wave scattering length," *Phys. Rev. A*, vol. 84, p. 013618, 2011.

[164] W. Cairncross and A. Pelster, "Parametric resonance in Bose-Einstein condensates with periodic modulation of attractive interaction," *The European Physical Journal D*, vol. 68, p. 1, 2014.

[165] A. I. Nicolin, "Faraday waves in Bose-Einstein condensates subject to anisotropic transverse confinement," *Rom. Rep. Phys*, vol. 63, p. 7, 2011.

[166] I. Vidanović, H. Al-Jibbouri, A. Balaž, and A. Pelster, "Parametric and geometric resonances of collective oscillation modes in Bose-Einstein condensates," *Physica Scripta*, vol. 2012, p. 014003, 2012.

[167] H. Al-Jibbouri, I. Vidanović, A. Balaž, and A. Pelster, “Geometric resonances in Bose-Einstein condensates with two-and three-body interactions,” *Journal of Physics B: Atomic, Molecular and Optical Physics*, vol. 46, p. 065303, 2013.

[168] L. Pitaevskii and S. Stringari, “Landau damping in dilute Bose gases,” *Physics Letters A*, vol. 235, p. 398, 1997.

[169] L. Pitaevskii, “Phenomenological theory of mode collapse-revival in a confined Bose gas,” *Physics Letters A*, vol. 229, p. 406, 1997.

[170] R. Graham, D. Walls, M. Collett, M. Fliesser, and E. M. Wright, “Collapses and revivals of collective excitations in trapped Bose condensates,” *Phys. Rev. A*, vol. 57, p. 503, 1998.

[171] Y. Gao and Y. Cai, “Numerical methods for bogoliubov-de gennes excitations of Bose-Einstein condensates,” *Journal of Computational Physics*, vol. 403, p. 109058, 2020.

[172] A. Roy, S. Pal, S. Gautam, D. Angom, and P. Muruganandam, “Fact: Fortran toolbox for calculating fluctuations in atomic condensates,” *Comput. Phys. Commun.*, vol. 256, p. 107288, 2020.

[173] H. Wang, “A time-splitting spectral method for computing dynamics of spinor $f = 1$ Bose-Einstein condensates,” *Computer Mathematics*, vol. 84, p. 925, 2007.

[174] W. Bao and F. Y. Lim, “Computing ground states of spin-1 Bose-Einstein condensates by the normalized gradient flow,” *SIAM Journal on Scientific Computing*, vol. 30, p. 1925, 2008.

[175] W. Bao, I.-L. Chern, and Y. Zhang, “Efficient numerical methods for computing ground states of spin-1 Bose-Einstein condensates based on their characterizations,” *Journal of Computational Physics*, vol. 253, p. 189, 2013.

[176] J. Javanainen and J. Ruostekoski, “Symbolic calculation in development of algorithms: split-step methods for the Gross–Pitaevskii equation,” *Journal of Physics A: Mathematical and General*, vol. 39, p. L179, 2006.

[177] H. Wang, “An efficient numerical method for computing dynamics of spin $f = 2$ Bose-Einstein condensates,” *Journal of Computational Physics*, vol. 230, p. 6155, 2011.

[178] H. Wang, “A projection gradient method for computing ground state of spin-2 Bose-Einstein condensates,” *Journal of Computational Physics*, vol. 274, p. 473488, 2014.

[179] H. Wang and Z. Xu, “Projection gradient method for energy functional minimization with a constraint and its application to computing the ground state of

spin–orbit-coupled Bose-Einstein condensates," *Comput. Phys. Commun.*, vol. 185, p. 2803, 2014.

[180] I. S. Duff and G. A. Watson, *The State of the Art in Numerical Analysis, Vol. 63.* 1997.

[181] P. Kaur, A. Roy, and S. Gautam, "Fortress: Fortran programs for solving coupled Gross–Pitaevskii equations for spin-orbit coupled spin-1 Bose-Einstein condensate," *Comput. Phys. Commun.*, vol. 259, p. 107671, 2021.

[182] P. Kaur, *Spin-orbit-coupled Ultracold Bosons in Continuum and Optical Lattices.* PhD thesis, Indian Institute of Technology Ropar, 2023.

[183] L. Salasnich, A. Parola, and L. Reatto, "Effective wave equations for the dynamics of cigar-shaped and disk-shaped Bose condensates," *Phys. Rev. A*, vol. 65, p. 043614, 2002.

[184] https://www.netlib.org/lapack/.

[185] S. Gautam and S. K. Adhikari, "Spontaneous symmetry breaking in a spin-orbit-coupled $f = 2$ spinor condensate," *Phys. Rev. A*, vol. 91, p. 013624, 2015.

[186] R. Burden and J. Faires, "Numerical differentiation & integration numerical differentiation I," *Numerical analysis*, pp. 174–184, 2011.

[187] M. Rezghi and L. Eldén, "Diagonalization of tensors with circulant structure," *Linear Algebra and its Applications*, vol. 435, p. 422, 2011.

[188] Y. Saad, *Iterative methods for sparse linear systems.* SIAM, 2003.

[189] O. Schenk, K. Gärtner, and W. Fichtner, "Efficient sparse lu factorization with left-right looking strategy on shared memory multiprocessors," *BIT Numerical Mathematics*, vol. 40, p. 158, 2000.

[190] A. L. Gaunt, T. F. Schmidutz, I. Gotlibovych, R. P. Smith, and Z. Hadzibabic, "Bose-Einstein condensation of atoms in a uniform potential," *Phys. Rev. Lett.*, vol. 110, p. 200406, 2013.

[191] B. M. Anderson, G. Juzeliūnas, V. M. Galitski, and I. B. Spielman, "Synthetic 3D spin-orbit coupling," *Phys. Rev. Lett.*, vol. 108, p. 235301, 2012.

[192] E. G. M. van Kempen, S. J. J. M. F. Kokkelmans, D. J. Heinzen, and B. J. Verhaar, "Interisotope determination of ultracold rubidium interactions from three high-precision experiments," *Phys. Rev. Lett.*, vol. 88, p. 093201, 2002.

[193] P. Banger, P. Kaur, and S. Gautam, "Semi-implicit finite-difference methods to study the spin-orbit-and coherently-coupled spinor Bose-Einstein condensates," *Int. J. Mod. Phys. C*, vol. 33, p. 2250046, 2021.

[194] P. Banger, P. Kaur, A. Roy, and S. Gautam, "Fortress: Fortran programs to solve coupled Gross–Pitaevskii equations for spin-orbit coupled spin-f Bose-Einstein condensate with spin $f = 1$ or 2," *Comput. Phys. Commun.*, vol. 279, p. 108442, 2022.

[195] Z. Wu, L. Zhang, W. Sun, X.-T. Xu, B.-Z. Wang, S.-C. Ji, Y. Deng, S. Chen, X.-J. Liu, and J.-W. Pan, "Realization of two-dimensional spin-orbit coupling for Bose-Einstein condensates," *Science*, vol. 354, p. 83, 2016.

[196] B. D. Cohen-Tannoudji and F. Laloë, *Quantum Mechanics, Volume 1: Basic Concepts, Tools, and Applications, 2nd Edition.* New York: Wiley, 1977.

[197] E. Van Kempen, S. Kokkelmans, D. Heinzen, and B. Verhaar, "Interisotope determination of ultracold rubidium interactions from three high-precision experiments," *Phys. Rev. Lett.*, vol. 88, p. 093201, 2002.

[198] A. Crubellier, O. Dulieu, F. Masnou-Seeuws, M. Elbs, H. Knöckel, and E. Tiemann, "Simple determination of Na 2 scattering lengths using observed bound levels at the ground state asymptote," *The European Physical Journal D-Atomic, Molecular, Optical and Plasma Physics*, vol. 6, p. 211, 1999.

[199] S. Gautam and S. K. Adhikari, "Phase separation in a spin-orbit-coupled Bose-Einstein condensate," *Phys. Rev. A*, vol. 90, p. 043619, 2014.

[200] Q. Zhao and H. Bi, "Vortex dynamics in spin-1 spin-orbit-coupled rotating Bose-Einstein condensates," *International Journal of Theoretical Physics*, vol. 60, p. 2778, 2021.

[201] S. Mardonov, E. Y. Sherman, J. Muga, H.-W. Wang, Y. Ban, and X. Chen, "Collapse of spin-orbit-coupled Bose-Einstein condensates," *Phys. Rev. A*, vol. 91, p. 043604, 2015.

[202] A. Widera, F. Gerbier, S. Fölling, T. Gericke, O. Mandel, and I. Bloch, "Precision measurement of spin-dependent interaction strengths for spin-1 and spin-2 ^{87}Rb atoms," *New Journal of Physics*, vol. 8, p. 152, 2006.

[203] Z. F. Xu, Y. Kawaguchi, L. You, and M. Ueda, "Symmetry classification of spin-orbit-coupled spinor Bose-Einstein condensates," *Phys. Rev. A*, vol. 86, p. 033628, 2012.

[204] Z. F. Xu, R. Lü, and L. You, "Emergent patterns in a spin-orbit-coupled spin-2 Bose-Einstein condensate," *Phys. Rev. A*, vol. 83, p. 053602, 2011.

[205] P. Banger, R. K. Kumar, A. Roy, and S. Gautam, "Effective potentials in a rotating spin-orbit-coupled spin-1 spinor condensate," *J. Phys.: Condens. Matter*, vol. 35, p. 045401, 2022.

[206] P. Banger, "Vortex lattice formation in spin-orbit-coupled spin-2 Bose-Einstein condensate under rotation," *Journal of Low Temperature Physics*, vol. 213, p. 155, 2023.

[207] R. Ravisankar, D. Vudragović, P. Muruganandam, A. Balaž, and S. K. Adhikari, "Spin-1 spin-orbit-and rabi-coupled Bose-Einstein condensate solver," *Comput. Phys. Commun.*, vol. 259, p. 107657, 2021.

[208] M. Theis, G. Thalhammer, K. Winkler, M. Hellwig, G. Ruff, R. Grimm, and J. H. Denschlag, "Tuning the scattering length with an optically induced feshbach resonance," *Phys. Rev. Lett.*, vol. 93, p. 123001, 2004.

[209] M. A. Khamehchi, Y. Zhang, C. Hamner, T. Busch, and P. Engels, "Measurement of collective excitations in a spin-orbit-coupled Bose-Einstein condensate," *Phys. Rev. A*, vol. 90, p. 063624, 2014.

[210] S.-C. Ji, L. Zhang, X.-T. Xu, Z. Wu, Y. Deng, S. Chen, and J.-W. Pan, "Softening of roton and phonon modes in a Bose-Einstein condensate with spin-orbit coupling," *Phys. Rev. Lett.*, vol. 114, p. 105301, 2015.

[211] Rajat, A. Roy, and S. Gautam, "Collective excitations in cigar-shaped spin-orbit-coupled spin-1 Bose-Einstein condensates," *Phys. Rev. A*, vol. 106, p. 013304, 2022.

[212] V. M. Perez-Garcia, H. Michinel, J. Cirac, M. Lewenstein, and P. Zoller, "Low energy excitations of a Bose-Einstein condensate: A time-dependent variational analysis," *Phys. Rev. Lett.*, vol. 77, p. 5320, 1996.

[213] P. Banger, Rajat, A. Roy, and S. Gautam, "Quantum phases and the spectrum of collective modes in a spin-1 Bose-Einstein condensate with spin-orbital-angular-momentum coupling," *Phys. Rev. A*, vol. 108, p. 043310, 2023.

[214] Y. Li, L. P. Pitaevskii, and S. Stringari, "Quantum tricriticality and phase transitions in spin-orbit coupled Bose-Einstein condensates," *Phys. Rev. Lett.*, vol. 108, p. 225301, 2012.

[215] X.-L. Chen, X.-J. Liu, and H. Hu, "Quantum and thermal fluctuations in a raman spin-orbit-coupled Bose gas," *Phys. Rev. A*, vol. 96, p. 013625, 2017.

[216] G. I. Martone, Y. Li, L. P. Pitaevskii, and S. Stringari, "Anisotropic dynamics of a spin-orbit-coupled Bose-Einstein condensate," *Phys. Rev. A*, vol. 86, p. 063621, 2012.

[217] W. Zheng and Z. Li, "Collective modes of a spin-orbit-coupled Bose-Einstein condensate: A hydrodynamic approach," *Phys. Rev. A*, vol. 85, p. 053607, 2012.

[218] L. Chen, H. Pu, Z.-Q. Yu, and Y. Zhang, “Collective excitation of a trapped Bose-Einstein condensate with spin-orbit coupling,” *Phys. Rev. A*, vol. 95, p. 033616, 2017.

[219] K. T. Geier, G. I. Martone, P. Hauke, and S. Stringari, “Exciting the goldstone modes of a supersolid spin-orbit-coupled Bose gas,” *Phys. Rev. Lett.*, vol. 127, p. 115301, 2021.

[220] K. T. Geier, G. I. Martone, P. Hauke, W. Ketterle, and S. Stringari, “Dynamics of stripe patterns in supersolid spin-orbit-coupled Bose gases,” *Phys. Rev. Lett.*, vol. 130, p. 156001, 2023.

[221] T.-L. Ho and S. Zhang, “Bose-Einstein condensates with spin-orbit interaction,” *Phys. Rev. Lett.*, vol. 107, p. 150403, 2011.

[222] Y. Li, G. I. Martone, L. P. Pitaevskii, and S. Stringari, “Superstripes and the excitation spectrum of a spin-orbit-coupled Bose-Einstein condensate,” *Phys. Rev. Lett.*, vol. 110, p. 235302, 2013.

[223] W.-L. Xia, L. Chen, T.-T. Li, Y. Zhang, and Q. Zhu, “Metastable supersolid in spin-orbit-coupled Bose-Einstein condensates,” *Phys. Rev. A*, vol. 107, p. 053302, 2023.

[224] G. I. Martone and S. Stringari, “Supersolid phase of a spin-orbit-coupled Bose-Einstein condensate: A perturbation approach,” *SciPost Phys.*, vol. 11, p. 092, 2021.

[225] Rajat, Ritu, A. Roy, and S. Gautam, “Temperature-induced supersolidity in spin-orbit-coupled Bose gases,” 2023.

[226] R. B. Lehoucq, D. C. Sorensen, and C. Yang, “Arpack users’ guide - solution of large-scale eigenvalue problems with implicitly restarted arnoldi methods,” in *Software, Environments, and Tools*, 1998.